RADAR OBSERVATIONS OF COMETARY NUCLEI

by

PAUL GASTON DAVID KAMOUN

Ingenieur, Radiocommunications & Radar
Ecole Superieure d'Electricite, France
(1977)
D.U.E.S. Math. & Phys. (1973)
& Cert. d'Astronomie, Universite d'Orsay, France (1977)

SUBMITTED TO THE DEPARTMENT OF
EARTH AND PLANETARY SCIENCES
IN PARTIAL FULFILLMENT OF
THE REQUIREMENTS FOR THE
DEGREE OF
DOCTOR OF PHILOSOPHY

at the
MASSACHUSETTS INSTITUTE OF TECHNOLOGY
May 1983

Signature of Author____
Department of Earth and Planetary Sciences, May 1983

Certified by____
Gordon H. Pettengill, Thesis supervisor

Accepted by____
Theodore R. Madden, Chairman, Department Committee

RADAR OBSERVATIONS OF COMETARY NUCLEI

by

PAUL KAMOUN

Submitted to the Department of Earth and Planetary Sciences
on May 18, 1983 in partial fulfillment
of the requirements for the degree of
Doctor of Philosophy in Planetary Sciences

ABSTRACT

The main goal of this research has been the detection of comet nuclei by radar in order to discriminate among the different models proposed to account for the properties of these nuclei. Indeed radar astronomy is the only astronomical technique presently available which allows the direct probing of a comet nucleus. Following the successful detection of two of these nuclei, an attempt has been made to identify some of their physical properties.

In the first part of this thesis, a comprehensive study of the interests and problems attached to radar astronomical observations of comets is attempted. Then, the observations of comet P/Encke (1980), the observations of comet P/Grigg-Skjellerup (1982), and the attempts on comet Austin (1982) and P/Churyumov-Gerasimenko (1982), along with the corresponding data reduction procedures are described. These observations have been made using the Arecibo Observatory's S-band radar system, which is the most sensitive system presently available for radar astronomy. The first two comets have been detected at a level of, respectively, about 6 and 10 times the standard deviations of the associated noise, while the comets Austin and P/Churyumov-Gerasimenko did not return a detectable echo.

In the following section, it is shown how the radar results are compatible only with the discrete single-body model and rule out dust-swarm or sand-bank models for the nucleus. The analysis and quantitative interpretation of the radar results in terms of the physical properties of the nuclei are then carried out successively for each of the four comets, P/Encke, P/Grigg-Skjellerup, Austin and P/Churyumov-Gerasimenko. In particular the radar cross-sections, sizes, and reflectivities of these nuclei are discussed. The radius of the nucleus has been found to lie in the range 0.4-3.6 km for Encke, and in the range 0.4-2.2 km for Grigg-Skjellerup, with a most likely value of the order of 1 km in both cases. Upper limits of about 2 km and 3 km have been estimated for the nuclear radii of comets Austin and Churyumov-Gerasimenko, respectively. Upper limits on the number density of millimeter- and centimeter-sized ice and dust particles in the comae have also been estimated for all four comets.

Finally, future opportunities for radar observations of comets, including a detailed discussion of comet P/Halley, are presented.

Thesis Supervisor: Gordon H. Pettengill

Title: Professor of Planetary Physics

ACKNOWLEDGEMENTS

I am very grateful to all those from whom I have learned, from my parents to my professors at M.I.T.

I would like to express my deep thanks to Gordon Pettengill, my thesis advisor, for his constant interest, receptiveness and support during my years at M.I.T., as well as for carefully and very kindly reading and correcting the successive drafts of this thesis. I am very grateful to Irwin Shapiro for so generously serving as my advisor during Gordon's sabbatical leave, for his friendliness, and for his numerous beneficial remarks and suggestions during the past years. It has been a unique privilege to learn about comets with Fred Whipple and Zdenek Sekanina. I owe particular thanks to Fred Whipple for being a member of my thesis committee and for granting me so many rewarding discussions. I owe special thanks to Zdenek Sekanina for his kindness and permanent willingness to answer and discuss my questions.

I would like to thank Donald Campbell for scheduling the observations, in particular on short notice for comet Austin, and for ensuring that the radar system was in good operating condition. I would like to thank Steven Ostro for introducing me to some of his software and for explaining several aspects of the observing procedure in the early stages of my research. In general, I would like to thank the whole NAIC staff at the Arecibo Observatory for its collaboration during the observations. Beside special thanks to Rey Velez, Ernesto Ruiz, and Gerry Giles, I address my thanks to all the computer and telescope operators whose friendship and humor will be my best "souvenirs" from Arecibo.

I am very grateful to Brian Marsden and Dan Green for many discussions and for communication of unpublished data. I would like to thank Peter Ford for his invaluable help and for his constant readiness to share some of his expertise in software. To Paul Feldman, Steve Larson, Hyron Spinrad, and William Westphal, I owe special thanks for communication of many results (often unpublished) and for many encouraging and very valuable discussions.

I would like to thank Ted Madden for being chairman of my thesis committee and for his great kindness during the past few years. I would like to thank Jim Elliot for serving on my thesis committee and, along with Sam Conner and Ted Dunham, for generous assistance during optical observations of comets. I had the chance of having a very fine friend and office-mate in the person of Nathaniel "Chip" Cohen. Interacting with Chip has always been invaluable. The very rewarding and friendly interaction with Sue Wyckoff, Michel Festou, and John Lewis is gratefully acknowledged. I would like to thank Joan Caplin for teaching me the use of the word-processor.

It would be impossible to mention all those who have contributed to this enterprise in one way or another. I deeply thank all of them.

To my parents Robert and Suzanne Kamoun, I would like to express my extreme gratitude for having faithfully paved the way for so many years.

Along with Ruth, my wife, whose role and merit could never be emphasized enough, I would like to thank all our friends who filled our years at M.I.T. with so many good memories.

This research has been supported by NASA grant NGR 22-009-672

CONTENTS

PART A. INTRODUCTION

Chapter 1. The study of comets and the contribution of radar astronomy

1.1 Introduction....17
1.1.1. Observations and theories regarding the nature and origin of comets....17
1.1.2. Motivations for radar studies of comets....23
1.2 Radar detectability of comets....24
1.2.1. Introduction....24
1.2.2. Detectability of the components of a comet....25
1.2.3. Past attempts to observe comets with available radar systems....31

PART B. COMET P/ENCKE: OBSERVATIONS AND DATA REDUCTION

Chapter 2. The periodic comet Encke

2.1 History....37
2.2 Physical characteristics....38
2.2.1. Optical appearance....38
2.2.2. Light curve and spectrum....39
2.2.3. Non-gravitational motion and spin of the nucleus....40
2.2.4. Structure and evolution....42

Chapter 3. The 1980 radar observation of P/Encke

3.1 Introduction. Facility and observing conditions....50
3.2 Ephemerides and antenna pointing....51
3.3 The Arecibo S-band radar system....52
3.3.1. The transmitting chain....52
3.3.2. The receiving chain....55
3.3.3. Recorded data description....57
3.3.4. Summary of the observing parameters for P/Encke....58

Chapter 4. Data reduction

4.1 The background free spectra....65
4.2 Weighted summation and calibration of spectra....66

PART C. COMET P/GRIGG-SKJELLERUP: OBSERVATIONS AND DATA REDUCTION

Chapter 5. The periodic comet P/Grigg-Skjellerup

5.1 History....85
5.2 Physical characteristics....86
5.2.1. Optical appearance....86
5.2.2. Non-gravitational motion and spin of nucleus....86

Chapter 6. P/Grigg-Skjellerup: radar observation and data reduction

6.1 Observations..90
6.2 Radar system configuration.......................................90
6.3 Data reduction..92
6.4 Spectra..92

PART D. COMET AUSTIN AND COMET P/CHURYUMOV-GERASIMENKO: OBSERVATIONS AND DATA REDUCTION

Chapter 7. Comet Austin: observations and data reduction

7.1 History..108
7.2 The radar observations..109
7.3 Data reduction and results.....................................109

Chapter 8. Comet Churyumov-Gerasimenko: Observations and data reduction

8.1 The periodic comet Churyumov-Gerasimenko................121
8.2 The radar observations..122
8.3 Data reduction..122

PART E. MODELING THE NUCLEUS

Chapter 9. Modeling the nucleus

9.1 Introduction: Competing models...............................137
9.2 Model selection using the radar results...................137

PART F. COMET P/ENCKE: DATA ANALYSIS AND INTERPRETATION

Chapter 10. Comet Encke: data analysis and results

10.1 Cross-correlation and maximization of the signal-to-noise ratio..142
10.1.1. Cross-correlation...142
10.1.2. The standard deviation of the smoothed spectrum.....144
10.2 Least-Squares estimation of the signal parameters......146
10.2.1. Least-squares technique.....................................146
10.2.2. Scattering law exponent and limb-to-limb bandwidth of the echo...152
10.2.3. Center frequency of the echo...............................153
10.3 Estimating the radar cross-section..........................155

Chapter 11. Interpretation

11.1 Size of the nucleus of P/Encke................................174
11.2 Other physical properties of the nucleus...................176
11.3 Limits on the number density of grains in the coma.....179

PART G. COMET GRIGG-SKJELLERUP: DATA ANALYSIS AND INTERPRETATION

Chapter 12. Comet Grigg-Skjellerup: data analysis and interpretation

12.1 Center frequency and limb-to-limb bandwidth of the echo..194

12.2 Radar cross-section....................................196
12.3 Size of the nucleus....................................203
12.4 Limits on the number of grains in the coma.............206

PART H. COMET AUSTIN AND COMET P/CHURYUMOV-GERASIMENKO: DATA ANALYSIS AND INTERPRETATION

Chapter 13. Comet Austin. Data analysis and interpretation

13.1 Cross-correlation......................................213
13.2 Upper limits on the radar cross-section and size of the target...214
13.3 Upper limits on the number of grains in the coma.......215

Chapter 14. Comet C-G. Data analysis and interpretation

14.1 Cross-correlation......................................225
14.2 Upper limits on the radar cross-section and size of the target...225
14.3 Upper limits on the number of grains in the coma.......226

PART I. THE NATURE OF COMET NUCLEI

Chapter 15. Implications of the radar results for the nature of comet nuclei

15.1 Summary of the results.................................230
15.2 Discussion...231

Chapter 16. Conclusion

16.1 Further related work needed............................237
16.2 The case of comet P/Halley.............................239
16.3 Conclusion...243

Appendices

Appendix 1. The radar equation and its application to the case of a comet nucleus.............................244
Appendix 2. The frequency switching technique...................251
Appendix 3. Processing of the echo signal.......................256

References...261

LIST OF FIGURES

Chapter 1

1.1 Components of a comet....................................34

1.2 Nucleus rotation and non-gravitational forces....................34

1.3 Comet West 1976 VI, photograph (Courtesy H. Giclas, Lowell Obs.)..35

Chapter 2

2.1 Photograph of comet P/Encke (Courtesy F. Whipple)................45

2.2 Photograph of comet P/Encke (Courtesy H. Spinrad & J. Stauffer)...46

2.3 Mean lightcurve of P/Encke (From Sekanina, 1979).................47

2.4 (a,b) Image dissector scanner spectra of P/Encke (From Spinrad, 1981)..48

2.5 P/Encke: variation of the nucleus pole position with time (From Whipple and Sekanina, 1981).....................................49

Chapter 3

3.1 P/Encke. Configuration of the Sun-Earth-Comet system for the 1980 radar observations...60

3.2 Arecibo Observatory, photograph (Courtesy G. Giles, Arec. Obs.)...61

3.3 Scattering functions of various forms of targets (From Green, 1968) 62

3.4 Radar system configuration for the observations of P/Encke (Courtesy D. Campbell, Arecibo Observatory)..............................63

3.5 Antenna gain calibration..64

3.6 System temperature calibration....................................64

Chapter 4

4.1 through 4.7 P/Encke. Raw radar spectra for each day from November 2 through November 8, 1980.....................................73-79

4.8 P/Encke. Weighted sum of the data of November 2, 3, and 4, 1980...80

4.9 P/Encke. Weighted sum of the data of November 5 and 6, 1980......81

4.10 P/Encke. Weighted sum of the data of November 7 and 8, 1980.....82

4.11 P/Encke. Weighted sum of all the radar data.....................83

Chapter 5

5.1 Comet P/Grigg-Skjellerup. CCD image (Courtesy S. Larson)..........89

Chapter 6

6.1 P/Grigg-Skjellerup. Configuration of the Sun-Earth-Comet system for the 1982 radar observations.......................................96

6.2 through 6.10 P/Grigg-Skjellerup. Weighted sum of the radar data for each day, from May 21 through June 2, 1982...................97-105

6.11 P/Grigg-Skjellerup. Weighted sum of all the radar data..........106

Chapter 7

7.1 Comet Austin, Photograph (Courtesy J. Kielkopf).................113

7.2 Austin. Ephemeris corrections..................................114

7.3 through 7.7 Austin. Weighted sum of the radar data for each day, from August 8 through August 12, 1982.......................115-119

7.8 Austin. Weighted sum of the data of August 8 to 11, 1982.........120

Chapter 8

8.1 Comet P/Churyumov-Gerasimenko (C-G). Configuration of the Sun-Earth-Comet system for the 1982 radar observations.....................126

8.2 through 8.9 P/C-G. Weighted sum of the data for each day of observation between November 8 and November 15, 1982.........127-134

8.10 P/C-G. Weighted sum of all the data..............................135

Chapter 10

10.1a Cross-correlation algorithm...................................159

10.1b Least-squares algorithm.......................................160

10.2 Smoothing filter shape...161

10.3 P/Encke. Signal-to-noise ratios obtained with various filters...161

10.4 Least-squares estimates of bandwidth............................162

10.5 through 10.11 P/Encke. Final smoothed spectra for each day from November 2 through 8, 1980...............................163-169

10.12 through 10.15 P/Encke. Final normalized smoothed spectra for the combinations November 2, 3, 4, November 5, 6, November 7, 8, and November 2 through 8, 1980...............................170-173

Chapter 11

11.1 P/Encke. Angle between the nucleus spin axis and the radar line-of-sight as a function of the nucleus pole position.........190

11.2 P/Encke. Radius of the nucleus as a function of the angle between spin axis and radar line-of-sight..................................191

11.3 P/Encke. Path of the subradar point on the nucleus..............192

Chapter 12

12.1 (a-d) P/Grigg-Skjellerup. Results of test of reality of echo....... 209-210

12.2 P/Grigg-Skjellerup. Variations of the nucleus radar cross-section as a function of time..211

Chapter 13

13.1 through 13.5 Comet Austin. Final smoothed spectra for each day from August 8 through August 12, 1982.............................218-222

13.6 Austin. Final smoothed spectra for the combination August, 8, 9, 10, and 11, 1982...223

13.7 Absolute upper limit on the echo bandwidth of comet Austin and upper limit on the nuclear radius...................................224

Chapter 14

14.1 P/C-G. Final smoothed spectra for the sum of all data, November 8 through 15, 1982...228

Chapter 15

15.1 Model of cometary nucleus.......................................236

LIST OF TABLES

Chapter 2. P/Encke

2.1 Orbital elements..38

Chapter 3. P/Encke

3.1 Receiving ephemerides..50
3.2 Effective observing parameters...............................58

Chapter 4. P/Encke

4.1 Tabulated echo power...71

Chapter 5. P/Grigg-Skjellerup

5.1 Orbital elements...85

Chapter 6. P/Grigg-Skjellerup

6.1 Receiving ephemerides..91
6.2 Effective observing parameters...............................93
6.3 Tabulated echo power...94

Chapter 7. Comet Austin

7.1 Orbital elements..108
7.2 Receiving ephemerides.......................................111
7.3 Effective observing parameters..............................111

Chapter 8. Comet Churyumov-Gerasimenko

8.1 Orbital elements..121
8.2 Receiving ephemerides.......................................123
8.3 Effective observing parameters..............................123
8.4 Tabulated echo power..124

Chapter 10. P/Encke

10.1 Tabulated echo power.......................................155
10.2 Echo bandwidth and radar cross-section.....................156

Chapter 11. P/Encke

11.1 Angle between nucleus spin axis and radar line-of-sight. Phase angle....174

11.2 Estimation of the nuclear radius....175

11.3 Radius and albedo of the nucleus....178

11.4 Number of particles in the coma....186

Chapter 12. P/Grigg-Skjellerup

12.1 Nucleus: Radius as a function of rotation period and angle between spin axis and line-of-sight....206

12.2 Number of particles in the coma....206

Chapter 13. Austin

13.1 Tabulated echo power....213

Chapter 15

15.1 Radar cross-sections and radii for the four comets: summary.....230

15.2 Number of particles in the coma for the four comets: summary....231

Chapter 16

16.1 P/Halley. Geocentric distance and declination at the 1985/1986 close approaches to the Earth (from D. Yeomans, 1981)....241

FOREWORD

To our children

"Praise His name! Praise Him from the heavens; Praise Him in the heights. Praise Him, all his angels; praise Him all his hosts. Praise Him, sun and moon; praise Him all you stars of light. Praise Him highest heavens and waters above the heavens. Let them praise His name; for He commanded and they were created. He fixed them fast forever and ever. He gave a law which none transgresses."

King David, Psalms 148:1-6 (circa 900 BCE)

"It is a special blessing to belong among those who can and may devote their best energies to the contemplation and exploration of objective and timeless things. How happy and grateful am I for having been granted this blessing, which bestows upon one a large measure of independence from one's personal fate and from the attitude of one's contemporaries. Yet this independence must not inure us to the awareness of the duties that constantly bind us to the past, present and future of humankind at large.

Our situation on this earth seems strange. Every one of us appears here involuntarily and uninvited for a short stay, without knowing the why and the wherefore. In our daily lives we feel only that man is here for the sake of others, for those whom we love and for many other beings whose fate is connected with our own.

I am often worried at the thought that my life is based to such an extent on the work of my fellow human beings, and I am aware of my great indebtness to them...

...Although I am a typical loner in daily life, my consciousness of belonging to the invisible community of those who strive for truth, beauty and justice has preserved me from feeling isolated.

The most beautiful and deepest experience a man can have is the sense of the mysterious. It is the underlying principle of religion as well as of all serious endeavour in art and science. He who never had this experience seems to me, if not dead, then at least blind. To sense that behind anything that can be experienced there is a something that our mind cannot grasp and whose beauty and sublimity reaches us only indirectly and as a feeble reflexion, this is religiousness. In this sense I am religious. To me it suffices to wonder at these secrets and to attempt humbly to grasp with my mind a mere image of the lofty structure of all that there is."

Albert Einstein
in "My Credo", recorded at the initiative of the "German League of Human Rights" in Berlin, autumn 1932, a few days before Einstein left Europe forever.

PART A. INTRODUCTION

CHAPTER 1

THE STUDY OF COMETS AND THE CONTRIBUTION OF RADAR ASTRONOMY

1.1 Introduction

1.1.1. Observations and theories regarding the nature and origin of comets

Comets have always been among the most fascinating celestial objects, not only because of their spectacular appearance but also because little was known of their nature and origin. Their small mass and long period of revolution indicate that they should not have evolved considerably since their time of formation. Thus they are believed to be samples of the original solar nebula, or perhaps objects coming from interstellar space. Moreover, it has recently been hypothesized that they may have played a role in the initiation of life on Earth. We will first review some observational data relative to the nature of comets, then we will digress on the current hypotheses about their origin.

a. Observations. Comets describe solar trajectories which are elliptical, parabolic or hyperbolic, depending on their origin and the perturbations they have experienced in the process of their evolution in the solar system. The elliptical trajectories, in turn, may be classed as either long-period or short-period, depending on whether their aphelion distance exceeds about 50 AU or not.

As seen through a telescope, the appearance of a comet changes while the object is moving inwards toward the sun and then away from the sun after reaching its perihelion. At large heliocentric distances, the image of a comet on a photographic plate is almost stellar in nature. This image gets fuzzier as the comet approaches the sun and eventually one or more tails may develop, oriented approximately in the antisolar direction. Comets are seldom observed when they are much further away from the sun than the planets Jupiter or Saturn. At that distance, they are usually very faint and their spectra closely resemble that of the sun, a fact suggesting that they are composed of solid particles reflecting sunlight.

More than 15 years ago, it was already known that when a comet is within about three astronomical units from the sun, its spectrum changes. Superimposed upon the spectrum of reflected sunlight there are bright emission lines (or series of many closely spaced lines or bands) due to evaporated chemical species: C_2, OH, CN, NH, NH_2.

Some comets, passing within a few hundred thousand kilometers of the solar surface at perihelion, were also known to reach temperatures as high as 4500K. If a comet approaches very closely to the sun, its spectrum changes again and bright emission lines of various metals appear: sodium, iron, silicon, magnesium, and others.

When a comet is fully developed, it may present all or only some of the following components (Fig. 1.1): 1) a head composed of a nucleus and a coma surrounding the nucleus; 2) a tail that can be several tens of million kilometers long.

A very popular model for the nucleus in the early twentieth century predicated a "dust-swarm" or swarm of solid particles of unknown sizes, each particle carrying with it an envelope of gas, mostly hydrocarbons. However, this model faced a number of difficulties, eventually leading to a "dirty snowball" model developed by Fred Whipple (1950). A major objection to the dust-swarm model grew out of the observation that sun-grazing comets persist after passage through the inner solar corona, a feat not possible for a dust-swarm nucleus. Indeed, not only should tidal disruption destroy a dust-swarm, but the efficient vaporization of large quantities of volatiles would quickly deplete it. Lyttleton (1953) tried to adapt this model assuming a vast irregularly-shaped swarm of widely separated dust particles of meteoric dimensions moving in individual orbits, not held together by mutual gravitation, thus eliminating the problem of tidal disruption during a close approach to the sun. He assumed that "collisions between particles when the comet is on the perihelion side of its orbit, and especially near perihelion, bring about emission of light and release of gas, and will cause fragmentation into a host of far smaller particles" (Lyttleton, 1977). The relative speeds of the collisions would be of the order of 1 km/s and would depend on both the orbital speed and the size of the swarm.

Another clue was provided by the variation of the orbital period of some comets with time. In the early 19th century, the motion of P/Encke was observed to be affected by "non-gravitational" forces , the orbital period decreasing by about 2.5 hrs with every revolution around the sun. The hypothesis of a resisting medium acting on a "sand bank" nucleus (instead of a solid nucleus which would be affected far less) was still considered in the 1940's, although no reasonable description of such a medium could be given. Besides this, it has been observed that not only did some comets have decreasing orbital periods while others, like P/Halley, had increasing periods, but also the rate of change of this period for a given comet could vary by a large amount over many orbits.

The orbital period of P/Encke is for instance only a few minutes shorter at each revolution today, whereas it was formerly shortened by a few hours at each apparition. These phenomena led Fred Whipple to suggest that a comet nucleus may be more like a rotating "dirty (or dusty) snowball", with ices sublimating mostly from the sunward parts of the surface but at a rotational lag angle with respect to the sun-nucleus direction. This model (see chapter 2), applied by Whipple and Sekanina to P/Encke, explains in detail the behavior of this comet as observed over the last two centuries. Basically, as shown in figure 1.2, for a nucleus spinning in a sense opposite to its sense of orbital motion, an outflow of gas will arise from the sublimating ices, mostly on the "afternoon" side of the nucleus, resulting in a reactive jet force on the nucleus, directly opposite to the direction of maximum sublimation. In this case this force will tend to decrease the semi-major axis of the orbit and shorten the orbital period. A nucleus rotating in the same sense as its orbital motion would be accelerated to a larger orbit with a larger orbital period.

Using this model, Fred Whipple (1982) has obtained rotation periods for 47 comets for which non-gravitational effects have been observed, the sample containing both short- and long-period comets. Whipple's model accounts for most of the observed properties of comet heads. In particular, when the comet approaches within a few astronomical units of the sun, the volatile ices (NH_3, CH_4, CO_2, H_2O) present in the outer layers of such nuclei would sublimate and liberate the dust grains trapped in them, thus forming a cloud of gases, ice and dust particles: the coma.

One of the main goals of this research has been the use of radar observations to discriminate between the two main models proposed for the nucleus.

As seen visually from Earth, a comet shows a head or a coma consisting of neutral molecules (primarily water within 1 AU of the sun), ions resulting from photodissociation by solar radiation and molecular collisions inside the coma, and grains of ice, which sublimate quickly, and silicate dust. Stretched out "behind" the coma are one or more tails produced by the interaction of the solar wind with the material in the coma. The ionized gas forms a plasma tail, trapped nearly in the antisolar direction by the interplanetary magnetic field. The neutral gas and dust particles released from the coma are repulsed by solar radiation pressure, forming a dust tail curved backward with respect to the plasma tail and to the sense of comet motion, because of the conservation of angular momentum.

Sometimes an antitail pointing toward the solar direction is observed. This phenomenon has been explained as an optical illusion associated with a projection effect of the grains located in the orbit plane; thus it is seen best when the Earth crosses the comet's orbital plane. Comets, depending on their characteristics and history, can exhibit all or only some of the features described above.

b. Origin. For centuries comets have been considered bad omens. In medieval times, the idea that comets consisted of poisonous vapors wandering in the Earth's atmosphere was commonly accepted, and it was not until the sixteen century that careful studies by the Danish astronomer Tycho Brahe showed comets to be objects in orbit around the sun, much further from the Earth than the Moon is. Since then, several theories resting mainly on astrometric and photometric observations have been proposed to explain the origin of comets. One of the first plausible theories, proposed by Laplace (1904), assumed that the parabolic and long-period comets are captured from interstellar space, but this was discarded since it gives rise mainly to hyperbolic orbits in the solar system, a fact not in accordance with the observations. Instead, new comets are observed to enter the inner solar system (defined here as the region within the orbit of Jupiter) in near parabolic orbits, which means that most probably they were almost at rest with respect to the sun before being thrown into the inner solar system. Accepting that comets are members of the solar system leaves three contending theories: 1) that comets were condensed from the solar nebula and then, later, collected into a vast cloud at about 50,000 to 100,000 AU from the sun, the "Oort cloud" (Oort, 1950), where they are likely to have experienced very little alteration (perhaps only bombardment by cosmic rays) since they took residence in this region; 2) that comets were recently condensed "in situ" outside of the planetary system; 3) that comets are by-products of either the disruption of a former planet or grandiose eruptions on the giant planets.

The first of these best explains the observed distribution of semi-major axes of new long-period comets as well as the random distribution of their orbital planes and perihelia. Short-period comets are considered to have been captured by Jupiter from the general field of long-period comets. The second theory has been put aside since no sound model for the accretion of the solar system has ever been proposed to support it. The third theory has been put forward by Lagrange (1814). His hypothesis about explosion has been rejected since it implies constraints on the orbits of long-period elliptical and parabolic comets that are not observed. His eruption theory has been studied in detail by Tisserand (1890) who concludes that in order to be detected from Earth, new comets would have to be expelled in specific directions and with specific velocities, which he estimates to be quite improbable. Vsekhsvyatskii (1930, 1931, 1934) has shown that eruption from the giant planets could account for several properties of short-period comets, although it implies a different origin for short- and long-period comets. Furthermore, Van Woèrkom (1948) believes that the capture theory can better account for the origin of short-period comets than the eruption theory. But more recent work (Joss, 1973) asserts that the capture mechanism cannot account for the number of short-period comets. The controversy continues!

1.1.1. Motivations for radar studies of comets

Using the whole arsenal of astronomical techniques, considerable data have been obtained on the nature, composition and physics of the coma and tails. However, very few techniques permit the study of the nucleus itself, and the radar observations discussed here represent the first direct detections of a comet nucleus. Indeed, not only can the most powerful ground-based optical telescopes not resolve cometary nuclei, but even photometric methods face the difficulty of separating the light reflected by the nucleus from that scattered by the coma (Hellmich and Keller, 1981). If the molecules constituting the coma result from the vaporization of ices more volatile than water, then the heliocentric distance where a coma should first appear would be about 140 AU for CO or N_2, 70 AU for CH_4, 10 AU for CO_2, and 7 AU for NH_3.

Observing a comet at such large heliocentric distances, in order to be sure of observing only the bare nucleus, is almost impossible. On the other hand, radiowaves can travel almost unaffected through the coma and can thus directly probe the surface of the nucleus. Because of the low surface temperature and small size of the nucleus, very little radio emission is expected from it. Also, the reflected sunlight contains very little power in the radio range. Thus detection of echoes from a radar signal sent from Earth may be the only practical means of obtaining information on the properties of the nucleus itself.

1.2. Radar Detectability of Comets.

1.2.1. Introduction.

The main motivation for using radar to study comets thus lies in the fact that unlike other ground-based astronomical techniques, radar offers the possibility of observing the nucleus directly, simultaneously obtaining information on its surface-scattering properties, size, spin rate, and orbit.

The history of radar as a research tool began in 1926 when Breit and Tuve (1926) demonstrated the radar principle by obtaining echoes of transmitted radiopulses from the ionosphere. The development of radar astronomy did not occur until after the enormous development of radar during the second world war.

True radar astronomy had its beginning in 1946 when echoes were obtained from the Moon by De Witt and Stodola (1949) and by Bay (1946), and radar was applied to the study of meteor trails by Hey and Stewart (1947) in England. These studies were followed successively by radar observations of the Sun in 1957, the inner planets Venus, Mercury, and

Mars (early to mid 1960's), the asteroid Icarus in 1968, Saturn's rings in 1973, the Galilean satellites of Jupiter in 1976, and, over the last six years, about a dozen asteroids. Comet Encke in 1980 was the first comet to be detected by radar (Kamoun et al., 1982); this detection came more than 30 years after the first radar studies of the ionized trails left by meteoroids, believed to be derived from comets, as they enter the Earth's atmosphere!

So far, six attempts have been made to detect a comet by radar (Section 1.2.4), but only the attempts on P/Encke and P/Grigg-Skjellerup have been successful. Indeed, it will be shown in section 1.2.2. that favorable opportunities to observe comets by radar are rare. Past attempts at observation are briefly summarized in section 1.2.3.

1.2.2. Detectability of the components of a comet.

A comet usually contains two other components, in addition to the nucleus, each of which scatters radio waves differently: the ice and dust particles in the coma and dust tail, and the plasma in the coma and ion tail. We discuss the three components: nucleus, particles and plasma, in turn.

a. Nucleus. The nucleus is the component of a comet most likely to return a radar echo. The radar detectability of comet nuclei is governed by the radar equation (see Appendix 1):

$$\frac{S}{N} = \frac{P_t G^2 \lambda^{5/2} \tau^{1/2}}{4\pi k T_s} \left[\frac{\sigma}{32\pi D^4 L} \frac{R^{3/2}}{\Omega_p^{1/2}} \right] \eta \quad , \qquad (1.1)$$

where S/N is the signal-to-noise ratio (in units of the standard deviation of the background noise fluctuations), R the radius of the (assumed) hard target, σ the ratio of its radar cross-section to its geometric cross-section, Ω_p the magnitude of its apparent rotation vector projected on the celestial sphere, L the attenuation in the coma, and D the geocentric distance of the comet. The effect on the radar detectability of the scattering law obeyed by the comet is characterized by η; it is unity if the spectral density is constant between the maximum and minimum (limb-to-limb) frequency limits, and greater than unity otherwise. The parameters of the radar system are λ the wavelength of the transmitted signals, P_t the transmitted power, G the gain of the antenna relative to an isotropic radiator, T_s the effective system temperature, and τ the integration time. These characteristics differ from one radar system to another but even for the most sensitive of these systems, the S-band radar configuration at Arecibo, a typical comet nucleus, assumed to be a rotating rigid body, can be detected only if it falls within the declination coverage of that telescope and only when it is at a distance less than about 0.3 AU, the exact limit depending on the radius, rotation rate, and reflecting properties of the nucleus.

As for observations of minor planets (see, for example, Pettengill _et al_., 1979), a typical radar experiment to detect echoes from comets consists of the transmission of a CW (continuous-wave), nearly monochromatic signal for the duration of the round-trip echo time delay, followed by the reception of the echo for about the same amount of time. The detectability of the nucleus is not only a function of the parameters of the radar system, but, as is clear from equation (1.1), also depends on the target's surface scattering properties, rotation and size, and, more importantly, on the inverse fourth power of its geocentric distance. This last factor, as mentioned, places the principal limit on detectability. Another problem is often the lack of sufficiently accurate ephemerides, even for periodic comets. The latter problem is especially relevant to radar observations since one needs to know precisely not only the angular position of the object, but also its velocity in order to correct for the Doppler shift introduced by the radial component of the velocity of the target relative to the Earth. Usually inaccuracies of a few seconds of arc for the angular position and of a few tens of meters per second for the radial velocity are tolerable. For most comets the uncertainty is such that, for S-band radar frequencies, it is necessary to search for the echo in a frequency range of a few kilohertz, corresponding to a radial velocity uncertainty of the order of 100 meters per second. Moreover, the rate of change of the Doppler shift needs to be known with less than a 10^{-3} Hz/s uncertainty in order to be able to efficiently combine the data from several days of observations.

The total broadening of the echo spectrum is related to the size and rotation of the nucleus. Thus, a knowledge of the maximum echo bandwidth and of the spin vector, the latter perhaps obtained from optical observations (Sekanina 1979, Whipple 1982), would allow the determination of the nuclear radius. Unfortunately, estimates of rotation rate, spin axis direction, shape and size have been made for very few comets so that in most cases a radar observation could only place some constraints on the values of the physical parameters of the nucleus.

Polarization properties of the radar echoes are useful for determining the surface scattering characteristics of the nucleus. For instance, from echoes received in the sense of circular polarization opposite to that transmitted, one learns mostly about the "quasi-specular" scattering properties of the target, since a single reflection reverses the sense of circular polarization. Receiving the same sense of circular polarization as that transmitted yields information on the "diffuse" or incoherent scattering properties. From Earth, the directions of illumination and observation of the target are nearly identical, so that, for a nearly spherical target, the quasi-specular scattering component of the echo arises mainly from reflections near the subradar point. On the other hand the diffusely scattered component arises from irregularities widely distributed over the surface.

From the echo power received, the radar (backscattering) cross-section is deduced and, when possible, its variation with rotational phase of the target is studied. The ratio of the radar cross-section to the geometric cross-section is related to the shape and reflectivity of the surface and is generally a function of polarization and radar wavelength. When dual polarization (for instance both left and right circular) receiving systems are available, the geometric albedo can be estimated by combining the power received in the two polarizations.

b. Ice and dust particles. The radar detectability of dust depends strongly on the size distribution of the grains. While Rayleigh scattering applies for particles with sizes d small compared to the wavelength ($d/\lambda<0.01$) and geometrical optics applies for large particles ($d/\lambda>100$), Mie theory applies throughout, in particular for millimeter- and centimeter-sized particles at S-band. Thus, a cloud of particles assumed to be spherical in Mie theory, of radius a small compared to the wavelength λ (λ is usually about 10 centimeters) will present a radar cross-section which varies as the fourth power of the ratio a/λ in addition to the square of the radius as in geometric optics. For a compact cloud of N such spherical particles of complex dielectric constant E_c, the radar cross-section is approximately (Kerr, 1951):

$$4N\pi a^2 \left(\frac{2\pi a}{\lambda}\right)^4 \left|\frac{E_c - 1}{E_c + 2}\right|^2 , \qquad (1.2)$$

when multiple scattering is unimportant.

The assumption of sphericity in this analysis is not severely constraining. In particular, Cuzzi and Pollack (1978), in their studies of the radar properties of the dust present in Saturn's rings, quote laboratory results obtained by Greenberg et al. (1971) and others showing that albedo and extinction efficiency are not significantly affected by non-sphericity. However, they note that non-sphericity chiefly affects the phase function and show that the spherical shape is the least effective in multiple scattering, particularly because "spheres allow no total internal reflection, and scatter at large angles (>90°) only the small fraction of incident energy that enters the particle after striking the sphere nearly tangentially".

At the shortest available radar wavelengths, the number of millimeter- to centimeter-sized particles will determine the strength of the echo from ice and dust. The number density of such particles probably depends importantly on the particular comet, but, so far, no useful data have been obtained for this "high" end of the size distribution. However, it has been inferred that most of the grains in the coma and dust tail have sizes of a few tenths of a micron (Whipple, 1978), and, consequently, it is very unlikely that the dust will return a detectable radar echo.

c. Plasma. For a radar echo to be detectable from a plasma, the electron density must be high enough that the critical plasma frequency is greater than the radar signal frequency. There is no generally accepted detailed theory for ion production in comets, although photoionization seems to be the primary process involved. The ions appear to be formed in the close vicinity of the nucleus, the source size being quite small. An estimate of the ion density in the coma may be determined approximately by assuming that the coma plasma pressure is comparable to the solar wind ram pressure. This condition at a distance from the sun of about 1 AU requires an electron density of about 10^4 to 10^5 cm^{-3} (Ip and Axford, 1982), corresponding to a critical plasma frequency lower than a few megahertz. This density is far too low to sustain an echo, the radar signal frequency being restricted to values well above the critical plasma frequency in order to propagate through the earth's ionosphere. The same considerations apply to the ion tail where the density should on average be even smaller. Scattering from irregularities within the ion tail, where knots are known to exist, must be negligible given their small total cross-section. Therefore, no echo from plasma should be expected in radar observations.

d. Attenuation of radar waves in the coma. The coma of a comet is essentially neutral, the ion concentration being several orders of magnitude lower than the molecular concentration. The predominant gaseous species in the coma at a heliocentric distance of about 1 AU is believed to be water with a production rate of about 10^{29}-10^{30} molecules per second for moderately active comets (Whipple and Huebner, 1976), or perhaps 10^{27} molecules per second for an old comet like Encke. The gas concentration is estimated to be about 10^{14} molecules per cubic centimeter near the surface of the nucleus; for typical ambient temperature and pressure conditions of about 200 K and 1 dyne/cm^2, respectively, in the coma (Delsemme and Miller, 1971), the attenuation caused by water vapor at S-band is less than about 10^{-6} db/km for such a concentration (Kerr, 1951). Therefore, the attenuation of radar waves by the gaseous component of a cometary coma is completely negligible.

1.2.3. Past attempts to observe comets by radar

The history of cometary radar astronomy includes few attempts, partly because close approaches of comets to the Earth are rare and partly because the necessary radar sensitivity only became available in the mid 1970's. The first attempt to study a comet by radar was made in January 1974, when Chaisson _et_ _al_. (1975) attempted to observe Comet Kohoutek, 1973 XII, using the Haystack Observatory X-band (3.8 cm) radar. Although the sensitivity of that system was not sufficient to detect the nucleus nor to place a useful upper limit on its radius, Chaisson _et_ _al_. concluded that the density of millimeter-sized particles in a coma of diameter 10^4 km was less than 1 m^{-3}. The second attempt, to detect comet d'Arrest, was made by Pettengill _et_ _al_. (unpublished) at the Arecibo Observatory in July 1976. This attempt was also unsuccessful, but implied that the nucleus of d'Arrest was less than 1 km in radius.

In the following chapters, results concerning the first detections of comet nuclei by radar are presented and an attempt is made to interpret them in the framework of what is known about cometary nuclei.

Figure Captions for Chapter 1.

Figure 1.1. Schematic drawing of the main cometary components, showing nucleus, coma and tails, and their respective positions with respect to the sun and to the comet's orbit.

Figure 1.2. A diagram showing how the rotation of a comet's nucleus and its asymmetrical ejection of gas and dust can result in non-gravitational forces, the effect of which is to alter significantly the comet's orbital parameters.

Figure 1.3. Photograph of comet West 1976 VI taken on March 9, 1970, and showing well-defined head and tails. (Courtesy of Henry Giclas, Lowell Observatory).

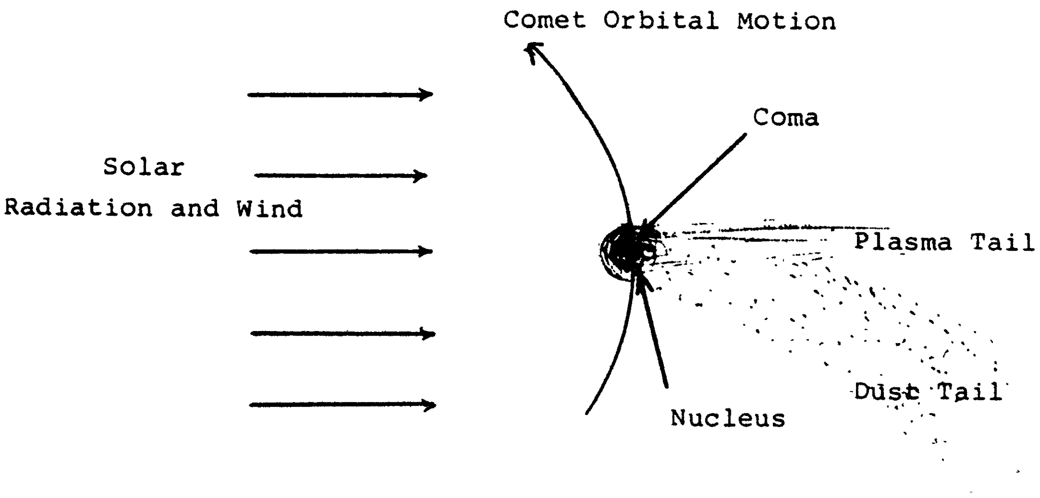

Fig. 1.1. Components of a comet.

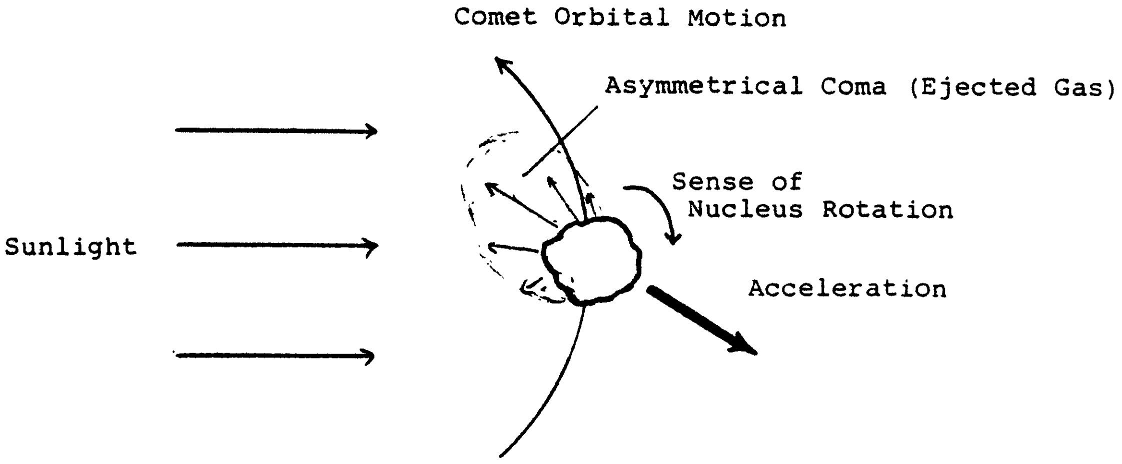

Fig. 1.2

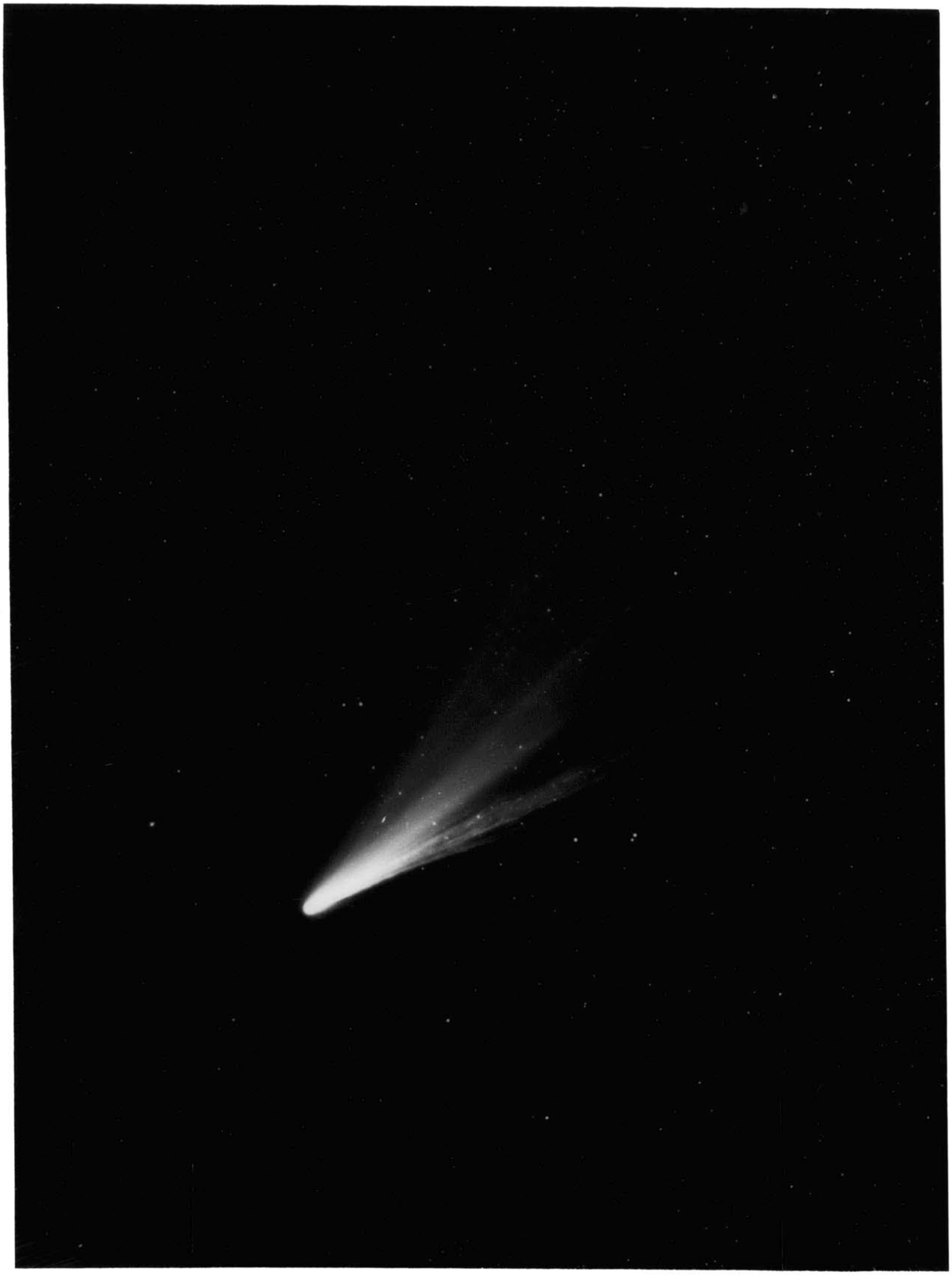

Fig. 1.3

PART B. COMET P/ENCKE: OBSERVATIONS AND DATA REDUCTION

CHAPTER 2

THE PERIODIC COMET ENCKE

2.1 History

The comet P/Encke was discovered as a naked-eye object on the evening of January 17, 1786, by the French astronomer Pierre Mechain. Its brightness was then about 6th magnitude and was reported comparable to the nebula M2. Only one other observation, by Charles Messier and Mechain on January 19, was reported at this appearance. This object was observed again about 10 years later by Caroline Herschel on the evening of November 7th, 1795, while her brother William Herschel reported it as visible to the naked-eye. Again a decade later, three independent observers: Pons (Marseille), Hurth (Frankfurt) and Bouvard (Paris), on the morning of October 20, 1805, reported observations, but did not realize that they corresponded to the same comet seen earlier. After several unsuccessful attempts were made to fit parabolic solutions to the orbit of the 1805 object, the German mathematician and physicist Johann Encke, a disciple of Gauss, suggested an elliptical orbit with a 12.2 years period (Bortle, 1980). It was not until November 28, 1818, that this comet was again observed (by Pons), and as a naked-eye object. It was followed for about seven weeks, and from the set of positional data obtained, J. Encke calculated that the comet's orbit was elliptical with a period of 1207 days (about 3.3 years), the shortest period of any known comet. Prior to this, only a few comets with elliptical orbits but with much longer periods had been known. The similarity between the path of the 1786, 1795, 1805 and 1818 comets led him to extrapolate his calculation backwards, taking into account planetary perturbations.

After a few weeks, Encke concluded that these four reported objects were indeed the same comet, and his prediction for an 1822 return was successfully verified. Because of his conclusive work, published in the Transactions of the Berlin Academy (Encke, 1844), Encke had his name attached to this comet. Having been observed at 52 apparitions, including all but one (1944) of those possible since its orbit was calculated, P/Encke is by far the most frequently observed comet. With an aphelion of 4.1 AU, it does not approach very closely to Jupiter, so that its orbit has remained quite stable over several centuries.

The comet orbital elements ("Catalog of cometary orbits", Brian Marsden ed.) are given in table 2.1:

TABLE 2.1

Ecliptic Coordinates, Equinox 1950.0

T (Time of perihelion passage)	:	Dec. 6, 1980
P (Orbital period)	:	3.31 yrs
Q (Perihelion distance)	:	0.341 AU
e (Eccentricity)	:	0.846
I (Orbital inclination)	:	11.9°
Argument of Perihelion	:	186.0°
Longitude of Ascending Node	:	334.2°

2.2. Physical characteristics

2.2.1 Optical appearance

As mentioned above, P/Encke was a naked-eye object of about magnitude 6 at each of its early sightings. Since then, it seems to have faded somewhat, probably because of the irreversible loss of part of the surface ices, although a recent detailed evaluation by Whipple and Sekanina yields a fading of no more than one magnitude per century. Since its discovery, this comet has always showed a bright central condensation with a short tail. At its seventeenth apparition in 1861 a fan-shaped nebulosity wider and brighter on the sunward side was first noticed. As will be seen in 2.2.3, this sunward pointing fan is a very characteristic feature of Encke, which has been recently explained by Whipple and Sekanina (1979). Two photographs of Encke, taken in 1937 and 1980 are presented in Figures 2.1 and 2.2.

At its 1980 appearance, P/Encke was reported to exhibit not only a sunward fan, but also multiple small tails and, particularly, a straight narrow gas tail which could have been as much as 150,000-300,000 km long on November 9 (Green and Morris, 1981). A maximum coma diameter of about 15 arcmin ($\simeq 1.7 \times 10^5$ km) was reported at 1.2 AU from the sun, decreasing in size with approach to the sun. Because of the comet's proximity to the sun, no post-perihelion observation of this phenomenon was reported.

2.2.2. Light curve and spectra

a. Light Curve. While the brightness of most comets increases almost uniformly on the way to perihelion and then decreases more slowly after perihelion, P/Encke presents a peculiar light curve in that while it is brightest near perihelion, it is dimmer after perihelion than before perihelion, at a given geocentric distance, the difference reaching as much as 3 magnitudes when the brightness is compared fifty days on either side of perihelion. Whipple interpreted this anomaly as due to the fact that one polar hemisphere of the nucleus may be much more active than the other (see section 2.2.4). Figure 2.3 shows a mean light curve obtained from the 1937-1947 pre- and post-perihelion observations.

b. Spectra. Two spectra of P/Encke obtained by H. Spinrad (1981) on November 5, 1980, using the 3-meter Lick Observatory telescope are shown in Figures 2.4a and 2.4b. The date corresponds approximately to the mid-point of the radar observations. Spinrad reported that Encke showed "strong gaseous emission bands (CN, C_2, C_3, NH_2, [OI]) superimposed upon a weak solar reflected-light continuum". He obtained an oxygen production rate of about 1.7×10^{27} atoms/sec. on November 4, 1980 ($r = 0.83$ AU) and suggests that water is the sole parent molecule for the oxygen produced.

2.2.3. Non-gravitational motion and the spin of the nucleus

It has been shown in 1.2.2.a that an independent determination of the rotation vector of the nucleus is especially important for interpreting the radar results; it is thus of interest to briefly outline the procedures used for the determination of a comet nucleus spin axis and rotation period.

The decrease in P/Encke's orbital period with time provided the first indication of the existence of deviations from Newtonian motion for comets. Since that discovery, variations of orbital period have been recorded for many comets, the most satisfying explanation for these being non-gravitational forces related to the rotation of the nuclei

(1.1.1). Since no cometary nucleus has been resolved optically, the study of nuclear rotations can only be made via observation of cometary comae. Sekanina (1979) used such observations to estimate the direction of the spin axis of four nuclei, based on Whipple's model. Since the transfer of heat into the surface on the sunlit hemisphere of the nucleus is not instantaneous, there will be a time lag between irradiation and the sublimation of the ices and the liberation of the dust particles. Thus the direction of maximum ejection of material will not be toward the sun but be at an angle θ to the sun's direction. The anisotropic outgassing will result in a fan-shaped coma oriented asymmetrically with respect to the sun. For some comets, the variation of the position angles of this fan with time as the Earth-Comet geometry changes has been carefully recorded by visual observers. Using such data and applying an iterative technique, Sekanina first found the possible ranges of spin-axis direction for each observation, and then adjusted these to be compatible with the whole set of observations. He also estimated the sublimation time lag from the offset of the direction of maximum outgassing from the sun direction, this parameter yielding information on the nature of the surface of the nucleus.

There are in particular two methods by which the rotation period can be determined. The first (Whipple, 1982) uses measurements of halo diameters and requires areas of differing activity on the nucleus, so that periodic structure appears in the coma as the nucleus rotates with respect to the sun. The second aims at obtaining a photometric light curve, as for asteroids, but is difficult to apply to comets since it is hard to separate the light reflected by the nucleus from that scattered by the coma, unless the comet is observed at large heliocentric distances.

2.2.4 Structure and evolution

The most plausible model presently available to account for the observed properties of P/Encke stems from a very detailed study by Whipple and Sekanina (1979) of the huge collection of data recorded during past appearances. Starting with Whipple's theory of the nucleus as a ball of dirty ice, they postulate an oblate spheroid rotating about its axis of maximum moment of inertia, and calculate the pressure exerted on the nucleus by sublimation.

Using the observed light curve, they solve for the jet force which acts on the nucleus, resolving it into both a torque causing precession of the spin axis and a force acting through the center of gravity to perturb the orbital motion. Remaining "peculiarities" of the light curve are explained as latitudinal variations in the sublimation rate. This approach has allowed them to estimate the direction of the nuclear spin axis and sublimation lag angle, and, independently, the rotation period. They find that P/Encke rotates in a direction opposite to its sense of orbital motion, a result consistent with its observed non-gravitational acceleration, and demonstrate how the rate of change of orbital period is consistent with the estimated precession of the nucleus. They have successfully checked their results against observed orientations and structures of P/Encke's comae, and deduce that, for centuries before 1700, the poles were oriented nearly along the long axis of the orbit. Thus, almost all the comet's mass loss during that period occurred from one polar hemisphere when the comet was close to the sun. Oddly enough, today this hemisphere seems to be the more active of the two. Whipple and Sekanina suggest that the other "protected" hemisphere, which faced the sun directly only near aphelion during the earlier period, is covered with dusty or rocky debris, and is, therefore, less active today. This model accounts very well for the peculiar light curve of P/Encke.

Sekanina and Whipple's calculations yield a nuclear rotation period of 6h33m, with a spinup rate of about minus 21 minutes per century, a loss rate by sublimation of about one percent of the comet mass per revolution, a total mass of less than 10^{16} g, and an oblateness of about 4 percent. In Figure 2.5 is presented the variation of the nucleus pole position as a function of time, showing that the spin axis should have precessed by about 100° in longitude and 30° in latitude between 1786 and 1977. The data imply a nuclear radius of less than 1.5 km.

Because of its short period and low activity, P/Encke is usually considered the oldest of the known comets (loss of acivity due to number of perihelion passages). Its activity is indeed less than that of most newly discovered or long-period comets, probably because of the removal of volatile upper layers. A spotty surface, i.e a surface covered mostly with material that does not vaporize readily, seems indicated; the comet's activity is certainly consistent with a surface partially covered by H_2O ice. Whether or not the nucleus contains a rocky core is not known.

Figure Captions for Chapter 2.

Figure 2.1. Comet P/Encke. Photograph made on November 22, 1937, 35 days before perihelion, by G. Van Biesbrock (Yerkes Observatory). The asymmetry of the coma with respect to the sun direction is evidence that the nucleus is spinning (Courtesy of Fred Whipple).

Figure 2.2. Comet P/Encke. Photograph obtained by H. Spinrad and J. Stauffer on October 9, 1980, using the Kitt Peak National Observatory's 4-meter telescope (IIIa-F(red) plate). The heliocentric and geocentric distances of the comet at the time of observation were respectively 1.24 AU and 0.47 AU.

Figure 2.3. Mean lightcurve of P/Encke. Reproduced with permission, from Sekanina (1979).

Figure 2.4a and 2.4b. Image dissector scanner spectrum of P/Encke, obtained by H. Spinrad at Lick Observatory. Scattered solar light from dust removed. Strong C_2 and [OI] bands are evident, as well as CN and weak NH2.

Figure 2.5. P/Encke: Variation of the nucleus pole position with time. The pole position is given in ecliptic coordinates. From Whipple and Sekanina (1979), with permission.

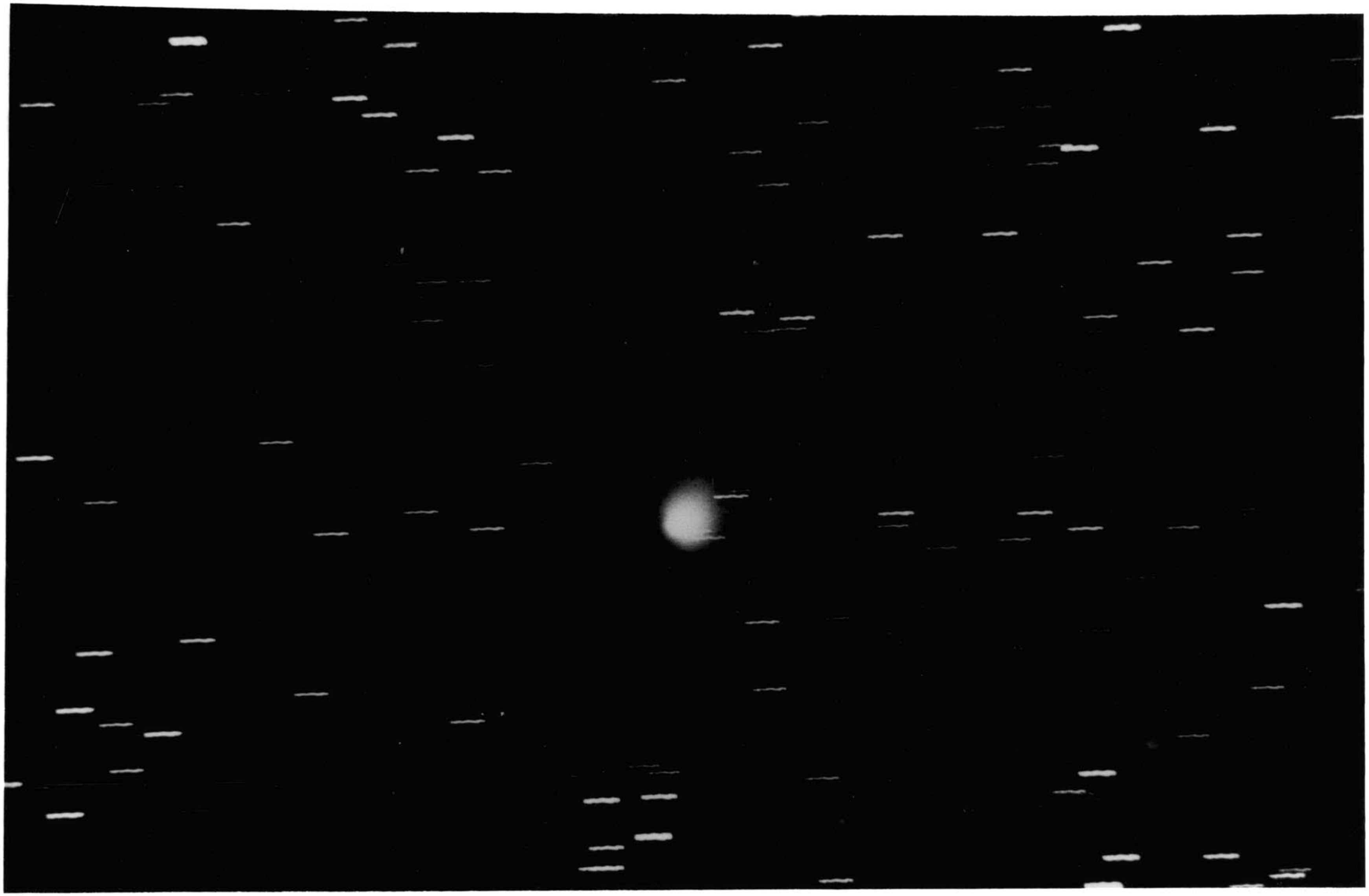

Fig. 2.1

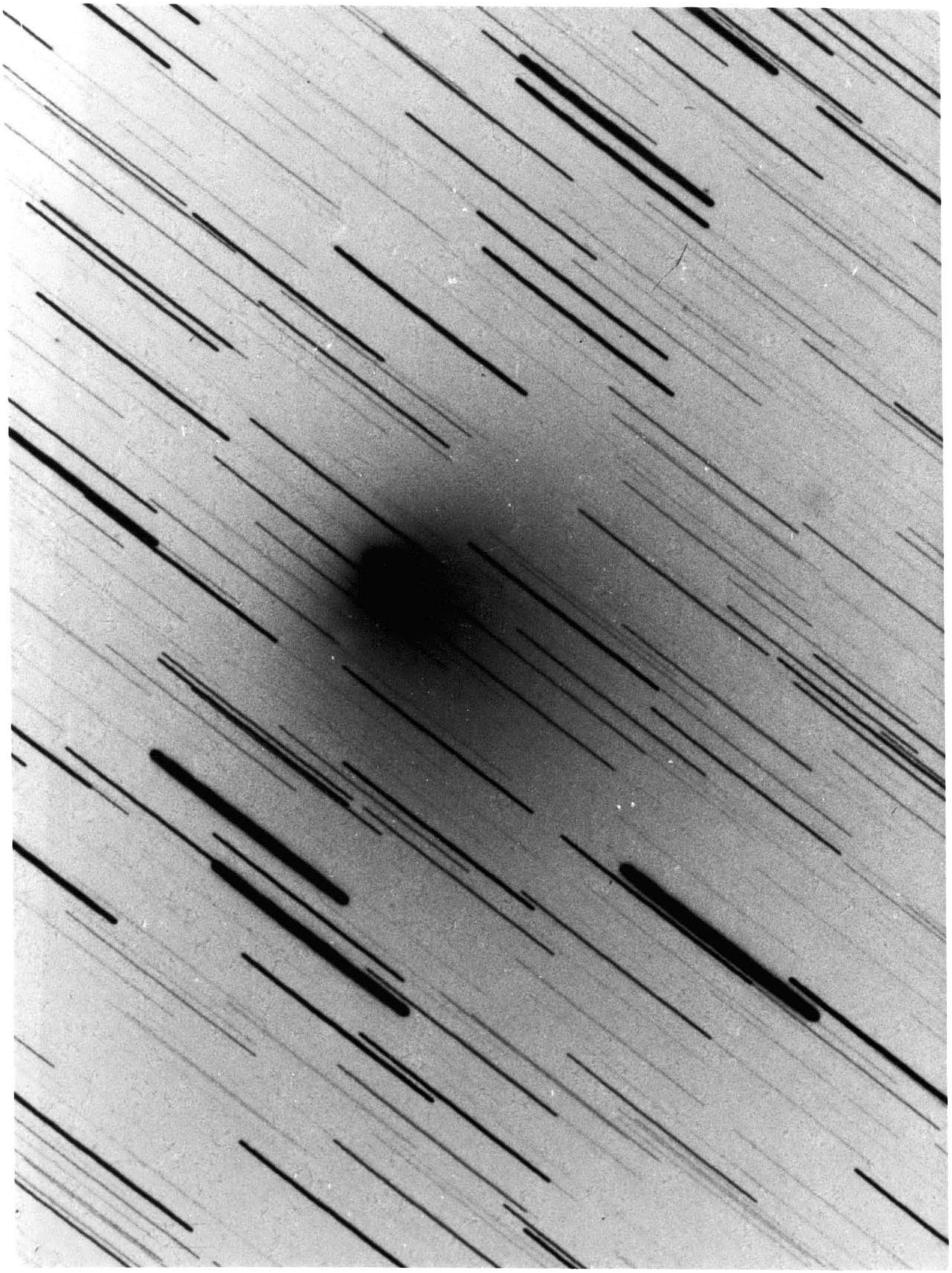

Fig. 2.2

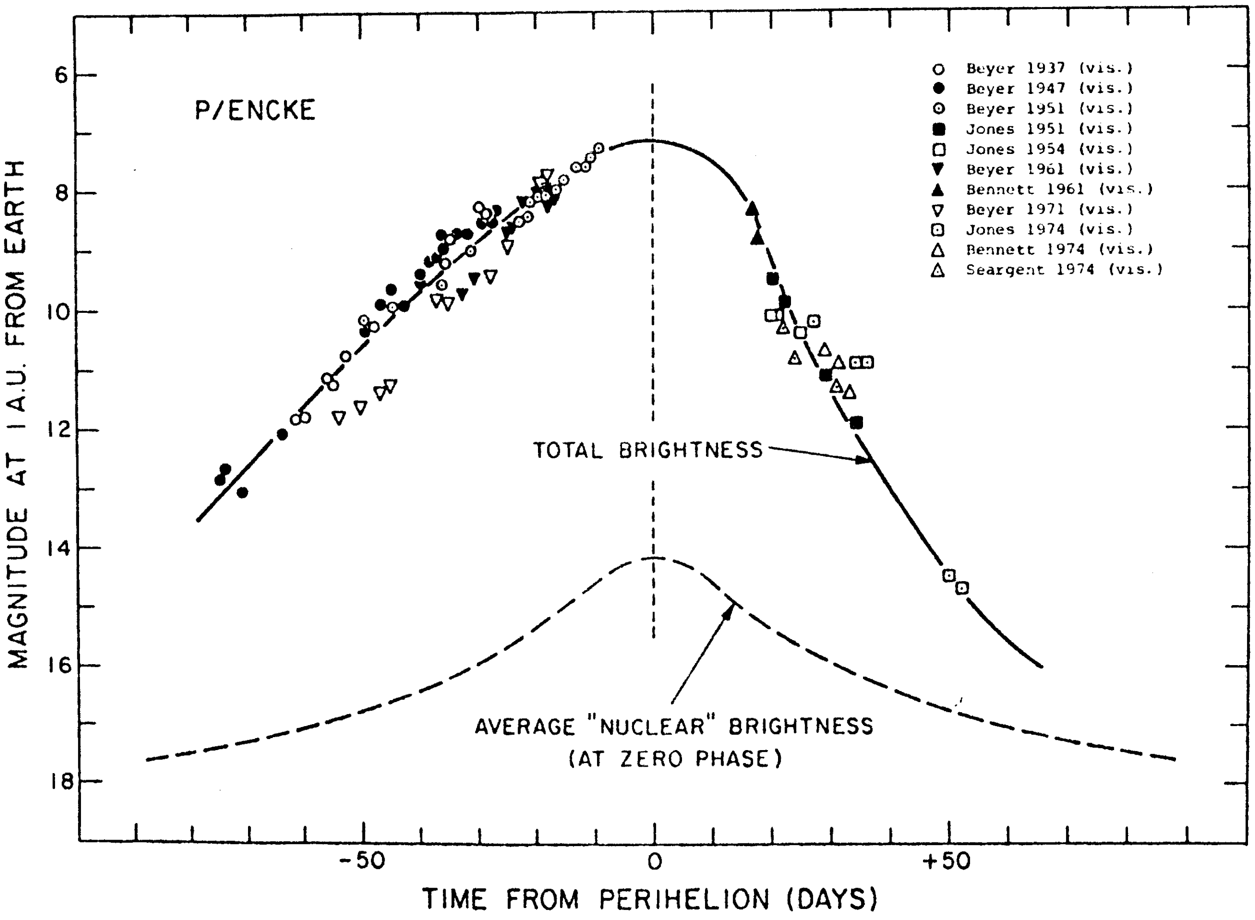
P/ENCKE
○ Beyer 1937 (vis.)
● Beyer 1947 (vis.)
⊙ Beyer 1951 (vis.)
■ Jones 1951 (vis.)
□ Jones 1954 (vis.)
▼ Beyer 1961 (vis.)
▲ Bennett 1961 (vis.)
▽ Beyer 1971 (vis.)
⊡ Jones 1974 (vis.)
△ Bennett 1974 (vis.)
△ Seargent 1974 (vis.)
TOTAL BRIGHTNESS
AVERAGE "NUCLEAR" BRIGHTNESS
(AT ZERO PHASE)
MAGNITUDE AT 1 A.U. FROM EARTH
6
8
10
12
14
16
18
-50
0
+50
TIME FROM PERIHELION (DAYS)

Fig. 2.3

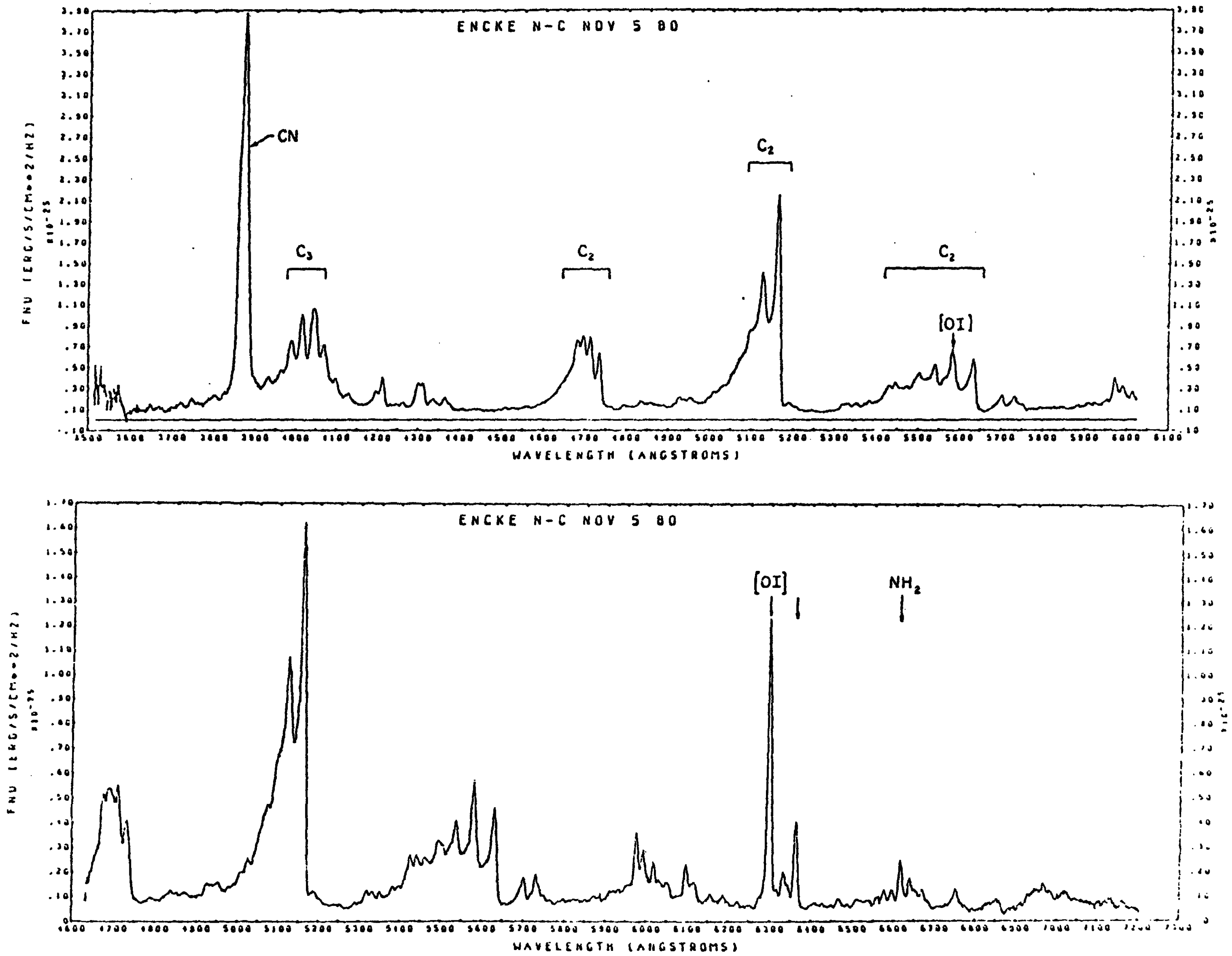

Fig. 2.4a (top) and 2.4b (bottom)

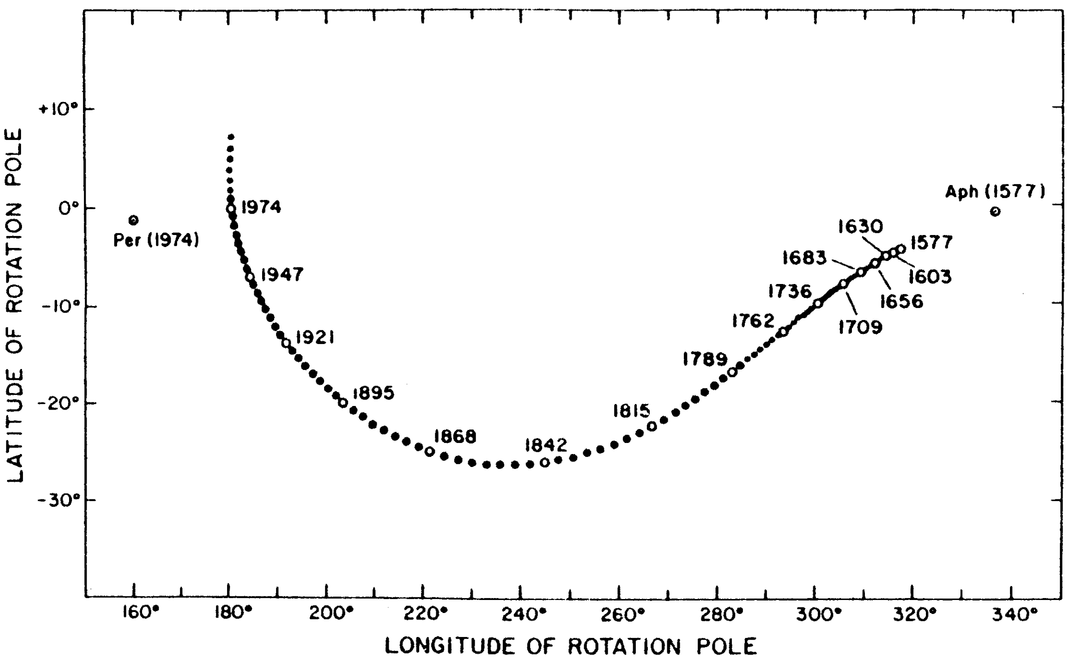

+10°
0°
-10°
-20°
-30°
LATITUDE OF ROTATION POLE
160°
180°
200°
220°
240°
260°
280°
300°
320°
340°
LONGITUDE OF ROTATION POLE
Per (1974)
Aph (1577)
1974
1947
1921
1895
1868
1842
1815
1789
1762
1736
1709
1683
1656
1630
1603
1577

Fig. 2.5

CHAPTER 3

THE 1980 RADAR OBSERVATIONS OF P/ENCKE

3.1. Introduction. Facility and observing conditions

The radar observation of the comet P/Encke took place at the Arecibo Observatory (Puerto Rico) on seven consecutive days from November 2 to November 8, 1980, about 30 days before the comet reached its perihelion and at a distance of slightly more than 0.3 AU from Earth. Figure 3.1 gives a schematic account of the Sun-Earth-Comet geometry at the time of observation. Table 3.1 lists the geocentric (1950.0) right ascension and declination, and the zenith angle at Arecibo for the comet at transit on each day of observation. This is given along with the corresponding Doppler shift in Hertz at 2380 MHz, and the round-trip delay.

TABLE 3.1
RECEIVING EPHEMERIDES AT ARECIBO TRANSIT

DATE	UT	RA	DEC	Z.A.	DOPPLER	R-T DELAY
(1980)	hr mn	hr mn sc	° ' ''	(deg)	(Hz)	(secs)
Nov 2	14 29	12 49 04	34 23 16	16.0	-184,577	294.28
Nov 3	14 35	12 59 21	31 20 02	13.0	-218,290	301.63
Nov 4	14 40	13 08 33	28 22 10	10.0	-250,225	310.17
Nov 5	14 44	13 16 50	25 30 55	7.2	-280,342	319.83
Nov 6	14 48	13 24 19	22 47 00	4.4	-308,728	330.56
Nov 7	14 50	13 31 06	20 11 05	1.8	-335,388	342.28
Nov 8	14 53	13 37 18	17 43 00	0.6	-360,605	354.95

The Arecibo Observatory is located at a latitude of about 18° 21' North and a longitude of about 66° 45' West. The antenna is a fixed spherical reflector 300 hundred meters in diameter, with an effective aperture at 12-cm wavelength of about 20,000 m^2. The feed moves along an arc on an arm that is rotatable in azimuth; the arm is supported about 150 meters above the center of the spherical reflector (see Figure 3.2).

3.2 Ephemerides and antenna pointing.

The observing ephemerides were computed by Irwin Shapiro and Antonia Forni (Lincoln Laboratory) from orbital elements estimated using (optical) data both from past appearances and from new observations associated with the 1980 recovery. Both sets of data were obtained from Brian Marsden of the Smithsonian Astrophysical Observatory. Although P/Encke has the best-known cometary orbit, the optical observations made both before and after the radar observations were neither sufficiently numerous nor sufficiently accurate to allow the Doppler shift to be calculated solely from them with an uncertainty of less than 20 Hz. The angular position in the sky was estimated to be accurate to within a few arc seconds, an error which is small compared to the radar system's beamwidth of 2 arc minutes.

The antenna has a pointing accuracy of about 10 arc sec rms. The motion of the telescope is computer controlled, using a prestored digital ephemeris. During reception one must point towards the apparent position of the target, while during transmission one must "lead" the apparent position by twice the aberration to correct for the translational motion of the target with respect to the observer.

3.3 The Arecibo S-band radar system

3.3.1. The transmitting chain

a. Waveform and polarization. The detectability of a target depends on its scattering function, which specifies the distribution of the target cross-section as a function of time delay and Doppler frequency. Figure 3.3 illustrates several types of scattering functions, where B is the effective Doppler spread and L is the delay dispersion of the echo. In particular, if we assume that the target's radar echo has a negligible dispersion in delay but that its spin and finite radius introduce some significant Doppler broadening in frequency, then the scattering function is as shown in Figure 3.3c.

Indirect estimates of the radius of the nucleus of comet Encke have yielded values ranging from 1 to 5 km (Table 11.3), with a rotation period of the order of 6 hours. For a nucleus 1-km in radius rotating with a 6-hr period, $B < 9$ Hz and $L < 7$ µs. We note in passing that the dimensionless product $BL < 6\times10^{-5} \ll 1$, and that this target is thus highly "underspread", i.e. it presents no difficulties in obtaining simultaneous, unambiguous resolution of the echo in delay and frequency (Green, 1968). However, searching for an echo simultaneously over the vast extent of delay-frequency space corresponding to the a-priori prediction uncertainty is expensive and requires rather elaborate data-taking and storage procedures. We opted, therefore, to suppress delay resolution in this first experiment and to limit our search to Doppler frequency alone. This conservative approach is also dictated by the low echo signal strength expected: the parameters given above, combined with an integration time of one hour and an assumed surface radar reflectivity of 0.1 yield a calculated signal only three times the standard deviation of the associated noise! Since we are not looking for delay information, simple continuous-wave transmission is preferred.

Circular polarization of the transmitted signal was used for operational convenience, since its use suppresses the effects of Faraday rotation in the Earth's ionosphere, and does not require matching of the position angle between transmission and reception as would the use of linearly polarized transmissions.

Since single coherent reflection at the surface of a target reverses the sense of circular polarization of the signal, most of the echo power usually is found in the circular sense opposite to that transmitted. When possible, it is best to receive in both senses of circular polarization, of course, in order to separate the quasi-specular (coherent) and diffuse (incoherent) parts of the echo and thus to gain more information on the scattering properties of the nucleus. Unfortunately, because only one receiver was available at the time of the Encke observations, it was possible to receive only one sense of polarization. Reception in the sense of circular polarization orthogonal to that transmitted was chosen, since this mode usually maximizes the received echo power.

b. The radar configuration. The radar system configuration used for the Encke observations is shown in Figure 3.4. The heart of the system is the master oscillator or frequency standard : all the frequencies required in the system are synthesized from this oscillator, which also controls the clocks used in establishing the timing. Since the frequency width of the echo from a comet nucleus is only a few hertz, and since the predicted strength of the echo necessitates the integration of data from a number of days, both short- and long-term frequency stability is essential. At Arecibo the standard is a rubidium vapor oscillator (based on a fundamental line resonance of the rubidium atom) and is referred in the long term to the U.S. Naval Observatory through Loran-C radio signals with an accuracy of about 0.2 μs. The short term stability of the rubidium vapor oscillator is about one part in 10^{13}, while the day to day stability is of the order of one part in 10^{12}. The output signal from this oscillator is fed into different blocks containing frequency synthesizers, which drive, in turn, both the local oscillators of the receiver circuits and the transmitter exciter.

In order to correct for the background noise baseline arising from variations in the spectral response of the radar's receiver system due to instrumental effects, a frequency switching technique was used which is described in detail in Appendix 2. The transmitted carrier frequency was switched consecutively among four different frequencies, $\Delta f_s = 448$ Hz apart, dwelling a time $T = 10$ seconds on each of them. The spacing of these frequencies was chosen to comfortably accommodate not only the widest conceivable echo broadening but also a reasonable estimate of possible errors in the a priori predicted Doppler frequency shift of the echo. The switched frequencies were $F_k = 2379{,}999{,}328$ Hz + $(k-1) \times \Delta f_s$ Hz, where k is an integer ranging from 1 to 4. The one-watt switched output from the frequency synthesizer and exciter chain drives a simple coherent high-power five-cavity klystron having a power gain of about 56 dB. The DC power needed by the klystron is obtained from a 60-kV, 15-a power supply driven by turbines; the efficiency of the DC - RF conversion in the klystron is about 50%. The output of the klystron is, thus, about 400 kW (average). The transmitter-receiver switch at the feed is mechanical and takes about 0.1 second for switchover, which is much less than the approximately five minutes for the round trip time of the signal. The transmitted energy is radiated from a feed directly below the klystron into the fixed main dish and the tracking of the target is done by moving the cabin in which the feed and klystron is located.

3.3.2. The receiving chain

a. Radio-frequency (R.F.) section. The echo signal returned by the target represents the convolution of the transmitted signal waveform with the scattering function of the target. The receiver bandwidth must accomodate both the rotational Doppler broadening of the target, and the uncertainty in the location of the expected center frequency of the echo. An optimum receiver would use a passband which has the same spectral shape as the echo. Since this distribution is not known *a priori*, different "software filters" will instead be applied to the echo power spectrum during the data analysis to maximize the signal-to-noise ratio. The overall instability in the frequency control system of the radar is of the order of 0.01 Hz and thus is negligible.

The echo signal collected by the reflector is focused into the dual circular polarization feed where the circularly polarized component orthogonal to the transmitted mode is attached to the receiver. The one-way antenna gain as a function of zenith angle for the feed used is indicated in figure 3.5. This calibration curve as well as the system temperature calibration curve in figure 3.6 were measured by M. Davis and S. Ostro. The gain calibration is obtained by observing standard radio sources. These curves apply strictly only to the observations of comet P/Grigg-Skjellerup in 1982, but the system performance was nearly comparable for the observations of P/Encke in 1980.

The S-band receiver front-end amplifier at Arecibo is a low-noise helium-cooled maser with 24-dB gain. The system temperature T_S, including the contributions of the receiver, sky, antenna sidelobes on the ground and feed-line losses is shown in Figure 3.6. It varies with zenith angle because of the varying amounts of feed "spill-over" that see the warm ground outside the spherical reflector. During the period of observation, a calibrated noise is occasionally injected in front of the receiver to verify the actual value of T_S.

The input to the receiver is a signal of center frequency $F_T + D$, where F_T is the frequency of the transmitted signal and D is the Doppler shift introduced by the radial component of the velocity of the target relative to the radar. The amplified R.F. signal is heterodyned against a higher-frequency signal to yield a nominally 30-MHz intermediate frequency (I.F.) signal. This mixing removes the expected Doppler shift as computed from the ephemerides. A frequency synthesizer, driven by computer using the ephemeris prediction data prepared at MIT, continuously generates a frequency correcting for the expected Doppler shift; the receiving bandwidth is thus kept tuned to the incoming signal. A residual offset relative to the expected center frequency exists in the final spectra, of course, because of the transmitting frequency shifts and also because of errors in the a priori elements used to describe the comet's orbit.

b. IF section. The 30-MHz I.F. signal is passed through a 10-kHz wide filter and presented to a pair of phase-quadrature "video" detectors in order to preserve both sidebands following conversion to near zero frequency. In each of these detectors the signal is mixed with a reference at 30 MHz. In one of them the reference is shifted in phase by 90 degrees with respect to the other. The quadrature signals go through 1.25-kHz wide low-pass filters and are then digitally sampled simultaneously at a 2.5-kHz rate. The total bandwidth preserved, set by the need to accommodate the frequency switching, is about 2 KHz. The digital data are Fourier analyzed in an array processor at 0.82 sec intervals, with the output spectral power estimates from consecutive intervals summed to yield an average spectrum for every 10 seconds of received signal corresponding to the dwell time of the transmitted frequency F_i. The resulting frequency resolution is about 1.2 Hz. These spectra are then recorded on tape. A more detailed description of the detection system and of the signal processing before recording is given in Appendix 3.

3.3.3. Recorded-data description

The data stored on 9-track magnetic tape consists of successive files, each of which is associated with a single transmission/reception cycle (called a "run"). Each file consists of many records, each record R_i containing a 10-second-average spectrum corresponding to a matched transmission and reception pair for a given transmitting interval at frequency F_i. Thus each file may be decomposed into successive blocks of four records: R_1, R_2, R_3, and R_4, corresponding to the transmission and reception of four consecutive switched frequencies, till the end of the reception interval is reached. A truncated block usually remains at the end of the file.

3.3.4. Summary of the observing parameters for P/Encke

A summary of the observing parameters for P/Encke is given in Table 3.2 for the dates of observation.

TABLE 3.2

Date	Δ	RTT	G	P_t	T_s	t_i
(1980)	(a.u.)	(sec)	(db)	(kw)	(K)	(sec)
Nov. 2	0.295	294	69.2	390	79	189
Nov. 3	0.303	302	70.2	300	59	1947
Nov. 4	0.311	310	70.4	345	63	864
Nov. 5	0.321	320	70.6	350	51	3135
Nov. 6	0.332	331	70.8	375	48	3259
Nov. 7	0.343	342	70.8	380	49	3708
Nov. 8	0.355	354	70.8	400	50	3488

In this table, Δ is the geocentric distance of Encke, RTT the round trip time of the radar signals, G the isotropic antenna gain, P_t the transmitted power, T_s the receiving system temperature, and t_i the total received time. The wavelength of the radar signals was 12.6 cm (corresponding to a carrier frequency of 2380 MHz). G and T_s represent effective values, obtained from a consideration of the actual observations achieved.

Figure Captions for Chapter 3.

Figure 3.1. Configuration of the Sun-Earth-Comet Encke system at midtime of the radar observations, November 26, 1980.

Figure 3.2. Aerial photograph of the Arecibo Observatory (Courtesy of G. Giles, Arecibo Obs.).

Figure 3.3. Scattering function of various forms of targets. The total volume under the function is equal to the overall radar cross-section σ. Case c) applies particularly to a comet nucleus. (Reproduced from "Radar Astronomy", Evans and Hagfors, 1968, p.32, with permission).

Figure 3.4. Radar system configuration for the comet observations.

Figure 3.5. One-Way antenna gain calibration curve for the Arecibo S-band radar system.

Figure 3.6. System temperature calibration curve for the Arecibo S-band radar system.

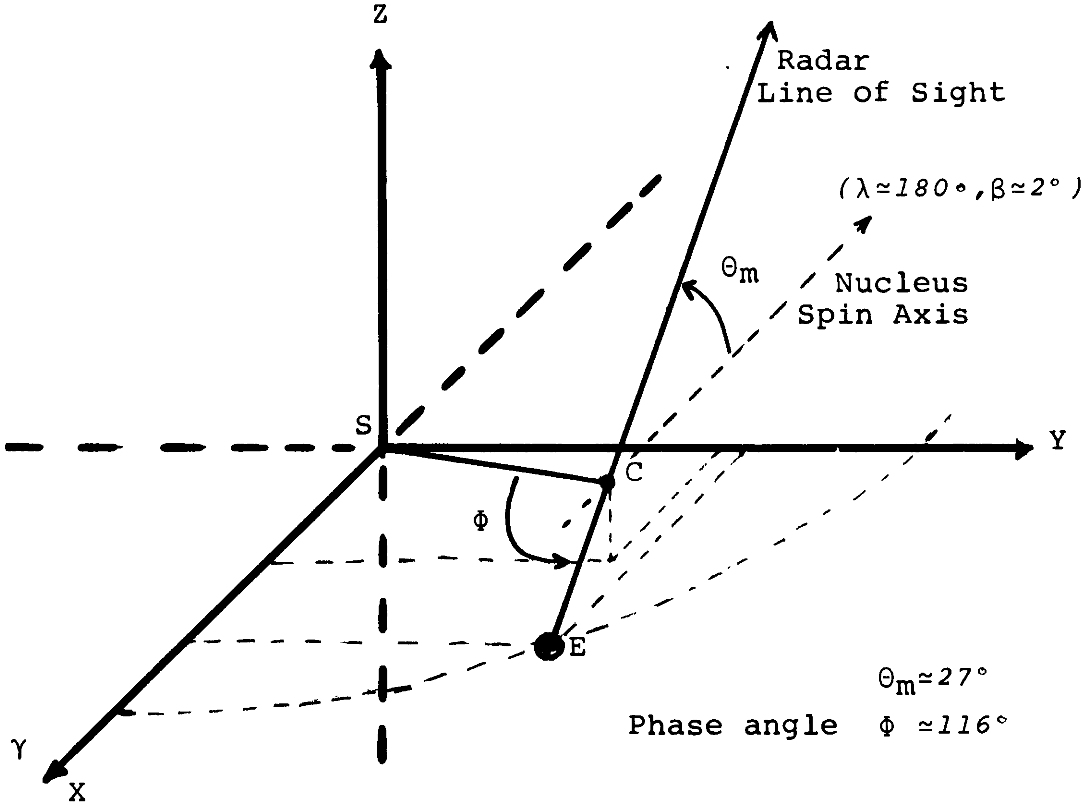

Fig. 3.1. Configuration of the Sun-Earth-Comet P/Encke System.

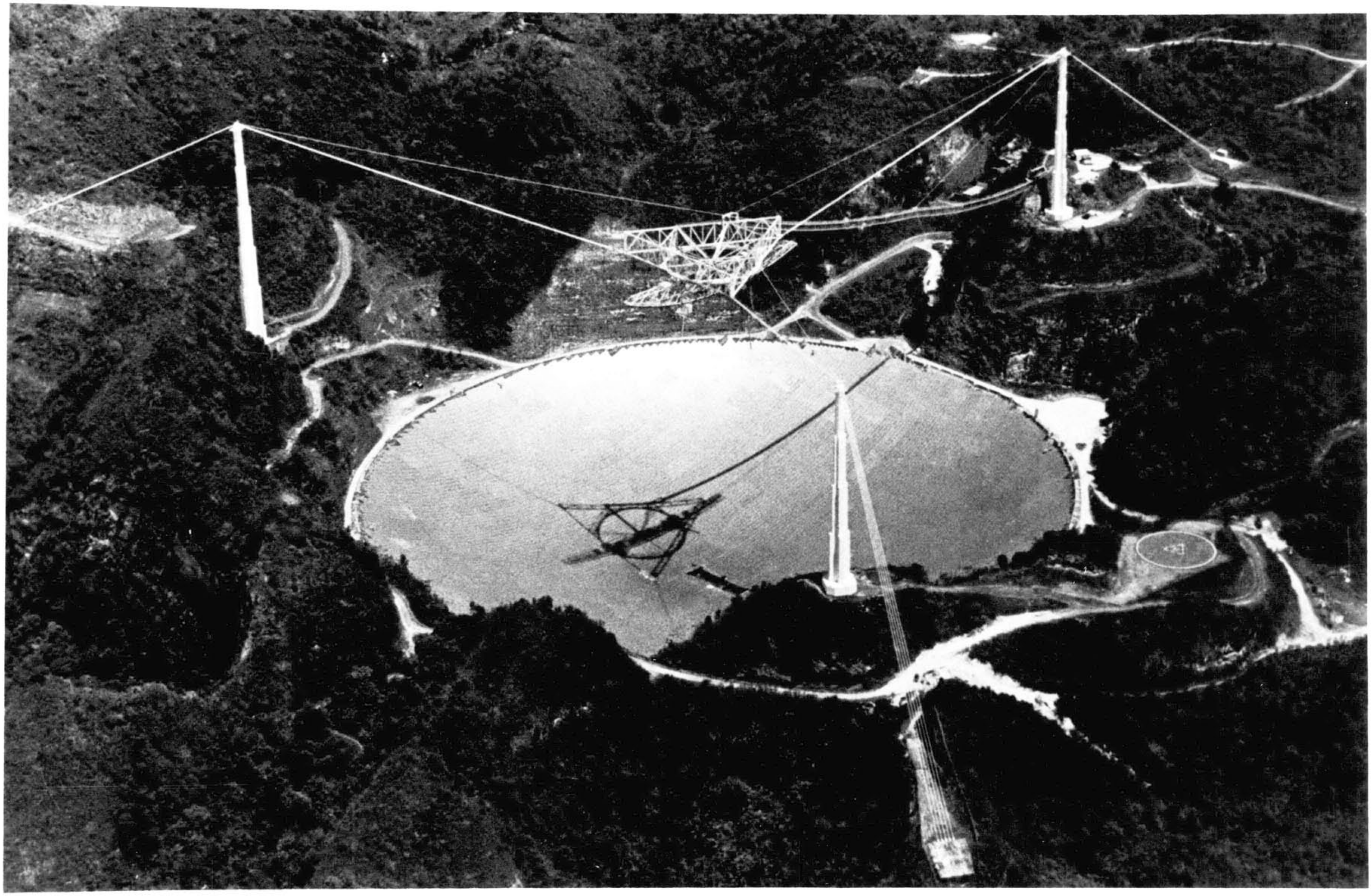

Fig. 3.2

(a) Stationary point target at delay τ_d.

(b) Point target at delay τ_d moving with velocity $cf_d/2f_o$.

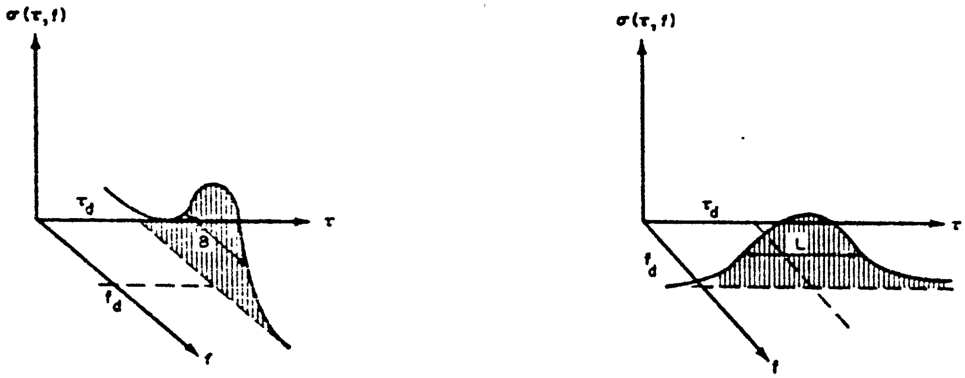

(c) Point fluctuating target of fluctuation rate B.

(d) Deep nonfluctuating target of depth L.

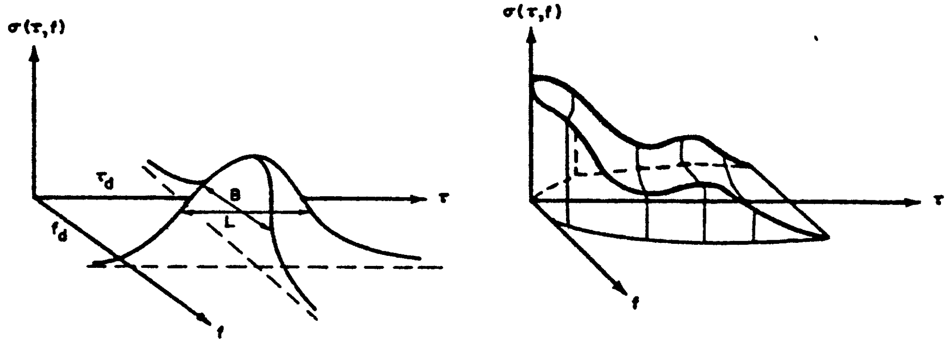

(e) Deep fluctuating target.

(f) Uniform rotating sphere.

Fig. 3.3

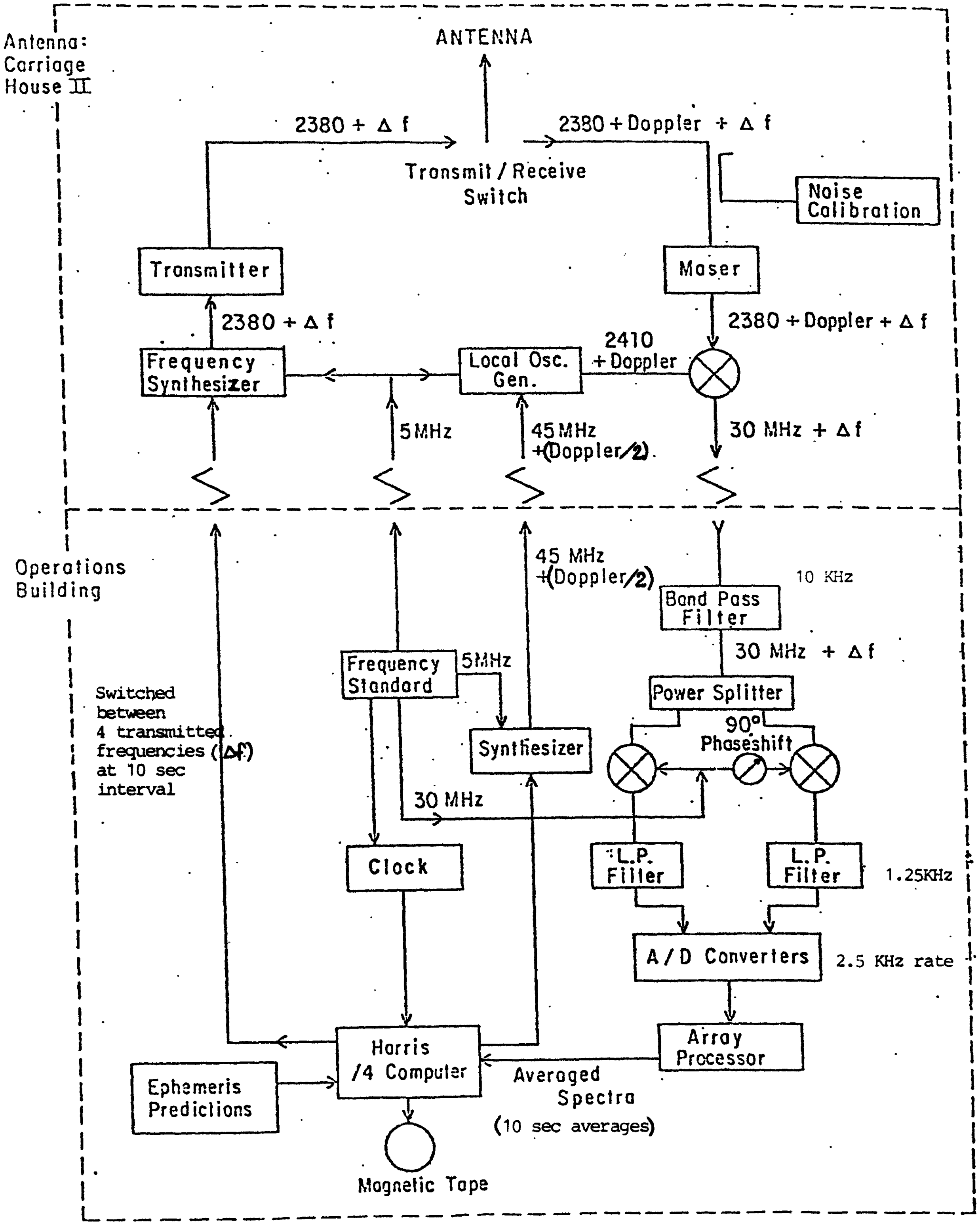
Antenna:
Carriage
House II
ANTENNA
2380 + Δ f
2380 + Doppler + Δ f
Transmit / Receive
Switch
Noise
Calibration
Transmitter
Maser
2380 + Δ f
2380 + Doppler + Δ f
2410
+ Doppler
Frequency
Synthesizer
Local Osc.
Gen.
5 MHz
45 MHz
+(Doppler/2)
30 MHz + Δ f
Operations
Building
45 MHz
+(Doppler/2)
10 KHz
Band Pass
Filter
30 MHz + Δ f
Switched
between
4 transmitted
frequencies (Δf)
at 10 sec
interval
Frequency
Standard
5 MHz
Synthesizer
Power Splitter
90°
Phaseshift
30 MHz
Clock
L.P.
Filter
L.P.
Filter
1.25KHz
A / D Converters
2.5 KHz rate
Array
Processor
Harris
/4 Computer
Averaged
Spectra
(10 sec averages)
Ephemeris
Predictions
Magnetic Tape

Fig. 3.4

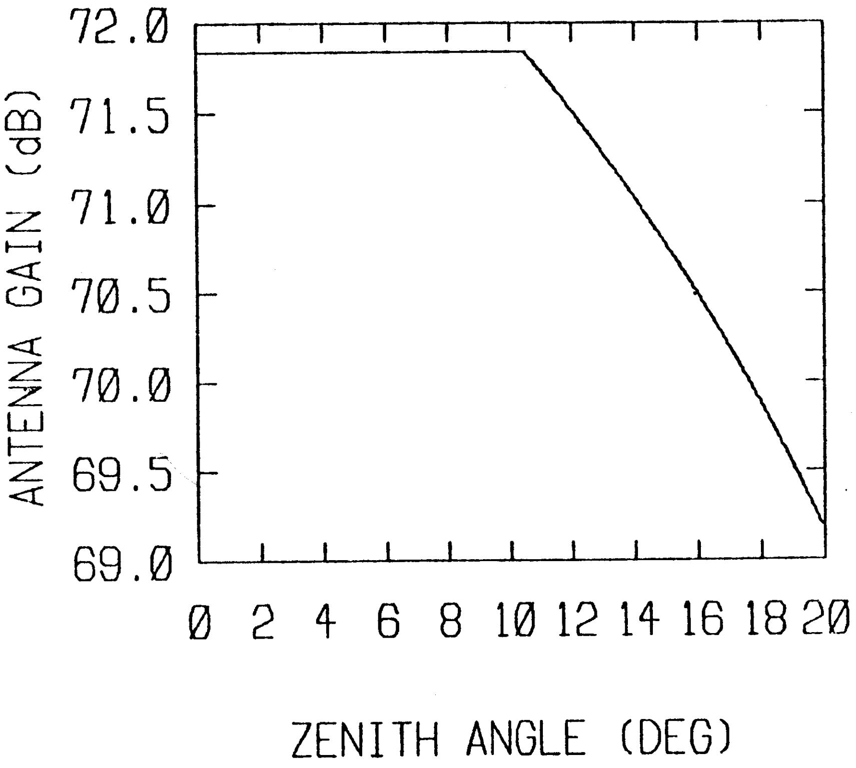

Fig. 3.5. Gain calibration

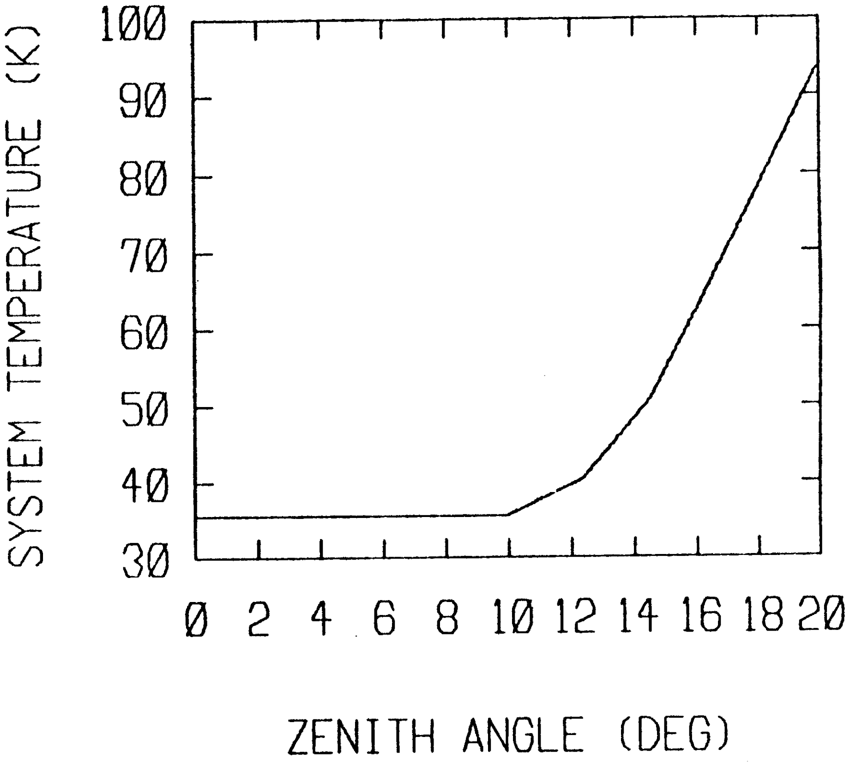

Fig. 3.6. Temperature calibration

CHAPTER 4

P/ENCKE: DATA REDUCTION

4.1 The background-free spectra

Each of the files recorded on the data tape is analyzed separately, with the possibility of combining files at a later stage. As described in section 3.3.3. a file consists of a series of consecutive blocks of four records each: R_i, i= 1→4, each block containing data corresponding to a full switching cycle. As a first step, all records of a given file corresponding to the transmission of the same switched frequency F_i are summed together, yielding a group of four spectra, each 2.5-kHz wide. For a given spectrum, only 1792 Hz is actually used (4 times the frequency step: Δf_s = 448 Hz); the remainder is severely attenuated by the edges of the low-pass filter and is discarded.

Briefly described, in each of the four intermediate summed spectra, a single, but different, 448-Hz spectral subinterval will bracket the expected echo; the other three subintervals of each spectrum provide signal-free background information which may be matched against the corresponding "signal" subinterval in one of the other three intermediate sums. It is clear that for each signal subinterval there will be three matched "background" subintervals among the group of four. Thus the additional random noise introduced in the background removal is only $3^{-1/2}$ times as large as that originally present in the signal subinterval. After the subtraction and normalization, we have four 448-Hz subintervals containing echo signal for which the background frequency variation has been removed. These four subintervals are then shifted in frequency by the appropriate multiple of 448 Hz and combined to yield a single "background-free" spectrum for each file. This process is described in more detail in Appendix 2.

4.2. Weighted summation and calibration of spectra.

The spectra obtained for all the files, each corresponding to data from a receiving interval approximately equal to the round-trip time of the signal are combined, first expressing each in units of the standard deviation of its associated noise (see Appendix 2). The adjustment required in this step usually differs little from run to run. However, there were a few files for which the difference between the calculated and observed rms noise fluctuations was larger than 10% and for one file was as large as 45%. We, therefore, decided to normalize the spectra in this way so that each had comparable noise statistics (unit variance) before weighted summation.

The spectra were summed for individual days as well as for combinations of days. The weights were calculated as follows: for each individual file characterized by index i (i.e. 10-min run), we have a corresponding spectral array comprising 365 elements at 1.23 Hz intervals; we label the elements (j) as $S_i(j)$. Let us associate with each of these a new array, $\sigma_i(j)$ which represents the radar cross-section equivalent to each element of received spectral power:

$$\sigma_i(j) = \frac{(4\pi)^3 c^4 t_i^4}{16\, P_{T_i} G_{T_i} G_{R_i} \lambda^2} P_{R_i}(j) \qquad (4.1)$$

where λ is the radar wavelength and t_i, P_{Ti}, G_{Ti}, G_{Ri}, are, respectively, the round-trip echo delay of the target, the power transmitted, and the gains of the antenna at transmission and reception for the i^{th} file. P_{Ri} represents the power received in a spectral element. Expressing P_{Ri} in terms of the system and data-analysis parameters yields:

$$\sigma_i(j) = \frac{(4\pi)^3 c^4 t_i^4}{16\, P_{t_i} G_{T_i} G_{R_i} \lambda^2} \cdot kT_{si} \cdot \left(\frac{N\Delta B}{(N-1)\tau_i}\right)^{1/2} S_i(j) \qquad (4.2)$$

where k is Boltzmann's constant, T_{si} the system temperature, ΔB (= 1.23 Hz) the frequency resolution, N (=4) the number of separate frequencies used in the frequency-switching pattern, and τ_i the integration time. Equation (4.2) may be written as:

$$\sigma_i(j) = \sigma_{rmsi}\ S_i(j). \qquad (4.3)$$

with σ_{rmsi} the radar cross-section equivalent to a standard deviation of the output noise, defined (using eq. 4.2) as

$$\sigma_{rms_i} = \frac{(4\pi)^3 c^4 k}{16\lambda^2} \times \frac{t_i^4\ T_{si}}{P_{T_i} G_{T_i} G_{R_i}} \left(\frac{N\Delta B}{(N-1)\tau_i}\right)^{1/2} \qquad (4.4)$$

In order to carry out a weighted summation over (i), we assume that the data, whether noise or echo signal, are Gaussianly distributed. Whatever the original distribution, the central limit theorem argues for a Gaussian convergence and this is verified to be the case here. A given spectral element $\sigma(j)$ will yield $\langle\sigma(j)\rangle = 0$ for pure noise, and $\langle\sigma(j)\rangle > 0$ for an echo signal. In any case, if the distribution is Gaussian with a mean $\bar{\sigma}(j)$ and a standard deviation, σ_{rmsi}, the probability of observing the value $\sigma_i(j)$ is given by:

$$P_{ij} = \frac{1}{(2\pi)^{1/2}\sigma_{rms_i}} \exp\left\{ -\frac{1}{2} \left(\frac{\sigma_i(j) - \bar{\sigma}(j)}{\sigma_{rms_i}}\right)^2 \right\} \qquad (4.5)$$

For a given element $\sigma(j)$, we have I measurements (I files) of the radar cross-section, so that the probability of observing the set $(\sigma_i(j))$, i = 1,I) is given by the product:

$$P_j\,(\bar{\sigma}(j)) = \prod_{i=1}^{I} P_{ij}$$

$$= \frac{1}{\prod_{i=1}^{I} \sigma_{rms_i} (2\pi)^{1/2}} \exp\left\{-\frac{1}{2} \sum_{i=1}^{I} \left(\frac{\sigma_i(j) - \bar{\sigma}(j)}{\sigma_{rms_i}}\right)^2\right\} \tag{4.6}$$

However we do not know $\bar{\sigma}(j)$. According to the method of maximum likelihood, the best estimate of $\langle\sigma(j)\rangle$ is the value $\bar{\sigma}_o(j)$, which maximizes $P_j(\bar{\sigma}(j))$.

Thus, we must find $\bar{\sigma}_o$ which minimizes the expression:

$$\sum_{i=1}^{I} \frac{[\sigma_i(j) - \bar{\sigma}_o(j)]^2}{\sigma_{rms_i}} \tag{4.7}$$

yielding

$$-2 \sum_{i=1}^{I} \frac{\sigma_i(j) - \bar{\sigma}_o(j)}{\sigma_{rms_i}} \times \frac{1}{\sigma_{rms_i}} = 0 \tag{4.8}$$

and

$$\bar{\sigma}_o(j) = \frac{\sum_{i=1}^{I} \frac{\sigma_i(j)}{\sigma_{rms_i}^2}}{\sum_{i=1}^{I} \frac{1}{\sigma_{rms_i}^2}} \tag{4.9}$$

So, the best estimate of $\bar{\sigma}(j)$, or most probable value, is given by the weighted average of the data points $\sigma_i(j)$, using $w_i = 1/\sigma_{rmsi}^2$ as weight.

We thus associate a weight $\omega_i = 1/\sigma_{rmsi}^2$ with each file, or array $\sigma_i(j)$, and the weighted mean spectrum is:

$$\sigma_{wm}(j) = \bar{\sigma}_o(j)$$

or, written in terms of $S_i(j)$,

$$\sigma_{wm}(j) = \frac{\sum\limits_{i=1}^{I} \frac{S_i(j)}{\sigma_{rmsi}}}{\sum\limits_{i=1}^{I} \frac{1}{\sigma_{rms_i}^{2}}} \tag{4.10}$$

Now calculate the theoretical standard deviation of σ_{wm}:

$$\sigma_{rms_T}^{2} = \frac{1}{k_c-1} \sum_{k} [\sigma_{wm}(k) - \bar{\sigma}_{wm}]^2 \tag{4.11}$$

where k_c = number of frequency elements considered (total size (NP) of array less number of elements containing "echo signal"), while the index k identifies an individual element.

For simplicity, we assume $\langle\sigma_{wm}\rangle = 0$. (In practice, a small residual bias may exist but this is easily calculated and removed).

Then:

$$\sigma_{rms_T}^{2} = \frac{1}{k_c-1} \sum_{k} \sigma_{wm}^{2}(k)$$

$$= \frac{1}{k_c-1} \left(\frac{1}{\sum\limits_{i=1}^{I} \frac{1}{\sigma_{rms_i}^{2}}}\right)^2 \sum_{k} \left(\sum_{i=1}^{I} \frac{S_i(k)}{\sigma_{rms_i}}\right)^2 \tag{4.12}$$

Assuming that values of S_i are uncorrelated, we find:

$$\sigma_{rms_T}^{2} = \frac{1}{k_c-1} \left(\frac{1}{\sum\limits_{i=1}^{I} \frac{1}{\sigma_{rms_i}^{2}}}\right)^2 \sum_{i=1}^{I} \left\{\frac{1}{\sigma_{rms_i}^{2}}\right\} \sum_{k} S_i^{2}(k)$$

$$= \left(\frac{1}{\sum\limits_{i=1}^{I} \frac{1}{\sigma_{rms_i}^{2}}}\right)^2 \sum_{i=1}^{I} \frac{1}{\sigma_{rms_i}^{2}} \frac{1}{k_c-1} \sum_{k} S_i^{2}(k) \tag{4.13}$$

Since we have assumed the variance of (S_i) to be unity, we can write:

$$\sigma_{rms_T}^{2} = \left(\frac{1}{\sum_{i=1}^{I} \frac{1}{\sigma_{rms_i}^{2}}}\right)^2 \sum_{i=1}^{I} \frac{1}{\sigma_{rms_i}^{2}} = \frac{1}{\sum_{i=1}^{I} \frac{1}{\sigma_{rms_i}^{2}}} \qquad (4.14)$$

However, since the assumptions that $\langle\sigma_{wm}\rangle = 0$ and that array elements are uncorrelated are not perfectly verified (indeed, for the sample $\langle\sigma_{wm}\rangle \approx 0.06$), we calculated the mean $\langle\sigma_{wm}\rangle$ and standard deviation σ_{rms} of the distribution $\sigma_{wm}(j)$ and obtained the results listed in Table 4.1 from

$$YS(j) = [\sigma_{wm}(j) - \langle\sigma_{wm_{sample}}\rangle]/\sigma_{rms_{sample}} \qquad (4.15)$$

where σ_{rms} is calculated with respect to the mean, i.e. standard deviation of $(\sigma_{wm} - \langle\sigma_{wm}\rangle)$.

The resulting spectrum, after summation, was normalized to its rms, calculated with respect to its mean. The final spectrum, i.e. the normalized weighted sum of the spectra, for each particular combination of files indicated, is shown for the spectral elements of interest. Hereafter this spectrum will be referred to as the "unsmoothed spectrum".

In particular, the absence of any detectable signal for the combination November 2-4 is easily understood when looking at the values of the parameters listed in table 3.2, and used to calculate the necessary weights.

Figures 4.1 to 4.11 present the raw (unsmoothed) spectra for different combinations of daily data.

TABLE 4.1 Raw spectral values for elements surrounding suspected echo

Dates	Element number (predicted center = #183.5). Inverted spectra.									
(1980)	173	174	175	176	177	178	179	180	181	182
Nov 2-4	-1.1	-0.1	0.2	1.5	0.3	0.4	-0.3	0.4	-0.3	-0.4
Nov 5	0.3	-0.8	2.1	1.3	1.6	1.9	-0.5	1.7	-1.1	0.4
Nov 6	-0.3	-0.1	1.0	1.9	1.7	0.7	1.7	-0.4	-0.3	-0.8
Nov 7	-0.2	-0.4	-0.3	0.1	2.9	4.0	0.8	-0.3	1.4	0.3
Nov 8	0.9	0.6	-1.4	-0.2	2.6	2.7	-0.8	1.9	-0.2	-0.3
Nov 2-8	-0.1	-0.4	0.9	2.1	4.2	4.3	0.6	1.4	-0.2	-0.3

The lines Nov. 2-4 and Nov. 2-8 represents the sums of the data obtained during the corresponding days.

Figure Captions for Chapter 4.

Figures 4.1. through 4.7. Radar observations of comet Encke from November 2 through November 8, 1980. (Top) plot of the entire raw spectrum at a 1.2-Hz frequency resolution; (bottom) central region expanded.

Figure 4.8. Weighted sum of the data of November 2, 3, and 4, 1980.

Figure 4.9. Weighted sum of the data of November 5 and 6, 1980.

Figure 4.10. Weighted sum of the data of November 7 and 8, 1980. The presence of an echo signal of almost 4σ at the same frequency location (7.5 Hz) as a peak observed in figure 4.9 is evidence for a credible echo.

Figure 4.11. Weighted sum of all the radar data obtained during the whole period of observation of P/Encke: November 2 through November 8, 1980. The spectrum exhibits a peak of about 4.5σ at a frequency offset of about 7.5 Hz with respect to the predicted echo center frequency.

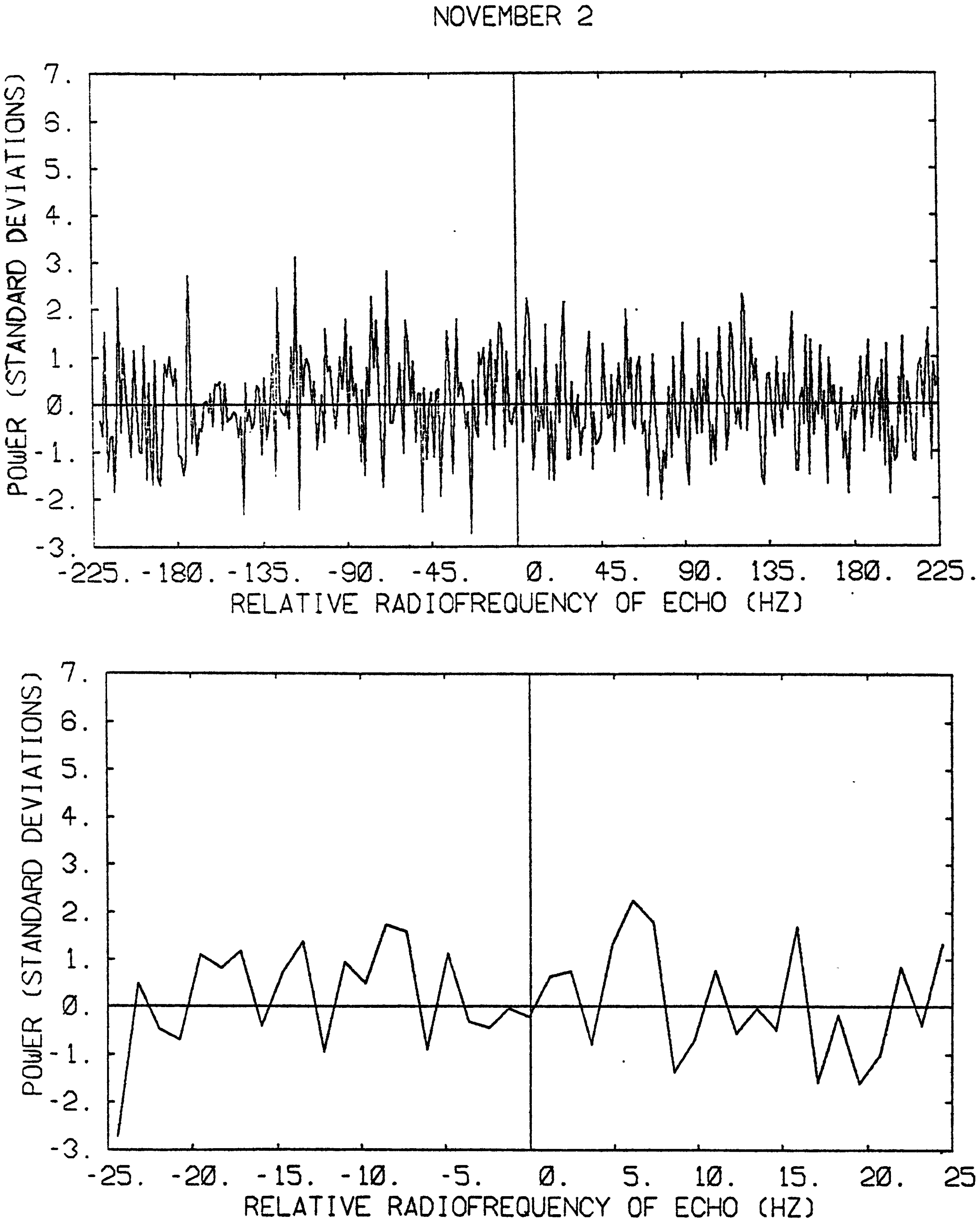
NOVEMBER 2
POWER (STANDARD DEVIATIONS)
7.
6.
5.
4.
3.
2.
1.
0.
-1.
-2.
-3.
-225.
-180.
-135.
-90.
-45.
0.
45.
90.
135.
180.
225.
RELATIVE RADIOFREQUENCY OF ECHO (HZ)
POWER (STANDARD DEVIATIONS)
7.
6.
5.
4.
3.
2.
1.
0.
-1.
-2.
-3.
-25.
-20.
-15.
-10.
-5.
0.
5.
10.
15.
20.
25
RELATIVE RADIOFREQUENCY OF ECHO (HZ)

Fig. 4.1

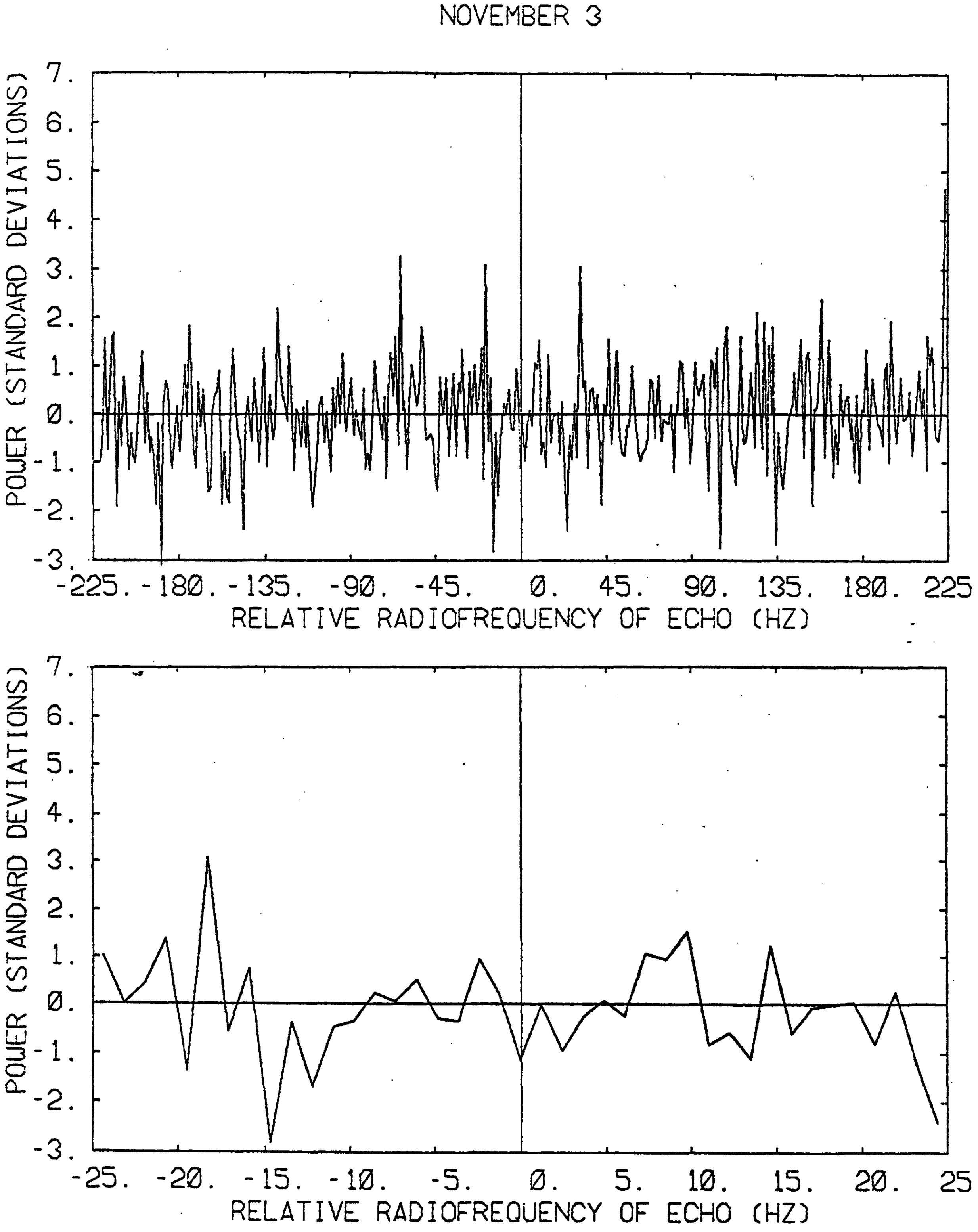
NOVEMBER 3
POWER (STANDARD DEVIATIONS)
7.
6.
5.
4.
3.
2.
1.
0.
-1.
-2.
-3.
-225.
-180.
-135.
-90.
-45.
0.
45.
90.
135.
180.
225
RELATIVE RADIOFREQUENCY OF ECHO (HZ)
POWER (STANDARD DEVIATIONS)
7.
6.
5.
4.
3.
2.
1.
0.
-1.
-2.
-3.
-25.
-20.
-15.
-10.
-5.
0.
5.
10.
15.
20.
25.
RELATIVE RADIOFREQUENCY OF ECHO (HZ)

Fig. 4.2

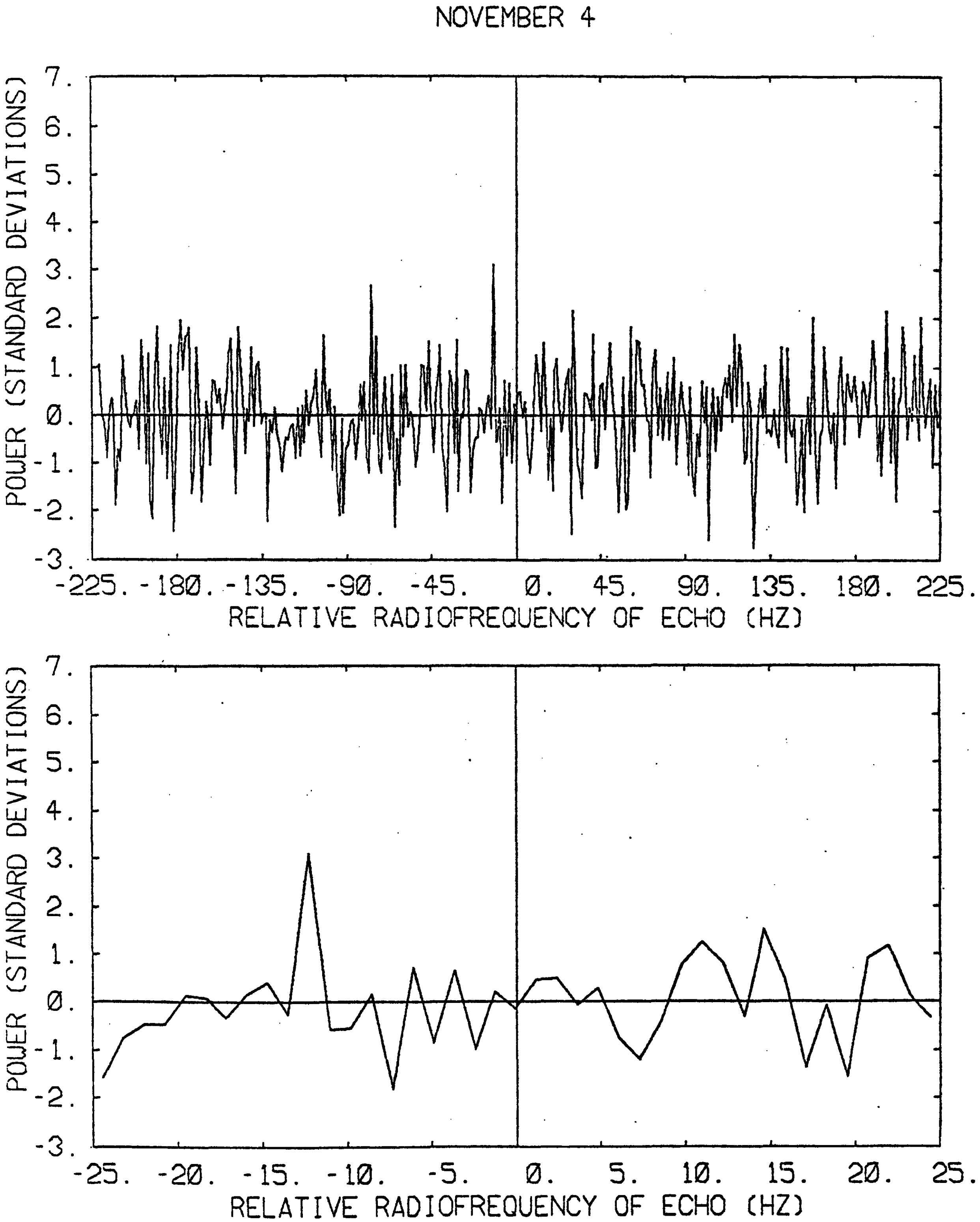
NOVEMBER 4
POWER (STANDARD DEVIATIONS)
7.
6.
5.
4.
3.
2.
1.
0.
-1.
-2.
-3.
-225.
-180.
-135.
-90.
-45.
0.
45.
90.
135.
180.
225.
RELATIVE RADIOFREQUENCY OF ECHO (HZ)
POWER (STANDARD DEVIATIONS)
7.
6.
5.
4.
3.
2.
1.
0.
-1.
-2.
-3.
-25.
-20.
-15.
-10.
-5.
0.
5.
10.
15.
20.
25.
RELATIVE RADIOFREQUENCY OF ECHO (HZ)

Fig. 4.3

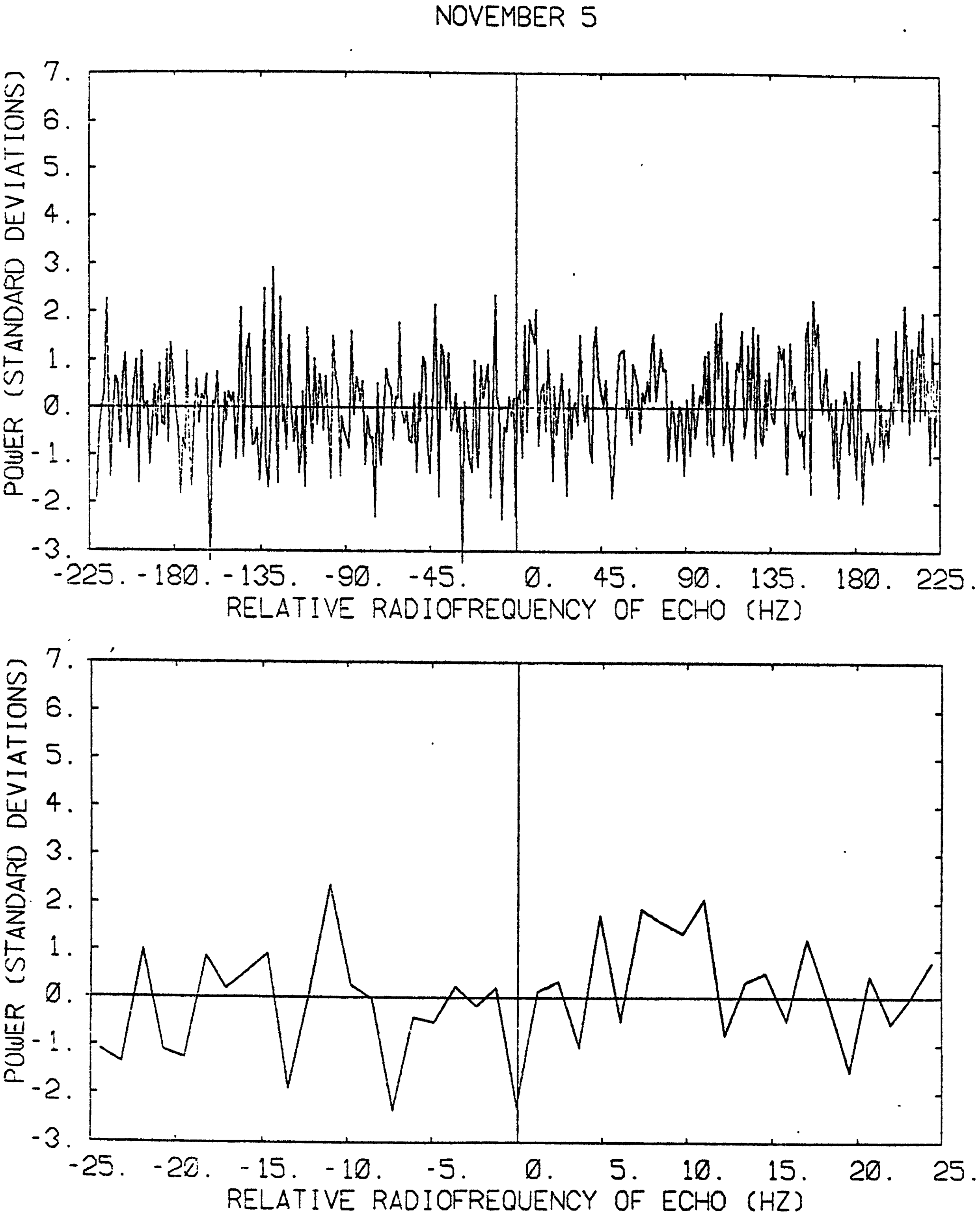
NOVEMBER 5
POWER (STANDARD DEVIATIONS)
7.
6.
5.
4.
3.
2.
1.
0.
-1.
-2.
-3.
-225.
-180.
-135.
-90.
-45.
0.
45.
90.
135.
180.
225.
RELATIVE RADIOFREQUENCY OF ECHO (HZ)
POWER (STANDARD DEVIATIONS)
7.
6.
5.
4.
3.
2.
1.
0.
-1.
-2.
-3.
-25.
-20.
-15.
-10.
-5.
0.
5.
10.
15.
20.
25.
RELATIVE RADIOFREQUENCY OF ECHO (HZ)

Fig. 4.4

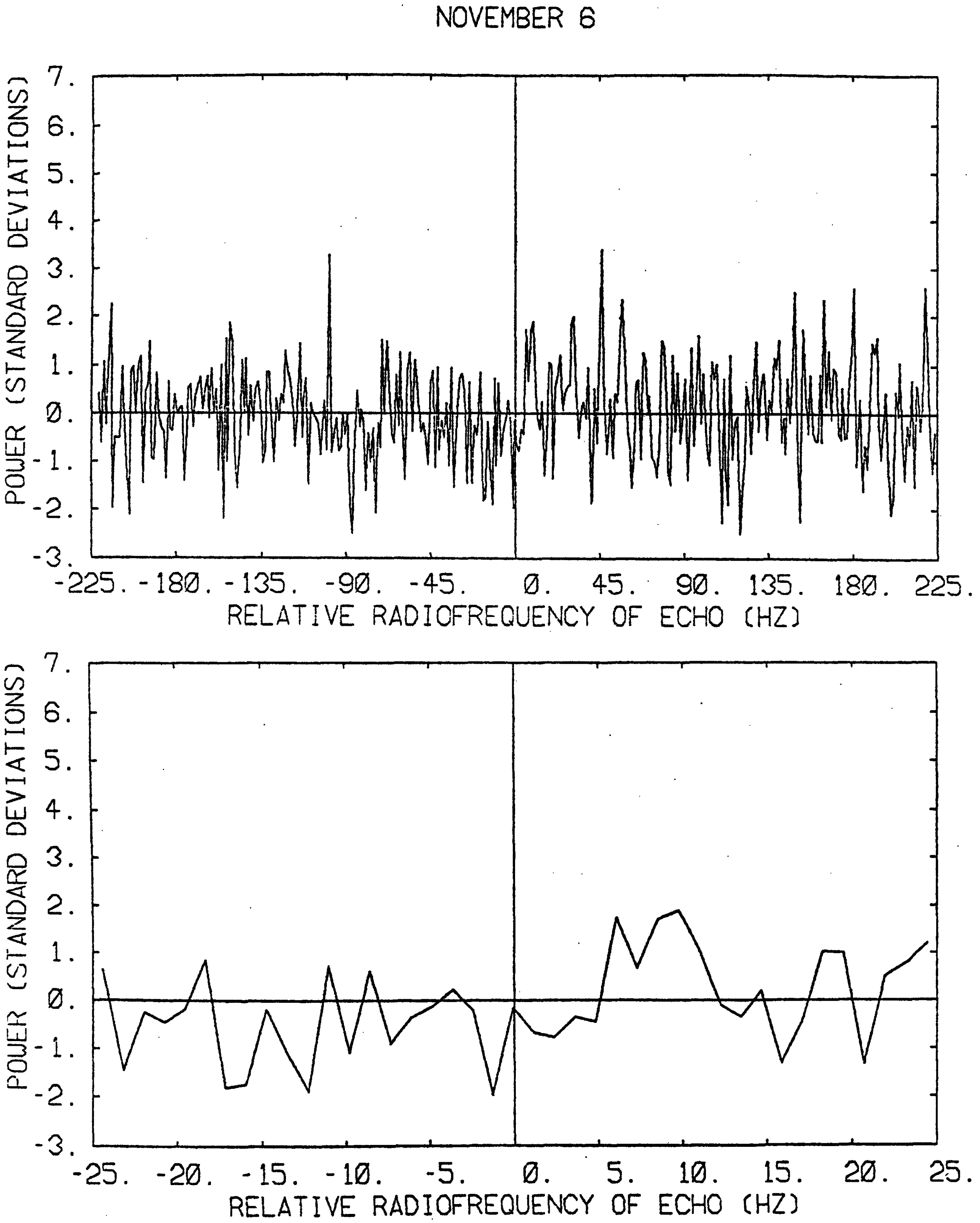
NOVEMBER 6
POWER (STANDARD DEVIATIONS)
7.
6.
5.
4.
3.
2.
1.
0.
-1.
-2.
-3.
-225.
-180.
-135.
-90.
-45.
0.
45.
90.
135.
180.
225.
RELATIVE RADIOFREQUENCY OF ECHO (HZ)
POWER (STANDARD DEVIATIONS)
7.
6.
5.
4.
3.
2.
1.
0.
-1.
-2.
-3.
-25.
-20.
-15.
-10.
-5.
0.
5.
10.
15.
20.
25.
RELATIVE RADIOFREQUENCY OF ECHO (HZ)

Fig. 4.5

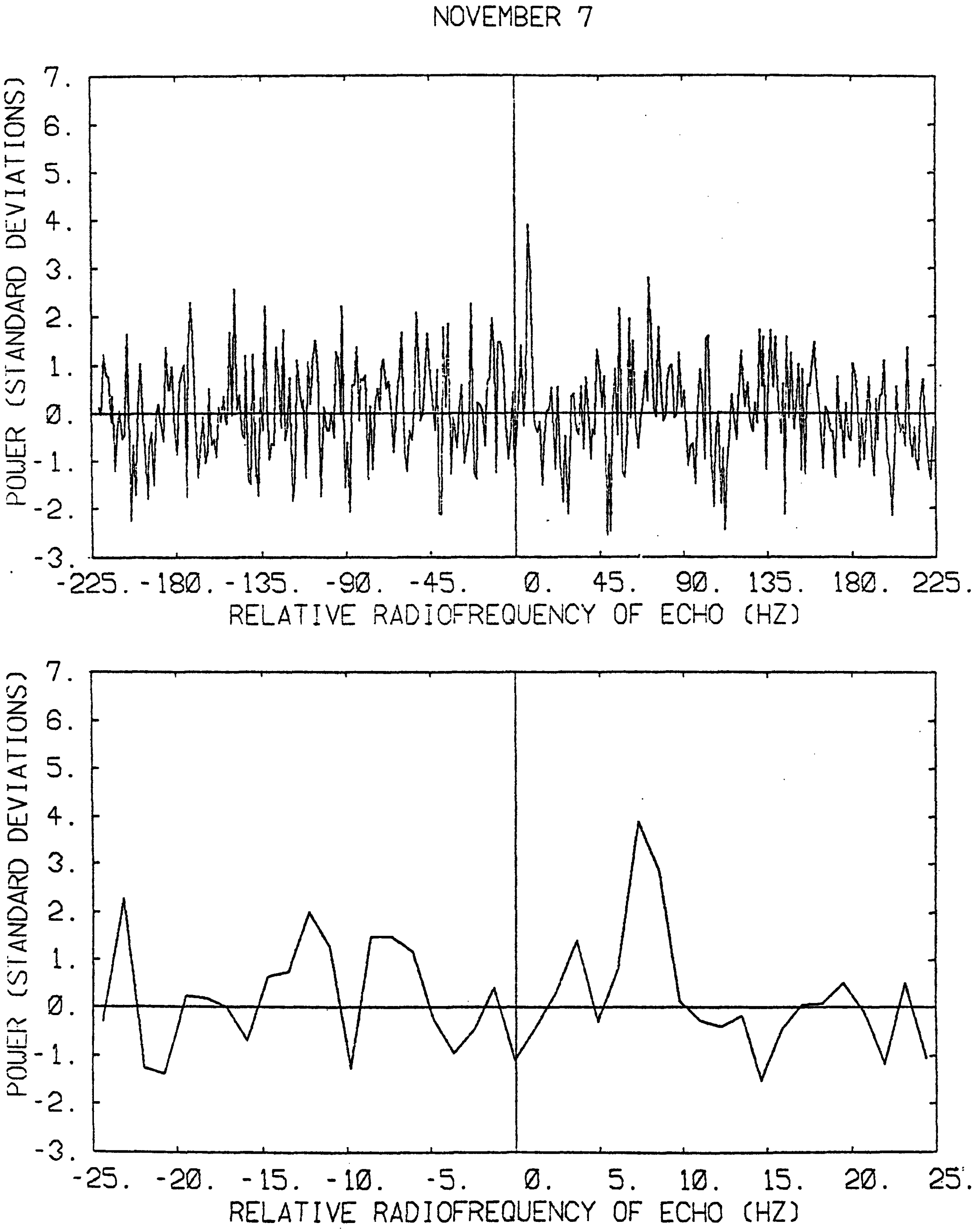
NOVEMBER 7
POWER (STANDARD DEVIATIONS)
7.
6.
5.
4.
3.
2.
1.
0.
-1.
-2.
-3.
-225.
-180.
-135.
-90.
-45.
0.
45.
90.
135.
180.
225.
RELATIVE RADIOFREQUENCY OF ECHO (HZ)
POWER (STANDARD DEVIATIONS)
7.
6.
5.
4.
3.
2.
1.
0.
-1.
-2.
-3.
-25.
-20.
-15.
-10.
-5.
0.
5.
10.
15.
20.
25.
RELATIVE RADIOFREQUENCY OF ECHO (HZ)

Fig. 4.6

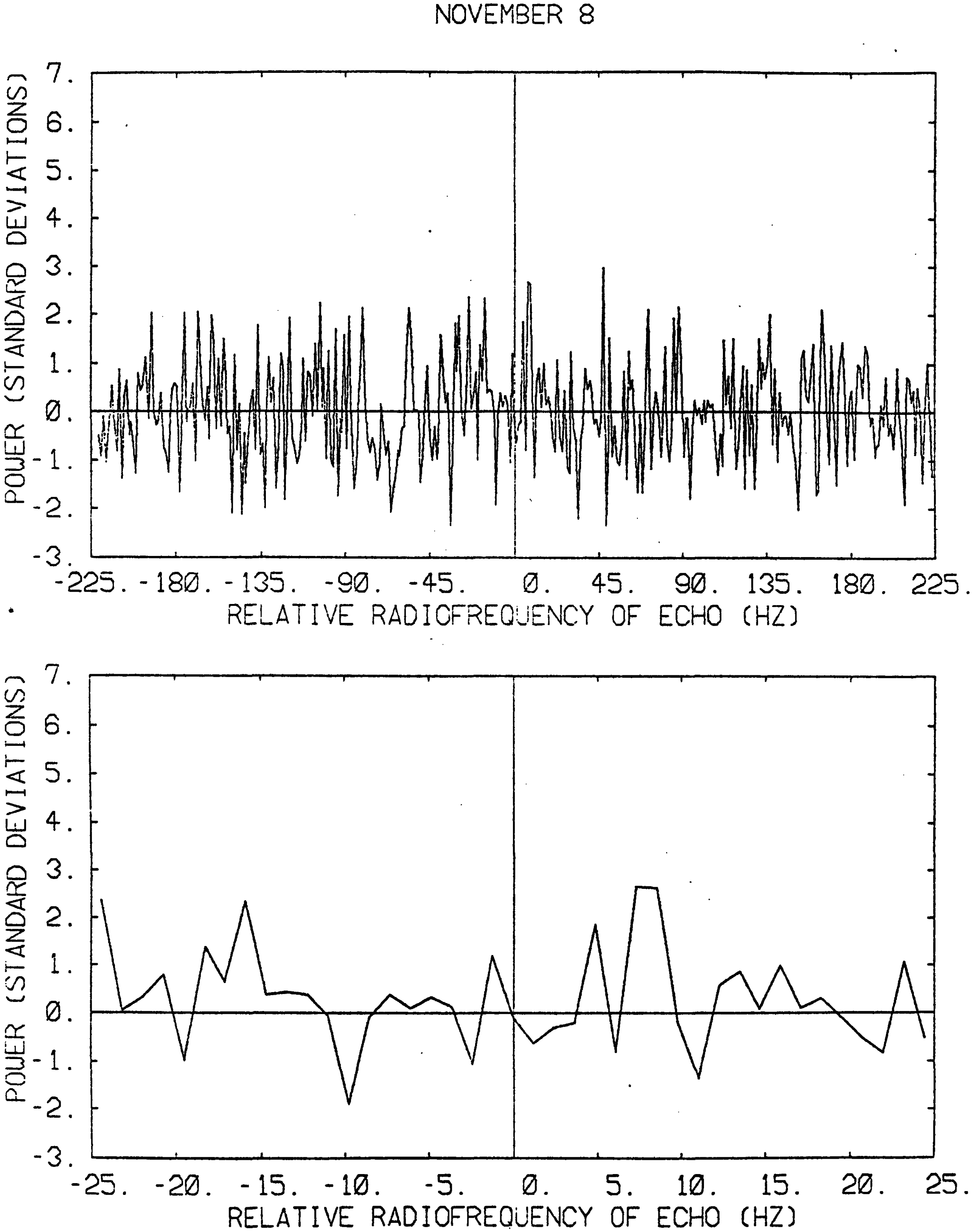
NOVEMBER 8
POWER (STANDARD DEVIATIONS)
7.
6.
5.
4.
3.
2.
1.
0.
-1.
-2.
-3.
-225.
-180.
-135.
-90.
-45.
0.
45.
90.
135.
180.
225.
RELATIVE RADIOFREQUENCY OF ECHO (HZ)
POWER (STANDARD DEVIATIONS)
7.
6.
5.
4.
3.
2.
1.
0.
-1.
-2.
-3.
-25.
-20.
-15.
-10.
-5.
0.
5.
10.
15.
20.
25.
RELATIVE RADIOFREQUENCY OF ECHO (HZ)

Fig. 4.7

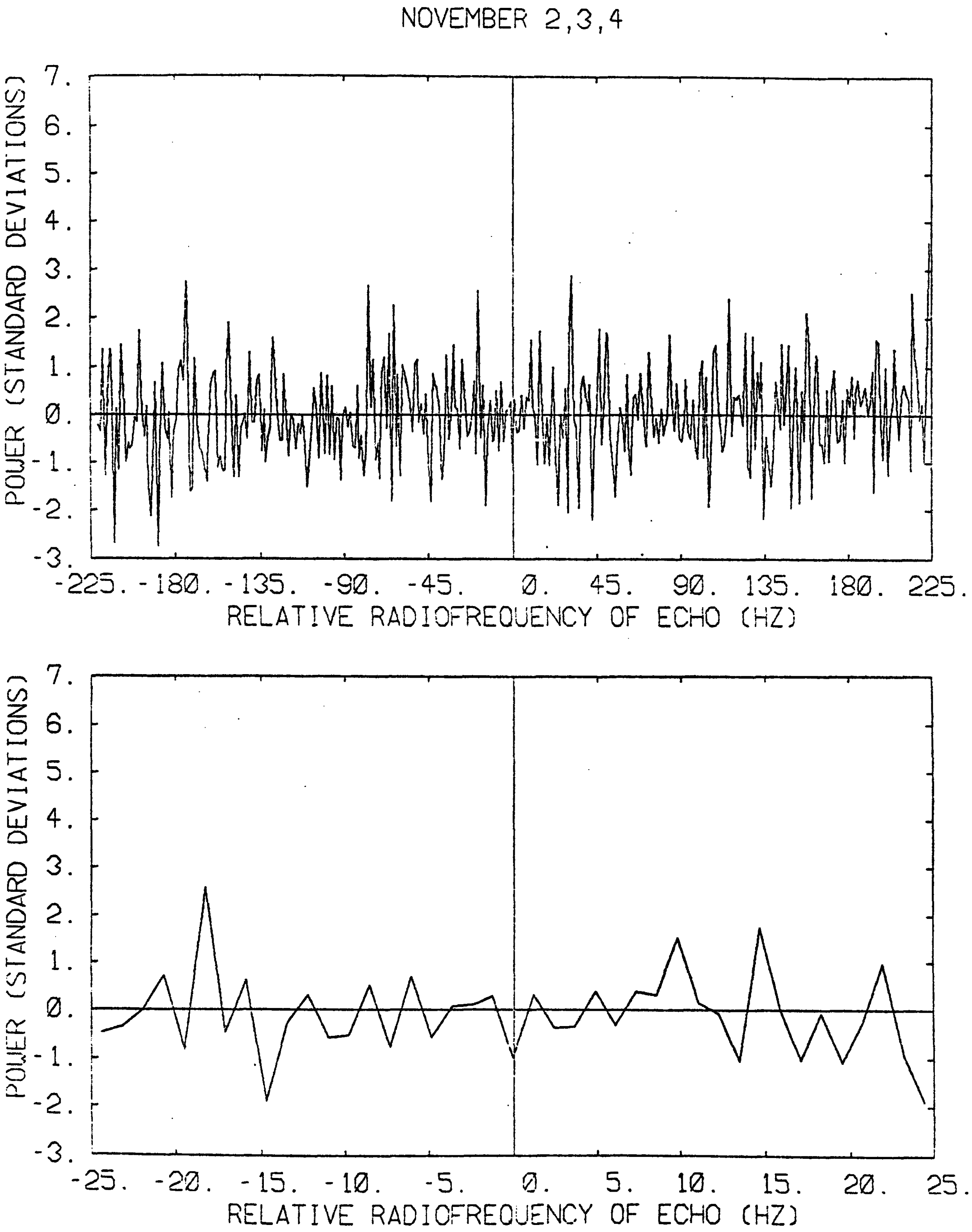
NOVEMBER 2,3,4
POWER (STANDARD DEVIATIONS)
7.
6.
5.
4.
3.
2.
1.
0.
-1.
-2.
-3
-225.
-180.
-135.
-90.
-45.
0.
45.
90.
135.
180.
225.
RELATIVE RADIOFREQUENCY OF ECHO (HZ)
POWER (STANDARD DEVIATIONS)
7.
6.
5.
4.
3.
2.
1.
0.
-1.
-2.
-3.
-25.
-20.
-15.
-10.
-5.
0.
5.
10.
15.
20.
25.
RELATIVE RADIOFREQUENCY OF ECHO (HZ)

Fig. 4.8

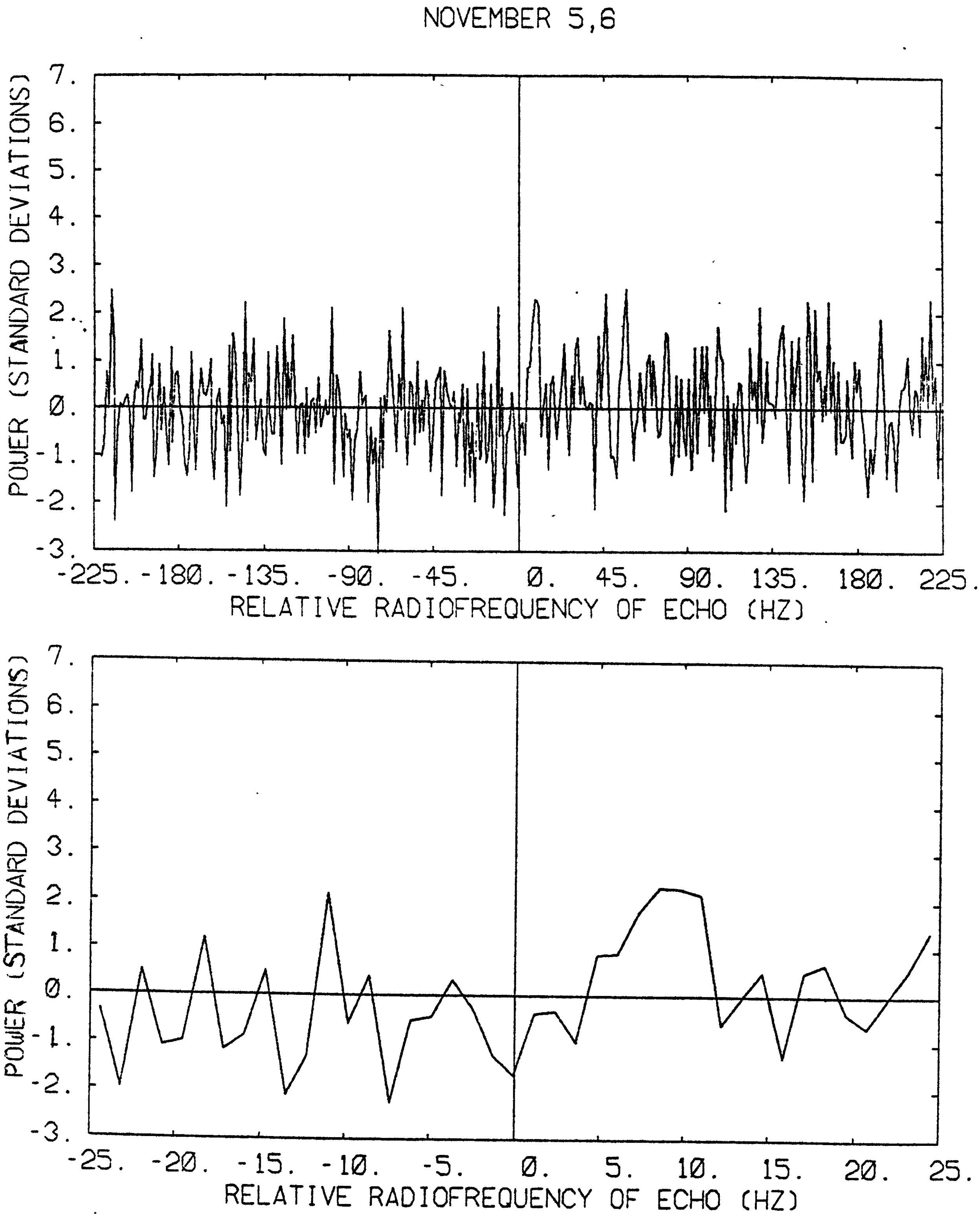
NOVEMBER 5,6
POWER (STANDARD DEVIATIONS)
7.
6.
5.
4.
3.
2.
1.
0.
-1.
-2.
-3.
-225.
-180.
-135.
-90.
-45.
0.
45.
90.
135.
180.
225.
RELATIVE RADIOFREQUENCY OF ECHO (HZ)
POWER (STANDARD DEVIATIONS)
7.
6.
5.
4.
3.
2.
1.
0.
-1.
-2.
-3.
-25.
-20.
-15.
-10.
-5.
0.
5.
10.
15.
20.
25.
RELATIVE RADIOFREQUENCY OF ECHO (HZ)

Fig. 4.9

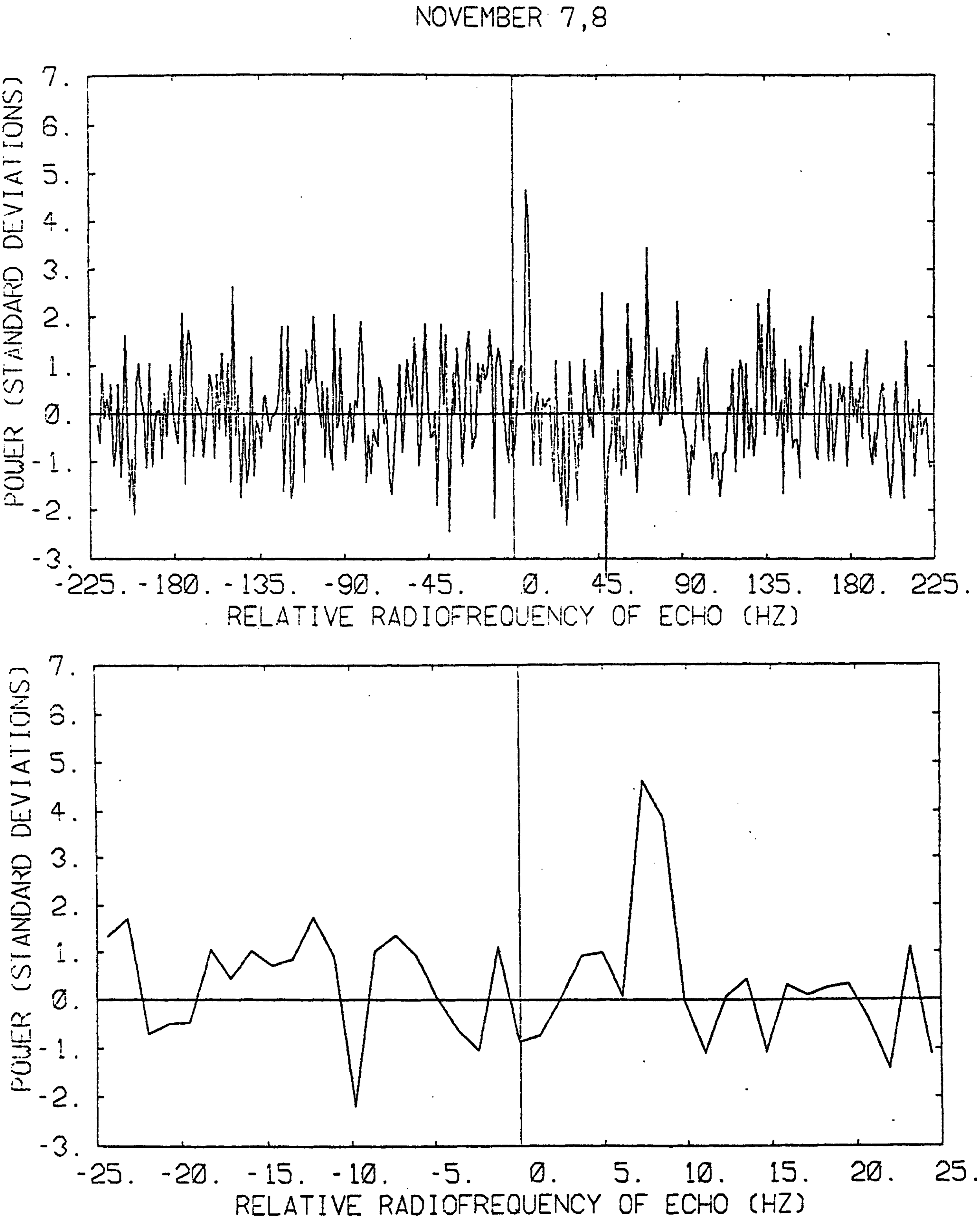
NOVEMBER 7,8
POWER (STANDARD DEVIATIONS)
7.
6.
5.
4.
3.
2.
1.
0.
-1.
-2.
-3.
-225.
-180.
-135.
-90.
-45.
0.
45.
90.
135.
180.
225.
RELATIVE RADIOFREQUENCY OF ECHO (HZ)
POWER (STANDARD DEVIATIONS)
7.
6.
5.
4.
3.
2.
1.
0.
-1.
-2.
-3.
-25.
-20.
-15.
-10.
-5.
0.
5.
10.
15.
20.
25.
RELATIVE RADIOFREQUENCY OF ECHO (HZ)

Fig. 4.10

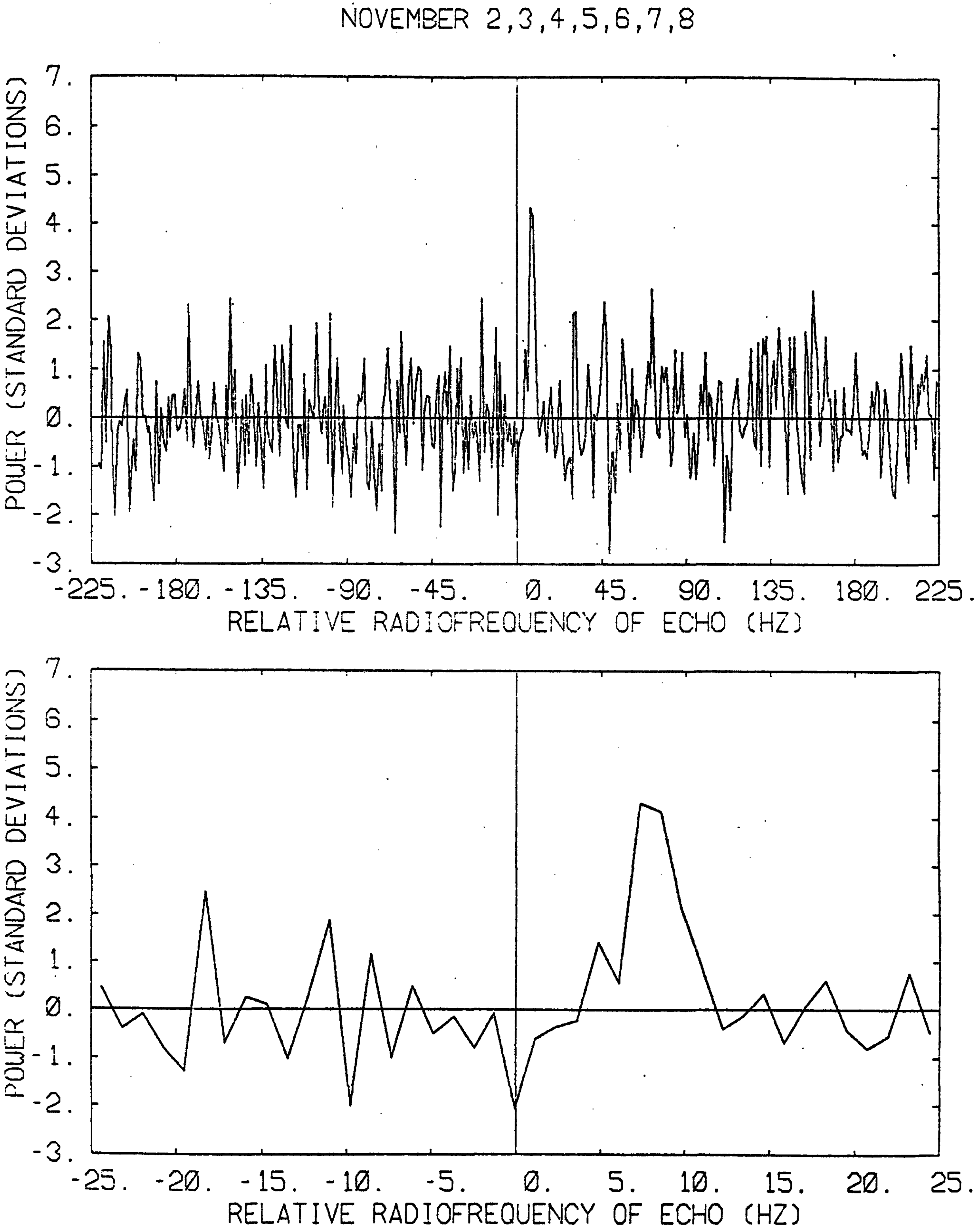
NOVEMBER 2,3,4,5,6,7,8
POWER (STANDARD DEVIATIONS)
7.
6.
5.
4.
3.
2.
1.
0.
-1.
-2.
-3.
-225.
-180.
-135.
-90.
-45.
0.
45.
90.
135.
180.
225.
RELATIVE RADIOFREQUENCY OF ECHO (HZ)
POWER (STANDARD DEVIATIONS)
7.
6.
5.
4.
3.
2.
1.
0.
-1.
-2.
-3.
-25.
-20.
-15.
-10.
-5.
0.
5.
10.
15.
20.
25.
RELATIVE RADIOFREQUENCY OF ECHO (HZ)

Fig. 4.11

PART C. COMET P/GRIGG-SKJELLERUP

OBSERVATIONS AND DATA REDUCTION

CHAPTER 5

THE PERIODIC COMET GRIGG-SKJELLERUP

5.1. History

The periodic comet Grigg-Skjellerup was discovered on July 22, 1902 by Grigg in New Zealand. Because of a delay in the report of the discovery and its southerly declination, Grigg was the only observer at this appearance. This comet was not recovered at its three following passages (1907,1912, and 1917) but was reported as a new comet by Skjellerup (South Africa) in the evening of May 17, 1922, at a geocentric distance of about 0.3 AU. Since then, it has been recovered at each passage, mostly as a diffuse object with variable appearance, occasionally showing some central condensation. Comet Grigg-Skjellerup is, with a 5.1-yr orbital period, the second-shortest-period comet (after P/Encke). The comet orbital elements are listed in Table 5.1:

TABLE 5.1

Ecliptic Coordinates, Equinox 1950.0

T(time of perihelion passage)	:	May 15, 1982
P(Orbital period)	:	5.1 yrs
Q(Perihelion distance)	:	0.989 AU
e(Eccentricity)	:	0.666
i(Orbital inclination)	:	21.1°
Argument of Perihelion	:	359.3°
Longitude of Ascending Node	:	212.6°

5.2. Physical characteristics

5.2.1. Optical appearance

At most of its appearances, Grigg-Skjellerup was reported as being a diffuse object, without definite structure. However, the presence of near-nucleus dust structures, such as spiral jets or parabolic envelopes has been noticed on occasion, allowing an estimate of the nucleus rotation vector. The estimates are rough, however, because of the few good photographs or drawings available. At its 1982 appearance, Grigg-Skjellerup has exhibited some near-nucleus structure which were observed on the CCD images obtained by Steve Larson on June 19, 1982 (Fig. 5.1, private communication), and on drawings done by some amateur astronomers (M. Verdenet, private communication).

A light curve of comet Grigg-Skjellerup for its 1982 appearance is given by Morris (1983).

5.2.2. Non-gravitational motion and spin of the nucleus

The "Catalog of cometary orbits", Marsden (1979), lists the non-gravitational parameters estimated for several comets. The non-gravitational transverse force parameter A_2 for Grigg-Skjellerup has a negative value of small amplitude. The catalog gives the value of A_2 for different periods:

1922-1942	$A_2 = 0.0010$
1942-1961	$A_2 = -0.0025$
1952-1972	$A_2 = -0.0008$

These changes may reflect a precession of the spin axis. In any case, these values are among the smallest for nuclei showing non-gravitational effects and suggest that the nucleus rotation is slow and retrograde. These results are fully compatible with the approximately 80-hr retrograde rotation period obtained by Steve Larson. These data will be used in section 12.3 to aid in the estimation of the size of the nucleus.

Figure Captions for Chapter 5.

Figure 5.1. CCD image of comet P/Grigg-Skjellerup obtained by Steve Larson using the space telescope wide field planetary ground-based camera, on June 19, 1982. Jets may be seen near the nucleus which have been used to estimate the spin vector of the nucleus.

Fig. 5.1

CHAPTER 6

P/GRIGG-SKJELLERUP: RADAR OBSERVATION AND DATA REDUCTION

6.1. Observations

The comet was observed between May 20 and June 2, 1982 while at a geocentric distance of about 0.33 A.U., and about a week after it passed its perihelion. The Sun-Earth-Comet geometry on May 26, which approximately corresponds to the midtime of observation is shown in figure 6.1. The target coordinates for each day for which a radar data set was available are summarized in Table 6.1. The dates of May 22, 25, 28, 30 and June 1 have not been entered since technical problems in the operation of the radar system prevented the acquisition of meaningful data.

6.2. Radar system configuration

The observations were carried out using the same experimental setup as described before for the P/Encke observations, except for the values of the following parameters. In the Grigg-Skjellerup case, the transmitted carrier frequency was switched among four different frequencies, Δf_s = 380 Hz apart, and dwelt a time T = 10 seconds on each of them. The four transmitted frequencies were:

F_k = 2379,999,430 + (k-1) Δf Hz, where k is the integer 1,2,3 or 4

Reception of the echo signal was made in both senses of circular polarization (same as and orthogonal to the transmitted sense). The signals at the output of the two phase detectors were passed through 1-kHz wide low-pass filters, sampled at a 2.09-kHz rate and Fourier transformed to yield a final spectrum having a frequency resolution

TABLE 6.1

RECEIVING EPHEMERIDES
AT ARECIBO TRANSIT

DATE (1980)	UT hr mn	RA hr mn sc	DEC ° ' "	Z.A. (deg)	DOPPLER (Hz)	R-T DELAY (secs)
May 20	21 58	09 24 05	22 43 07	4.4	80,215	349.99
May 21	22 01	09 30 45	23 40 32	5.3	73,492	347.19
May 23	22 07	09 44 39	25 34 38	7.2	59,420	342.36
May 24	22 10	09 51 53	26 30 58	8.2	52,105	340.33
May 26	22 17	10 06 57	28 21 11	10.0	36,973	337.09
May 27	22 21	10 14 46	29 14 40	10.9	29,195	335.89
May 29	22 29	10 30 56	30 57 15	12.6	13,351	334.35
May 31	22 38	10 47 46	32 32 37	14.2	-2,754	333.97
June 2	22 48	11 05 10	33 59 12	15.6	-18,926	334.76

of about 1.0 Hz.

The system parameters for the observations of P/Grigg-Skjellerup are given in Table 6.2.

6.4. Data Reduction

The reduction procedure used is in all ways similar to described for P/Encke in Chapter 4. The Grigg-Skjellerup data however consist of individual records, 2.09-kHz wide (as compared to 2.5 kHz for Encke). The analyzed bandwidth covering 380 Hz has a resolution of about 1 Hz.

The weighted sum of the spectra corresponding to the different data files (each file contains data for a given round-trip cycle) was carried out as described in Section 4.2., with a total number I = 90 files for each polarization obtained during the total period of observation; the corresponding total integration time was about 6 1/2 hours.

6.5. Spectra

Figures 6.2 through 6.10 show the resulting same-sense and orthogonal-sense circularly polarized spectra for each day of observation, while Figs. 6.11 and 6.12 show SC and OC spectra for the weighted sum of the whole set of data. In Table 6.3 are listed the signal-to-noise ratios for the spectral elements adjacent to the frequency containing the maximum signal-to-noise ratio. The *a priori* center frequency of the echo was expected to fall in the spectral element 185, so that the frequency of actual echo was about 4 Hz lower than predicted from the ephemerides.

TABLE 6.2

SUMMARY OF THE SYSTEM PARAMETERS FOR THE OBSERVATIONS OF P/GRIGG - SKJELLERUP

Date	Δ	RTT	G	P_t	$T_{s'}$	t_i
(1982)	(a.u.)	(sec)	(dB)	(Kw)	(K)	(sec)
May 20	0.351	350	71.5	400	43	2222
May 21	0.348	347	71.4	400	46	2904
May 23	0.343	342	71.4	400	46	2904
May 24	0.341	340	71.2	400	50	3043
May 26	0.338	337	71.1	400	53	3406
May 27	0.337	336	71.3	400	47	2620
May 29	0.335	334	71.0	400	50	1214
May 31	0.335	334	70.5	400	63	2620
June 2	0.336	335	70.2	400	70	2358

All parameters (Δ, RTT, G, P_t, t_i) have the same meaning as in Section 3.3.4; ex. $T_{s'}$ represents here the system temperature associated with the opposite-sense circular port of the antenna feed. G and T_s represent effective values.

TABLE 6.3

P/GRIGG-SKJELLERUP

SIGNAL-TO-NOISE RATIOS (STANDARD DEVIATIONS)

	O.C.					S.C.				
SPECTRAL ELEMENT #	179	180	181	182	183	179	180	181	182	183
May 20	0.8	0.0	3.1	-0.7	-1.0	0.4	1.0	1.2	-1.7	2.7
May 21	2.2	-1.2	2.5	0.5	1.5	0.4	-0.1	0.6	0.8	0.9
May 23	-0.5	2.0	2.8	-0.4	0.1	0.6	0.0	-0.8	-0.4	0.7
May 24	1.5	1.5	3.2	0.7	0.6	0.9	0.4	0.9	-0.1	0.7
May 26	-0.3	1.0	3.7	-0.7	0.9	0.2	0.9	0.5	-0.7	-0.1
May 27	-0.7	0.8	4.7	0.9	-1.9	-0.3	-0.1	-0.6	-0.6	-0.2
May 29	0.0	0.6	4.3	0.9	0.8	-0.7	1.0	-0.2	-1.6	-2.1
May 31	0.9	-0.5	2.8	1.2	0.5	0.5	-0.2	1.1	-2.1	-0.9
June 2	1.1	0.8	2.4	-0.7	-2.3	-1.2	0.1	-0.1	-0.5	0.6
WEIGHTED SUM	1.4	1.9	9.7	0.5	0.1	0.7	0.9	0.8	-1.7	1.3

Here, frequency is increasing to the right.

Figure Captions for Chapter 6

Figure 6.1. Configuration of the Earth-Sun-Comet G-S system at midtime of the radar observations (May 26, 1982).

Figure 6.2 through 6.10. Radar observation of comet G-S. Weighted sum of the radar data for each day on which radar observations took place between May 21 and June 2, 1982, with S.C. polarization on top, and O.C. at bottom. The frequency resolution is about 1 Hz. On Fig. 6.2 (May 20) for instance, a 3σ echo is seen at a -4 Hz with respect to the expected center frequency (shown as zero on the X-axis).

Figure 6.11. Weighted sum of all the radar data obtained during the observations of comet Grigg-Skjellerup (S.C. spectrum on top and O.C. spectrum at bottom). An echo with a 10σ signal-to-noise ratio is evident, offset by about 4 Hz from the a priori center frequency. The echo is unresolved, with a width significantly smaller than 1 Hz. The absence of a detectable echo in the S.C. sense indicates that there is no significant depolarization of the radar signal at the surface of the nucleus.

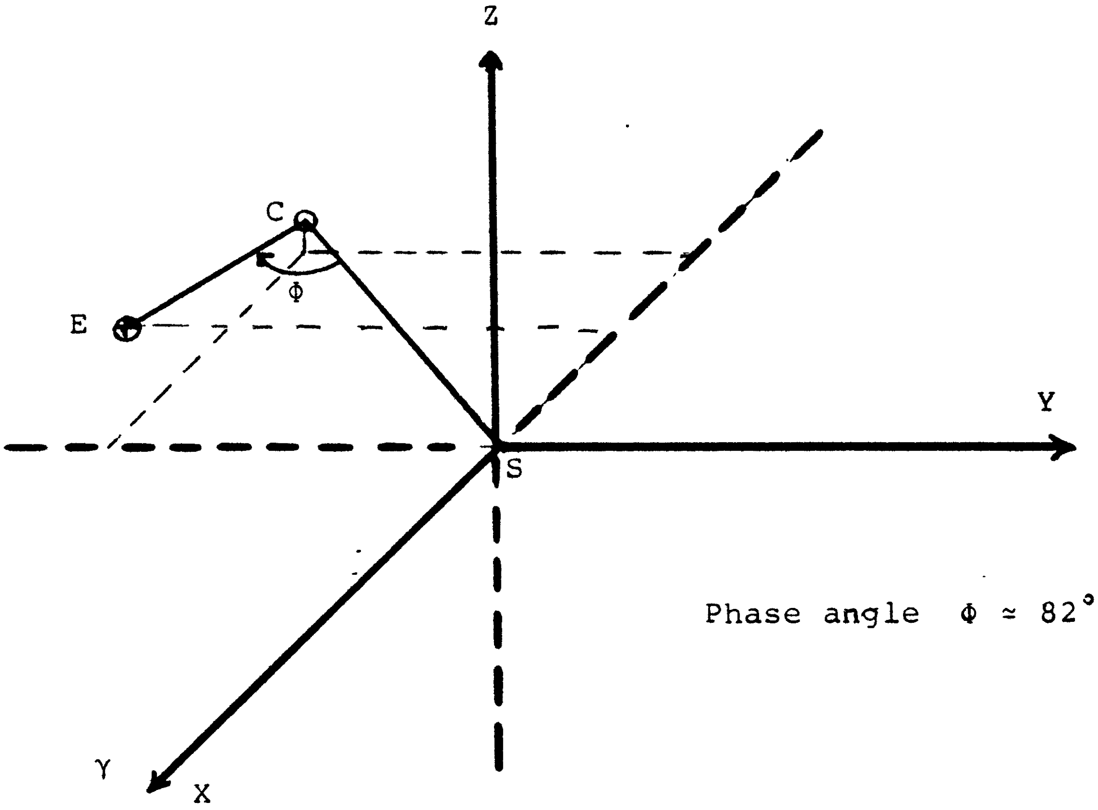

Fig. 6.1. Configuration of the Sun-Earth-Comet System

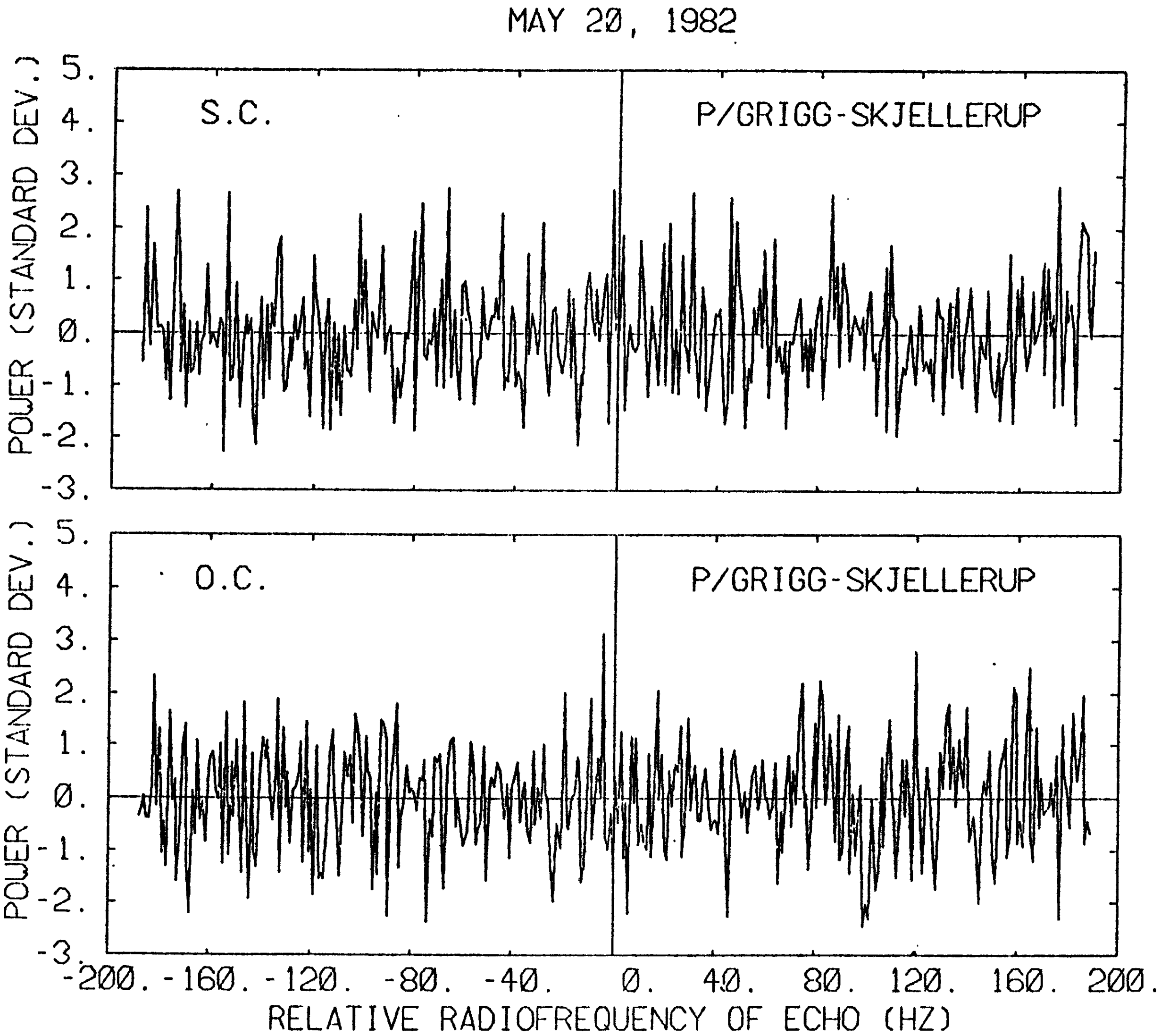
MAY 20, 1982
S.C.
P/GRIGG-SKJELLERUP
O.C.
P/GRIGG-SKJELLERUP
POWER (STANDARD DEV.)
POWER (STANDARD DEV.)
5.
4.
3.
2.
1.
0.
-1.
-2.
-3.
-200. -160. -120. -80. -40. 0. 40. 80. 120. 160. 200.
RELATIVE RADIOFREQUENCY OF ECHO (HZ)

Fig. 6.2

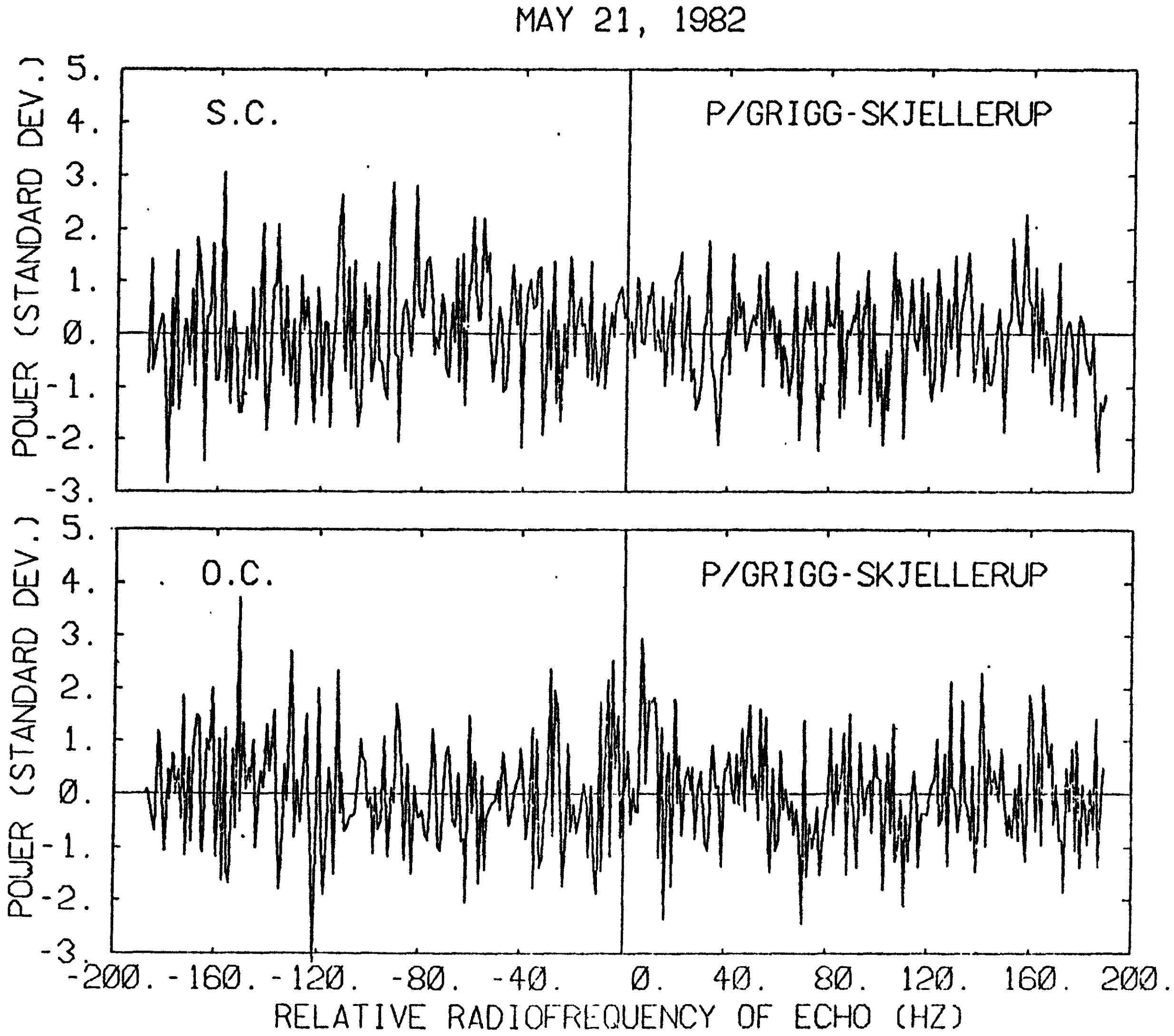
MAY 21, 1982
S.C.
P/GRIGG-SKJELLERUP
O.C.
P/GRIGG-SKJELLERUP
POWER (STANDARD DEV.)
5.
4.
3.
2.
1.
0.
-1.
-2.
-3.
-200.
-160.
-120.
-80.
-40.
0.
40.
80.
120.
160.
200.
RELATIVE RADIOFREQUENCY OF ECHO (HZ)

Fig. 6.3

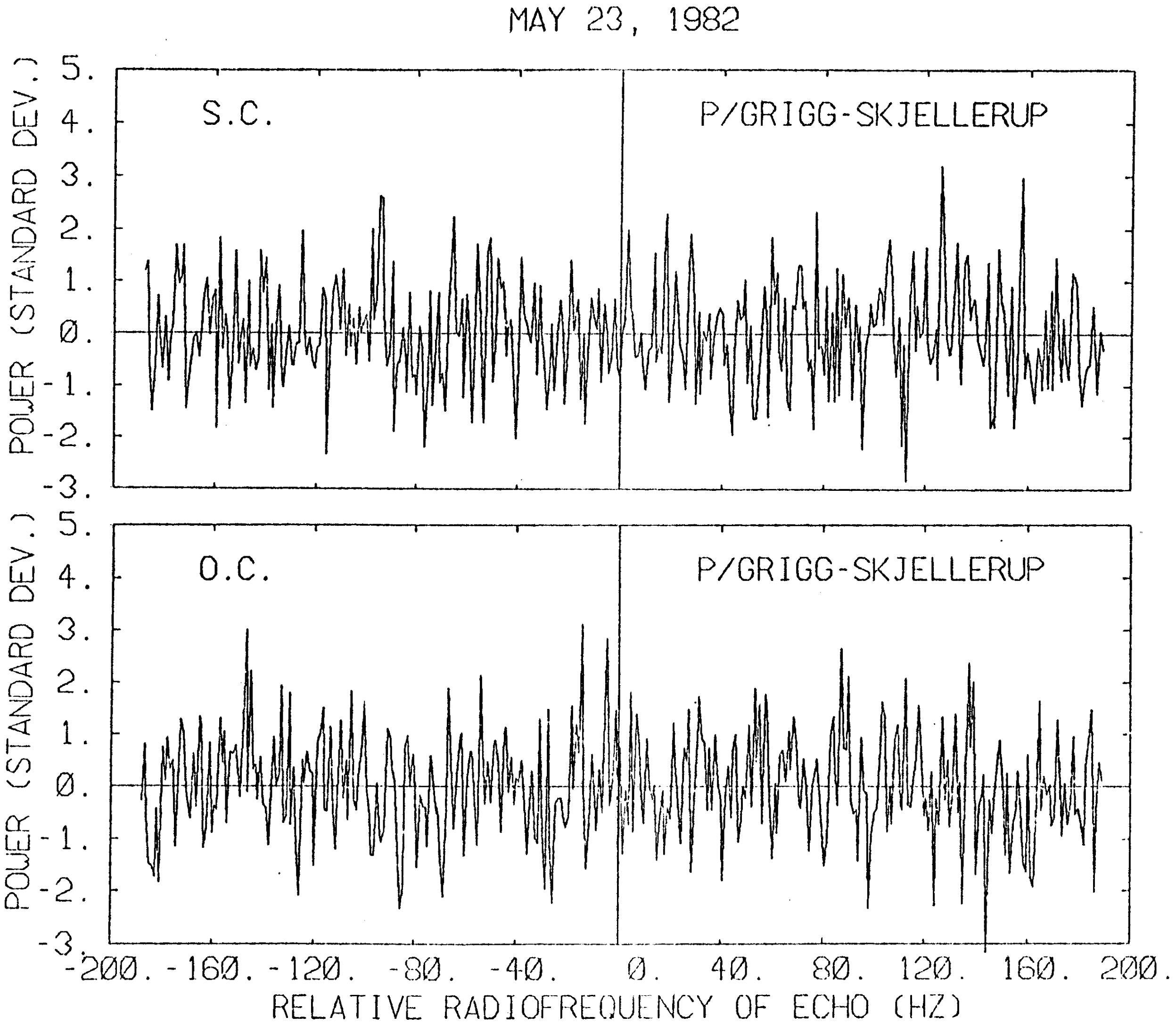
MAY 23, 1982
S.C.
P/GRIGG-SKJELLERUP
O.C.
P/GRIGG-SKJELLERUP
POWER (STANDARD DEV.)
5.
4.
3.
2.
1.
0.
-1.
-2.
-3.
-200.
-160.
-120.
-80.
-40.
0.
40.
80.
120.
160.
200.
RELATIVE RADIOFREQUENCY OF ECHO (HZ)

Fig. 6.4

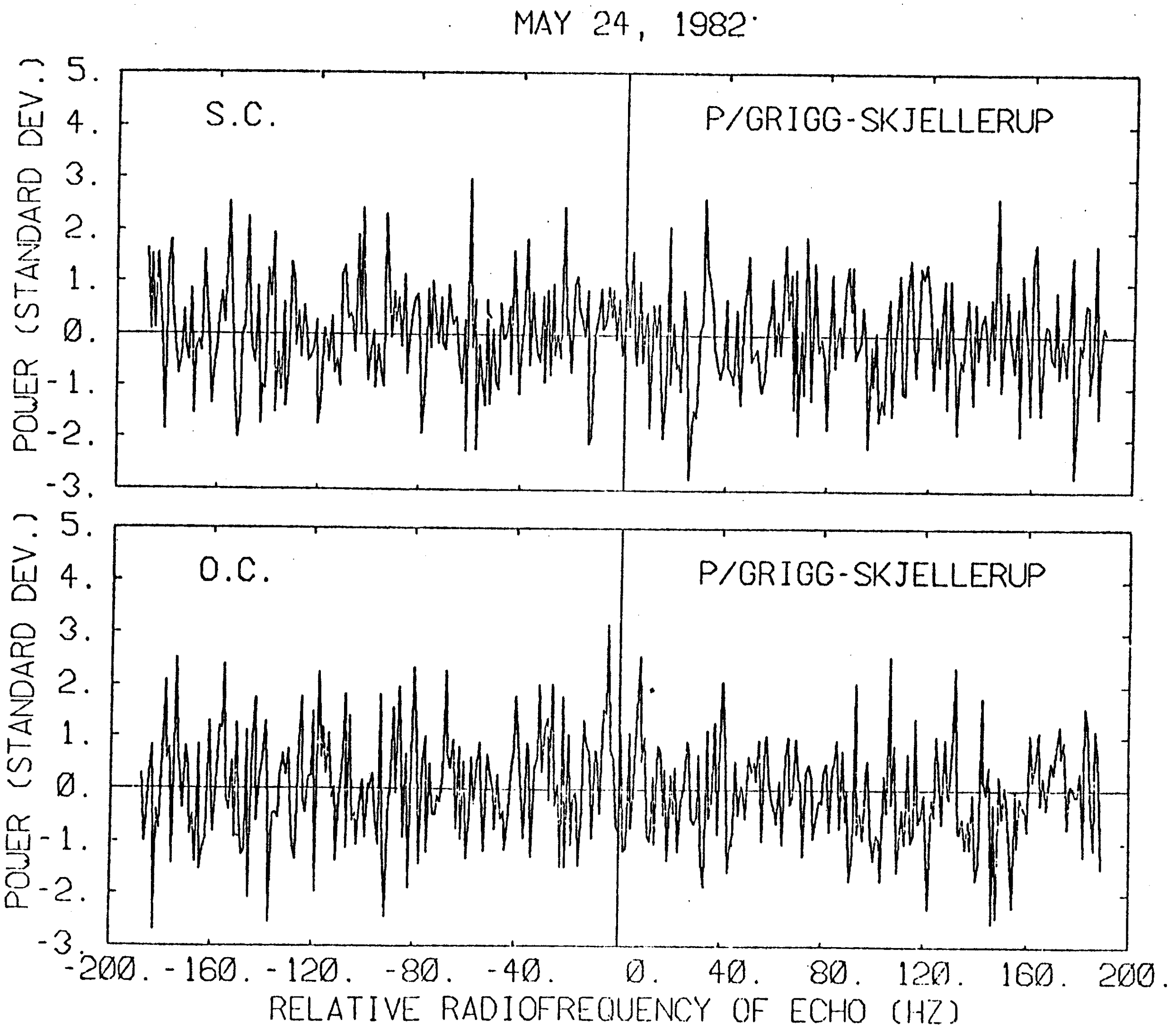
MAY 24, 1982
S.C.
P/GRIGG-SKJELLERUP
O.C.
P/GRIGG-SKJELLERUP
POWER (STANDARD DEV.)
5.
4.
3.
2.
1.
0.
-1.
-2.
-3.
-200.
-160.
-120.
-80.
-40.
0.
40.
80.
120.
160.
200.
RELATIVE RADIOFREQUENCY OF ECHO (HZ)

Fig. 6.5

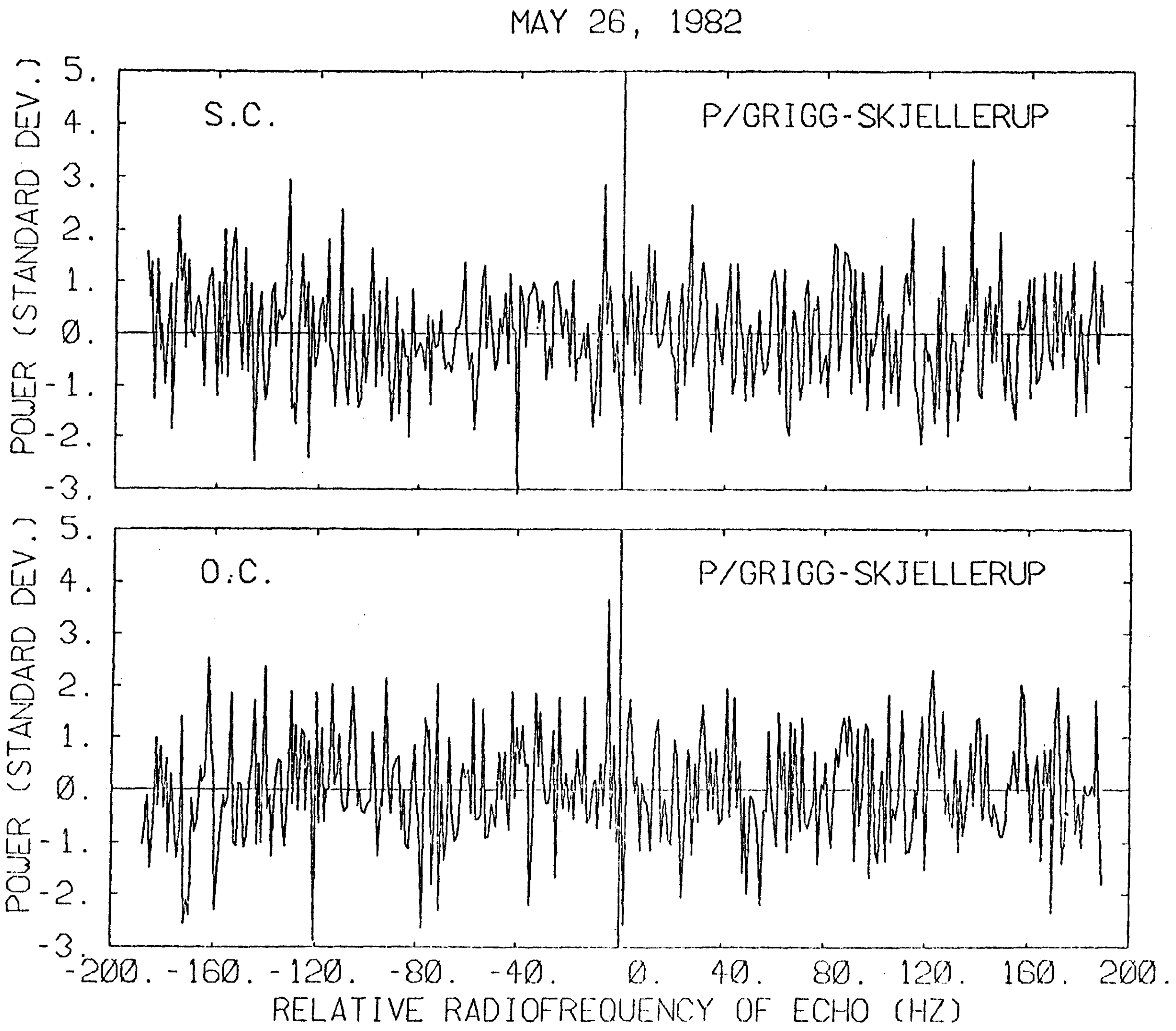
MAY 26, 1982
S.C.
P/GRIGG-SKJELLERUP
O.C.
P/GRIGG-SKJELLERUP
POWER (STANDARD DEV.)
POWER (STANDARD DEV.)
5.
4.
3.
2.
1.
0.
-1.
-2.
-3.
-200. -160. -120. -80. -40. 0. 40. 80. 120. 160. 200.
RELATIVE RADIOFREQUENCY OF ECHO (HZ)

Fig. 6.6

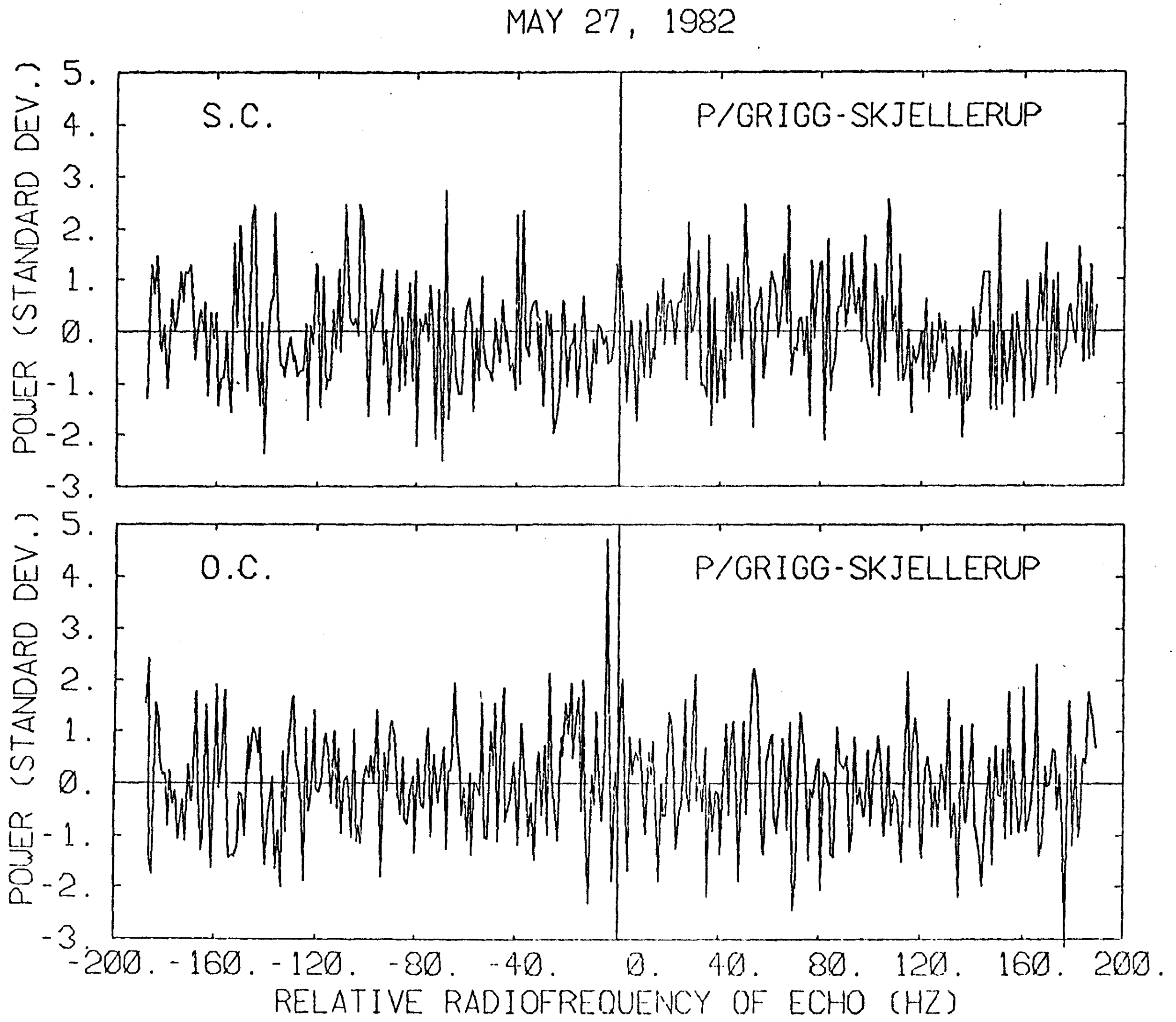
MAY 27, 1982
S.C.
P/GRIGG-SKJELLERUP
O.C.
P/GRIGG-SKJELLERUP
POWER (STANDARD DEV.)
5.
4.
3.
2.
1.
0.
-1.
-2.
-3.
-200.
-160.
-120.
-80.
-40.
0.
40.
80.
120.
160.
200.
RELATIVE RADIOFREQUENCY OF ECHO (HZ)

Fig. 6.7

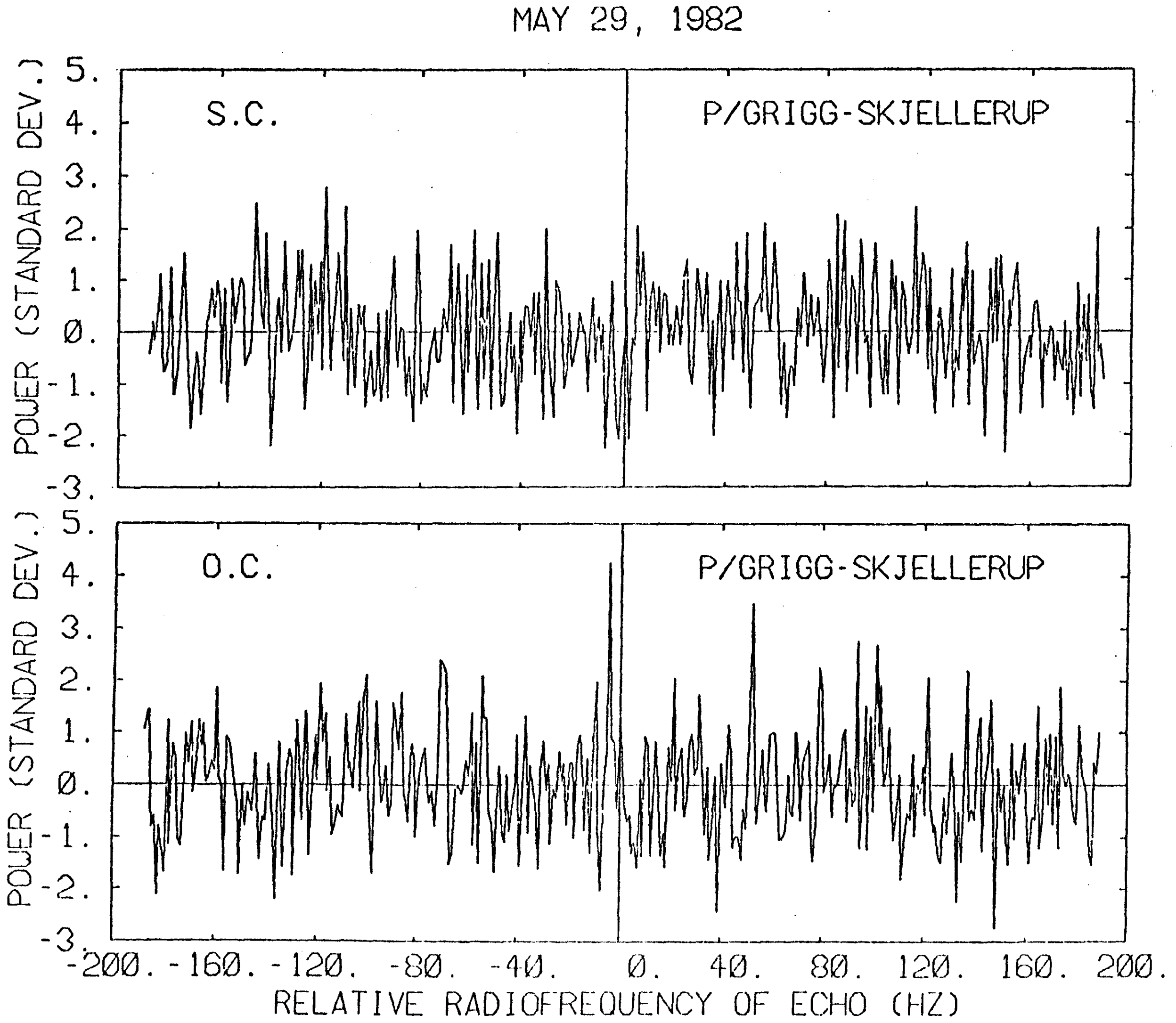
MAY 29, 1982
S.C.
P/GRIGG-SKJELLERUP
O.C.
P/GRIGG-SKJELLERUP
POWER (STANDARD DEV.)
POWER (STANDARD DEV.)
5.
4.
3.
2.
1.
0.
-1.
-2.
-3.
-200. -160. -120. -80. -40. 0. 40. 80. 120. 160. 200.
RELATIVE RADIOFREQUENCY OF ECHO (HZ)

Fig. 6.8

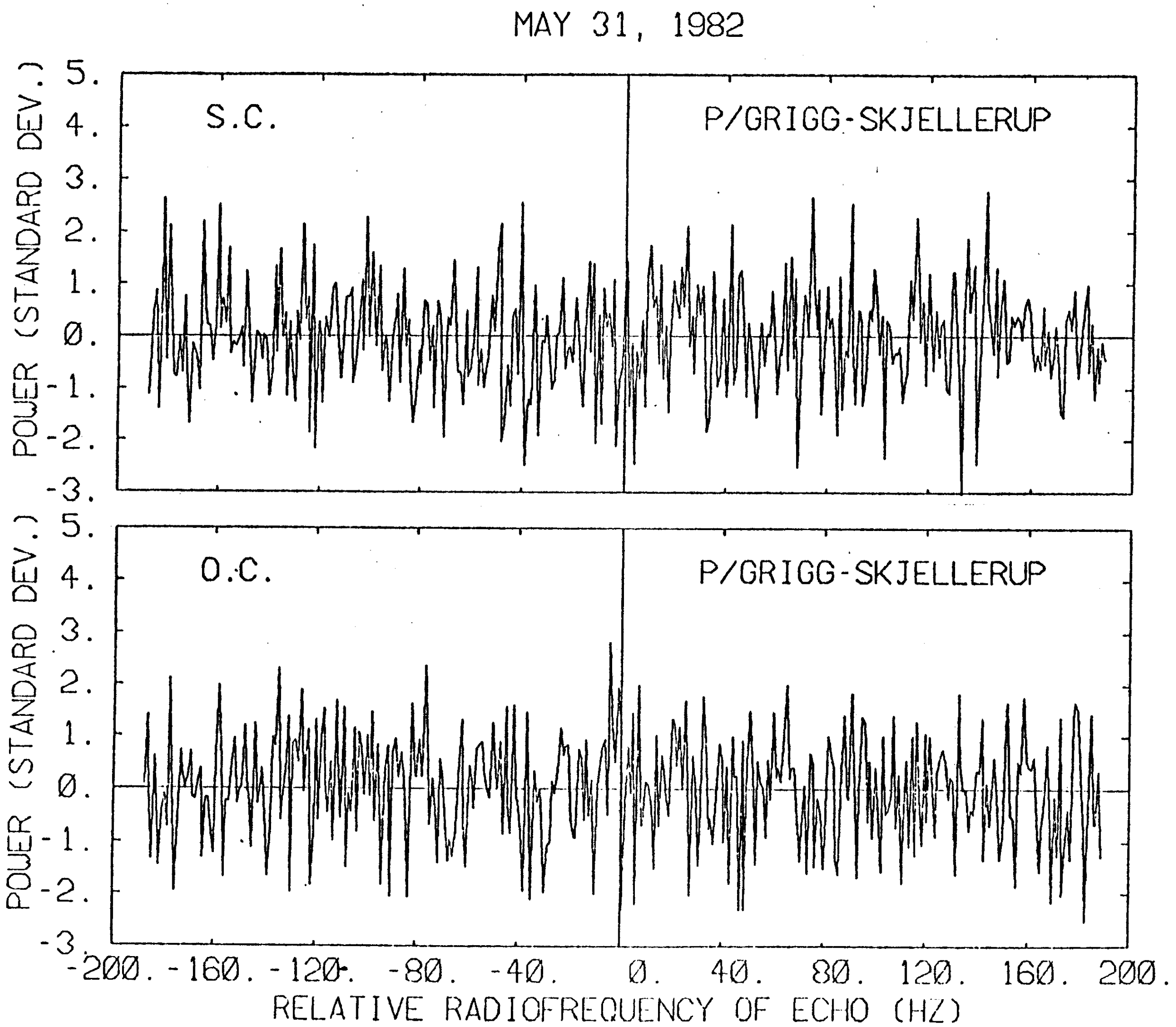
MAY 31, 1982
S.C.
P/GRIGG-SKJELLERUP
O.C.
P/GRIGG-SKJELLERUP
POWER (STANDARD DEV.)
5.
4.
3.
2.
1.
0.
-1.
-2.
-3.
-200.
-160.
-120.
-80.
-40.
0.
40.
80.
120.
160.
200.
RELATIVE RADIOFREQUENCY OF ECHO (HZ)

Fig. 6.9

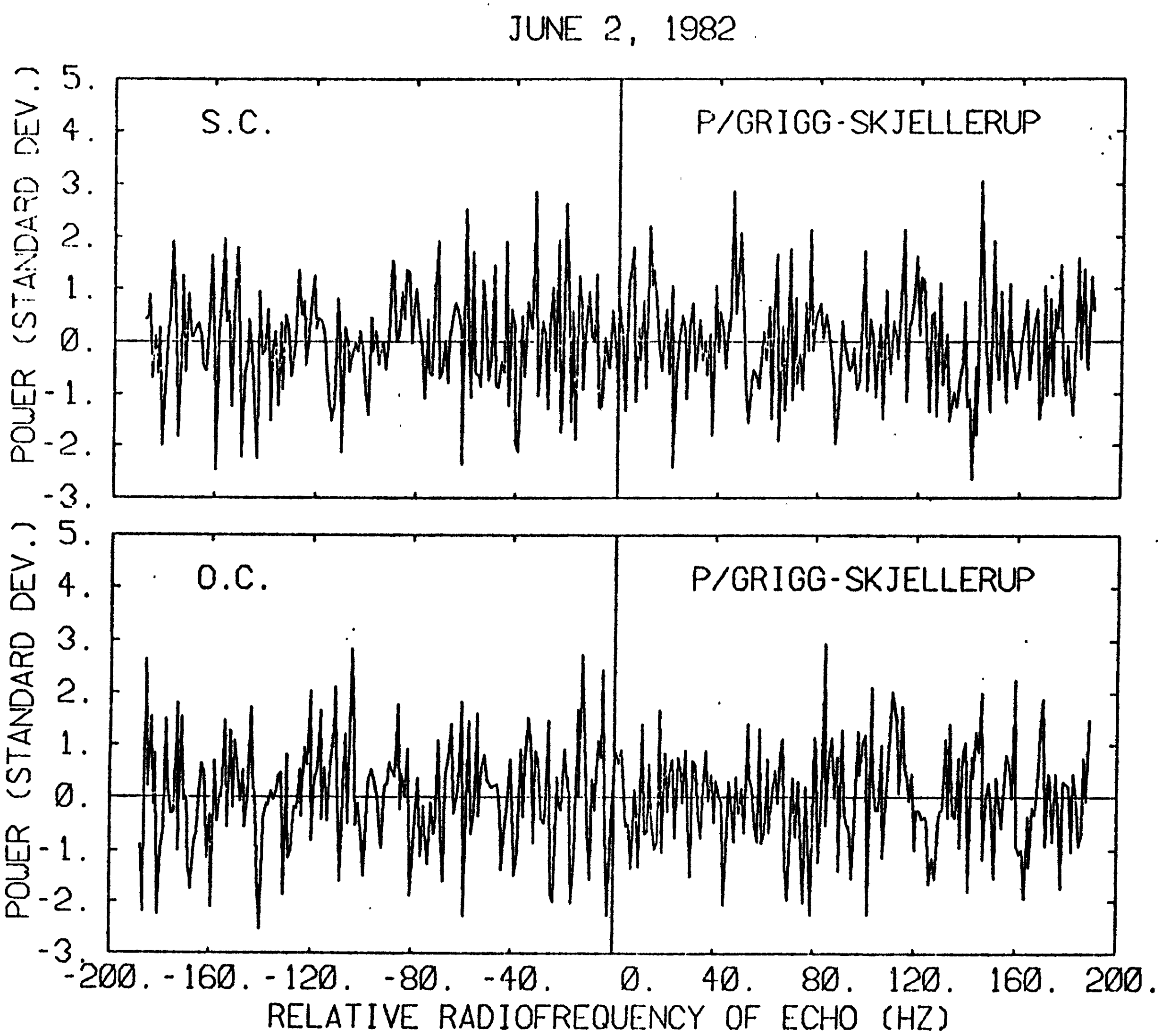
JUNE 2, 1982
S.C.
P/GRIGG-SKJELLERUP
O.C.
P/GRIGG-SKJELLERUP
POWER (STANDARD DEV.)
5.
4.
3.
2.
1.
0.
-1.
-2.
-3.
-200.
-160.
-120.
-80.
-40.
0.
40.
80.
120.
160.
200.
RELATIVE RADIOFREQUENCY OF ECHO (HZ)

Fig. 6.10

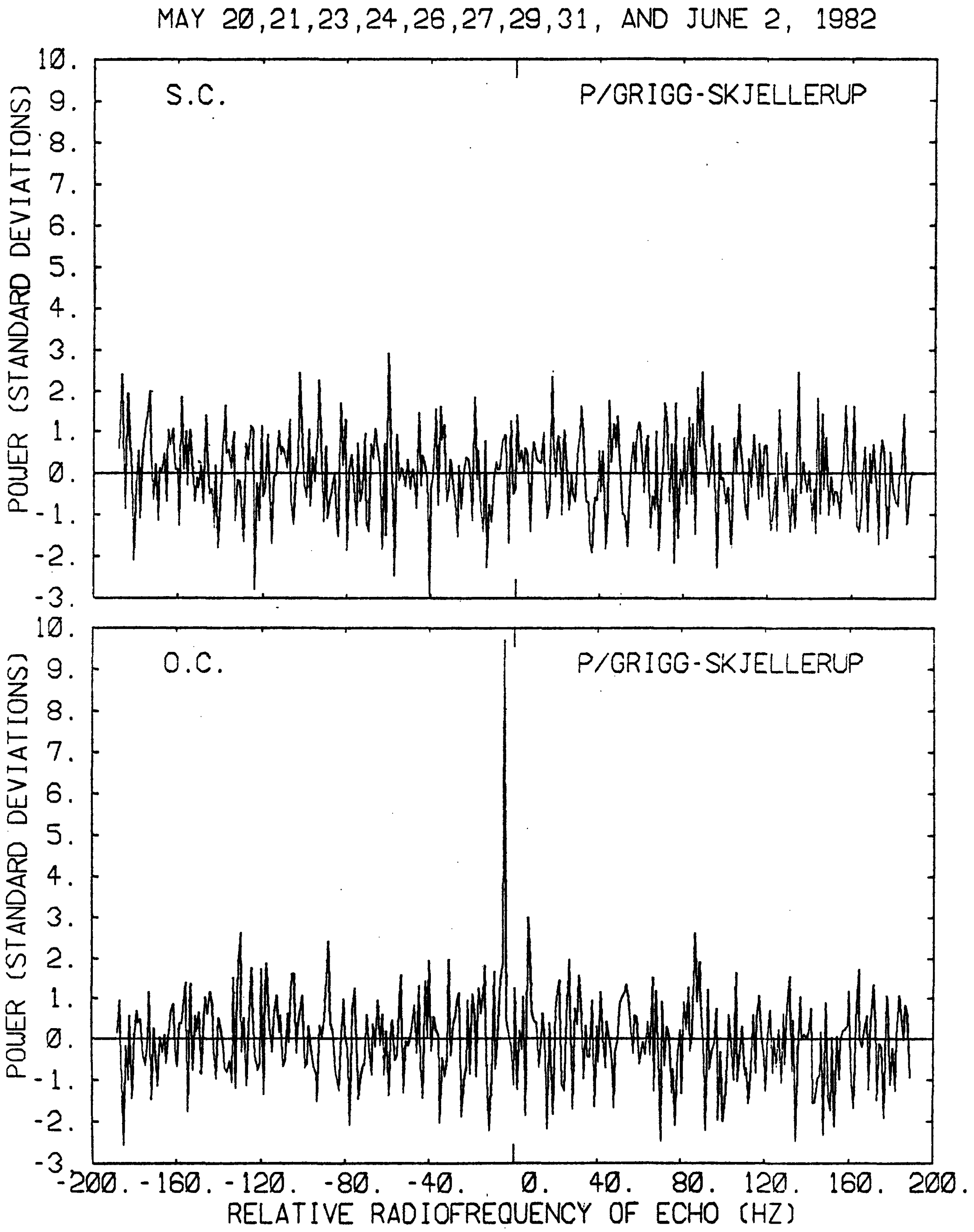
MAY 20,21,23,24,26,27,29,31, AND JUNE 2, 1982
S.C.
P/GRIGG-SKJELLERUP
O.C.
P/GRIGG-SKJELLERUP
POWER (STANDARD DEVIATIONS)
10.
9.
8.
7.
6.
5.
4.
3.
2.
1.
0.
-1.
-2.
-3.
-200.
-160.
-120.
-80.
-40.
0.
40.
80.
120.
160.
200.
RELATIVE RADIOFREQUENCY OF ECHO (HZ)

Fig. 6.11

PART D. COMET AUSTIN AND COMET CHURYUMOV-GERASIMENKO

OBSERVATIONS AND DATA REDUCTION

CHAPTER 7

COMET AUSTIN: OBSERVATIONS AND DATA REDUCTION

7.1. History

The comet Austin (Fig. 7.1) was discovered in the morning of June 19th, 1982, by Rodney Austin in New Zealand as a 10th magnitude object, and was reobserved on the following night by Alan Gilmore of Mount John University Observatory in New Zealand, who thus confirmed the discovery. Both observers described the object as having a bright, dense central region with a large diffuse halo. This comet was first reported on June 21, 1982, in IAU circular 3705 of the Central Bureau for Astronomical Telegrams by Brian Marsden, who also computed and made public a set of orbital elements showing that the comet was moving on a parabolic orbit. From this ephemeris it appeared that the comet could pass close enough to Earth to be detected by radar from Arecibo. The orbital elements are given in Table 7.1.

TABLE 7.1

Ecliptic Coordinates, Equinox 1950.0

Comet Austin

T(Time of perihelion passage)	:	Aug. 24, 1982
Q(Perihelion distance)	:	0.649 AU
e(Eccentricity)	:	1.
i(Orbital inclination)	:	84.5°
Argument of Perihelion	:	33.7°
Longitude of Ascending Node	:	325.4°

7.2. The radar observations

Following receipt of IAU circular 3706 containing the improved elements of Table 7.1, the task of obtaining telescope time and of preparing an adequate observing ephemeris was undertaken. Just enough astrometric determinations of position (mostly from Gilmore) were available to prepare an initial ephemeris with uncertainties in position of less than 15' and Doppler errors of less than a hundred Hertz. The radar observations took place on the mornings of August 8 through 12, 1982. Although the observations were plagued with equipment problems on August 8 and 9, which severely limited the transmitting power available, the last three days yielded normal performance. The radar system setup was identical to that used for the observations of Grigg-Skjellerup in May of the same year, except for the last day of observation on which the analyzing bandwidth was doubled from 380 to 760 Hz with a corresponding increase in the frequency resolution. This change was occasioned by the failure to obtain an observable result during the prior two days, and represented an attempt to widen the search window. Tables 7.2 and 7.3 summarized the comet's coordinates and system parameters for the period of observation.

7.3. Data reduction and results

The data reduction was carried out as described in chapter 4. However, the computed a posteriori ephemeris using all the astrometric observations available for this comet between June 1982 and November 1982 turned out to be substantially different from the ephemeris used during the actual radar observations. As a result, it appears that there could have been a drift of as much as 1 Hz per hour between the observing and a posteriori ephemerides used, so that significant smearing of the signal could have occurred even in the span of a few hours' observations. Thus, in the data analysis, we attempted to correct for this drift by combining the data using a different frequency offset for each file.

This was done as follows: First, the difference δ between the Doppler frequency predicted by the latest ephemeris and the Doppler used during the observations was computed (Irwin Shapiro and Antonia Forni, private communication). Figure 7.2 shows the variation of this difference as a function of time. Using these data, the difference δ was obtained for the midtime of each receiving cycle, and used to shift the spectrum during weighted summation with its neighbors. The first run of August 10 was chosen as reference, because it was comfortably centered in the observing sequence. Thus, since $\delta \simeq -12.4$ Hz for the spectrum of the first file of August 10, any echo in the weighted sum of the data for Aug. 8 (fig. 7.3), Aug. 9 (fig. 7.4), Aug. 10 (fig. 7.5), Aug. 11 (fig. 7.6), Aug. 12 (fig. 7.7), or for the set Aug. 8, 9, 10, and 11 (fig. 7.8) should be expected at that offset.

Since the data of August 12 have a different frequency resolution (2 Hz) than the other data, the superposition of the data from the other four days was not possible without distorting the results. It is clear from these spectra that no echo from Comet Austin was detected. The results of further searching using smoothing will be presented in chapter 13.

TABLE 7.2

RECEIVING EPHEMERIDES AT ARECIBO TRANSIT

DATE (1980)	UT hr mn	RA hr mn sc	DEC ° ' "	Z.A. (deg)	DOPPLER (Hz)	R-T DELAY (secs)
Aug 8	14 52	07 31 20	08 42 02	9.6	153,515	328.39
Aug 9	15 03	07 46 50	12 55 28	5.4	60,219	324.46
Aug 10	15 15	08 03 14	17 09 12	1.2	-36,657	324.03
Aug 11	15 28	08 20 23	21 15 46	2.9	-133,845	327.16
Aug 12	15 42	08 38 06	25 08 04	6.8	-228,078	333.81

TABLE 7.3

SYSTEM PARAMETERS

Date	D	RTT	G	P_t	T_s'	t_i
(1982)	(a.u.)	(sec)	(dB)	(kW)	(K)	(sec)
August 8	0.329	328	71.4	150	46	2210
August 9	0.325	324	71.7	190	39	2242
August 10	0.325	324	71.5	400	42	3234
August 11	0.328	327	71.5	400	43	3250
August 12	0.335	334	71.5	400	41	2900

The gain G and the system temperature T_s represents here effective values.

Figure captions for chapter 7.

Figure 7.1. Photograph of comet Austin obtained on September 6, 1982 by J. Kielkopf using the 35.5cm Schmidt camera at Moore Observatory (Ky.). 15 min. exposure.

Figure 7.2. Variation with time of the difference between the Doppler frequency predicted by the most accurate ephemeris presently available and the value used during the radar observations. The dates indicated on the X-axis corresponds to 0 hr UT on the corresponding day.

Figure 7.3. August 8, 1982. Weighted sum of the data. Each single run spectrum has been properly shifted so that the new expected center frequency should be at about -12 Hz on this plot as in the following plots.

Figure 7.4. through 7.6. Weighted sum of the data for each individual day between August 9 and August 11, 1982.

Figure 7.7. August 12, 1982. Weighted sum of the data. The frequency resolution is here 2 Hz as opposed to 1 Hz for the previous plots.

Figure 7.8. August 8, 9, 10, and 11. Weighted sum of the data.

Fig. 7.1

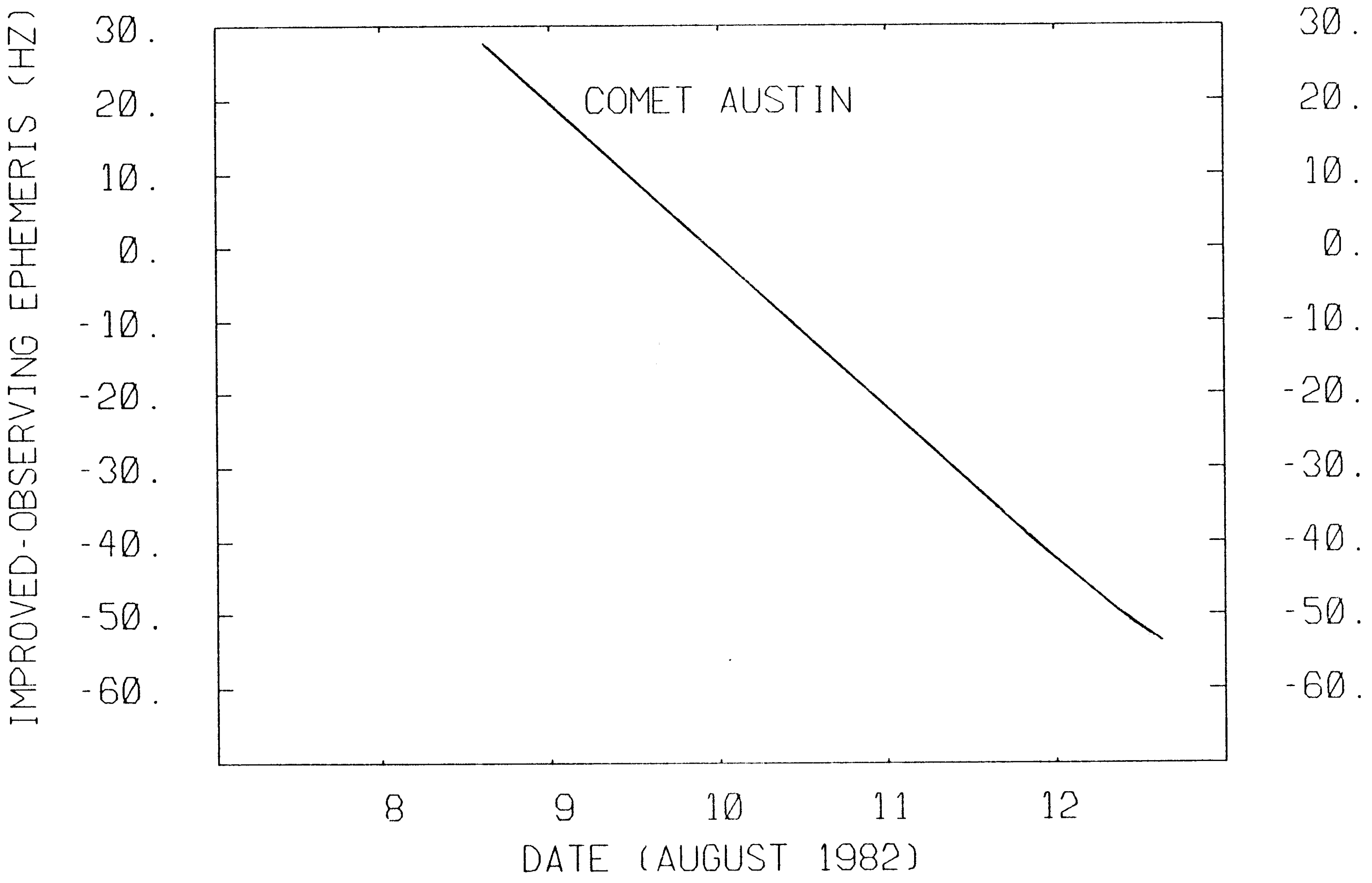
COMET AUSTIN
IMPROVED-OBSERVING EPHEMERIS (HZ)
30.
20.
10.
0.
-10.
-20.
-30.
-40.
-50.
-60.
8
9
10
11
12
DATE (AUGUST 1982)

Fig. 7.2

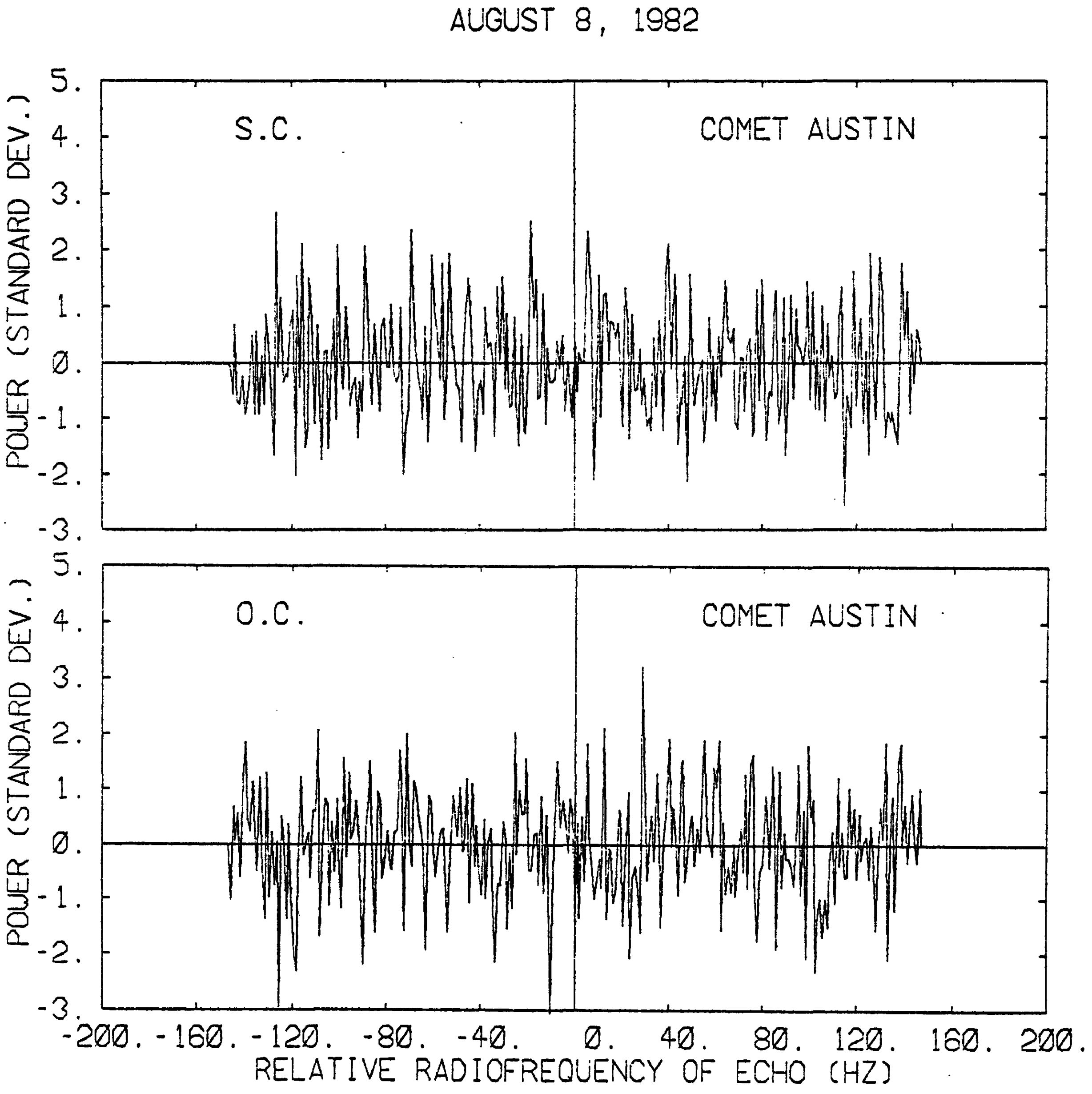
AUGUST 8, 1982
S.C.
COMET AUSTIN
O.C.
COMET AUSTIN
POWER (STANDARD DEV.)
POWER (STANDARD DEV.)
5.
4.
3.
2.
1.
0.
-1.
-2.
-3.
-200.
-160.
-120.
-80.
-40.
0.
40.
80.
120.
160.
200.
RELATIVE RADIOFREQUENCY OF ECHO (HZ)

Fig. 7.3

AUGUST 9, 1982

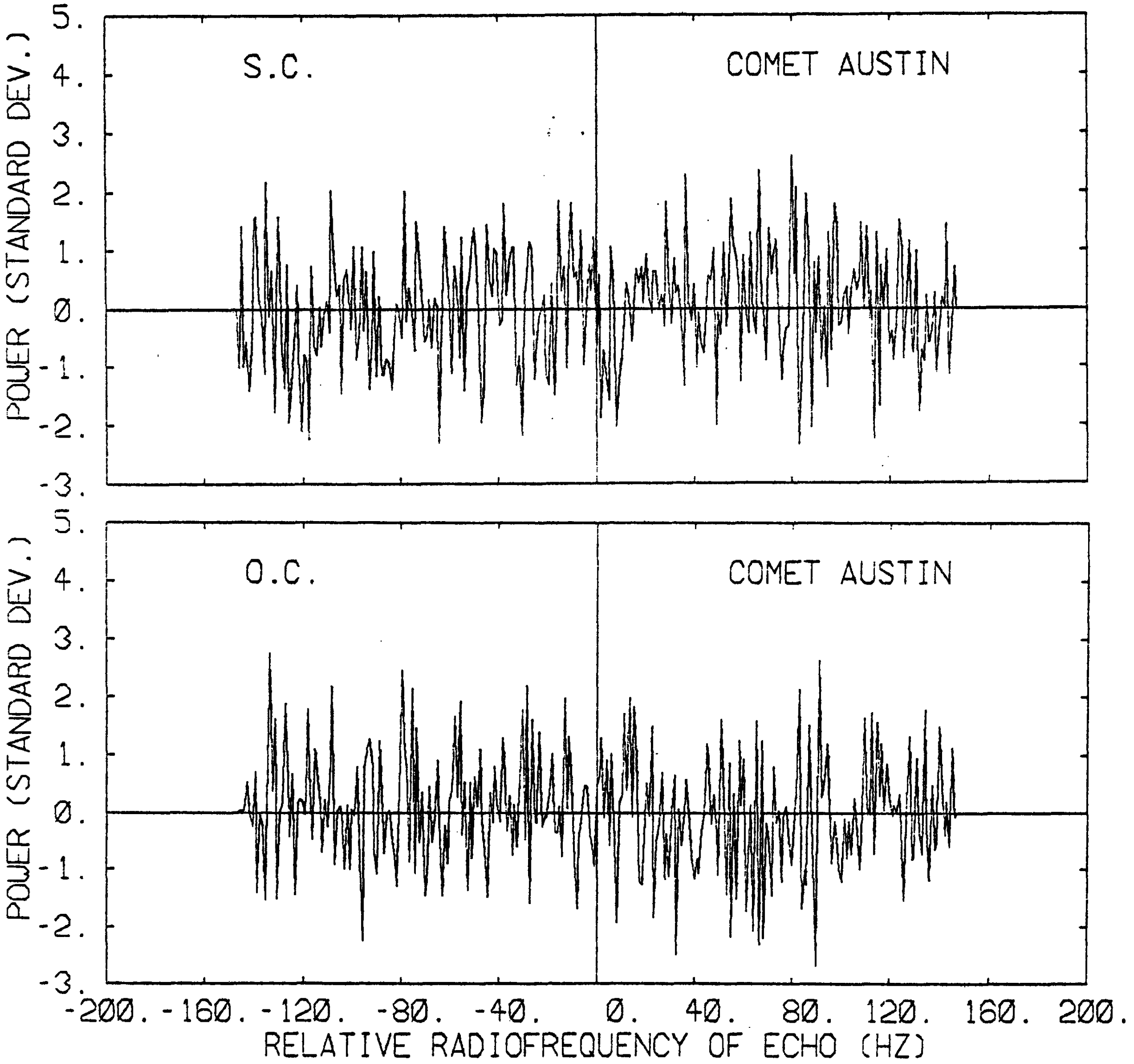

Fig. 7.4

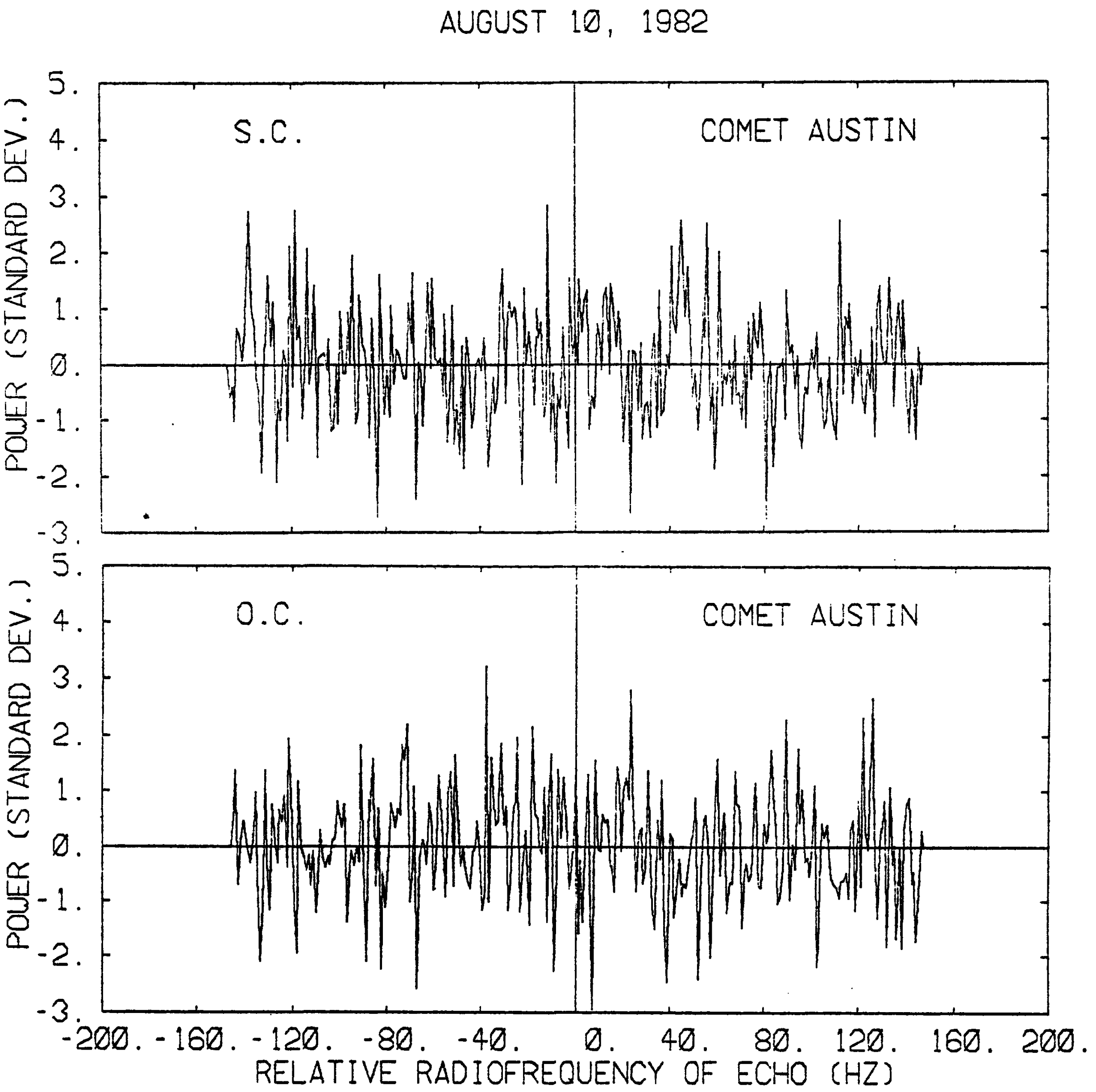
AUGUST 10, 1982
S.C.
COMET AUSTIN
O.C.
COMET AUSTIN
POWER (STANDARD DEV.)
5.
4.
3.
2.
1.
0.
-1.
-2.
-3.
-200.
-160.
-120.
-80.
-40.
0.
40.
80.
120.
160.
200.
RELATIVE RADIOFREQUENCY OF ECHO (HZ)

Fig. 7.5

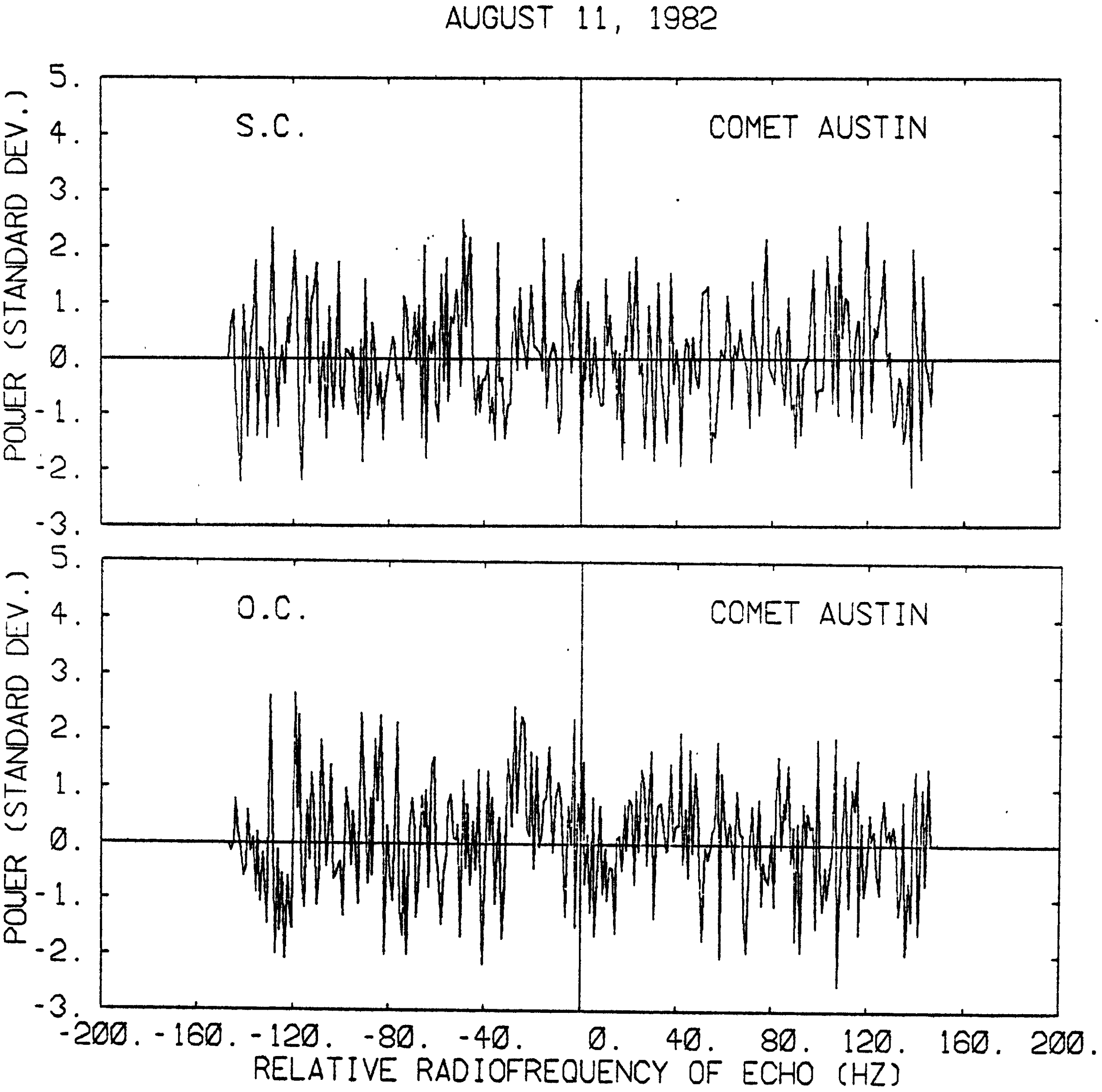
AUGUST 11, 1982
S.C.
COMET AUSTIN
O.C.
COMET AUSTIN
POWER (STANDARD DEV.)
POWER (STANDARD DEV.)
5.
4.
3.
2.
1.
0.
-1.
-2.
-3.
-200.
-160.
-120.
-80.
-40.
0.
40.
80.
120.
160.
200.
RELATIVE RADIOFREQUENCY OF ECHO (HZ)

Fig. 7.6

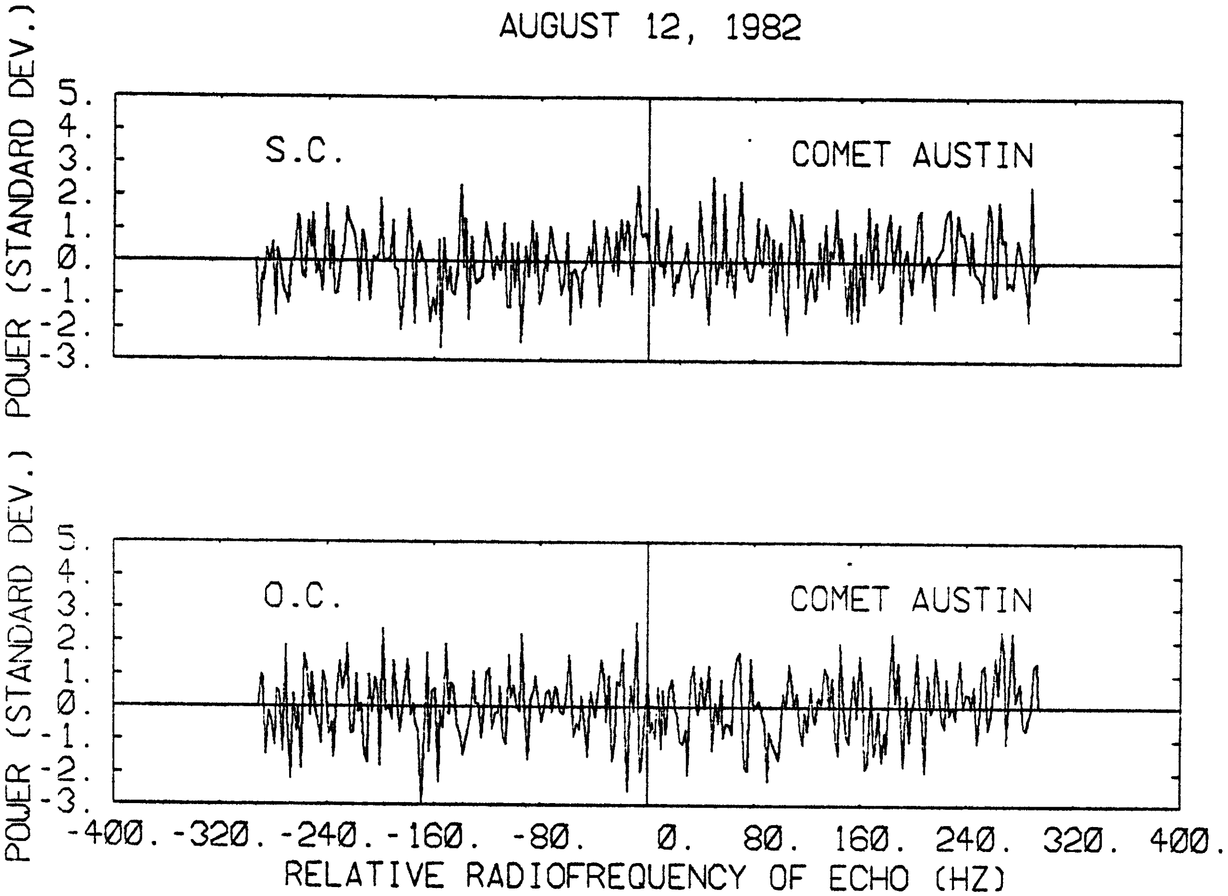
AUGUST 12, 1982
POWER (STANDARD DEV.)
5.
4.
3.
2.
1.
0.
-1.
-2.
-3.
S.C.
COMET AUSTIN
POWER (STANDARD DEV.)
5.
4.
3.
2.
1.
0.
-1.
-2.
-3.
O.C.
COMET AUSTIN
-400.
-320.
-240.
-160.
-80.
0.
80.
160.
240.
320.
400.
RELATIVE RADIOFREQUENCY OF ECHO (HZ)

Fig. 7.7

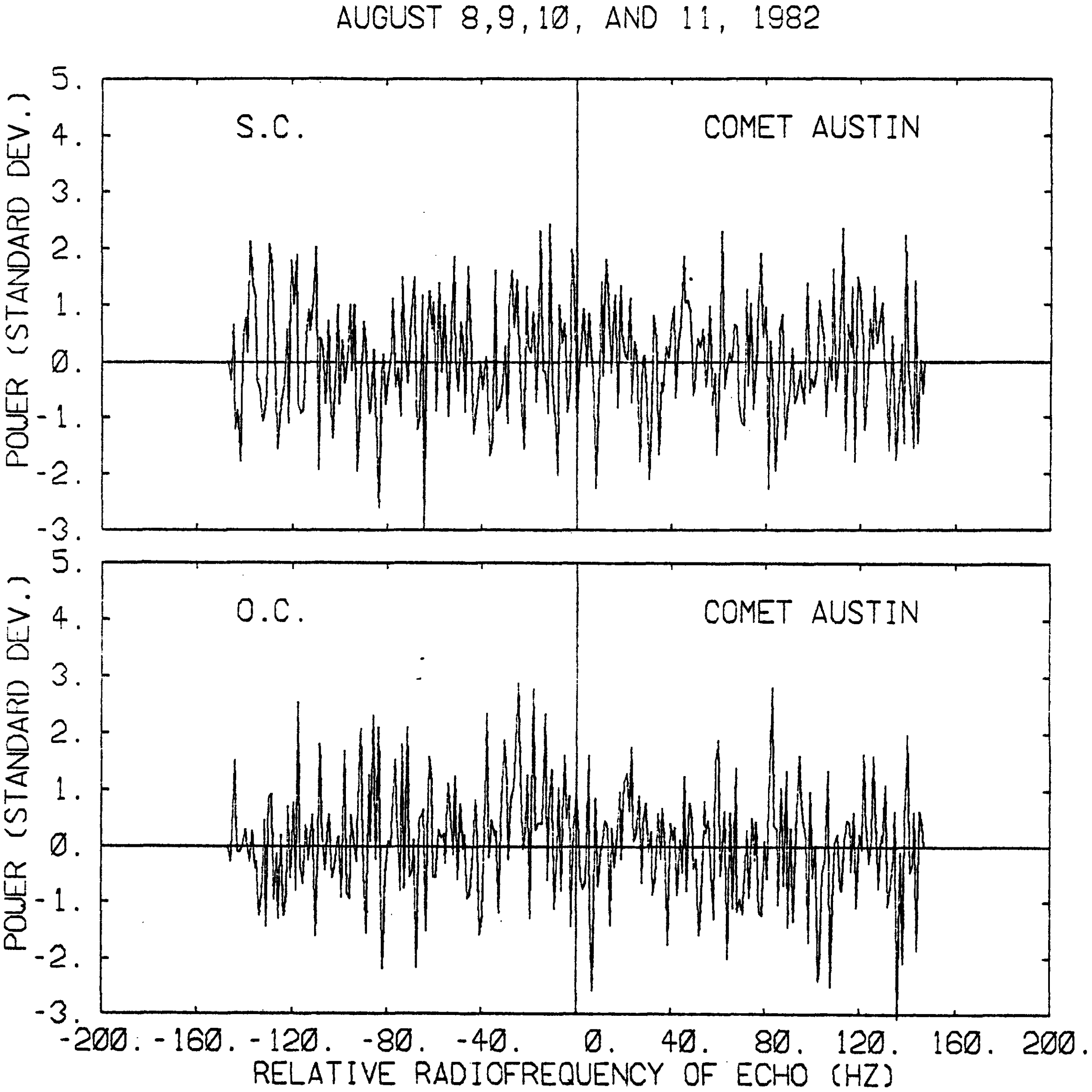
AUGUST 8,9,10, AND 11, 1982
S.C.
COMET AUSTIN
O.C.
COMET AUSTIN
POWER (STANDARD DEV.)
5.
4.
3.
2.
1.
0.
-1.
-2.
-3.
-200.
-160.
-120.
-80.
-40.
0.
40.
80.
120.
160.
200.
RELATIVE RADIOFREQUENCY OF ECHO (HZ)

Fig. 7.8

CHAPTER 8

COMET CHURYUMOV-GERASIMENKO

OBSERVATIONS AND DATA REDUCTION

8.1 The periodic comet Churyumov-Gerasimenko

8.1.1. History

This comet was discovered on a photograph taken on September 11, 1969 at the Alma-Ata observatory in USSR (Churyumov and Gerasimenko, 1972). At its unfavorable return in 1975, it was observed by only a few people, in particular by Elizabeth Roemer who described it as a faint object of about 18th magnitude, with a nearly stellar aspect. It passed perihelion on April 1976. The comet was later recovered at its 1982 appearance by J. Gibson with the 1.2 m telescope at Mt. Palomar on May 31, 1982. The comet was at opposition and at a geocentric distance of 0.39 AU in November 1982, at the time of our radar observations. The comet orbital elements are given in Table 8.1.

TABLE 8.1

Ecliptic Coordinates, Equinox 1950.0

Comet Churyumov-Gerasimenko

T(Time of perihelion passage)	:	Nov. 12, 1982
P(Orbital period)	:	6.61 yrs
Q(Perihelion distance)	:	1.306 AU
e(Eccentricity)	:	0.629
I(Orbital inclination)	:	7.1°
Argument of Perihelion	:	11.3°
Longitude of Ascending Node	:	50.4°

8.1.2. Physical properties

Comet Churyumov-Gerasimenko (or C-G) had been extensively studied by several observers at its 1982 appearance. Unfortunately very little in the way of final results are available at the time of completion of this thesis. In particular, there is no data available on the rotation of the nucleus of this comet.

8.2. The radar observations

These observations took place between November 7 and November 16, 1982. Serious technical problems on November 7 and on November 16 prevented the acquisition of data on these dates. Further difficulties were experienced on November 8 and November 11, causing the loss of part of the data on these two dates, as well. The experiment ran smoothly on the other days of observation. The radar setup was in all respects identical to that used for the observations of comet Grigg-Skjellerup (see Chapter 6). The relevant comet coordinates are summarized in Table 8.2, while the radar system parameters for the period of observation are given in Table 8.3.

8.3. Data reduction

Following the radar observations, a new ephemeris was computed for the orbit of this comet by Irwin Shapiro and Antonia Forni (Lincoln Laboratory) using all the astrometric data available from 1975 through November 1982. It appears that the differences between the new ephemeris and the one used during the radar observations change by less than 0.2 Hz, with an average offset of about 0.8 Hz, so that there should have been no significant smearing of the echo during the observing period. The data analysis was carried out as described in Chapter 4.

TABLE 8.2

RECEIVING EPHEMERIDES
AT ARECIBO TRANSIT

DATE (1982)	UT hr mn	RA hr mn sc	DEC ° ' "	Z.A. (deg)	DOPPLER (Hz)	R-T DELAY (secs)
Nov 8	07 30	06 11 23	26 36 44	8.3	60,960	411.49
Nov 9	07 28	06 13 56	26 56 39	8.6	57,807	409.34
Nov 10	07 27	06 16 28	27 16 36	8.9	54,628	407.30
Nov 11	07 25	06 18 56	27 36 31	9.3	51,480	405.38
Nov 12	07 24	06 21 23	27 56 25	9.6	48,303	403.58
Nov 13	07 22	06 23 46	28 16 17	9.9	45,155	401.89
Nov 14	07 21	06 26 07	28 36 07	10.3	41,978	400.31
Nov 15	07 19	06 28 26	28 55 54	10.6	38,830	398.85

TABLE 8.3
SYSTEM PARAMETERS

Date (1982)	D (a.u.)	RTT (sec)	G (dB)	P_t (kW)	T_{s1} (K)	t_i (sec)
November 8	0.412	411	71.1	400	55	939
November 9	0.410	409	71.3	400	47	3130
November 10	0.408	407	71.3	400	50	3130
November 11	0.406	405	71.4	400	43	1305
November 12	0.405	404	71.1	400	51	2738
November 13	0.403	402	71.3	400	46	2809
November 14	0.401	400	71.2	400	51	3050
November 15	0.400	399	71.0	400	55	3314

where G and T_s represent effective values (average over the observing session).

The following table shows the values of the signal-to-noise ratio in the spectral elements adjacent to the spectral element corresponding to the *a priori* center of the echo (spectral element number 186), for the weighted sum of all the data. For this table, frequency is increasing to the left, while for the plots frequency increases to the right.

TABLE 8.4

TABULATED ECHO POWER

O.C.

Spectral element # :	182	183	184	185	186	187	188	189	190
Echo Power:	0.7	1.1	-0.9	0.8	-0.1	0.6	2.6	1.6	-0.1

S.C.

Echo Power:	-0.8	-0.1	-0.9	0.6	2.8	-0.8	1.5	2.0	-0.6

Figure Captions for Chapter 8.

Figure 8.1. Configuration of the Earth-Sun-Comet C-G system at the midpoint of the observations (November 12, 1982).

Figure 8.2. through 8.9. Weighted sum of the raw data for each day of radar observation of comet Churyumov-Gerasimenko. November 8 through November 15, 1982. The spectral resolution was 1 Hz. The S.C. spectrum is plotted on top, the O.C. spectrum at bottom.

Figure 8.10. Weighted sum of all the data obtained during the radar observations of the comet Churyumov-Gerasimenko. The S.C. spectrum is on top while the O.C. spectrum is at the bottom.

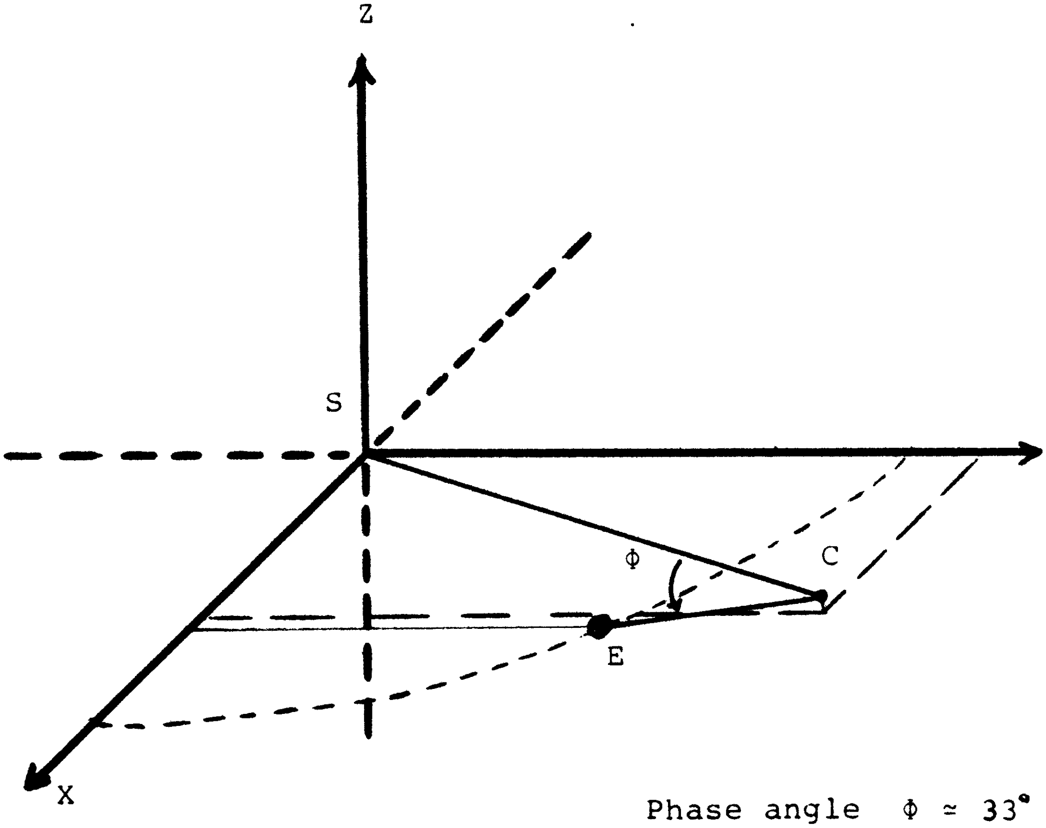

Fig. 8.1

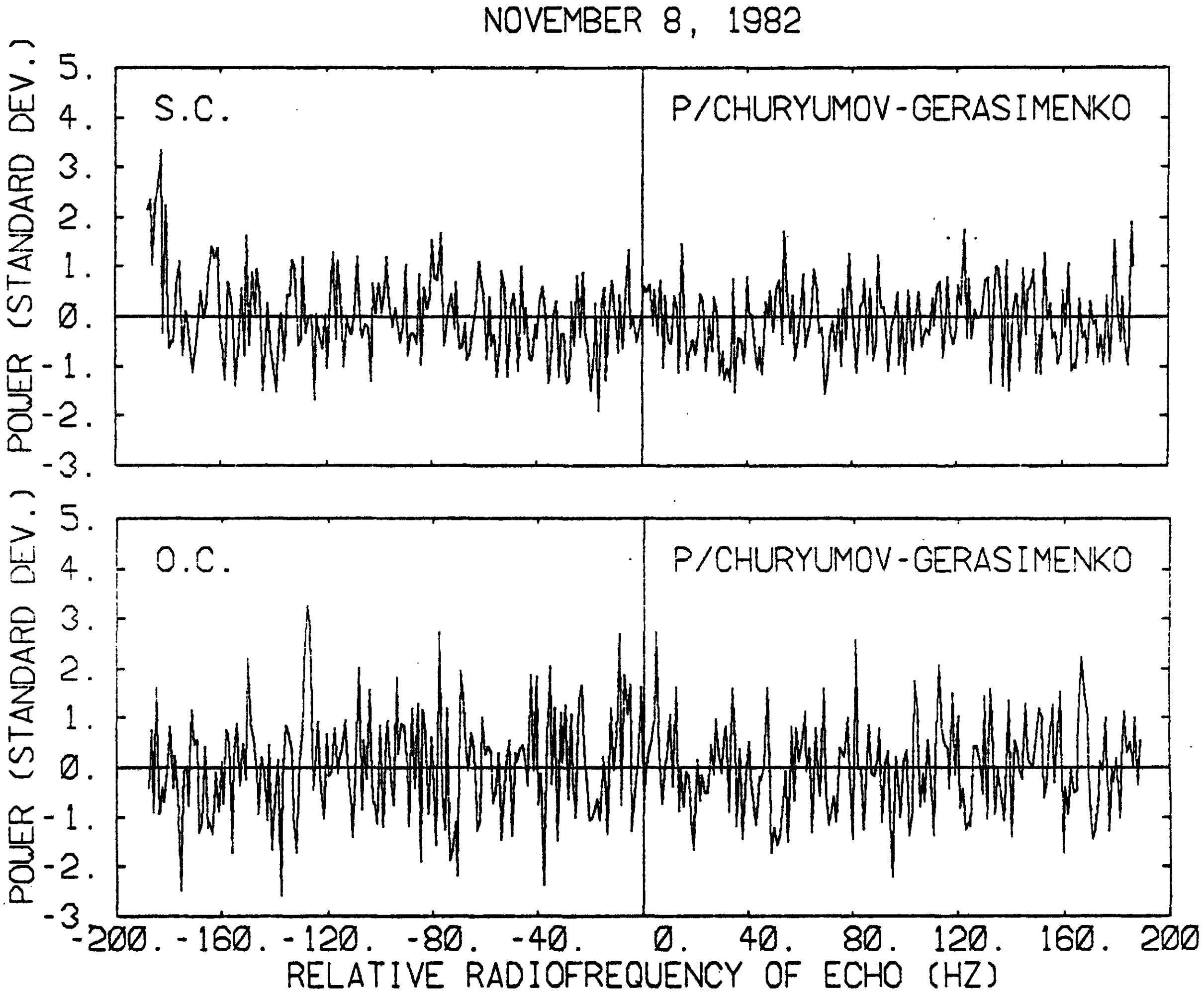
NOVEMBER 8, 1982
S.C.
P/CHURYUMOV-GERASIMENKO
O.C.
P/CHURYUMOV-GERASIMENKO
POWER (STANDARD DEV.)
5.
4.
3.
2.
1.
0.
-1.
-2.
-3.
-200.
-160.
-120.
-80.
-40.
0.
40.
80.
120.
160.
200
RELATIVE RADIOFREQUENCY OF ECHO (HZ)

Fig. 8.2

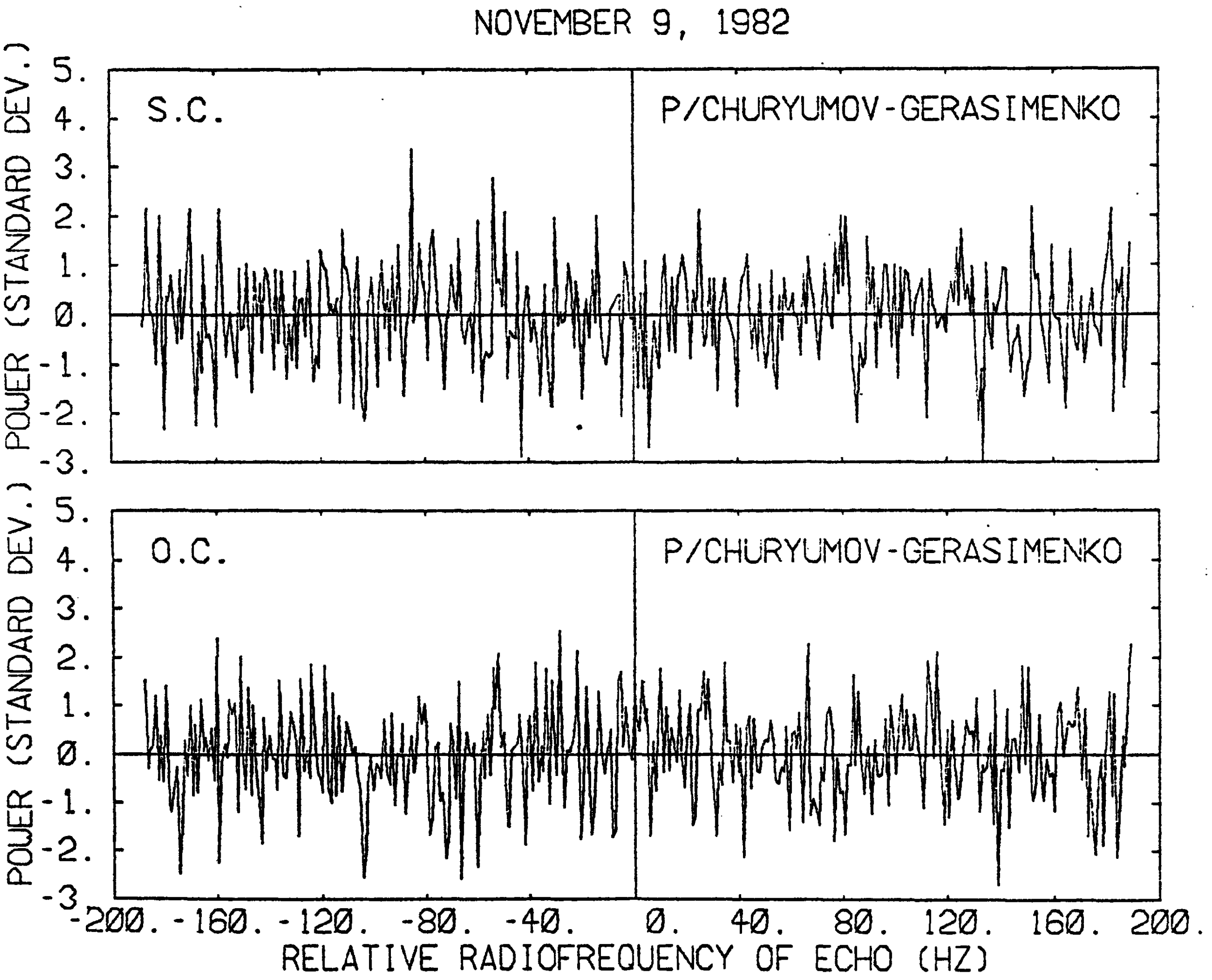
NOVEMBER 9, 1982
S.C.
P/CHURYUMOV-GERASIMENKO
O.C.
P/CHURYUMOV-GERASIMENKO
POWER (STANDARD DEV.)
POWER (STANDARD DEV.)
5.
4.
3.
2.
1.
0.
-1.
-2.
-3.
5.
4.
3.
2.
1.
0.
-1.
-2.
-3
-200.
-160.
-120.
-80.
-40.
0.
40.
80.
120.
160.
200.
RELATIVE RADIOFREQUENCY OF ECHO (HZ)

Fig. 8.3

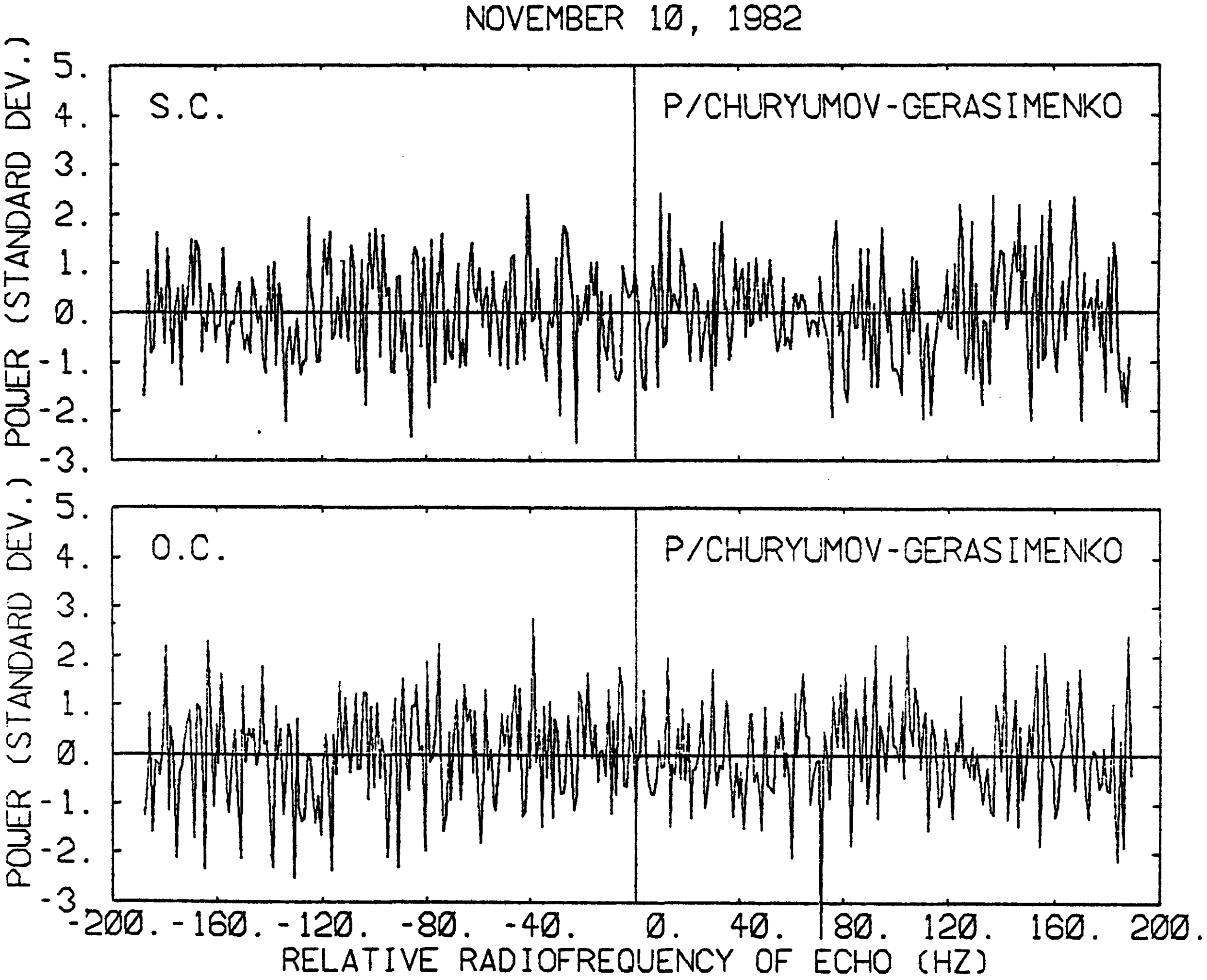
NOVEMBER 10, 1982
S.C.
P/CHURYUMOV-GERASIMENKO
O.C.
P/CHURYUMOV-GERASIMENKO
POWER (STANDARD DEV.)
POWER (STANDARD DEV.)
5.
4.
3.
2.
1.
0.
-1.
-2.
-3.
-200.
-160.
-120.
-80.
-40.
0.
40.
80.
120.
160.
200.
RELATIVE RADIOFREQUENCY OF ECHO (HZ)

Fig. 8.4

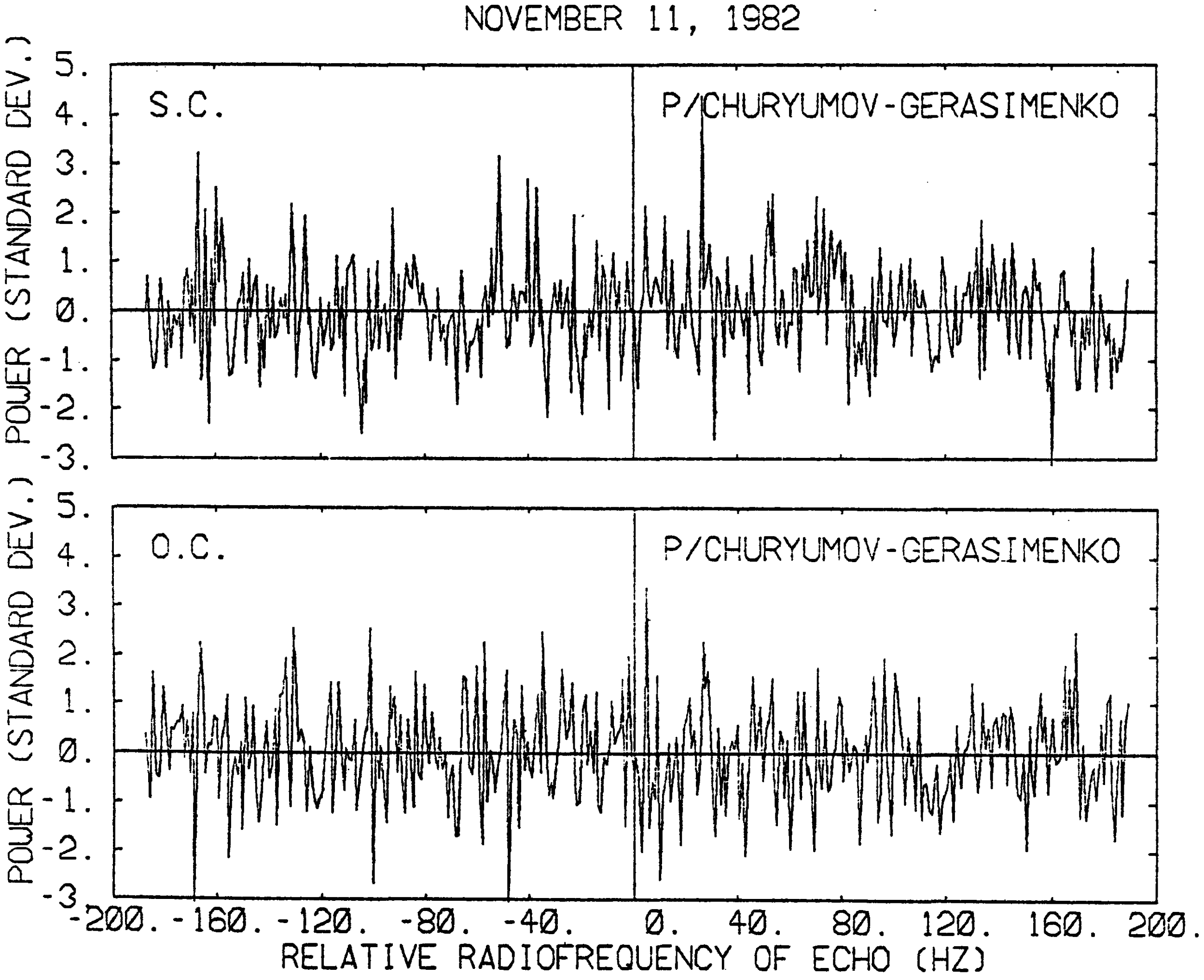
NOVEMBER 11, 1982
S.C.
P/CHURYUMOV-GERASIMENKO
O.C.
P/CHURYUMOV-GERASIMENKO
POWER (STANDARD DEV.)
POWER (STANDARD DEV.)
5.
4.
3.
2.
1.
0.
-1.
-2.
-3.
5.
4.
3.
2.
1.
0.
-1.
-2.
-3
-200.
-160.
-120.
-80.
-40.
0.
40.
80.
120.
160.
200.
RELATIVE RADIOFREQUENCY OF ECHO (HZ)

Fig. 8.5

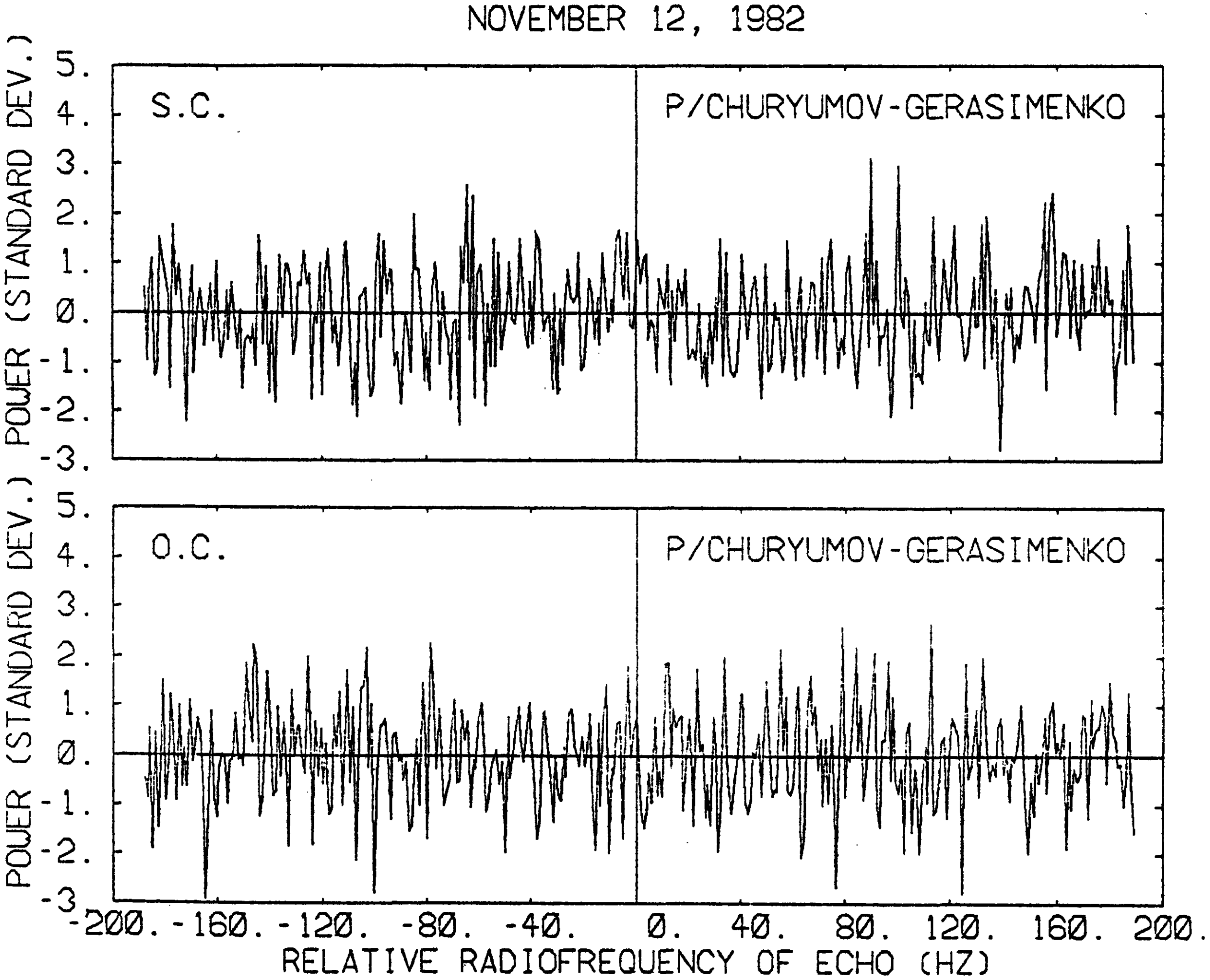
NOVEMBER 12, 1982
S.C.
P/CHURYUMOV-GERASIMENKO
O.C.
P/CHURYUMOV-GERASIMENKO
POWER (STANDARD DEV.)
POWER (STANDARD DEV.)
5.
4.
3.
2.
1.
0.
-1.
-2.
-3.
-200.
-160.
-120.
-80.
-40.
0.
40.
80.
120.
160.
200.
RELATIVE RADIOFREQUENCY OF ECHO (HZ)

Fig. 8.6

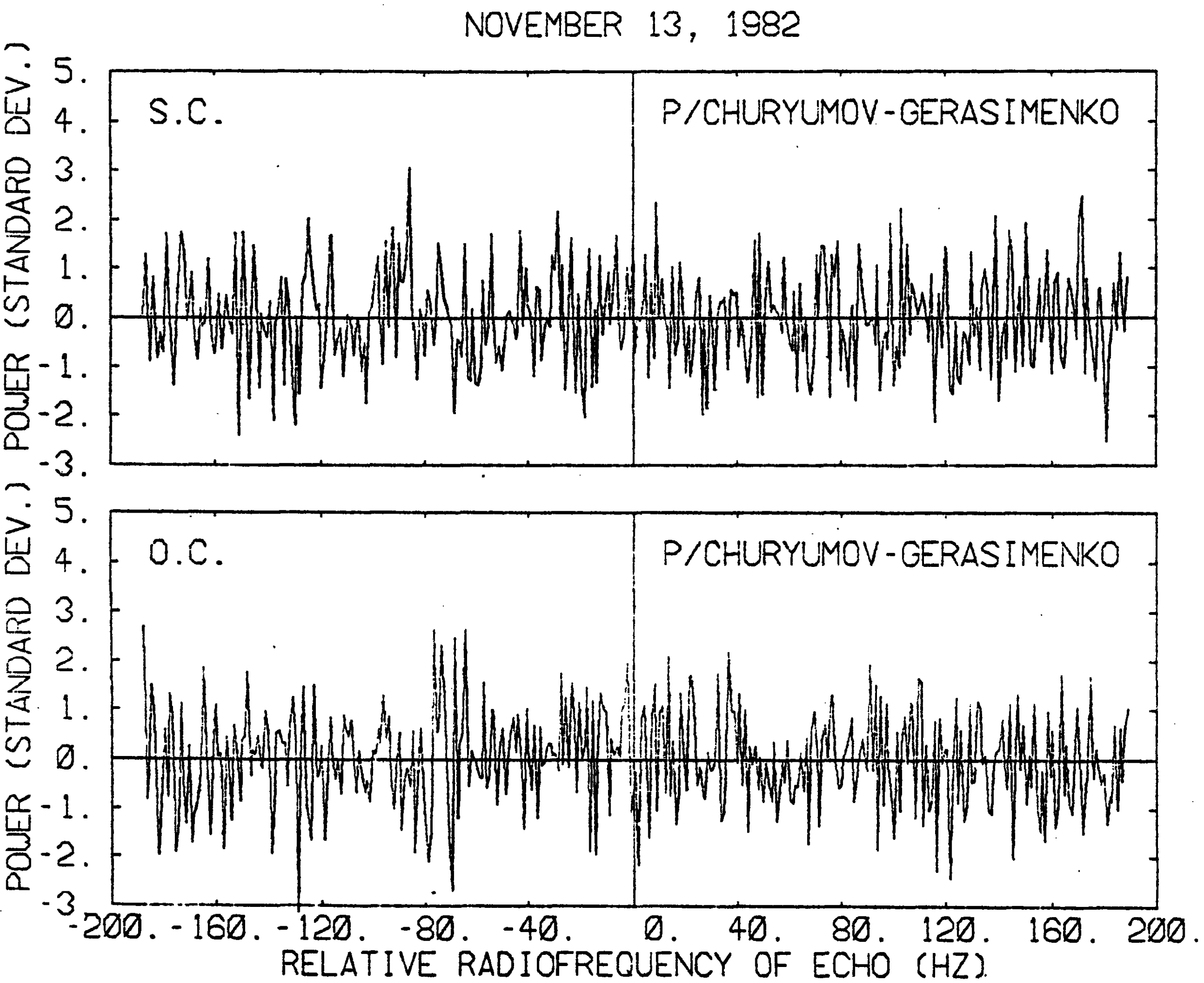
NOVEMBER 13, 1982
S.C.
P/CHURYUMOV-GERASIMENKO
O.C.
P/CHURYUMOV-GERASIMENKO
POWER (STANDARD DEV.)
POWER (STANDARD DEV.)
5.
4.
3.
2.
1.
0.
-1.
-2.
-3.
-200. -160. -120. -80. -40. 0. 40. 80. 120. 160. 200.
RELATIVE RADIOFREQUENCY OF ECHO (HZ)

Fig. 8.7

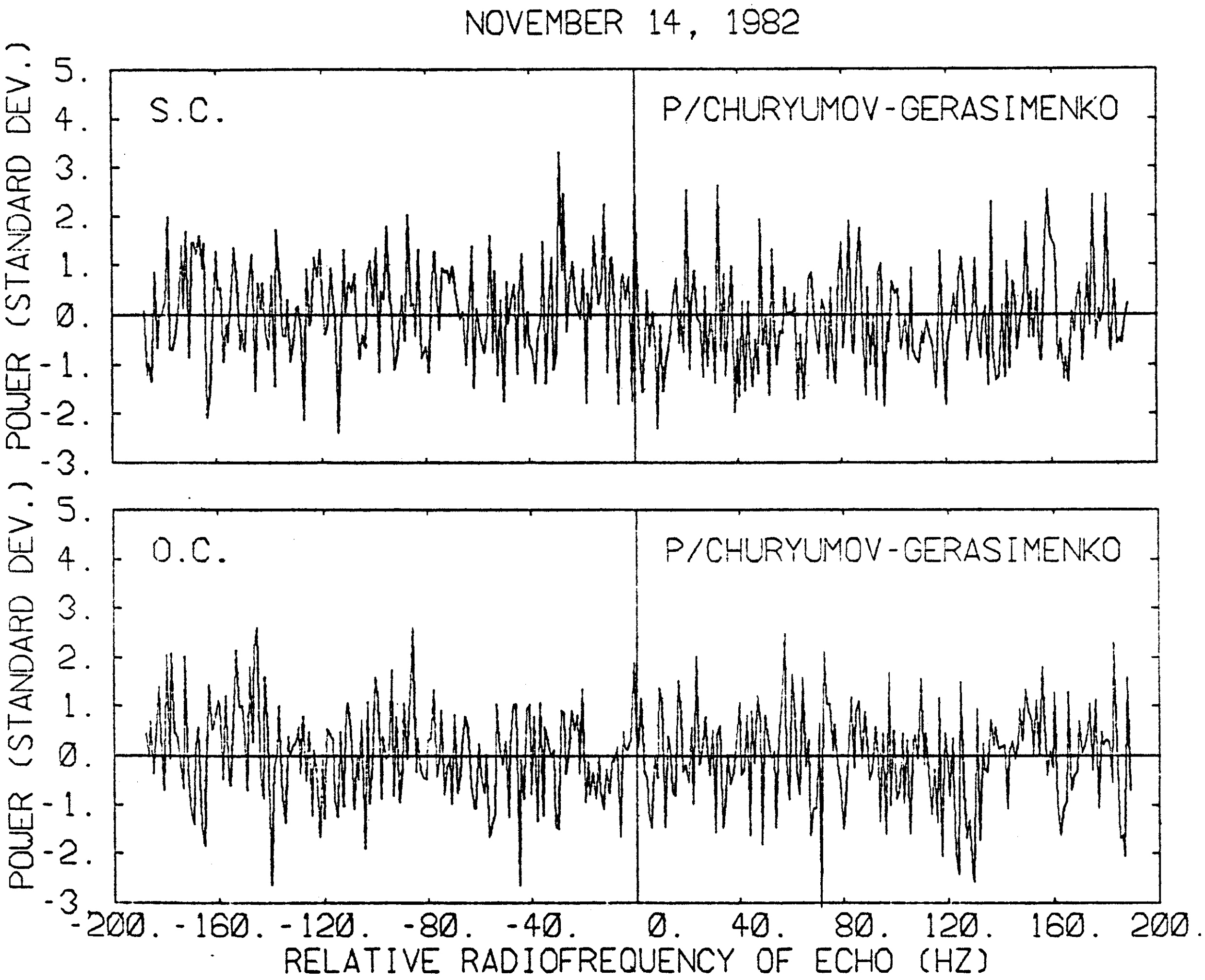
NOVEMBER 14, 1982
S.C.
P/CHURYUMOV-GERASIMENKO
O.C.
P/CHURYUMOV-GERASIMENKO
POWER (STANDARD DEV.)
POWER (STANDARD DEV.)
5.
4.
3.
2.
1.
0.
-1.
-2.
-3.
-200.
-160.
-120.
-80.
-40.
0.
40.
80.
120.
160.
200.
RELATIVE RADIOFREQUENCY OF ECHO (HZ)

Fig. 8.8

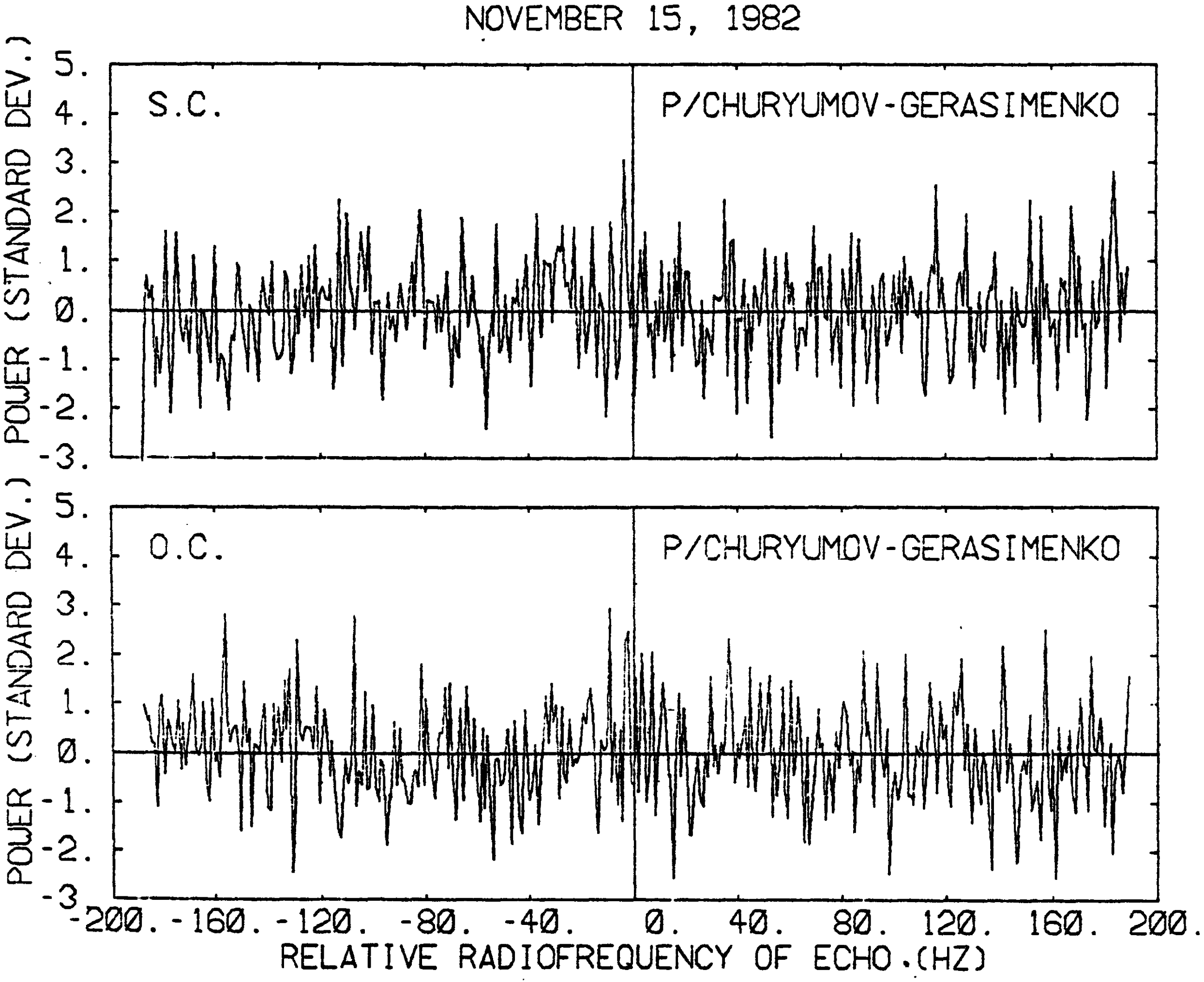
NOVEMBER 15, 1982
S.C.
P/CHURYUMOV-GERASIMENKO
O.C.
P/CHURYUMOV-GERASIMENKO
POWER (STANDARD DEV.)
POWER (STANDARD DEV.)
5.
4.
3.
2.
1.
0.
-1.
-2.
-3.
-200.
-160.
-120.
-80.
-40.
0.
40.
80.
120.
160.
200.
RELATIVE RADIOFREQUENCY OF ECHO (HZ)

Fig. 8.9

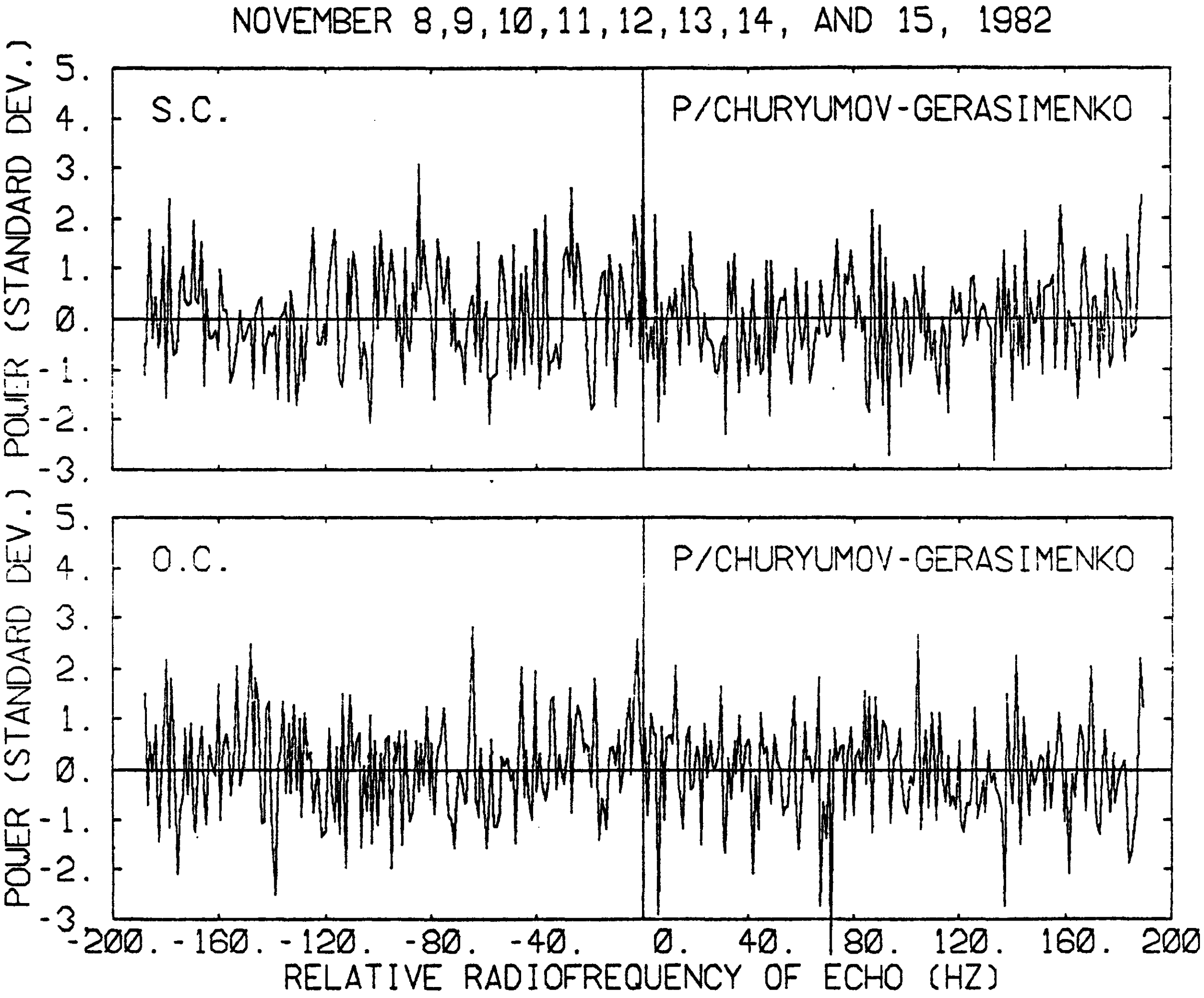
NOVEMBER 8,9,10,11,12,13,14, AND 15, 1982
S.C.
P/CHURYUMOV-GERASIMENKO
O.C.
P/CHURYUMOV-GERASIMENKO
POWER (STANDARD DEV.)
POWER (STANDARD DEV.)
5.
4.
3.
2.
1.
0.
-1.
-2.
-3.
-200.
-160.
-120.
-80.
-40.
0.
40.
80.
120.
160.
200
RELATIVE RADIOFREQUENCY OF ECHO (HZ)

Fig. 8.10

PART E. MODELING THE NUCLEUS

"I often say that when you can measure what you are speaking about, and express it in numbers, you know something about it; but when you cannot measure it, when you cannot express it in numbers, your knowledge is of a meagre and unsatisfactory kind; it may be the beginning of knowledge but you have scarcely, in your thoughts, advanced to the stage of science, whatever the matter may be."

William Thomson, Lord Kelvin (1889).
quoted after Misner *et al.* in "Gravitation"

CHAPTER 9

MODELING THE NUCLEUS

9.1 Introduction: Competing models

The quantitative interpretation of the radar results in terms of the physical properties of the nucleus is contingent on the adoption of a qualitative model compatible with the observed characteristics of the radar echo. As a starting basis we consider the two models discussed in 1.1, i.e. the dust swarm model and the dusty snowball model, to represent the nature of the so-called "nucleus", or source of all the gas and dust observed in the coma and tail of a comet.

In section 1.1.1. a brief account of the origin and problems of the dust swarm models has been given and the "dirty snowball" model has been introduced. We shall now study the compatibility of these different models with the radar results.

9.2 Model selection using the radar results

In Lyttleton's dust-swarm model, an average comet should consist of about 10^{25} particles of sizes in the range 10^{-3} cm to 1 cm for the most part, but also containing some much larger particles and many much smaller particles produced by collisions and of size of the order of 10^{-5} cm. In this latest dust-swarm model, each particle of the comet describes a separate orbit around the sun. When the comet approaches the sun, the nucleus is expected to contract in overall dimensions, perpendicularly to the orbital velocity vector and extend along the orbital direction in proportion to its speed. The distribution of particles should extend lengthwise along the orbit as the comet speeds up close to perihelion and the particles become more widely separated in this dimension. This effect would not be easily detected by an observer aligned with the comet velocity vector. Lyttleton (1953) has calculated the relative velocity of particles and found velocities of the order of a few hundred meters per second on the average in this model.

The echo spectra obtained from the radar observations of P/Encke and P/Grigg-Skjellerup indicate upper limits respectively of about B_e = 10 Hz and B_g = 1 Hz for the total bandwidths of the echoes. These imply cloud particles having relative radial velocities of V_{re} = 0.7 m/s for Encke and V_{rg} = 0.07 m/s for Grigg-Skjellerup where

$$V_r = cB/2f \qquad (9.1)$$

In eq. (9.1), c is the speed of light and f the transmitted frequency.

Because it requires a much larger value for the echo bandwidth than is observed, the latest dust-swarm model which insists that particles move in individual orbits and have large relative velocities is not compatible with the observations. The earlier diffuse models that assume a gravitationally bound dust swarm have already been rejected because of the persistence of sun-grazing comets (Lyttleton (1953), Whipple (1978a)).

With respect to a compact sand-bank model, where particles have negligible relative velocities, Whipple (1963) quotes Schatzmann's result (1953), that the time interval for collapse of a diffuse dust-swarm into a compact nucleus is astronomically long, and also expresses his opinion that the compact sand-bank itself "would eventually become a single structure, the adjacent particles tending to adhere". One would also expect a compact sand-bank to scatter the incident radar energy diffusely, with substantial depolarization. This has not been observed, although the radar sensitivity does not yet allow conclusions regarding the polarization ratio.

We are thus led to consider plausible only a discrete body model for the nucleus. We assume it to have an effective radius R in the following discussion, although it is understood that the shape may actually be quite irregular. At any given instant the maximum Doppler spread of the echo is determined by $B = 4\pi D \mathrm{Sin}\theta/\lambda P_s$, where D is the separation between the two points of the target having the largest radial velocities toward and away from the observer, θ is the angle by which the spin vector is inclined to the observer's line-of-sight, and P_s is the apparent spin period. Since integration of data over many hours was necessary to detect an echo, the observed bandwidth is related in a complex way to an average radius. Similarly, the radius deduced from the estimated radar cross-section using the relation $\sigma = A\pi R^2$, represents a different effective radius, i.e. the radius of the spherical target of scattering efficiency A which would present the same radar cross-section as the actual target. These radii may differ, of course, depending on the actual shape of the target. Lacking detailed information on the shape, however, we shall equivalence the two in our further discussion.

Whipple and Sekanina (1979) have estimated the oblateness of the nucleus of Encke to be less than 4%. The oblateness is defined as $\alpha = 1 - b/a$, where a is the equatorial radius and b is the polar radius of a representational biaxial ellipsoid. In our case, we hope the hypothesis of sphericity will prove satisfactory, when considering the uncertainties in the other physical parameters of the nucleus.

PART F. COMET P/ENCKE: DATA ANALYSIS AND INTERPRETATION

CHAPTER 10

COMET ENCKE: DATA ANALYSIS AND RESULTS

10.1 Cross-correlation and maximization of the signal-to-noise ratio

10.1.1. Cross correlation

The essential problem here is to decide whether or not the received signal contains any echo. An optimum processing is defined as the processing which provides the least number of erroneous decisions in this decision-making step (Price, 1968). To achieve this, the optimum receiver usually does the correlation of the actual received signal with a function having the characteristics of the expected echo. This can be done by letting the received signal through a matched filter (hardware), or, in our case, by cross-correlating the signal with a function (i.e. software filter) having the expected general shape of the echo.

We will attempt to maximize the signal-to-noise ratio, since it can serve as a satisfactory index of detectability (Price, 1968). In particular, we want to find the model spectrum shape S(f) which maximizes the result of the cross-correlation mentionned above. The algorithm used for cross-correlation is given in Figure 10.1a. The function to be cross-correlated with the total spectrum, will be referred to as the "smoothing function".

Scattering laws of the form $\mathrm{Cos}^n\theta$ (see Appendix 1), where θ is the angle of incidence on the target's surface, are useful to describe backscattering from rough planetary targets. For a rotating spherical target for which we consider the apparent axis as 0-frequency reference, the Doppler shift of any point on the Doppler equator can be expressed as a function of θ and B, where B is the limb-to-limb bandwidth of the echo:

$$f = B\ \mathrm{Sin}\theta/2 \qquad (10.1)$$

Using this identity, we choose a smoothing function of the type

$$S(f) = [1-(2f/B)^2)^{n/2}] \ , \ -B/2 \leq f \leq B/2 \qquad (10.2)$$

where n is the scattering law exponent, f the frequency with respect to the center of the echo, and B the width of the theoretical echo spectrum (with $f = B \sin\theta/2$, we get $S(f) = T(\theta) = \cos^n(\theta)$). For non-spherical targets, S(f) represents only a convenient model shape. S(f) is shown in Figure 10.2, for a scattering exponent n=1 and a total bandwidth B = 10 Hz.

The effective bandwidth of such a "filter" is defined by:

$$EFB = \int_{-B/2}^{B/2} [1-(2f/B)^2]^{n/2}\, df$$

$$= \int_{-\pi/2}^{+\pi/2} \cos^n\theta\ (B/2)\ \cos\theta d\theta$$

$$= B \cdot \int_0^{\pi/2} \cos^{n+1}\theta d\theta$$

therefore,

$$EFB = B \cdot g(n) \text{ with } g(n) = \int_0^{\pi/2} \cos^{n+1}\theta d\theta \qquad (10.3)$$

From Wallis' formula:

$$2/\pi \int_0^{\pi/2} \cos^{2m} x dx = 1/\pi^{1/2} \cdot \Gamma(m+2)/\Gamma(m+1)$$

we deduce $g(n) = (\pi/4)^{1/2}\ \Gamma[(n+2)/2]/\Gamma[(n+3)/2]$ (10.4)

and thus,

$g(0) = 1$ $\quad g(0.5) = 0.87$ $\quad g(1) = 0.79$

$g(1.5) = 0.72$ $\quad g(2.0) = 0.67$ $\quad g(5) = 0.49$

The results for $\underline{n} = 1$ and several values of the effective filter bandwidth are shown in figure 10.3 for the following cases:

Curve 1: November 5,6
Curve 2: November 7,8
Curve 3: All days (November 2 through 8)

The result of the cross-correlation, which we will call the "smoothed spectrum", has been normalized to the rms noise calculated for these correlated data (rms defined below).

It is shown above that the effective filter bandwidth is related to the limb-to-limb bandwidth by the relation:

$$\mathrm{EFB} = g(n) \;.\; B \qquad (10.5)$$

Although we see that the value of B which yields the maximum signal-to-noise ratio is close to 5 Hz, from the smoothed spectrum corresponding to the weighted sum of all the data (Curve 3), we see that this method does not place useful limits on the range in which B should lie. From inspection of the curves 1 and 2, we see that the effective filter bandwidth that yields the maximum SNR for the November 5, 6 data is different from that for the November 7, 8 data. The smoothing of the November 5,6 data alone would then yield a larger limb-to-limb bandwidth than the November 7,8 data, but the low signal-to-noise ratios involved render inferences unreliable on the physical nature of the separate aspects observed during each of these two periods.

10.1.2. The standard deviation of the smoothed spectrum.

As an example, let's assume a smoothing function which emcompasses three spectral elements ("three-channel smoothing"). The data set contains N data points which we will call x_i $(1 \leq i \leq N)$.

If we smooth using a symmetric function (with respect to its center), then we can call α_1, α_2, α_3 ($\alpha_1 = \alpha_3$) the values taken by this function at each of the three adjacent frequencies considered (see Fig. 10.1a). Then the smoothing process will associate a value x_{si} with a value x_i of the unsmoothed spectrum:

$$x_{si} = \frac{x_{i-1}\alpha_1 + x_i\alpha_2 + x_{i+1}\alpha_3}{\alpha_1 + \alpha_2 + \alpha_3} \qquad (10.6)$$

in the smoothed spectrum.

We call the standard deviations of the fluctuation σ_{uns} and σ_{sm}, for the unsmoothed and smoothed spectra, respectively; where

$$\sigma_{sm}^2 = \frac{1}{N-1}\sum_{i=1}^{N}\left[\frac{x_{i-1}\alpha_1 + x_i\alpha_2 + x_{i+1}\alpha_3}{\alpha_1 + \alpha_2 + \alpha_3}\right]^2 \qquad (10.7)$$

under the assumptions: $\bar{x}_i = 0$ (which implies $\bar{x}_{si} = 0$)

For commodity of computation, we assume a "folded" spectrum: that is for instance that, since x_{i-1} is not defined for i=1, we will set it equal to x_n as a convention. In the same way, we will set x_{i+1} for i=n as equal to x_1.

Therefore:

$$\sigma_{sm}^2 = \frac{1}{(N-1)(\alpha_1+\alpha_2+\alpha_3)^2} \cdot A$$

with:

$$A = \sum_{i=1}^{N}(x_{i-1}^2\alpha_1^2+x_i^2\alpha_2^2+x_{i+1}^2\alpha_3^2+2(x_{i-1}x_i\alpha_1\alpha_2+x_ix_{i+1}\alpha_2\alpha_3+x_{i+1}\alpha_1\alpha_3))$$

We have $\frac{1}{N-1}\sum_{i=1}^{N} x_{i-1}^2\alpha_1^2 = \alpha_1^2\sigma_{uns}^2$, $\frac{1}{N-1}\sum_{i=1}^{N} x_i^2\alpha_2^2 = \alpha_2^2\sigma_{uns}^2$,

$\frac{1}{N-1}\sum_{i=1}^{N} x_{i+1}^2\alpha_3^2 = \alpha_3^2\sigma_{uns}^2$

Under the additional assumption of uncorrelation between the different x_i, we have:

$$\sum_{i=1}^{N} x_i x_{i+1} = \sum_{i=1}^{N} x_{i-1} x_i = \sum_{i=1}^{N} x_{i-1} x_{i+1} = 0$$

We have then:

$$\sigma_{sm}^2 = \frac{\alpha_1^2 + \alpha_2^2 + \alpha_3^2}{(\alpha_1 + \alpha_2 + \alpha_3)^2} \sigma_{uns}^2 \qquad (10.8)$$

In the general case of smoothing with M channels (M is odd) we get:

$$\sigma_{sm}^2 = \frac{\sum_{j=1}^{M} \alpha_j}{\sum_{j=1}^{M} {}^{2}\, \alpha_j} \sigma_{uns}^2 \qquad (10.9)$$

In the particular case of a rectangular function $\alpha_i = \alpha_j$ $i \neq j$ we get:

$$\sigma_{sm} = \sigma_{uns} / M^{1/2} \qquad (10.10)$$

The normalized smoothed spectra using a smoothing filter of characteristic parameters n = 1 and EFB = 4 Hz are shown at the end of this chapter.

10.2. Least-Squares Estimation of the Signal Parameters

10.2.1. Least-Squares technique

The goal in this section is to find the model spectrum shape S(f) which "best fits" the shape of the radar echo spectrum in a "least-squares" sense. We define a measure of goodness of fit as:

$$\chi^2 = \sum_{i=1}^{NP} \{[Y_s(i) - S(f_i)]^2 / \sigma_i^2\} \qquad (10.11)$$

where σ_i is the uncertainty in the data point $Y_s(i)$ of the final raw spectrum Y_s obtained in 4.2, and f_i is the frequency associated with the element of index i. Since Y_s has been normalized and each data point is treated equally, we have $\sigma_i = 1$. NP is the total number of data points. As described earlier, we choose a model function S(f) of the type:

$$S(f) = A(1 - [\frac{2(f-f_o)}{B}]^2)^{n/2} \quad , \text{ for } |f-f_o| \leq B/2$$

$$S(f) = 0. \quad \text{for } |f - f_o| > B/2$$

where f_o is the center frequency of the echo signal, the signal being assumed to be symmetrical with respect to f_o. The peak amplitude of the signal is characterized by A, the limb-to-limb bandwidth by B, and the scattering exponent by n.

According to the method of least-squares, the optimum values of the parameters (B, n, A, f_o) which characterize S(f) are obtained by minimizing χ^2 simultaneously with respect to each of these four parameters. For simplicity in the following discussion we will use x_1 for B, x_2 for n, x_3 for A and x_4 for f_o.

Thus, we seek the solution

$$\frac{\partial\chi^2}{\partial x_j} = 0, \quad j = 1,4 \qquad (10.12)$$

Since S is not a linear function of the parameters x_j, iterative non-linear least-squares is used. We search for minima on the χ^2 hypersurface in x_j space by expanding the function χ^2 in Taylor's series around a "reasonable" point. In this way we expand the model function S(f) to first order as a function of the parameters x_1, x_2, x_3, x_4, iterating on each new estimate until convergence is obtained. The initially chosen set of values is $V_o = (x_{10}, x_{20}, x_{30}, x_{40})$ for $V = (x_1, x_2, x_3, x_4)$.

$$\frac{\partial\chi^2}{\partial x_j} = \frac{\partial}{\partial x_j} \sum_i (Y_s(i) - 2Y_s(i)S(f_i) + S(f_i)^2) = 0 \qquad (10.13)$$

$j = 1, k \quad (k = 4)$

Let's write $S_i = S(f_i)$ and $Y_{si} = Y_s(i)$, and let's use a first order expansion for S:

$$S_i = S_i^o + \sum_{m=1}^{k} \frac{\partial S_i}{\partial x_m})_{V_o} \; (x_m - x_{mo})$$

where $V_o = (x_{10}, x_{20}, x_{30}, x_{40})$ characterizes $S^o(f)$, an initial guess for S(f).

Let's set $a_{ij} = \left.\frac{\partial S_i}{\partial x_j}\right|_{V_o}$

Then linearizing χ^2, we get

$$\frac{\partial\chi^2}{\partial x_j} = \frac{\partial}{\partial x_j}(Y_{si}^{\;2} - 2Y_{si}[S_i^o + \sum_{m=1}^{k} a_{im}\,(x_m - x_{mo})] + [S_i^o + \sum_{m=1}^{k} a_{im}(x_m - x_{mo})]^2)$$

$j = 1, k$

And we have:

$$\frac{\partial}{\partial x_j} \sum_i Y_{si}^2 = 0$$

$$\frac{\partial}{\partial x_j} \sum_i (-2Y_{si}^2[S_i^o + \sum_{m=1}^{k} a_{im}(x_m - x_{mo})]) = -2\sum_i^k Y_{si}a_{ij}$$

$$\frac{\partial}{\partial x_j} \sum_i [S_i^o + \sum_{m=1}^{k} a_{im}(x_m - x_{mo})]^2 = 2\sum_i S_i^o a_{ij} + 2\sum_i a_{ij}\,[\sum_{m=1}^{k} a_{im}(x_m - x_{mo})]$$

and $\frac{\partial\chi^2}{\partial x_j} = 0$ becomes:

$$\sum_{i=1}^{NP} a_{ij}\,[\sum_{m=1}^{k} a_{im}(x_m - x_{mo})] = \sum_i a_{ij}(Y_{si} - S_i^o) \qquad j = 1, k \qquad (10.14)$$

In the general case, if each data point had a different associated uncertainty σ_i, or if the observational errors were correlated, one would have to use a weighted least-squares procedure and replace a_{ij} by a_{ij}/σ_i^2. As seen before, in our case $\sigma_i=1$ and each data point is weighted equally.

Equation (10.14) can be rewritten using matrix formulation: Let's define the following matrices:

$A=||a_{ij}||$ $B=||b_j||$ $b_j=\sum_i a_{ij}\,(y_{si}-\overset{\circ}{S}_i)$

and $D= V - V_o$; D is a 4-component column vector.

Equation (3) becomes: $A^T A D = B$, and if $C = A^T A$ is non-singular:

$D = C^{-1} B$ (10.15) $D = ||d_j||$

We thus obtain the correction D to apply to V_o in order to get a better estimate V of the set of parameters defining S. It can be shown (see for instance Bevington, 1969, p. 154) that the covariance matrix of the errors in the new estimates of the parameters x_j is the inverse of the coefficient matrix C of the normal equations so that:

$E = C^{-1}$, which is a 4 x 4 matrix.

Writing $E = ||e_{ij}||$ we have $\sigma_{xj} = e_{jj}^{1/2}$

Several iterations, using the estimated values of x_j $(j=1,4)$ as an *a priori* set of estimates V for the next iteration, are usually necessary to obtain small enough values for d_j. The algorithm is described in Figure 10.1b.

This analysis has been carried out as a search for the best estimates of x_1, x_2, x_3, and x_4, starting with different sets of *a priori* values. In all cases, the procedure converges for the fourth parameter $x_4 = f_o$, giving values approximately midway in the interval (bin 177 to bin 178). This result was expected, based on examination of the final raw spectrum (Table 4.1). However, for the first three parameters, convergence depends on the set of *a priori* estimates used and yields large errors in the estimates of the parameters. Thus, a simultaneous estimation of all four parameters, or even of the first three parameters, is impractical. This phenomenon is due to the low signal-to-noise ratio available and to the fact that the echo signal is contained in only a small number of spectral elements (Table 4.1), between four and six, thus even if the analysis spreads over the full set of NP=365 available data points, the "effective" number of useful data points is quite small. Consequently the direct resolution of

the system of equations $\frac{\partial x^2}{\partial x_j} = 0$

will not, in general, yield physically acceptable results. It is thus necessary to constrain some of the parameters within physically reasonable ranges, while freeing the remaining parameters.

It is a reasonable and not too constraining assumption to fix the center frequency of the echo to the value obtained above, or at least to the nearest frequency sample. We perform the following analysis successively for $x_4 = f_{01}$ (center of echo at center of bin 177), $x_4 = f_{02}$ (center of echo at middle of the interval (bin 177, bin 178), and $x_4 = f_{03}$ (center of echo at center of bin 178).

The range $3\sigma \leq A \leq 6\sigma$ has been adopted for the third parameter since the peak signal-to-noise ratio in the unsmoothed spectrum is at about 4.5 σ.

Since the parameters B and n are strongly correlated, we chose to find a least-squares estimate for B, starting with various fixed values for n, as well as different a priori values for B. We have to choose a physically meaningful range for n. The range $0 \leq n \leq 5$ was adopted since it encompasses virtually all of the estimates of n obtained from radar observations of the galilean satellites of Jupiter, and it includes the range obtained by Jurgens and Goldstein (1976) for the asteroid Eros, $1 \leq n \leq 1.5$ and by Pettengill *et al*. (1979) for Betulia, $0.5 \leq n \leq 1.5$.

An additional problem arose in the least-squares estimation of the limb-to-limb bandwidth. In many cases, for a given section of the hypersurface defined by a triplet of the estimated parameters n, A, f_o, the goodness-of-fit parameter χ^2 exhibits several minima, corresponding to different values of B. The existence of multiple local minima implies that the location of the convergence of the algorithm depends on the *a priori* parameters chosen. A coarse grid mapping of the parameter space in the region defined by the ranges given earlier has been necessary to identify all the regions of local and absolute minima. An increment was chosen for each of the parameters involved to divide the parameter space into elementary cells; for each of these cells, a value of χ^2 was calculated. A more elegant, but less visually satisfactory, way to obtain the same results would have been to combine a gradient or ravine search algorithm with the analytical linear procedure (Bevington, 1969).

When the general location of the deepest minimum has been found, the analytical solution of the matrix equation (10.15) can be carried out. Starting with different values of the parameter set (B, n, A, f_o) and solving for B, we obtained results via the iterative least-squares procedure for the three choices of *a priori* center frequency $x_4 = f_{01}$, $x_4 = f_{02}$, and $x_4 = f_{03}$. The results for $x_4 = f_{02}$ are presented in Figure 10.4. This figure contains the estimated values of the limb-to-limb bandwidth of the echo, the associated formal standard errors obtained from the covariance matrix E, and the sum of the squares of the post-fit residuals, for each pair of values (n, A) indicated.

In some cases the function being minimized had two minima, one local and one absolute causing the least-squares algorithm to converge to one or the other, depending on the starting values used. In Figure 10.4 for instance, we have included only the estimated limb-to-limb bandwidth yielding the absolute minimum. It happens that, for a priori combinations (A, n) yielding two minima, the absolute minimum may correspond for one pair (A_1, n_1) to the smallest of the two resulting bandwidths and for another (A_2, n_2) to the highest of the two bandwidths; this applies particularly to the "jump" in formal error observed in Figure 10.4 for $A = 5.0$ when one passes from $n = 0.5$ to $n = 1.0$. Thus the measurements yield essentially no sensitivity to B or n.

10.2.2. Scattering exponent and limb-to-limb bandwidth of the echo

For the ranges of values specified above for n, A, and f_o, we obtain estimated values for B in the range 2 - 11 Hz. Because of the strong correlation between n and B and in order to obtain meaningful results, we must restrict the range considered for these parameters. Considering the range $n = 1.5 \pm 1$, we get: $2.5 \leq B \leq 9$ as a reasonable range for B. The values obtained here for B are similar to the results of the cross-correlation presented in paragraph i.

Notice that as n increases, B also increases. The reason is simple: when n increases, the function S(f) falls off more sharply from its value at f = 0 and , especially in the neighborhood of the "central" bins (y > 0). The absolute values of the residuals $|y - S(f_i)|$, with $y > 0$ and $S(f_i) = A\ [1 - (2(f_i - f_o)/B)^2]^{n/2}$ will increase when n increases if B keeps a fixed value. The only way to either diminish the residuals or to prevent them from reaching a value too large is to increase B. The fact that the minima of the χ^2 cluster on the right of Figure 10.4 show that the increase in the value of B at convergence is large enough when n increases to imply a decreases in χ^2. There is thus a strong positive correlation between the estimates of n and B. Using the expression given in section 10.1.i. for the effective bandwidth:

$$EFB = B\ (\pi/4)^{1/2}\ \Gamma((n+2)/2)/\Gamma((n+3)/2)$$

we see that going from n=1.5 to n=0.5 implies a decrease of about 22% in B, while increasing n from 1.5 to 2.5 implies an increase of about 13% in B.

There is a negligible radial acceleration not accounted for in the ephemerides so that we can assume that the center frequency was at the same position on each of the last four days of observation. Thus the estimate of B is not biased by such systematic errors, the effect of which would have been to increase the estimate made for B.

10.2.3. Center frequency of the echo

The receiver frequency is adjusted so that compensation is made for the changing Doppler shift arising from the continuously varying radial velocity of the target. Because comet orbits are not well known (due in part to non-gravitational effects), the expected frequency of the center frequency of the echo spectrum (assumed to be symmetrical) is usually not identical to the actual received center frequency of the echo. Thus, it is not surprising that there is an offset of the actual with respect to the predicted center frequency.

In the case of comet Encke we have N = 365 data points in the final spectrum. From Table 4.1, we see that the a priori center of the echo is located midway between elements 183 and 184, while the center frequency of the echo appears close to midway between elements 177 and 178, with an uncertainty of about ± 0.6 Hz (± half the frequency sampling interval). The offset is equivalent to about 7.3 Hz.

Another effect has to be considered in the case of Encke. The setting of the local oscillator which establishes the receiver frequency according to the value predicted in the ephemerides was delayed in the instrumentation by 0.8216 sec relative to the nominal time. Since the comet was receding during the observations with a rate of change of the Doppler shift of

$r = - 0.81$ Hz/sec on November 3, and

$r = - 0.62$ Hz/sec on November 8

a correction in the observed offset must be made. If we take an average rate of change of

$r = - 0.72$ Hz/sec over the observing interval,

we find a difference d between the frequency set by the local oscillator and the a priori frequency set in the ephemerides of $d \simeq 0.72 \times 0.8216$

or $d \simeq 0.6$ Hz

Thus the receiver frequency was always about 0.6 Hz higher than called for by the ephemerides, and since the observed offset of the echo was 7.3 Hz higher than the received setting, we find a corrected observed offset of the echo center frequency with respect to the ephemerides of 7.9 ± 0.6 Hz. This information, useful for improving our knowledge of the comet's orbital motion, may be stated as an inferred doppler measurement of

$$- 308720.2 \pm 0.6 \text{ Hz} \quad \text{on November 6, 1980, at 14:48 UT}$$

for a transmitted frequency of 2380 MHz (frequencies are based on the UTC second).

10.3 Estimating the radar cross-section

We now consider the portions of the total "unsmoothed spectrum" (defined in paragraph 10.1) that contain the radar echo in an attempt to derive values of the observed radar cross-section, σ. The corresponding values of the echo power are given in Table 10.1.

TABLE 10.1

TABULATED ECHO POWER

Assumed Center Frequency of the echo

						↓				
Spectral Element :	173	174	175	176	177	178	179	180	181	182
Echo Power : (Std. dev'ns)	-0.12	-0.39	0.87	2.14	4.15	4.32	0.56	1.39	-0.22	-0.22

Using these values, one can compute the radar cross-section for various estimates of the echo bandwidth. For a given spread of the echo, for instance from spectral element # n_1 to n_2, the cross-section is obtained by multiplying the corresponding total echo power by the standard deviation σ_{rms} of the noise fluctuations per spectral element expressed in km^2. From equation (4.14) we get

$$\sigma_{rms} \simeq 0.094 \text{ km}^2.$$

The resulting radar cross-sections σ_{cr} are given in Table 10.2. The associated uncertainties ε_{cr} are evaluated by considering the contributions of both the standard errors σ_{rms} due to the noise fluctuations and the systematic errors due to uncertainties in the calibration of the radar system parameters P_T (transmitted power), G (antenna gain), and T_s (system temperature). These systematic errors represents about 25% of the estimated radar cross-section. The uncertainty ε_{cr} which is obtained as the square-root of the sum of the square of the contributions, is also indicated in Table 10.2.

TABLE 10.2

RADAR CROSS-SECTION

Assumed Spread of Echo (spectral elements)	B (Hz)	σ_{cr} (km^2)	ε_{cr} (km^2)
177-178	2.4	0.80	0.24
176-179	4.9	1.05	0.32
175-180	7.3	1.26	0.39
174-181	9.8	1.20	0.40

For a "worst case" combination of errors, we deduce a radar cross-section in the range $0.56 \leq \sigma \text{ km}^2 \leq 1.66$ with a mean value of about 1.1 km^2.

The lowest value of the radius consistent with the range of σ and the *ad hoc* constraint that the radar cross-section (in the o.c. sense) is less than the geometric cross-section is given by:

$$R_{min} = [0.56/\pi]^{1/2} \approx 0.42 \text{ km}$$

Figure Captions for Chapter 10.

Figure 10.1a. Cross-correlation algorithm

Figure 10.1b. Least-squares estimation algorithm.

Figure 10.2. Shape of the smoothing filter used to maximize the signal-to-noise ratio. $S(f) = [1 - (2f/B)^2]^{n/2}$. This figure shows this shape for $n = 1$ and $B = 10$ Hz.

Figure 10.3. This figure shows the signal-to-noise ratio obtained by smoothing the final raw spectra for November 5,6 (Curve 1), November 7,8 (Curve 2), and all the data (November 2 through November 8, Curve 3), with a filter of variable effective bandwidth and with $n = 1$.

Figure 10.4. Results of the least-squares estimation of the limb-to-limb bandwidth. This figure is discussed in section 10.2.

Figure 10.5. through 10.15. Normalized smoothed spectra for the individual days November 2 through November 8, then for the combinations November 2,3, and 4, November 5 and 6, November 7 and 8, and November 2,3,4,5,6,7, and 8. 365-points spectra on top and expanded plot between -25 Hz and +25 Hz at bottom.

Cross-correlation Algorithm

Unsmoothed data: U(I), I=1,NP
NP points in frequency domain.
Smoothed data: SM(I)
Choice of smoothing function
(Restricted to be bilaterally symmetric)

We want to find the value of the smoothed spectrum at the Nth freq. bin.

1. We find the number of bins encompassed by the filter of shape W(f,H,N) centered on the Nth bin.

For N=1 to N=NP

2. Then we find the value taken by the smoothing function at the center of each of these bins: W(I), with $N-m \leq I \leq N+m$; 2m+1 bins encompassed by the filter.

3. We compute SM(N):

$$SM(N) = \frac{\sum_{N-m}^{N+m} W(I)\,U(I)}{\sum_{N-m}^{N+m} W(I)}$$

NORMALIZATION

Calculate sample rms of SM

$$rms = \left(\frac{\Sigma(SM(k) - \overline{SM})^2}{NN-1}\right)^{1/2}$$

Where sum Σ carried out on NN bins of noise. Then normalize

$$N=1,NP: \quad SM(N) = \frac{SM(N)}{rms}$$

NN=NP-(Number of bins of "echo" signal.)

Figure 10.1a

ESTIMATION OF B BY LEAST-SQUARES TECHNIQUE
ALGORITHM USED

Total number of data points:
NP points in frequency domain.
data y_i for frequency f_i, $1 \leq i \leq NP$

Choice of the shape of the function to be fitted to the data S(f).

Choice of starting values for the unknown parameters defining the function S : x_{jo}.

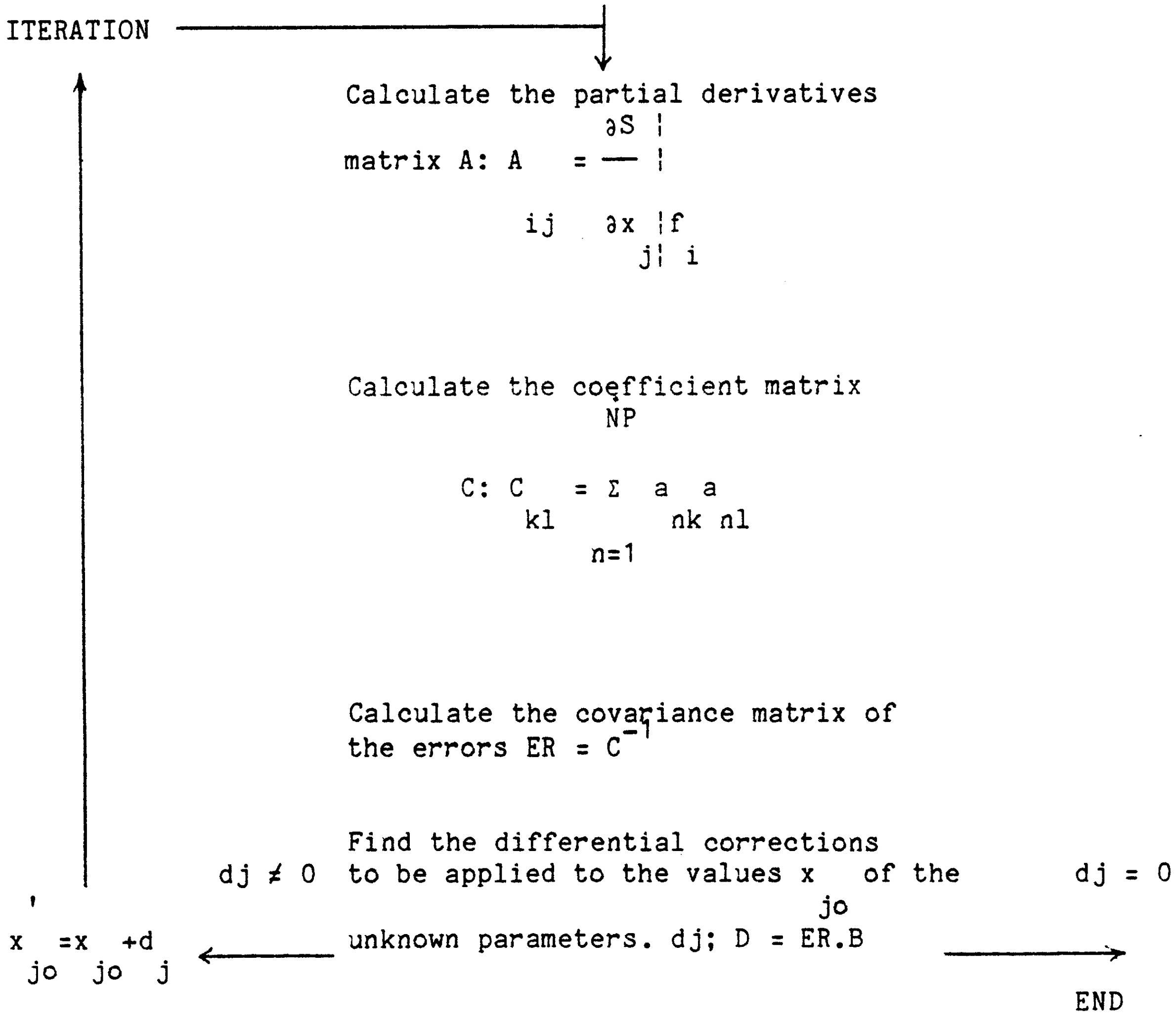

ITERATION

Calculate the partial derivatives matrix A: $A_{ij} = \left.\frac{\partial S}{\partial x_j}\right|_{f_i}$

Calculate the coefficient matrix C: $C_{kl} = \sum_{n=1}^{NP} a_{nk}\, a_{nl}$

Calculate the covariance matrix of the errors ER = C^{-1}

Find the differential corrections to be applied to the values x_{jo} of the unknown parameters. dj; D = ER.B

dj ≠ 0

$x'_{jo} = x_{jo} + d_j$

dj = 0

END

$E = ((e_{ij}))$ $\quad B = ((b_m))$: $\quad b_m = \sum_{i=1}^{NP} a_{im}\,.\,(y_i - s_{oi})$

Figure 10.1b

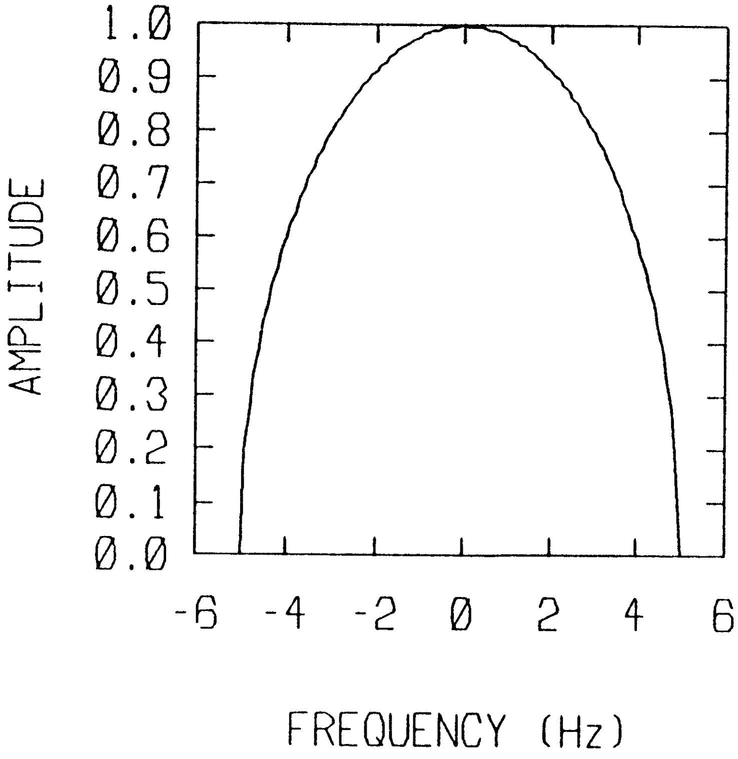

Fig. 10.2

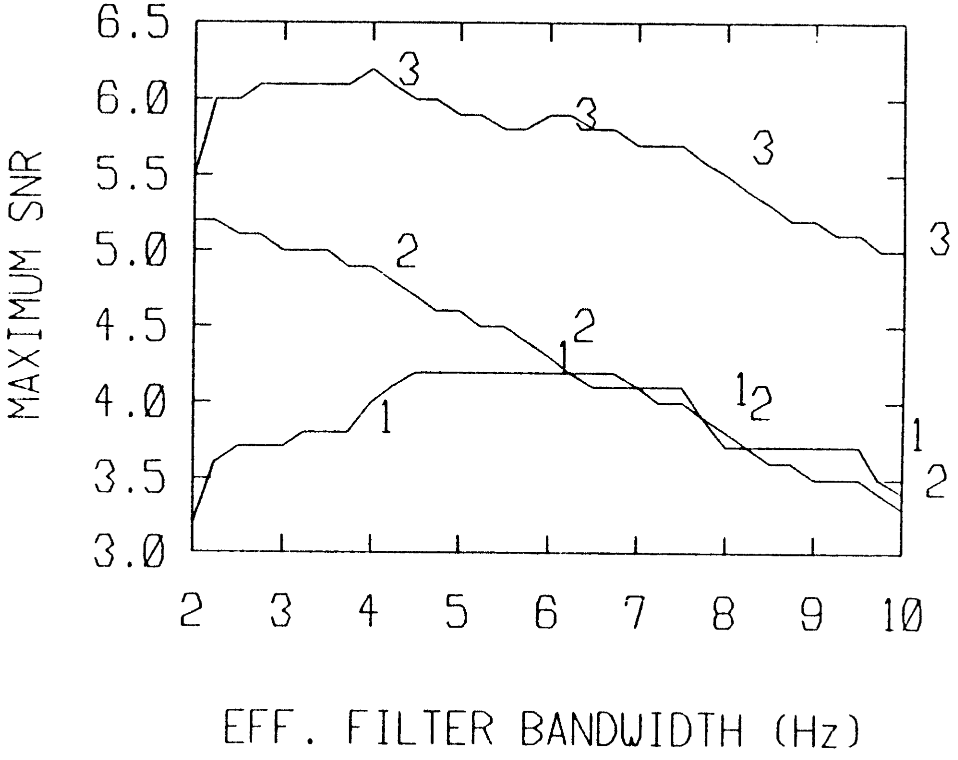

Fig. 10.3

ESTIMATES OF BANDWIDTH FOR CENTER FREQUENCY OF ECHO ASSUMED MIDWAY BETWEEN ELEMENTS 177 AND 178
ALL DATA USED

A	n	0.50	1.00	1.50	2.00	2.50	3.00	4.00	5.00
3.0	B	3.74	6.48	6.86	7.27	7.68	8.10	8.76	9.39
	ERROR	0.09	0.28	0.44	0.57	0.67	0.76	0.88	0.97
	CHISQ	362.90	362.68	362.23	361.99	361.84	361.75	361.66	361.65
4.0	B	3.69	3.90	4.21	4.55	4.88	5.21	7.41	7.89
	ERROR	0.03	0.13	0.23	0.31	0.37	0.43	0.57	0.65
	CHISQ	359.62	359.76	359.86	359.94	359.99	360.03	359.97	359.66
4.5	B	3.68	3.84	4.10	4.38	4.67	4.95	5.49	5.98
	ERROR	0.02	0.10	0.18	0.25	0.30	0.35	0.43	0.50
	CHISQ	359.38	359.35	359.36	359.37	359.38	359.40	359.42	359.44
5.0	B	1.77	3.80	4.02	4.26	4.51	4.76	5.24	5.68
	ERROR	0.32	0.08	0.15	0.20	0.25	0.29	0.36	0.42
	CHISQ	362.99	359.82	359.67	359.58	359.53	359.49	359.45	359.43
6.0	B	1.41	1.73	3.91	4.10	4.29	4.48	4.85	5.19
	ERROR	0.08	0.14	0.10	0.15	0.19	0.22	0.28	0.33
	CHISQ	362.99	362.99	362.78	362.36	362.05	361.83	361.52	361.33

FIGURE 10.4

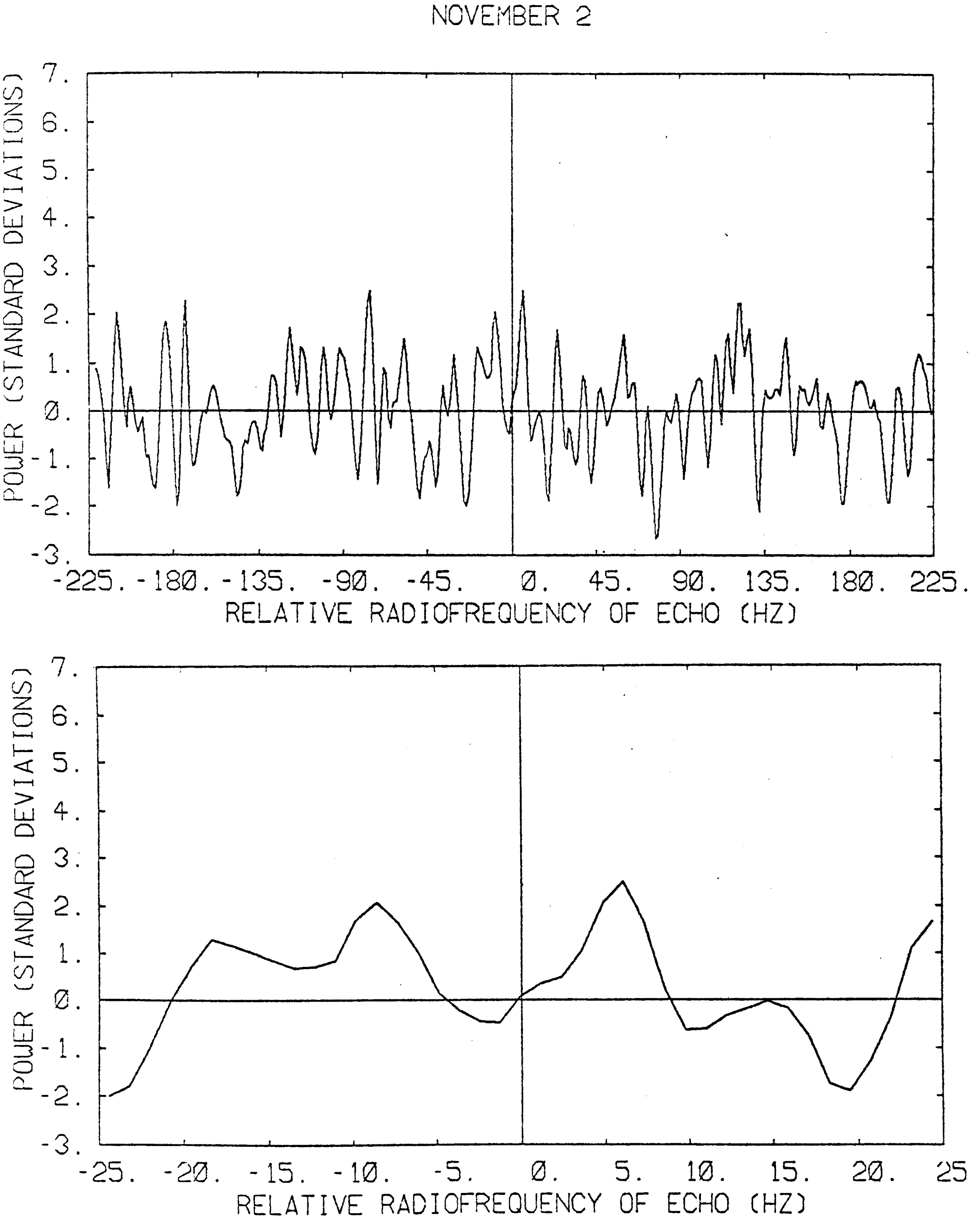
NOVEMBER 2
POWER (STANDARD DEVIATIONS)
7.
6.
5.
4.
3.
2.
1.
0.
-1.
-2.
-3.
-225.
-180.
-135.
-90.
-45.
0.
45.
90.
135.
180.
225.
RELATIVE RADIOFREQUENCY OF ECHO (HZ)
POWER (STANDARD DEVIATIONS)
7.
6.
5.
4.
3.
2.
1.
0.
-1.
-2.
-3.
-25.
-20.
-15.
-10.
-5.
0.
5.
10.
15.
20.
25
RELATIVE RADIOFREQUENCY OF ECHO (HZ)

Fig. 10.5

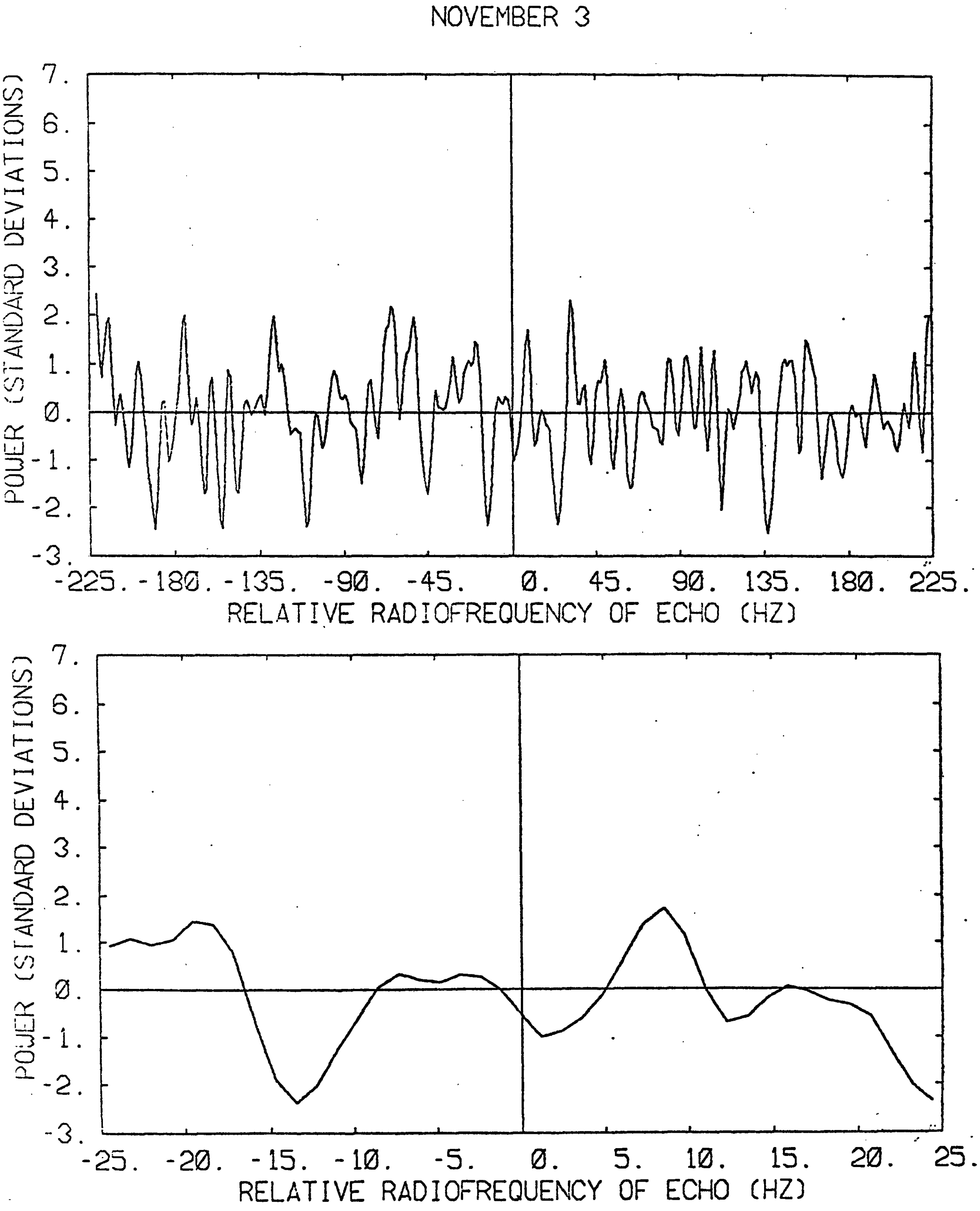
NOVEMBER 3
POWER (STANDARD DEVIATIONS)
7.
6.
5.
4.
3.
2.
1.
0.
-1.
-2.
-3.
-225.
-180.
-135.
-90.
-45.
0.
45.
90.
135.
180.
225.
RELATIVE RADIOFREQUENCY OF ECHO (HZ)
POWER (STANDARD DEVIATIONS)
7.
6.
5.
4.
3.
2.
1.
0.
-1.
-2.
-3.
-25.
-20.
-15.
-10.
-5.
0.
5.
10.
15.
20.
25.
RELATIVE RADIOFREQUENCY OF ECHO (HZ)

Fig. 10.6

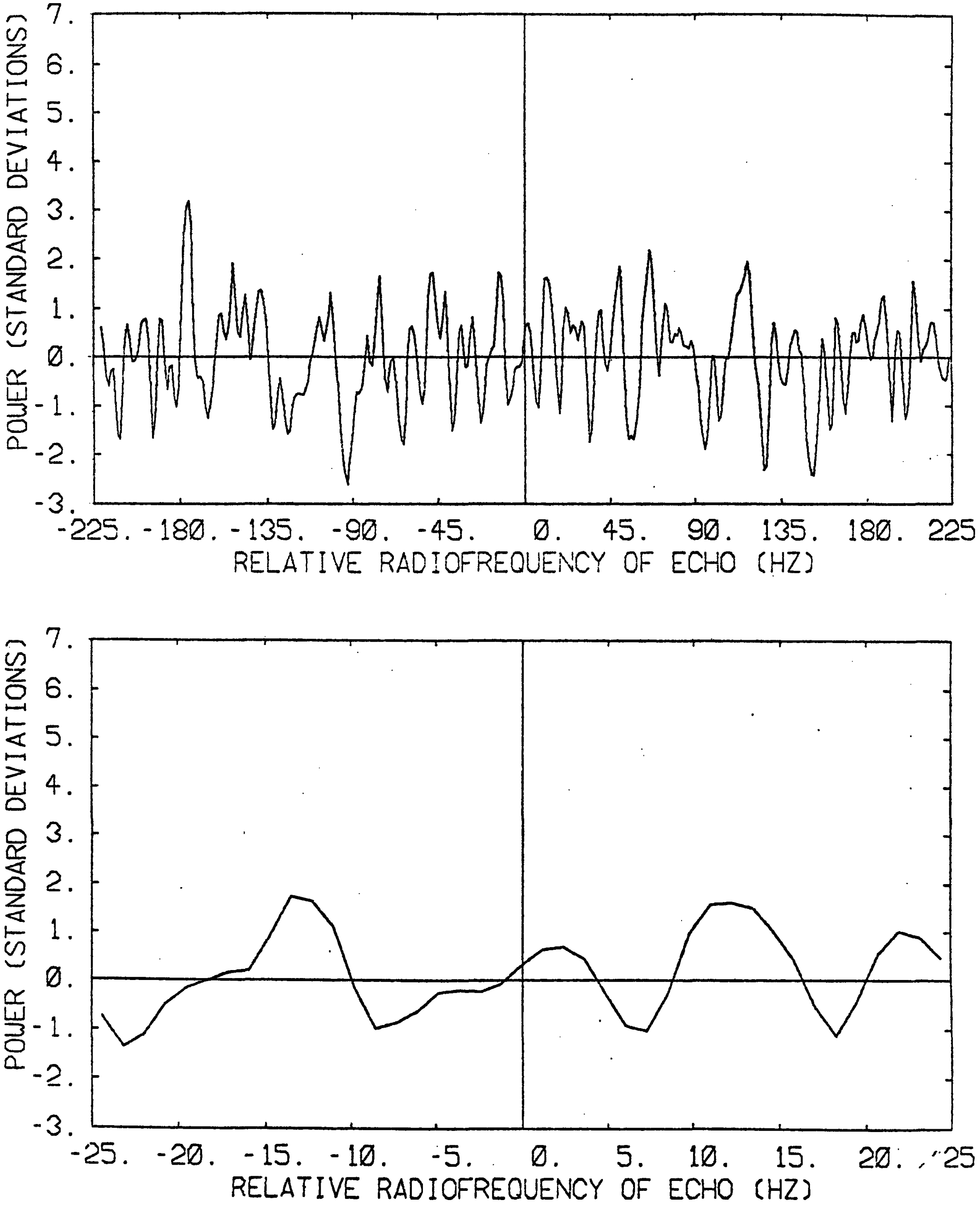
NOVEMBER 4

Fig. 10.7

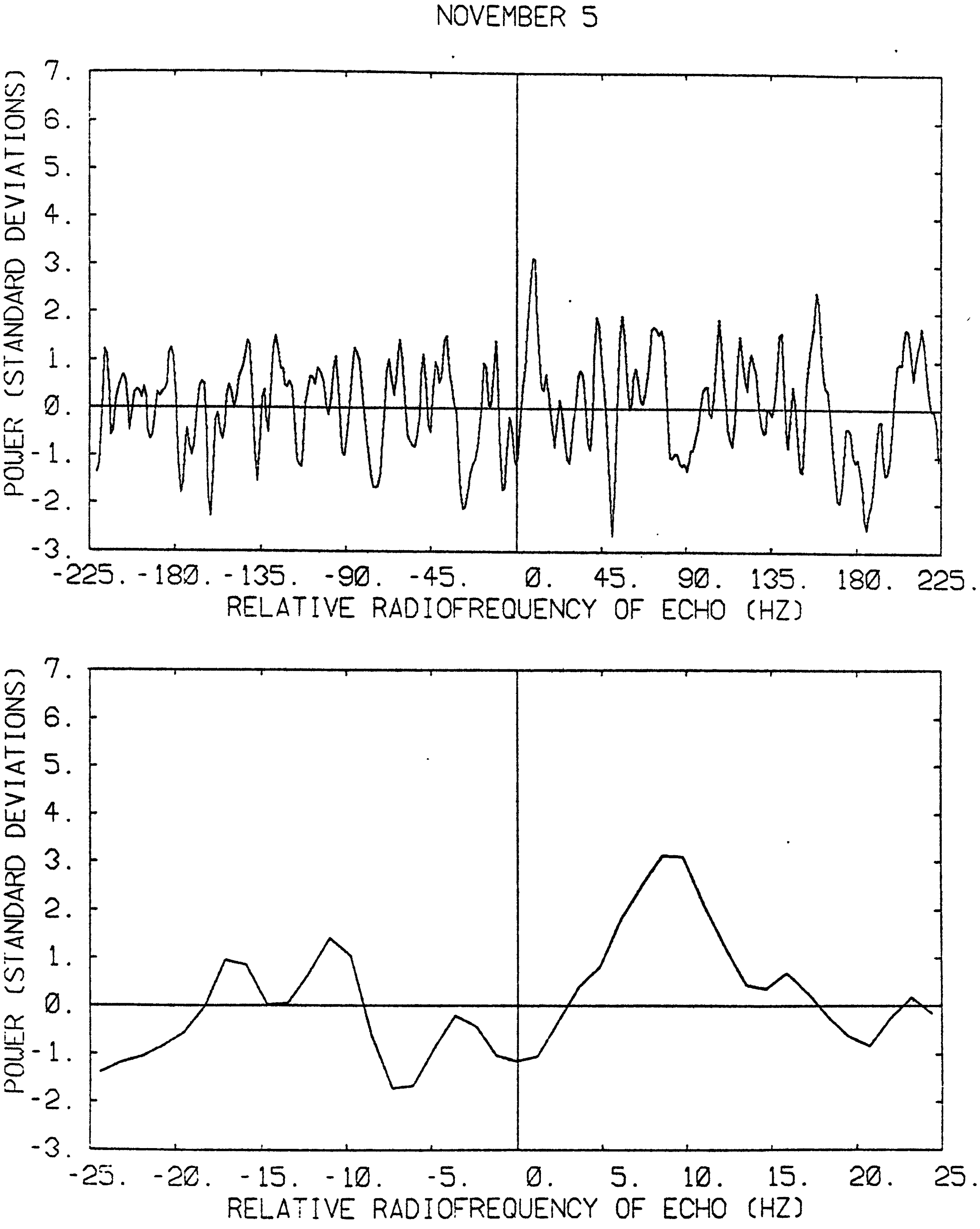
NOVEMBER 5
POWER (STANDARD DEVIATIONS)
7.
6.
5.
4.
3.
2.
1.
0.
-1.
-2.
-3.
-225.
-180.
-135.
-90.
-45.
0.
45.
90.
135.
180.
225.
RELATIVE RADIOFREQUENCY OF ECHO (HZ)
POWER (STANDARD DEVIATIONS)
7.
6.
5.
4.
3.
2.
1.
0.
-1.
-2.
-3.
-25.
-20.
-15.
-10.
-5.
0.
5.
10.
15.
20.
25.
RELATIVE RADIOFREQUENCY OF ECHO (HZ)

Fig. 10.8

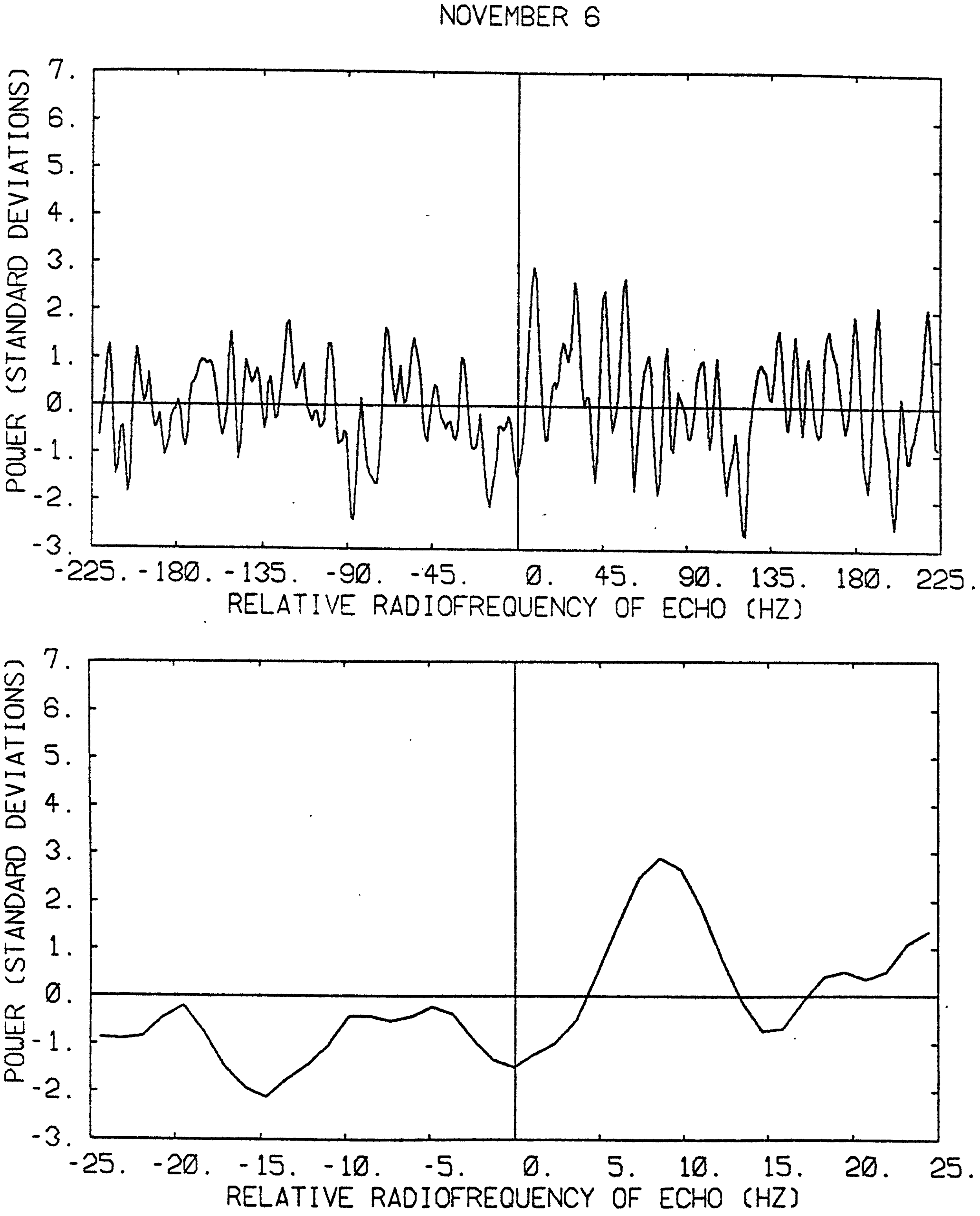
NOVEMBER 6
POWER (STANDARD DEVIATIONS)
7.
6.
5.
4.
3.
2.
1.
0.
-1.
-2.
-3.
-225.
-180.
-135.
-90.
-45.
0.
45.
90.
135.
180.
225.
RELATIVE RADIOFREQUENCY OF ECHO (HZ)
POWER (STANDARD DEVIATIONS)
7.
6.
5.
4.
3.
2.
1.
0.
-1.
-2.
-3.
-25.
-20.
-15.
-10.
-5.
0.
5.
10.
15.
20.
25.
RELATIVE RADIOFREQUENCY OF ECHO (HZ)

Fig. 10.9

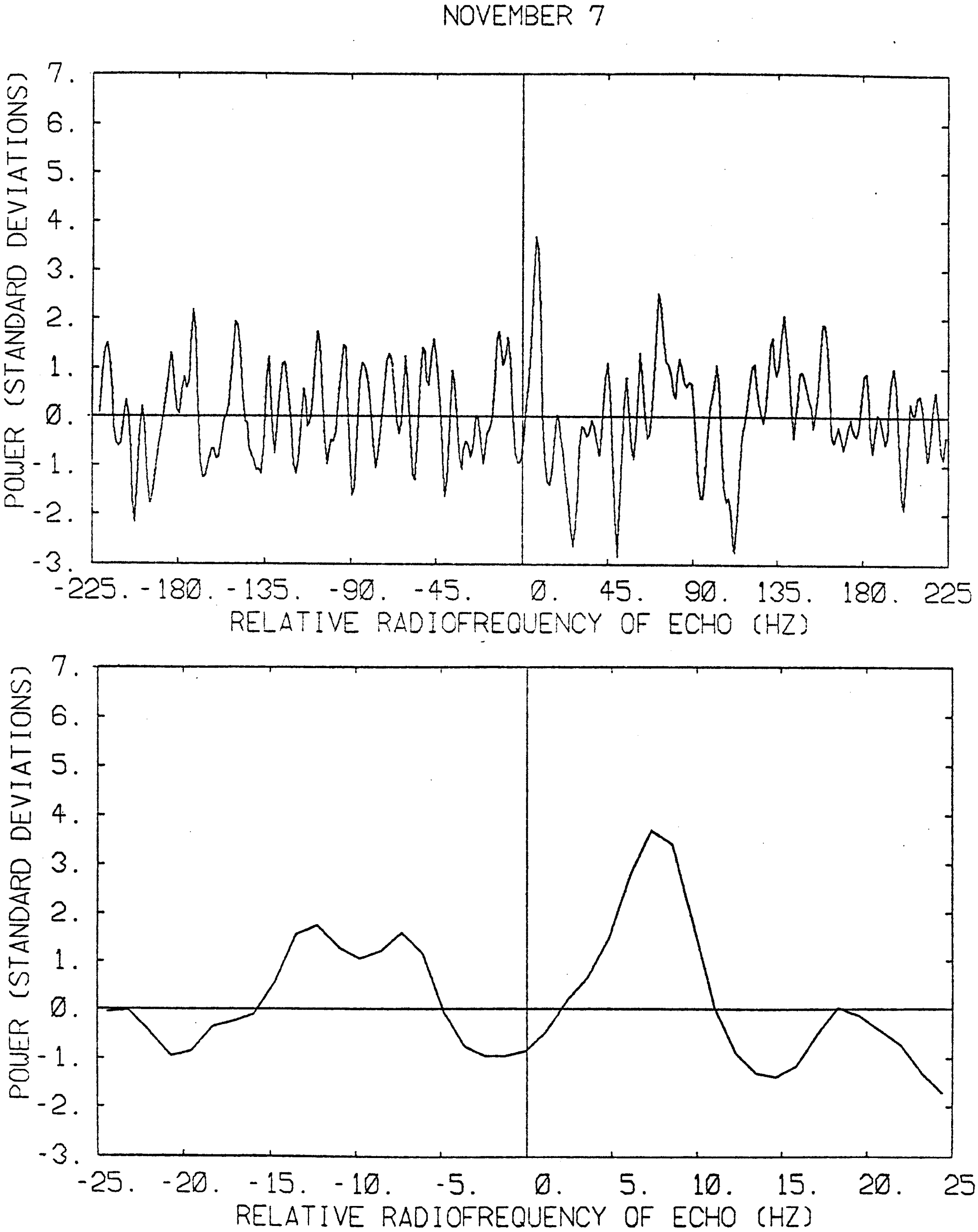
NOVEMBER 7
POWER (STANDARD DEVIATIONS)
7.
6.
5.
4.
3.
2.
1.
0.
-1.
-2.
-3.
-225.
-180.
-135.
-90.
-45.
0.
45.
90.
135.
180.
225
RELATIVE RADIOFREQUENCY OF ECHO (HZ)
POWER (STANDARD DEVIATIONS)
7.
6.
5.
4.
3.
2.
1.
0.
-1.
-2.
-3.
-25.
-20.
-15.
-10.
-5.
0.
5.
10.
15.
20.
25
RELATIVE RADIOFREQUENCY OF ECHO (HZ)

Fig. 10.10

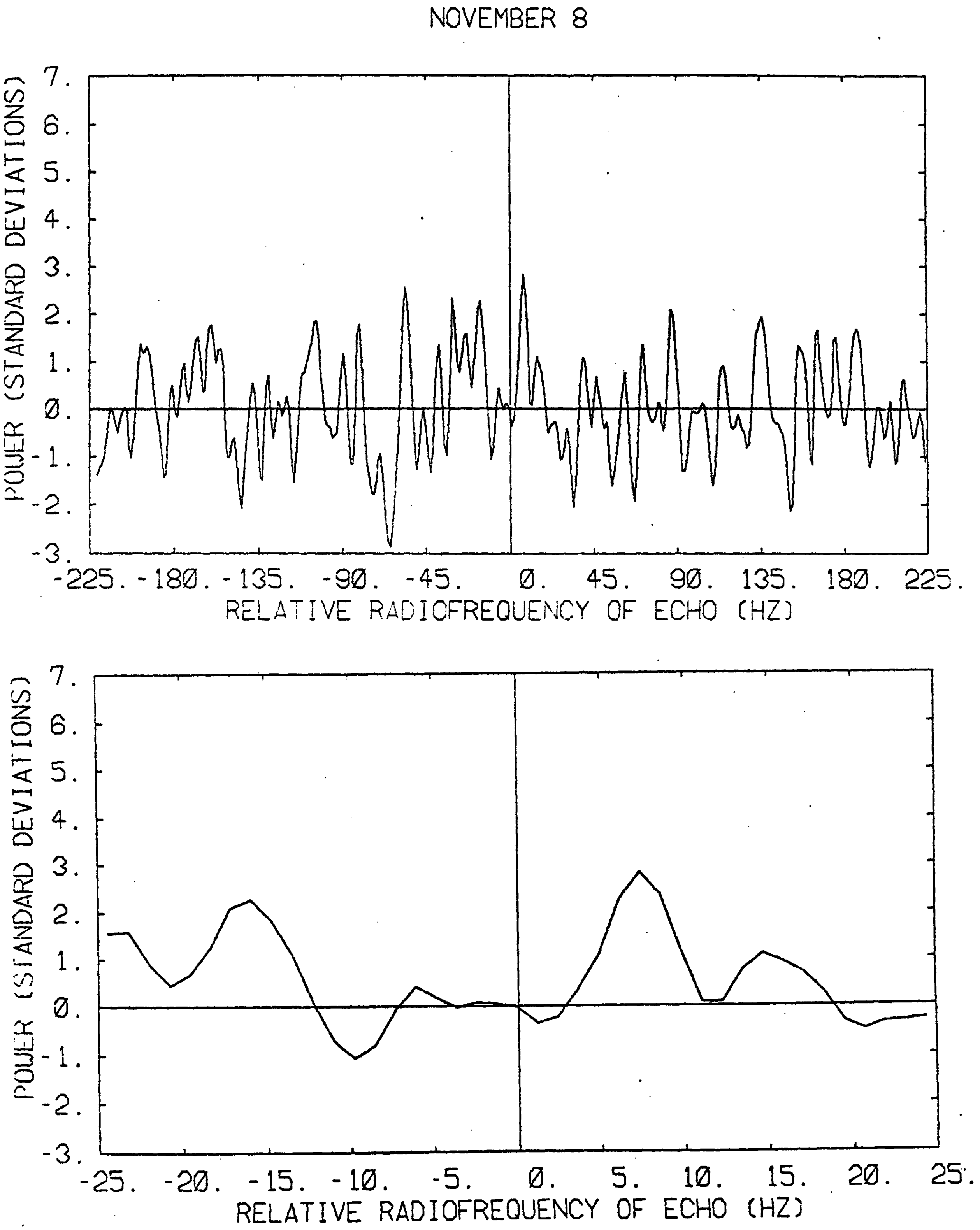
NOVEMBER 8
POWER (STANDARD DEVIATIONS)
7.
6.
5.
4.
3.
2.
1.
0.
-1.
-2.
-3.
-225.
-180.
-135.
-90.
-45.
0.
45.
90.
135.
180.
225.
RELATIVE RADIOFREQUENCY OF ECHO (HZ)
POWER (STANDARD DEVIATIONS)
7.
6.
5.
4.
3.
2.
1.
0.
-1.
-2.
-3.
-25.
-20.
-15.
-10.
-5.
0.
5.
10.
15.
20.
25.
RELATIVE RADIOFREQUENCY OF ECHO (HZ)

Fig. 10.11

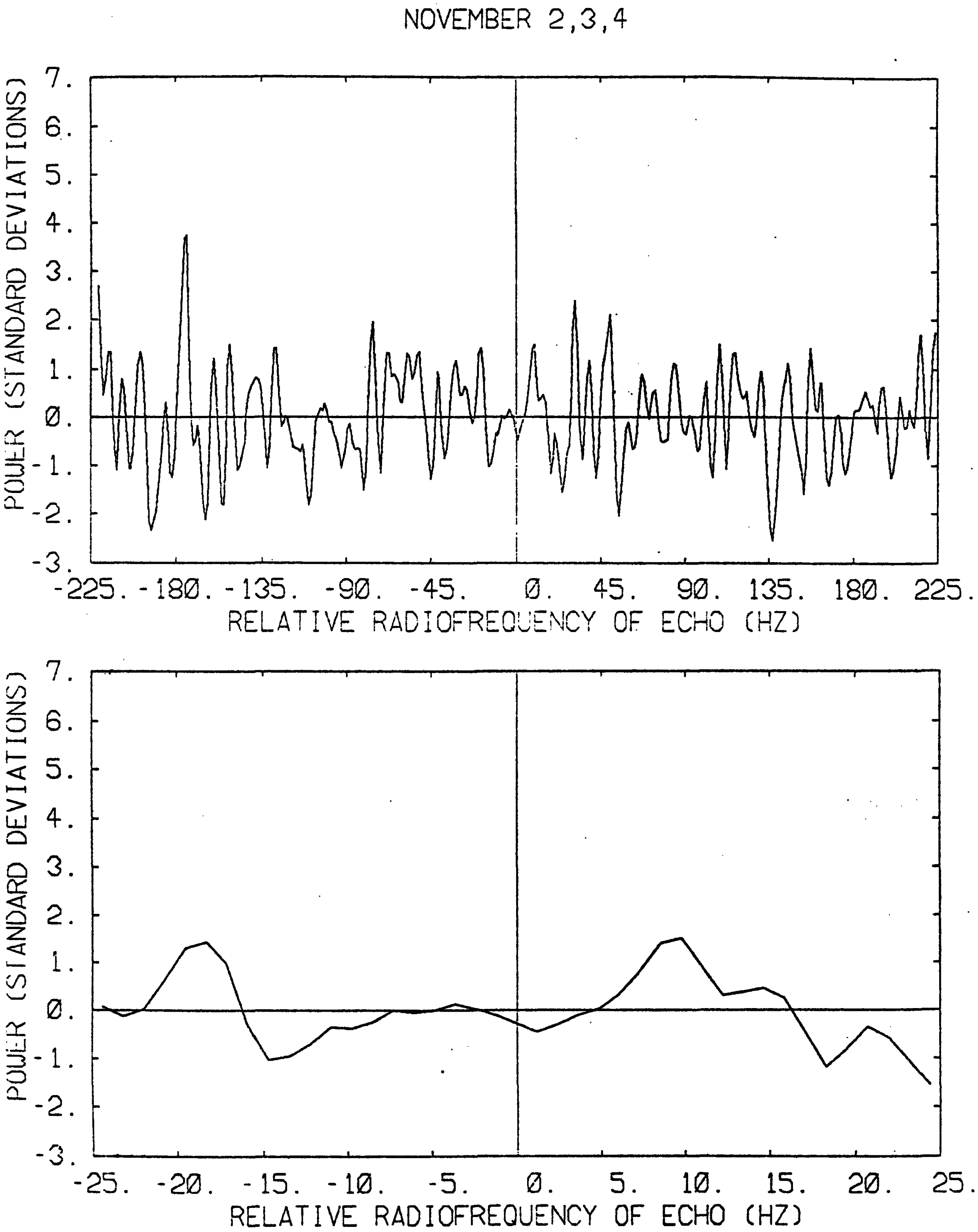
NOVEMBER 2,3,4
POWER (STANDARD DEVIATIONS)
7.
6.
5.
4.
3.
2.
1.
0.
-1.
-2.
-3.
-225.
-180.
-135.
-90.
-45.
0.
45.
90.
135.
180.
225.
RELATIVE RADIOFREQUENCY OF ECHO (HZ)
POWER (STANDARD DEVIATIONS)
7.
6.
5.
4.
3.
2.
1.
0.
-1.
-2.
-3.
-25.
-20.
-15.
-10.
-5.
0.
5.
10.
15.
20.
25.
RELATIVE RADIOFREQUENCY OF ECHO (HZ)

Fig. 10.12

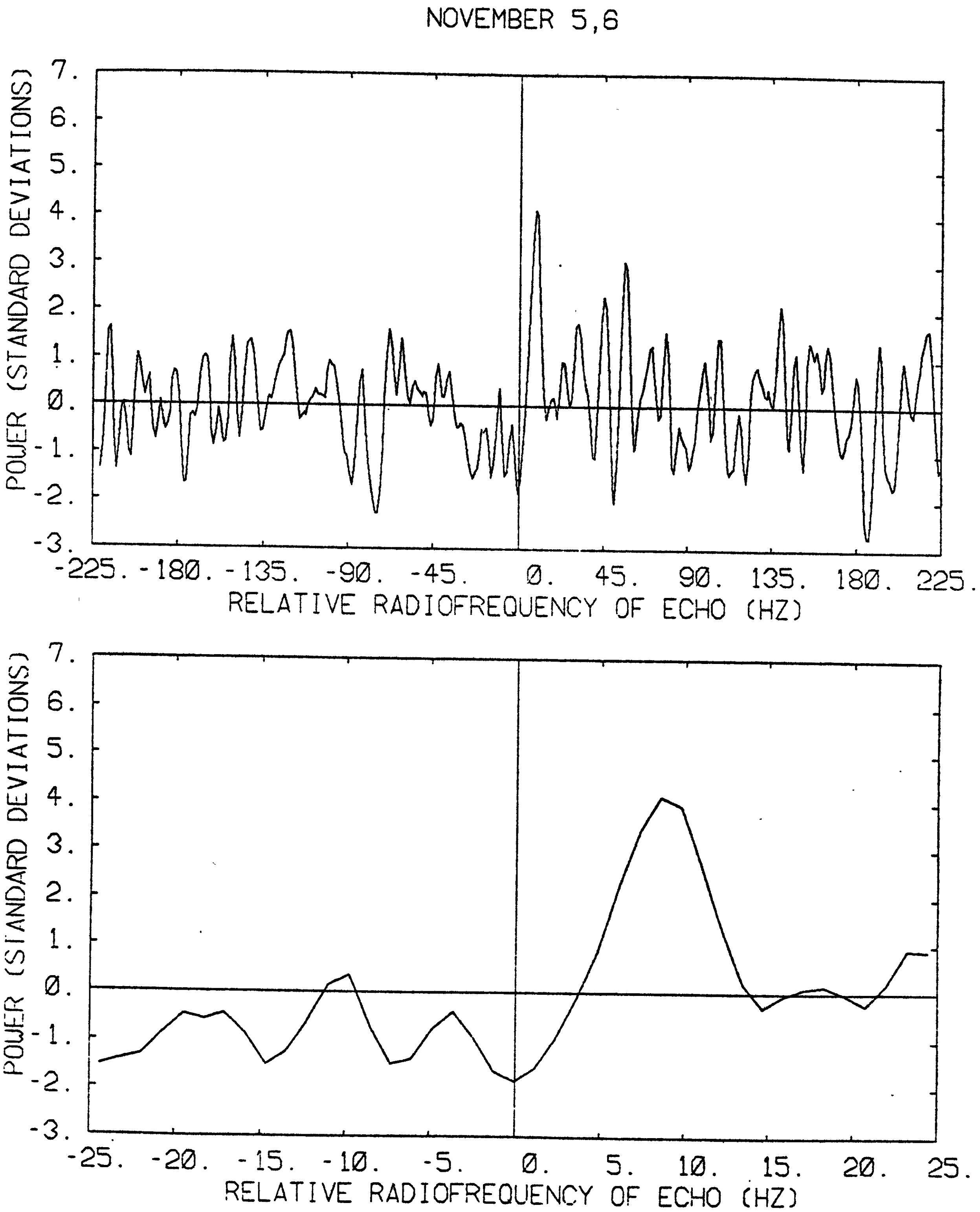
NOVEMBER 5,6
POWER (STANDARD DEVIATIONS)
7.
6.
5.
4.
3.
2.
1.
0.
-1.
-2.
-3.
-225.
-180.
-135.
-90.
-45.
0.
45.
90.
135.
180.
225.
RELATIVE RADIOFREQUENCY OF ECHO (HZ)
POWER (STANDARD DEVIATIONS)
7.
6.
5.
4.
3.
2.
1.
0.
-1.
-2.
-3.
-25.
-20.
-15.
-10.
-5.
0.
5.
10.
15.
20.
25.
RELATIVE RADIOFREQUENCY OF ECHO (HZ)

Fig. 10.13

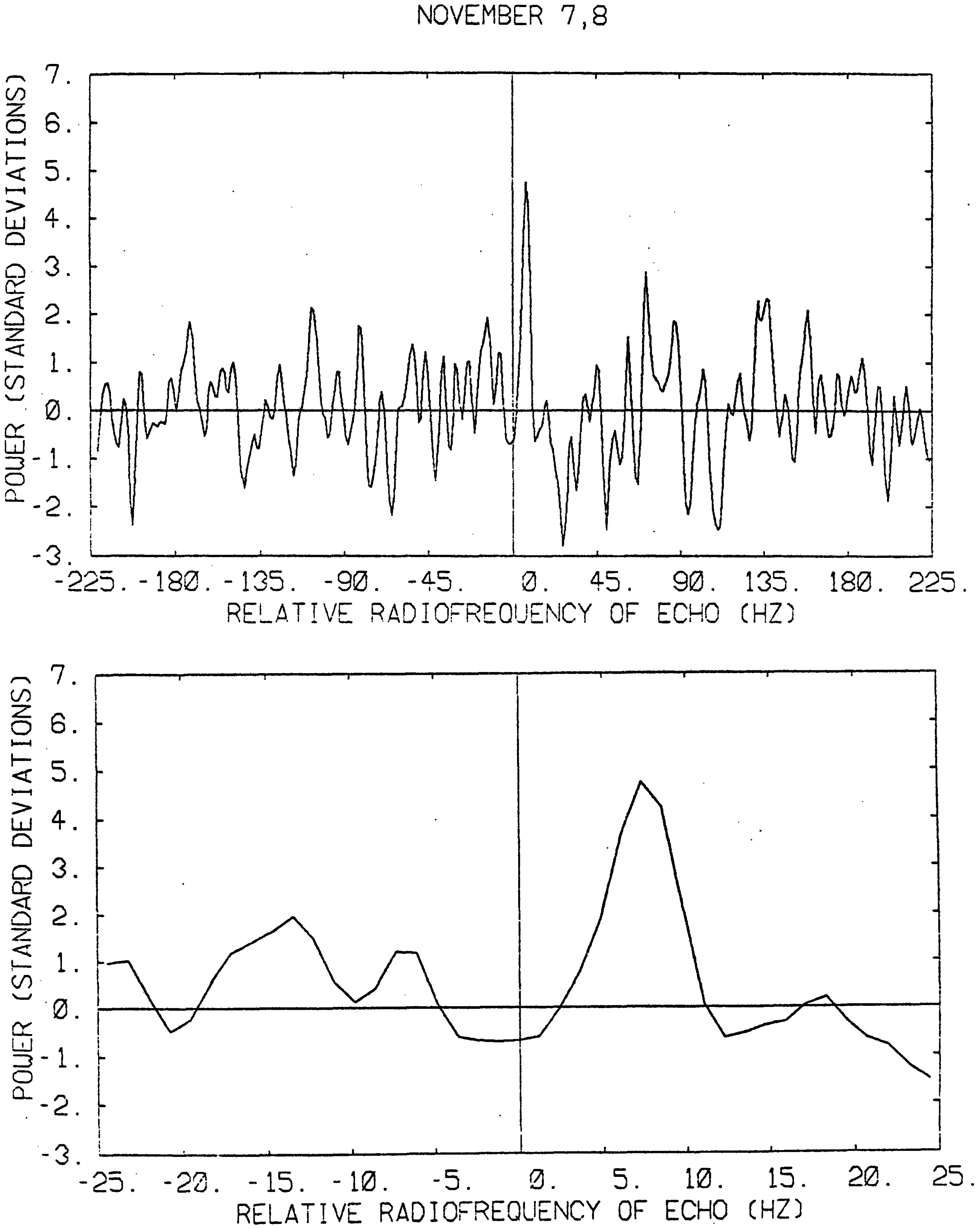

NOVEMBER 7,8

Fig. 10.14

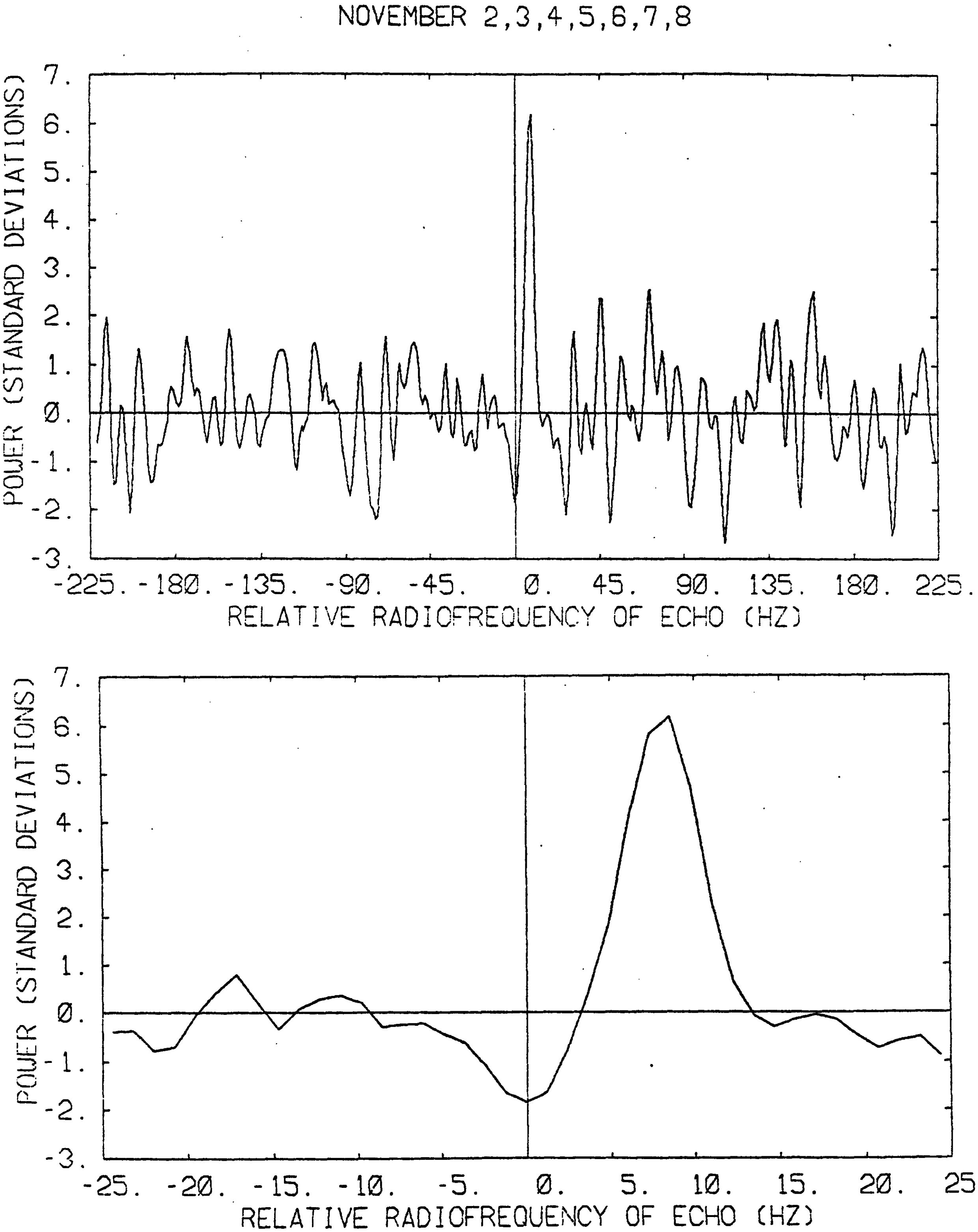
NOVEMBER 2,3,4,5,6,7,8
POWER (STANDARD DEVIATIONS)
7.
6.
5.
4.
3.
2.
1.
0.
-1.
-2.
-3.
-225.
-180.
-135.
-90.
-45.
0.
45.
90.
135.
180.
225.
RELATIVE RADIOFREQUENCY OF ECHO (HZ)
POWER (STANDARD DEVIATIONS)
7.
6.
5.
4.
3.
2.
1.
0.
-1.
-2.
-3.
-25.
-20.
-15.
-10.
-5.
0.
5.
10.
15.
20.
25
RELATIVE RADIOFREQUENCY OF ECHO (HZ)

Fig. 10.15

CHAPTER 11

INTERPRETATION

11.1 Size of the nucleus of P/Encke

For a spherical nucleus spinning with a period P_s, the radius R is related to the limb-to-limb bandwidth, B, by

$$R(P_s, \theta, B) = \frac{\lambda P_s B}{8\Pi \sin\theta} , \qquad (11.1)$$

where θ is the angle between the radar line of sight and the spin axis of the nucleus, and λ is the radar wavelength (12.6 cm). To determine θ, we first computed the cartesian ecliptic coordinates of the comet and of the Earth, using the elements of the orbit of the comet given in Section 2.1. Then, using the pole direction given by Whipple and Sekanina (1979), which we will refer to as paper (1), we obtained

$$\theta(t) = \mathrm{Arccos}\ \{ [x_c(t) - x_e(t)] \cos \Lambda \cos \beta + [y_c(t) - y_e(t)] \sin \Lambda \cos \beta + [z_c(t) - z_e(t)] \sin \beta / |CE(t)| \}, \qquad (11.2)$$

where $|CE(t)|$ is the distance from the comet to the Earth, and $\Lambda = 180°$ and $\beta = 2°$ are the longitude and latitude, respectively, of the pole in ecliptic coordinates (Paper 1 and Sekanina (1981), private comm.):

TABLE 11.1

Date (1980)	Angle (Spin Axis,Line of Sight) (Deg)	Phase Angle (S-C-E) (Deg)
Nov. 2	35	106
Nov. 5	28	114
Nov. 8	26	121

Using the same weighting as in the total spectrum for the sum of data from November 2 through 8, we find a weighted mean for the angle between the line of sight and the spin axis of the nucleus (see Table 11.1): $\theta_m \approx 28°$.

Although the formal standard errors for Λ and β are only about 1°, the values of these parameters are very model dependent. Considering other models leads to an estimate of 10° for the standard error for each parameter (Sekanina, personal communication, 1981). Using this, presumably more realistic, error leads to: $\theta_m \approx 28° \pm 11°$. Figure 11.1 demonstrates the sensitivity of the estimate of θ to the values used for Λ and β.

Paper 1 presents a detailed account of the determination of P_s and its associated uncertainty. From Table IV of paper 1, we conclude that $Ps \approx 6h20^m \pm 40^m$.

For such large uncertainties in θ_m and B, the assumption of linearity in the determination of the corresponding uncertainty associated with the estimate of R is not valid. The values of R for extreme values of P_s, B, and θ, in their respective range are given in Table 11.2.

TABLE 11.2

P_s hr mn	B Hz	θ °	R km
5 40	2.5	39	0.4
6 20	6.0	28	1.5
7 00	9.0	17	3.9

from which we deduce $R \simeq 1.5\text{km}^{+2.4\text{km}}_{-1.1\text{km}}$ for the "worst case" combination of errors. Figure 11.3 represents the sensitivity of the estimate of R to changes in θ and P_s (increment $\Delta P_s = 20^m$).

We can also estimate a range of values for the radius from the radar cross-section, assuming the scattering efficiency to lie between

0.04 and 1.

This is a reasonable assumption since this is the interval in which all the determinations for other bodies of the solar system fall. From the measured radar cross-section of 1.11 ± 0.55 km^2, we find:

$$0.4 \text{ km} < R < 3.6 \text{ km},$$

which is consistent with the range obtained from the Doppler broadening of the echo. For example, the mean value $R = 1.5$ km obtained from the Doppler broadening corresponds to a scattering efficiency of 0.15, which is an eminently reasonable value as compared to asteroids (Pettengill and Jurgens, 1979).

11.2 Implications for the physical properties of the nucleus

We can compare the range of values from the radar results against values obtained by other observers using optical techniques. Roemer (1966) has used estimates of "nuclear magnitude" for the comet at large heliocentric distances, obtained in 1957 and 1960 from plates where (presumably) little trace of the coma was recorded, to infer the radius of the nucleus. Using the relation established by Houziaux (1959):

$$m = m_{\odot} - 5[\log(R) - \log(r) - \log(\Delta)] - 2.5[\log(A) + \log(\phi(\theta))]$$

where $m_{\odot}$ is the magnitude of the sun ($\equiv -26.72$), A the geometric albedo, and ϕ the phase function according to Lambert's law, a lower limit of 0.6 km may be placed on the radius (for an assumed albedo of

0.7) and an upper limit of 3.5 km (for an albedo of 0.02). Our best estimate of 1.5 km for R corresponds to an albedo of 0.1 using Roemer's results. As can be seen in Table 11.3, most determinations seem compatible with such a value for the radius. Stauffer and Spinrad's photometry suggests a radius lower than 0.5 km unless the albedo is lower than 0.05. There is an incompatibility between these results and Roemer's, since in Roemer's estimation a radius of about 0.5 km would corresponds to an albedo much larger than 0.05. A way to attempt to resolve this contradiction would be to look at the orientation of the nucleus with respect to the observer during each one of the supporting observations. In particular the observations of Stauffer and Spinrad took place at the same period as the radar observations, that is while looking at the southern hemisphere of the nucleus (see figure 11.3, path of the subradar point on the nucleus, computed using the nucleus spin vector estimated by Whipple and Sekanina. During that period the subradar point was sweeping a range of cometocentric latitude going from approximately -60° to -65° while the subsolar point wandered between about +30° and +35°). The southern hemisphere has been recognized as being less active than the other and may well be blanketed by meteoroidal debris (paper 1). On the other hand the more active northern hemisphere may have a somewhat different albedo. Thus a comparison of the periods in which the observations took place and of the respective orientations of the nucleus is necessary to shed some light on this discrepancy. In any case, although most probably inhomogeneous, the surface of the nucleus seems quite dark, with an albedo of less than a few percent.

A density range of 1 to 2 gm/cm^3 and a radius in the range 0.5 km -

TABLE 11.3

Comet Encke: Radius and Albedo of the Nucleus

Radius (km)	Assumed Albedo	Reference: Method Used
0.6 - 3.5	0.7 - 0.02	Roemer (1966) Magnitudes at large heliocentric distances
1.3	0.2	Delsemme & Rud (1973): Magnitudes at large heliocentric distances and Water Vaporization rate
1.7	0.15	Kresak (1973): Magnitudes at large heliocentric distances and comet history (comments on this value by Sekanina (1976))
<1.5	----	Whipple & Sekanina (1979): Rate of mass loss from sublimation and rotation of nucleus
<0.5	>0.05	Stauffer & Spinrad (1981): Photometry of the red nuclear continuum
0.4 - 3.6	----	This work

3.6 km for a spherical nucleus leads to a mass M of the nucleus that lies between $5 \cdot 10^{14}$ and $4 \cdot 10^{17}$ g.

11.3 Limits on the number density of dust particles in the coma

As seen in section 1.2.2. the radar cross-section presented by a cloud of particles of radius a and dielectric constant ε_c is given by:

$$\sigma = 4N\pi a^2 \left(\frac{2\pi a}{\lambda}\right)^4 f(\varepsilon_c), \text{ where } f(\varepsilon_c) = \left|\frac{\varepsilon_c - 1}{\varepsilon_c + 2}\right|^2 \qquad (11.3)$$

and N is the number of particles lying in the beam. This expression assumes spherical particles. However, since spheres are less effective than particles of irregular shape in multiple scattering, this expression should yield a conservative upper limit to the number of particles actually present.

The radar signal-to-noise ratio is given by (see Appendix 1):

$$\mathrm{SNR} = \frac{P_t\, G^2\, \lambda^2}{4\pi\, (4\pi D^2)^2} \left(\frac{1}{k\, T_s}\right) (t/B)^{1/2}\, \sigma$$

For Encke we had:

$D = 0.33$ AU, $G \simeq 70.7$ dB, $P_t \simeq 370$ Kw,

$T_s \simeq 50°$ k and $t \simeq 17000$ sec.

so that $\mathrm{SNR} \simeq 1.3 \times 10^{-5}\, B^{-1/2}\, \sigma$

Using the above expressions for σ, we get:

$$\mathrm{SNR} = 10^3\, B^{-1/2}\, N\, a^6\, f(\varepsilon_c)$$

$$\text{and} \qquad N = 10^{-3}\, \mathrm{SNR}\, B^{1/2}\, a^{-6} / f(\varepsilon_c) \qquad (11.4)$$

a) Particle dielectric constant

From spectral observations of comets, it appears that the main components of cometary grains are ices and silicates. Laboratory studies of interplanetary dust particles or "Brownlee particles", collected from the stratosphere and from the sea floor, often show the presence of pyroxene, olivine, iron sulfide (FeS) and magnetite (Fe_3O_4), as well as non-crystalline carbonaceous material. Pyroxene and olivine are metallic silicates often encountered in meteorites. Pyroxene is characterized by a ratio of metal oxides (FeO, MgO) to SiO_2 of 1 to 1, while olivine is characterized by a 2 to 1 ratio. In particular, enstatite ($MgSiO_3$) is an Mg-rich pyroxene frequently encountered.

E. Ney (1982) has summarized the results of infrared observations of comets, and notes the presence of silicate signatures at wavelengths of 10 and 18 μm in a few comets, indicating the presence of small refractory grains in the coma. It has been shown in the laboratory that several amorphous silicates reproduce the 10-μm cometary feature, pyroxene and olivine being among the most common. Hanner (1980) has also shown that amorphous olivine gives a good fit to the observed 10- and 18-μm silicate features.

While olivine can be pure forsterite (Mg_2SiO_4) or pure fayalite (Fe_2SiO_4), it appears that in meteorites there is usually an equal mixture of the two minerals. Campbell and Ulrichs (1969) have measured the dielectric constants of some olivines, the basalt olivine being the one closest to the meteoritic composition. For this material, they found:

$$R(\varepsilon_c) \simeq 8.1 \text{ and } \tan\delta \simeq 0.05, \text{ which implies } f(\varepsilon_c) \simeq 0.5$$

Campins and Hanner (1982) have studied different models to account for the thermal emission from cometary dust. They find that the 4.8μm/3.5μm infrared flux ratios can be fitted with absorbing grains, for instance magnetite, which is present in matrices of carbonaceous chondrites. This material has a dielectric constant with high real and imaginary part (high conductivity), and yields a value of $f(\varepsilon_c)$ close to 1. Iron sulfide has a high dielectric constant, comparable to iron oxides and also yields a value of $f(\varepsilon_c)$ close to 1.

Finally, the case of ice grains has to be investigated. Water is known to be a major component of cometary nuclei but water ice grains have not been identified in comets (A'Hearn et al., 1981). The reason for the failure to detect ice in comets may be that ice is mixed with some other material. Indeed, Fink and Sill (1982) note that laboratory spectra of ices mixed with dark silicates show that the ice features are distinctly muted. Thus, we should consider both pure ice grains and ice mixed with silicates and iron compounds or ice coated dust grains. Also the presence of ices and their distribution in the coma are functions of the nature of the surface of the nucleus, since old, less active comets probably have surfaces depleted in volatiles compared with new, active comets. We should also expect variations as a function of the comet heliocentric distance. In particular, unless they are quite large or have a refractory core, icy grains would rapidly sublime at heliocentric distances smaller than about 2 AU. The comets considered in this work all had heliocentric distances in the range 0.7 AU to 1.3 AU at the time of observation, with, for comet Encke, values ranging from $r = 0.88$ AU on November 2, 1980 to $r = 0.75$ AU on November 8, 1980. This implies a small number, if any, of icy grains for this comet.

The dielectric parameters of ice have been given by Von Hippel (1954), and Westphal and Sils (1972): $\mathrm{Re}(\varepsilon_c) \simeq 3.2$, and $\tan\delta \simeq 9\ 10^{-4}$ at $T = 260$ K, so that $f(\varepsilon_c) \simeq 0.18$. For ice coated dust grains, one would expect values of $f(\varepsilon_c)$ intermediate between the values mentioned above.

b) Particle size distribution

As mentioned before, for a radar wavelength of 12.6 cm, we are most interested in the presence of millimeter- and centimeter-sized particles. In fact, there is an upper limit on the size of the particles which could be present in the coma, because of the conditions that such particles must satisfy in order to overcome gravity and be ejected from the nucleus. It is generally accepted that the forces which expel dust grains in the coma are due to outgassing from the nucleus. Assuming steady, radially symmetric outgassing, Wallis (1982) gives the equation of motion for the dust grains and the maximum radius a_{max} of grains that can escape from the nucleus, quoting results from Whipple (1951): $a_{max} = 3\mu Qu/2\rho MG$, where Q is the outflow rate of gas with mean molecular weight μ, u is the gas expansion velocity, ρ is the dust-grain bulk density and M is the mass of the nucleus. With typical values for these parameters, we obtain values for a_{max} of about 1 cm.

The best data available on the size distribution of dust particles in comets come from dynamical studies of dust tails (Sekanina and Miller, 1973) and anti-tails (Sekanina, 1974). Campins and Hanner (1982) have used the size distribution obtained for comet Bennett by Sekanina and Miller to model the infrared behavior of dust particles for different compositions. They find that this distribution can be used for other comets by a simple shift in mean particle size. This distribution predicts a variation in number density N approximately as $\underline{a}^{-4.2}$ for particles having radii larger than about 1μm (see also Sekanina and Schuster, 1978).

c) Grain velocity distribution, spectral width, signal-to-noise ratio

To estimate the spectral width to be used in the estimation of N, we must assume a velocity distribution for the dust grains. Wallis (1982) reviews models of dust grains dragged out by cometary gases and shows that a model treating the gas and dust as a two-phase degenerate gas is appropriate for active comets (e.g. Austin) but invalid for comets like Encke or Grigg-Skjellerup which have long gas-free paths. For the latter, a model intermediate between simple effusion and gas-dynamics would be more suitable.

First we must estimate the gas expansion velocity. The mean radial velocity is usually taken as some fraction of the thermal velocity associated with the nucleus temperature; in first approximation, assuming gas expansion with long free-paths, this fraction can be modeled as varying with the distance from the nucleus according to a Maxwellian distribution (Wallis, 1982). Wallis (1982), Huebner and Wiegert (1966) give:

$$v_{gas} = 0.5\ v_{th} \text{ with } v_{th} = (8kT/\pi m)^{1/2} \qquad (11.5)$$

Assuming the gas to be composed primarily of water molecules and the nucleus surface temperature to be of the order of 180 K (Delsemme and Miller, 1971), we get: $v_{gas} \simeq 250$ m/s.

From figures 1 and 2 of Wallis (1982) which give, respectively, the grain speeds in the simple effusion model and the acceleration of dust in supersonic flow in the gas-dynamics model, we can extract the necessary information related to the velocity of the grains in the coma to get a rough estimate of v_{dust}. For millimeter-sized grains $v_{dust}/v_{gas} \simeq 0.03$, yielding $v_{dust} = 7$ m/s, and for centimeter-sized grains

$v_{dust}/v_{gas} \simeq 0.005$, yielding: $v_{dust} = 1.5$ m/s.
We note that Wallis' curve has a singularity for centimeter-sized particles, so that the value extrapolated here should be used with caution.

These velocities are directed outwards from the nucleus assuming isotropic outgassing. Since the component of velocity along the radar line of sight is the important parameter in our case, we must consider the comet-Earth-Sun configuration. For simplicity, we will assume that only the sunlit hemisphere of the nucleus is outgassing and that there is a negligible lag angle between the direction of maximum outgassing and the comet-Sun direction. There are then two extreme cases of interest: at 0° and 90° phase angle.

The acceleration exerted by the radiation pressure, expressed in units of solar gravitational attraction is given by Sekanina (1976) as $1-\mu$:

$$1 - \mu = 0.585 \,.\, 10^{-4} \; Q_r \,/\, (a\,\rho) \qquad (11.6)$$

where Q_r is the scattering efficiency of the particle for radiation pressure, a the particle radius in cm, and ρ the particle density.

Taking $Q_r = 1$, a = 1 mm, and $\rho = 3$ g/cm^3 we get:

$1 - \mu \simeq 2 \times 10^{-4}$, so that the effect of solar radiation pressure is indeed very small, and we may neglect it.

In the 0° phase angle case, maximum outgassing is either directly toward or away from the observer and the radial velocity distribution is peaked at a frequency offset $B = 2v_r/\lambda$ with respect to the predicted center frequency f_o of the echo from the nucleus. In this case the dust echo spectrum should extend from f_o to $f_o + B$, peaking at $f_o + B$.

At 90° phase angle, the fastest particles are ejected toward the sun and contribute a peak in the echo spectrum centered at f_o. The slower particles ejected at 90° to the comet-Sun direction should not further broaden substantially the dust spectrum. In this case the dust spectrum bandwidth should be centered on the predicted frequency of the echo from the nucleus f_o and be $B = 4v_r/\lambda$ wide, where v_r is the largest particle radial velocity with respect to the observer (in this case it is equal to the ejection velocity). However the value for v_r should be smaller than that calculated above as v_{gas} because of the reduced thermal ejection velocities at 90° to the sun line.

In both cases we can take the values given above for v_{dust} as upper limits on the grain radial velocities and consider a flat spectrum extending over B as a worst case assumption. Thus, for mm-sized particles : $B = 220$ Hz, and for cm-sized particles : $B = 50$ Hz

A thorough treatment of this problem, of course, should involve the exact comet-Earth-Sun configuration, the rotation vector of the nucleus, the lag angle of the direction of maximum outgassing with respect to the Sun-comet direction, and the effect of the solar wind for each comet studied.

Since there is no suggestion of echo power broadened to the above extent, we conclude that dust particles do not contribute importantly to the observed echo. In the next section we discuss the applicable upper limits to the particles present which follow from this negative result.

d) Number density of dust grains

In this discussion we assume that there is no shadowing. Indeed the particles do not shadow each other if they have a mean separation $\underline{l}$ such that:

$$l > l_o \quad \text{with } l_o = (2\pi/\lambda)^{1/3} \cdot a^{4/3}$$

where a is the particle radius (Cuzzi and Pollack (1978), Brillouin (1949)). For $a = 1$ mm we have $l_o \simeq 0.4$ mm, and for $a = 1$ cm we have $l_o \simeq 0.8$ cm.

Now we can estimate an upper limit on the number of millimeter- and centimeter-sized grains in the coma for different compositions using equation (11.4) given before: $N = 10^{-3}\ \mathrm{SNR}\ B^{1/2}\ a^{-6} / f(\varepsilon_c)$, where we take SNR to have an upper limit of 5 for non-detection.

TABLE 11.4

Number of Particles in the Coma

	ice	olivine	magnetite (iron sulfide)
mm-sized	$4.5 \cdot 10^{17}$	$1.5 \cdot 10^{17}$	$7.5 \cdot 10^{16}$
cm-sized	$1.5 \cdot 10^{11}$	$6 \cdot 10^{10}$	$3 \cdot 10^{10}$

Assuming that the density is uniform within a coma of 1000 km radius, we find an upper limit on the number density of millimeter-sized particles of

$\rho_{max} = N/(\frac{4}{3}\pi R^3) \simeq 3\ 10^{-2}\ m^{-3}$; and for centimeter-sized particles we find $\rho_{max} \simeq 10^{-8}\ m^{-3}$.

We can compare these results with data obtained by Sekanina and Schuster (1978) for comet Encke, who have given the product of particle albedo and dust production rate as a function of time for the comet.

The mass-loss of dust for the pre-perihelion branch of the orbit prior to 15 days before perihelion is about $0.5\ 10^{10}$ / <p> grams, where <p> is the particle albedo. They state that the most likely value for <p> lies in the range 0.01-0.05.

Using these results with <p> = 0.03, we get a rough estimate of 10^{11} g as the mass of dust produced before the radar observations (about 30 days before perihelion). Assuming that this mass is in millimeter- or centimeter-sized particles of density $\rho = 3$ g/cm^3, we find an upper limit to the number of particles as $8 . 10^{12}$ for mm-size and $8 . 10^9$ for cm-size.

Our upper limit on millimeter-sized particles is much higher than this latter value while the value we obtained for centimeter-sized particles is in good agreement with the value deduced from Sekanina and Schuster's results. In any case, because of the assumptions made, these values should be taken as providing comfortable upper limits.

Figure Captions for Chapter 11.

Figure 11.1. Average angle θ_{avg} between radar line of sight and nucleus spin axis, over the period of the radar observations of comet Encke. This angle θ_{avg} is given in ordinate as a function of the celestial latitude of the nucleus rotation pole (abscissa) and of the celestial longitude of the rotation pole. Each curve corresponds to a different value of Λ, from 170° to 190°, in increments of 2°. The eleven curves from top to bottom correspond respectively to celestial longitudes of 170°, 172°, 174°, 176°, 178°, 190°, 180°, 188°, 182°, 186°, and 184°, i.e. for longitudes increasing from 170° to 184° the angle θ decreases and after reaching a minimum for $\Lambda \simeq 184°$, θ increases again for Λ higher than 184°.

Figure 11.2. Radius of the nucleus (assumed to be spherical) as a function of the angle between spin axis and line of sight (abscissa), and of the nucleus rotation period. The ten curves drawn from top to bottom correspond to values of the nucleus spin period decreasing from 8 hrs to 5 hrs by 20 minutes increments. The best estimate of P_s (6hr 20mn) corresponds to the sixth curve down from the top. These curves are plotted for a fixed value B = 6 Hz for the total limb-to-limb of the echo.

Figure 11.3. Path of the subradar point on the nucleus in

cometocentric coordinates, as a function of time, using the spin axis direction given by Whipple and Sekanina (1979). This shows that the radar was pointing toward the nucleus "southern hemisphere".

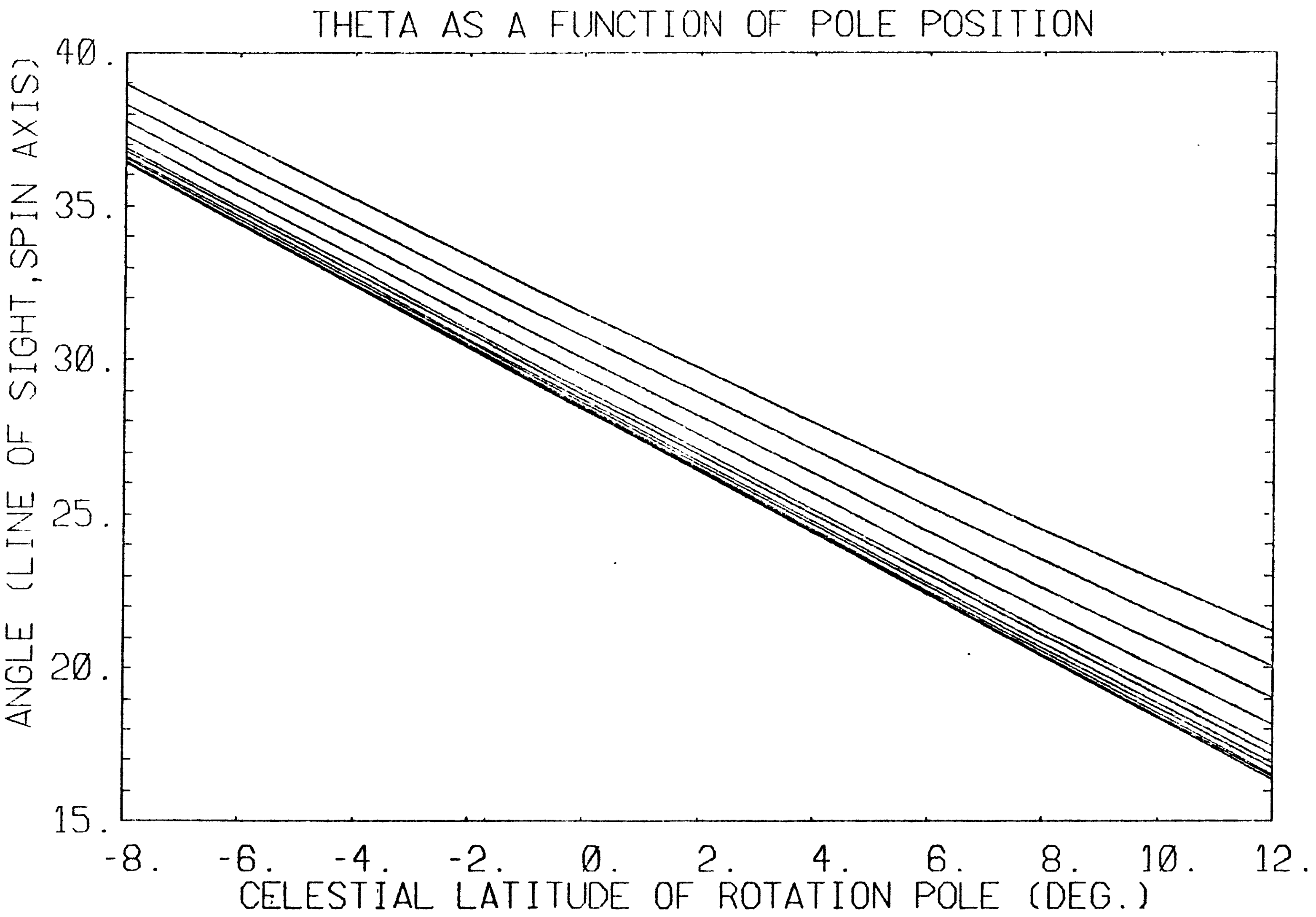
THETA AS A FUNCTION OF POLE POSITION
ANGLE (LINE OF SIGHT,SPIN AXIS)
40.
35.
30.
25.
20.
15.
-8.
-6.
-4.
-2.
0.
2.
4.
6.
8.
10.
12.
CELESTIAL LATITUDE OF ROTATION POLE (DEG.)

Fig. 11.1

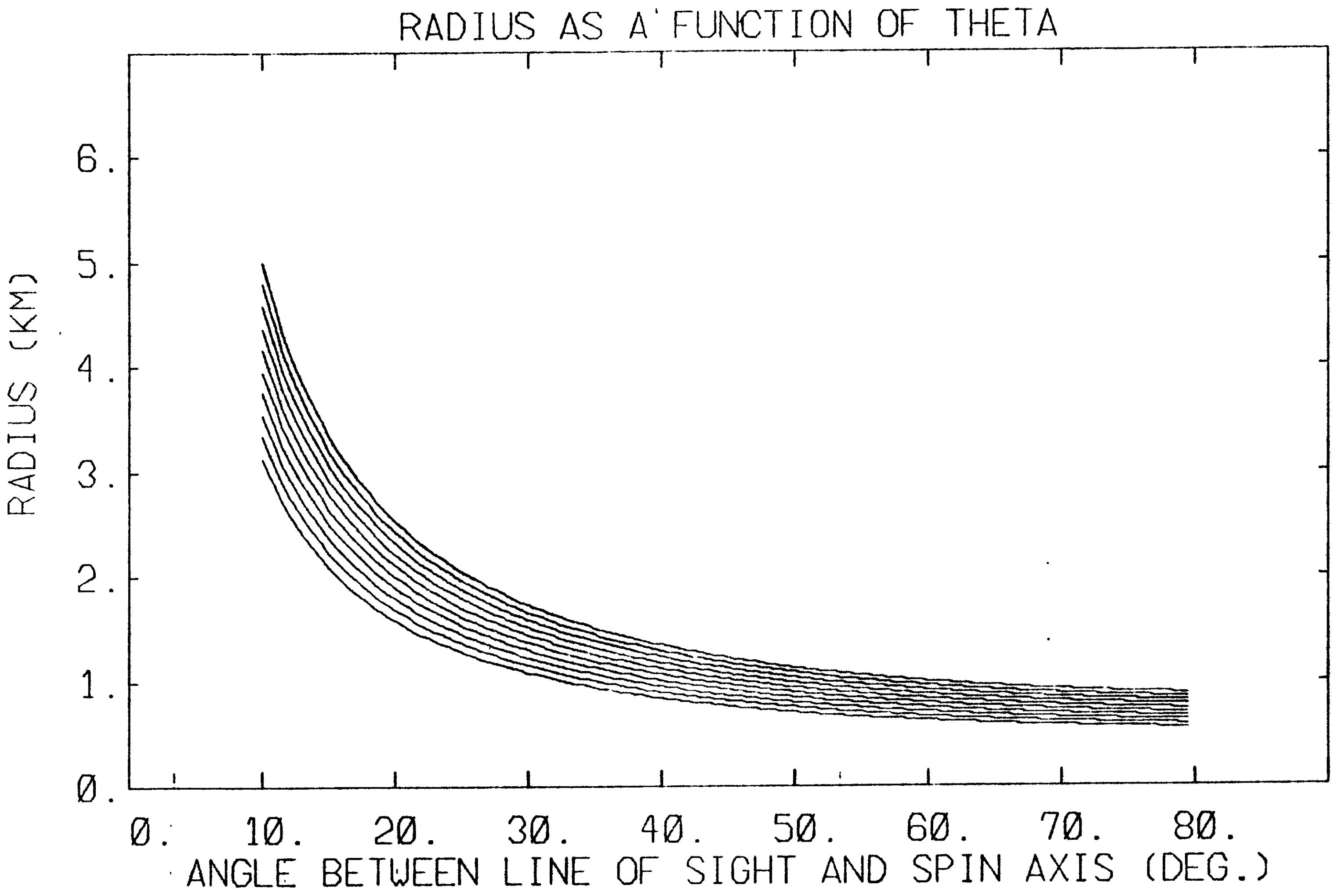
RADIUS AS A FUNCTION OF THETA
RADIUS (KM)
0.
1.
2.
3.
4.
5.
6.
0.
10.
20.
30.
40.
50.
60.
70.
80.
ANGLE BETWEEN LINE OF SIGHT AND SPIN AXIS (DEG.)

Fig. 11.2

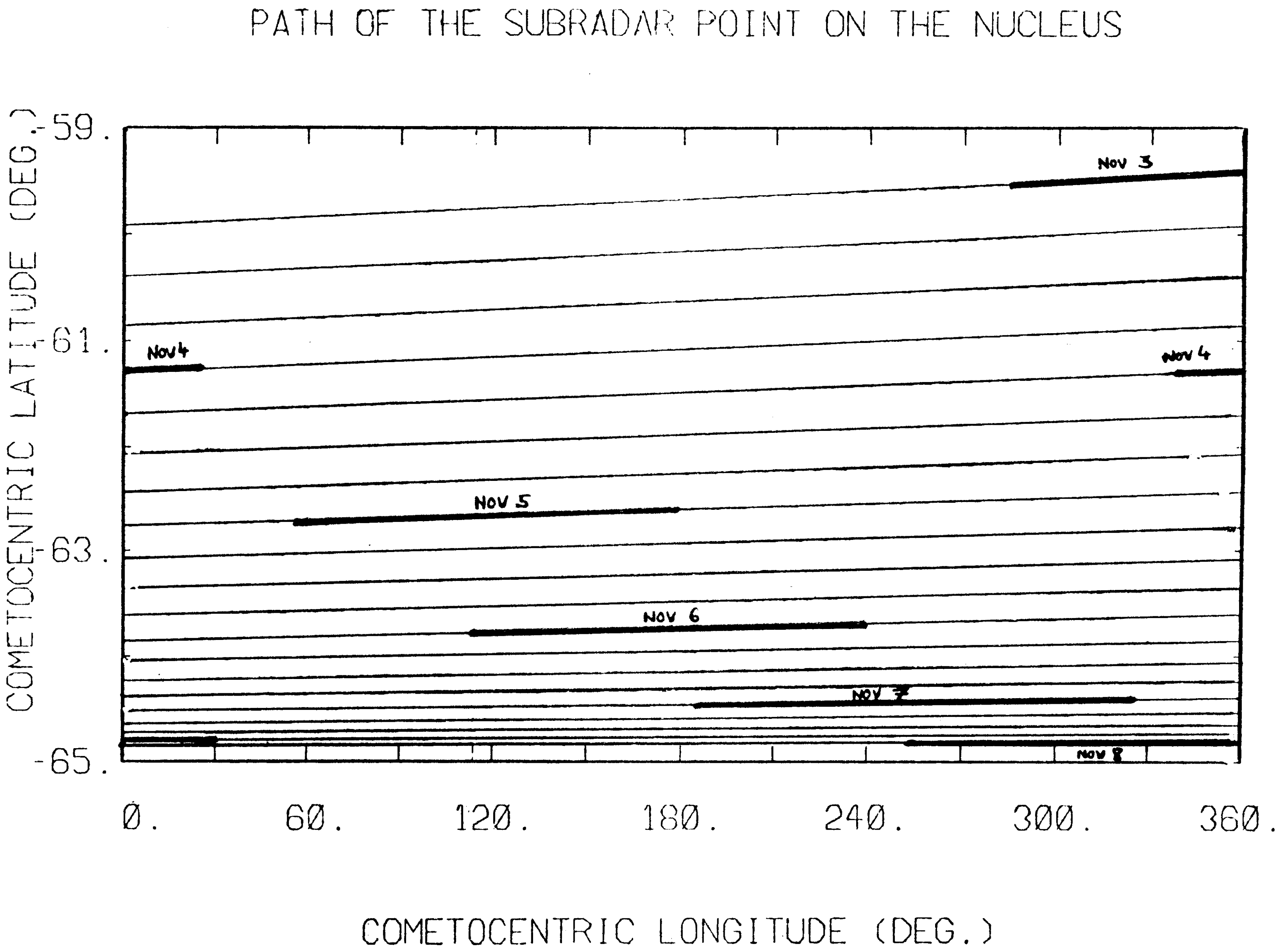
PATH OF THE SUBRADAR POINT ON THE NUCLEUS
COMETOCENTRIC LATITUDE (DEG.)
-59.
-61.
-63.
-65.
0.
60.
120.
180.
240.
300.
360.
COMETOCENTRIC LONGITUDE (DEG.)
Nov 3
Nov4
Nov 4
NOV 5
NOV 6
NOV 7
NOV 8

Fig. 11.3

PART G. COMET GRIGG-SKJELLERUP

DATA ANALYSIS AND INTERPRETATION

CHAPTER 12

COMET GRIGG-SKJELLERUP: DATA ANALYSIS AND INTERPRETATION

12.1. Center frequency and limb-to-limb bandwidth of the echo.

As can be seen in figure 6.12, the echo signal from the nucleus of P/Grigg-Skjellerup is unresolved. All the power received appears to fall inside a single frequency resolution cell having a width of about 1 Hz, and lying at a frequency offset of 4 Hz from the expected *a priori* center frequency of the echo. Such an offset is within the estimated uncertainty for the Doppler prediction. Optical astrometry carried out before, during and after the radar observations have been used by Irwin Shapiro and Antonia Forni to obtain an improved *a posteriori* orbit. Comparison of this with the *a priori* prediction ephemeris shows that the two ephemerides have a relative drift of the order of one Hertz over the 14-day observing interval, so that some smearing of the summed echo spectrum should have occurred. The fact that the observed echo seems to be located at precisely the same offset for every day of observation raises some concern over its reality. To dispel this concern, two tests have been performed, one at the time of the observations, the other during the data analysis. During the period of observation, simulation tests were carried out on May 25 and June 6, 1982, using exactly the same setup as for the normal comet observations, the only difference being that no transmissions were made. The results of a 1-hour integration on each of these two dates were negative, showing no sign of a spurious signal at the place where the echo was located under normal observing conditions.

The second test was carried out by processing the data in a manner different from that used normally. First we note that a spurious signal should not be expected to move across the received video bandwidth in synchronism with the four-frequency transmitted sequence (see Appendix 2 for details of the frequency-switching technique) as a real echo from the target should. Thus, we looked at the raw spectral data before shifting and superposing the contributions of the four spectral regions. The separate spectral regions corresponding to the transmission frequencies F_1, F_2, F_3 and F_4 (for the four days of observations May 20,21,23,24 only, for practical reasons) have each been combined separately to yield four sums S_1, S_2, S_3, and S_4. These four separate sums have been plotted as figures 12.1a,b,c,d. The presence of the echo in each of the four plots at the same offset with respect to the ephemeris center frequency is evidence for the reality of the echo. Thus we are overwhelmingly convinced that the echo is real.

Now, in order to explain the apparent lack of drift of the echo, we note that a drift of the echo as high as 1 Hz over the observing interval would not be detected if the echo were intrinsically very narrow and if its mean position were centered on the spectral element where the received power is observed to fall. In particular, we can deduce that, at least on the first and last days of observation, the echo bandwidth was probably less than about 0.2 Hz. We also note that a scattering law with a sharply varying angular response could yield an effective bandwidth comparable to the one observed while permitting the total bandwidth of the echo to be substantially larger. In the following discussion, a value of 0.5 Hz for the upper limit of the total (limb-to-limb) bandwidth of the echo is assumed.

Such a narrow spectrum could result from some combination of

- a very slow rotation of the nucleus
- a spin axis oriented nearly along the radar line of sight
- a very small nucleus.

We have seen above that the echo lies at a frequency offset of 4 Hz from its a priori center frequency. This information is useful for improving our knowledge of the comet's orbital motion, and may be stated as an inferred doppler measurement of

$$36969.2 \pm 0.5 \text{ Hz} \quad \text{at } 22^h{:}17^m \text{ UT on May 26, 1982,}$$

for a transmitted frequency of 2380 MHz.

12.2. Radar Cross-Section

12.2.1 Variation of the radar cross-section with time.

In figure 12.2 is shown the variation in measured radar cross-section with time, from May 20th to June 2nd, for those days on which the radar system was operating. Despite the large error bars, especially on the latter days, there appears to be a trend toward increasing radar cross-section between May 21 and May 29. Although the low signal-to-noise ratio prevents too strong an inference, we note that several factors could produce such an effect. Beside possible effects of a drift of the echo across the spectrum, the variation may result either from a change in geometric albedo, $\underline{p}$, or a change in the observed projected area S, as the target rotates. The radar geometric albedo $\underline{p}$ is defined as the ratio of the brightness of the target to that of a perfectly diffusing Lambert disc with an area equal to the projected area of the target. For a spherical target, we can write $\underline{p} = \sigma/4S$ where

σ is the radar cross-section and S is the projected area of the target (Campbell et al., 1977) .

We first discuss the variation in the projection of the comet spin axis along the radar line-of-sight over the observing interval. Then, using these results, we study the radar cross-section variation. First, assuming the target to be spherical, then assuming an irregular shape. Finally, we consider the effect of a drift of the echo across the spectrum.

12.2.1.1. Variation of the angle (spin axis,line-of-sight)

In a first step, we take a purely geometrical approach. We find that the angle between the two Earth-comet directions V_1 and V_2 defined at start ($V_1 = E_1C_1$) and end ($V_2 = E_2C_2$) of the total observing period is about 24°. This sets an upper limit of 24° on the variation of θ (angle between spin axis and line of sight) from the start to the end of the radar observations. We can also compute the minimum excursion in θ over this period and the corresponding spin axis direction, by simple geometrical considerations. In particular, if the line of sight, defined by a vector V is moving inside a fixed plane P during the observing period, then the minimal excursion in θ will be equal to zero, and will correspond to a spin axis direction defined by the vector U:

$$U = V_1 \times V_2,$$

i.e. U is normal to the plane P defined by V_1 and V_2. In fact, V does not usually move inside a fixed plane. However to estimate the minimum excursion in θ, we can first assume that U defines the spin axis. This yields an excursion of less than half a degree in θ, which is negligible for our purpose and which shows that V swept a surface having a very small curvature during the period of the radar observations.

Thus considering only geometrical aspects, we can say that over this period the change $\Delta\theta$ in the angle θ between the nucleus spin axis and the radar line of sight fell in the interval:

$$0^\circ < \Delta\theta < 24^\circ$$

although the 0° value (which would imply a spin axis normal to the radar line-of-sight) seems less likely because of the very narrow radar echo.

12.2.1.2 Assumption: spherical target

As a first step, we assume a spherical nucleus with areas of differing reflectivities on its surface. The projected area S is thus constant and equal to πR^2.

a) First extreme case: we assume a rotational pole-on configuration ($\theta = 0$) at the start or at the end of the observations.

As a result of the change in Earth-comet direction, the maximum change in θ is $\Delta\theta_{max} \simeq 24^\circ$. The maximum change in projected area between any two points in time during the observations will not exceed $\pi R^2 (1 - \text{Cos}\Delta\theta_{max})/2$ or about 4% of the total projected area.
Thus, in order to get a change in cross-section by a factor of 2, one would need a change in p by a factor of about 25, which is quite high. We conclude that if we have a sphere in a pole-on or nearly pole-on configuration, it is unlikely that a change in radar cross-section by a factor of 2 could result from nuclear rotation alone.

b) Second extreme case, $\theta = 90^\circ$.

In this case and with the assumption that the spin axis is defined by the vector U, as seen in 12.2.1.1., we have $\Delta\theta \simeq 0^\circ$, and the change in aspect due to a change in θ is negligible. Also, the effect of the change in the direction of the line-of-sight due to the Earth-comet relative motion is equivalent to a retrograde motion of the nucleus, of less than about 2° per day. This effect will thus add to an intrinsically retrograde rotation or subtract from it if the rotation is direct. In any case, this effect is small. Another small effect results from the daily change in the time of observation which amounts to about an hour between May 20 and June 2, 1982. For a spin period $P_s > 10$ hours, this is equivalent to an effective phase change of less than 2° per day. We are left, then, with the effect of the intrinsic spin itself as probably the most important consideration.

We assume that the sphere's surface has an overall homogeneous structure, except for a wedge of anomalous geometric albedo p_a, limited by two meridians, separated by an angle α ($\alpha < \pi/2$). We define a reference system (X,Y,Z) linked to the nucleus, where the X and Y axis define the equatorial plane, and the X axis represents the radar line-of-sight. We will call ϕ the angle between the X axis and the line which bisects the projection of the wedge in the equatorial plane: ϕ is the "longitude" of the center of the wedge. The area of the wedge is $2R^2\alpha$, and we will call S_1 the corresponding area projected in the plane normal to the line-of-sight (Y-Z plane). We will calculate S_1 for the two configurations possible, for which part of the wedge is in the visible hemisphere:

1. $\phi + \alpha/2 < \pi/2$ then $S_1 = \pi R^2 \operatorname{Cos}\phi \operatorname{Sin}\alpha/2$
2. $0 < \phi - \alpha/2 < \pi/2 < \phi + \alpha/2$ then $S_1 = \pi R^2 [1 - \operatorname{Sin}(\phi - \alpha/2)]/2$

For a variation of a factor of 2 in σ_{oc} to occur, due to the rotation of the target and the exposure of the zone of geometric albedo $\underline{p}_a$, one needs:

$$p_a S_1 + p_o (\pi R^2 - S_1) = 2 p_o \pi R^2,$$

i.e. $S_1/\pi R^2 = p_o/(p_a - p_o)$

Thus, we will need $\alpha > 7°$ if $p_a = 5\ p_o$, and $\alpha > 20°$ if $p_a = 2.5\ p_o$. So, we see that a narrow zone of anomalous scattering efficiency higher than twice the average value p_o can increase the radar cross-section by the necessary amount.

We now study the values of the spin period compatible with our observations. From examination of the radar cross-section curve (Figure 12.2), we consider a slow apparent rotation as a reasonable hypothesis. We thus assume that the observable rotation of the target amounts to $2\pi/n$ radians per day (whether this is an absolute rotational effect or apparent rotational effect resulting from near-commensurability of the rotation period to the interval between two short radar observations). We thus have: $\phi(t+1) = \phi(t) + 2\pi/n + 2\pi k$, where t is expressed in days. We neglect the effects of the motion of the target relative to the observer and we assume that on two consecutive days the observations are made 24 hours apart. Since $\phi(t) = 2\pi t/P_s + \phi_o$, where P_s is the nucleus spin period, we deduce: $P_s(\text{days}) = n/(1 + kn)$, with $|n| > 1$. We have $n < 0$ and $n > 0$ respectively for a direct and a retrograde apparent rotation.

* Case $n > 0$ (observed slow retrograde rotation):

This can be due to either (1).an intrinsically slow retrograde rotation with a spin period $P_s = n$ days, or (2).to a rapid direct rotation of period $P_s = n/(1 + nk)$, with $0 < k < 6$ since $P_{min} \simeq 0.17$ day.

* Case $n < 0$ (observed slow direct rotation):

This can be due to either (3).an intrinsically slow direct rotation of period $P_s = |n|$ days, or (4).to an intrinsically rapid retrograde rotation of period $P_s = |n/(k|n| - 1)|$ with $0 < k < 7$.

In cases (2) and (4) we have $P_s \approx 24$ hours, for n large and $k = 1$. From CCD observations, Steve Larson (Mt Lemmon Observatory) finds that most of the time, the near-nucleus region and the coma in general showed no structure. However, on June 19, 1982, he observed some near-nucleus jets and found evidence for a slow retrograde motion, with a nearly pole-on configuration. A slow retrograde rotation is compatible with the values of the non-gravitational parameters for this comet. He finds:

$$P_s = 80 \text{ hours} \pm 40 \text{ hours} \quad (3.3 \text{ days} \pm 1.6 \text{ days})$$

$$\text{and} \qquad -20° < \theta < +20° \text{ on June 19, 1982.}$$

Since the value of θ can change by as much as 50° between May 20 (beginning of the radar observations) and June 19, and by as much as 30° between June 2 (end of the radar observations) and June 19, it is possible to have a nearly pole-on configuration on June 19, and still have a value of θ of about 60° during the radar observations. We would then be in case (1) above and $P_s \approx 120$ hours would yield $n = 5$ and a rotation of about 70° per day.

On the other hand, using plates and drawings obtained at several appearances, Whipple (private comm.) finds that the observations are not inconsistent with a period of about one day (private communication), although the evidence is weak, partly because some observations were made at one-day intervals. This is compatible with the cases 2. and 4. above.

12.2.1.3 Assumption: target with irregular shape

Now we turn to the case where the target is not spherical and has a very irregular shape. Depending on the assumed value of the ratio of the maximum to the minimum projected areas, we can find a rotation vector which yields the desired variation in radar cross-section. In particular, for a low oblateness (nearly spherical shape), the orientation of the spin axis will be critical since the variation in p is then important, while for a high oblateness even a pole-on configuration could allow a variation in radar cross-section by a factor of 2, just because a substantial variation in projected area could be readily obtained either from intrinsic rotation or from a change in θ. For an oblateness of about 60% and a surface of constant albedo p for instance, σ_{oc} could change by a factor of 2, even with a nearly pole-on nucleus.

12.2.1.4 Effect of a frequency drift of the echo

An echo drift across the spectrum with time may imply a loss of power in the main spectral element considered for the evaluation of the cross-section. This power would fall in the adjacent spectral elements, although not always on the same side of the main element, and will be below detectability on each day of observation and when the total set of data is integrated. This effect may account for a substantial part of the variation in σ_{oc} and is likely to have occurred as suggested by the comparison between the *a priori* and the *a posteriori* ephemerides mentioned above.

We thus retain three effects as possibly causing a variation in radar cross-section by a factor of two during the 14 days of observation:

- Rotation of the nucleus, with θ larger than about 60°, and a variation in albedo by more than a factor of 2 over the surface
- Oblateness larger than 60% for a nucleus with a uniform surface
- Drift of the echo across the spectrum

12.2.2 Average radar cross-section

The echo power received in the O.C. sense, summed over all days, shows a signal-to-noise ratio of about 9.7 σ_{rms}, where the radar cross-section equivalent of the rms fluctuations σ_{rms} in received noise power is equivalent to 5.2×10^{-2} km^2. For the corresponding S.C. data we find σ_{rms} to be equal to about 4.8×10^{-2} km^2.

To calculate the radar cross-section in the O.C. sense, we consider only the single spectral element containing significant echo power. The average radar cross-section in the O.C. sense is thus:

$$\sigma_{o.c.} \simeq 0.50 \text{ km}^2$$

with an uncertainty of ±0.13 km^2 calculated as in section 10.3.

No echo was detected in the S.C. sense, so only an upper limit can be set on $\sigma_{s.c.}$. Assuming that the integrated power received in this sense is less than 3 standard deviations, we get

$$\sigma_{s.c.} < 0.15 \text{ km}^2,$$

for the radar cross-section in the S.C. sense.

By considering the lower bound on $\sigma_{o.c.}$ and the upper bound on $\sigma_{s.c.}$, we can put a conservative upper limit on the circular polarization ratio $\mu_c = \sigma_{s.c.}/\sigma_{o.c.}$: $\mu_c < 0.4$

Such an upper limit is not compatible with a pure solid ice surface for the nucleus, because such a surface would yield substantially more internal reflections.

12.3. Size of the Nucleus

12.3.1. Estimation from the radar cross-section.

It is possible to constrain the normalized O.C. radar cross-section ($A = \sigma_{o.c.}/S$, where S is the geometric cross-section πR^2) to a reasonable range, considering past observations of the planets and asteroids.

Using the range $0.04 < A < 1.0$, and using the value obtained above for the radar cross-section, we obtain a mean radius for the target assumed to be a roughly spherical body:

$0.4 \text{ km} < R < 2.2 \text{ km}$

In particular, for a value $A = 0.1$ we obtain $R \approx 1.3$ km.

12.3.2. Doppler broadening

We define R as the mean of the distances from the spin axis to the two limbs of extreme doppler; thus R will be equal to the radius for a perfectly spherical target. R is related to the total bandwidth B of the echo and to the nucleus spin parameters in the following way:

$$R=\frac{\lambda B P_s}{8\pi \sin\theta} \tag{12.1}$$

where λ is the radar wavelength (12.6 cm), P_s the nucleus spin period and θ the angle between the spin axis and the radar line of sight.

The direction of the spin axis has been estimated by Sekanina (private communication, 1982) using a set of plates obtained during earlier appearances of the comet. Tentatively, he finds a value $I \approx 100°$ for the obliquity of the orbital plane to the nucleus equator and a value $\Phi \approx 70°$ for the angle measured along the orbit plane from the ascending node on the equator to the subsolar point at perihelion. The conversion of these values into celestial coordinates yields an ecliptic longitude $\Lambda \approx 47°$ and a latitude $\beta \approx -16°$ for the rotational north pole. Using these values gives a variation of θ from about 90° on May 20 to about 70° on June 2, 1982, and 50° on June 19, 1982, i.e. the spin axis should have been almost normal to the line of sight during the radar observations.

On the other hand, we have seen earlier that Larson, using CCD images obtained on June 19, 1982 at Mount Lemmon Observatory, finds that the appearance of the near-nucleus jets present on his exposures are consistent with a nearly pole-on configuration, within ± 20°. Thus the preliminary results obtained by Sekanina seem incompatible with those obtained by Larson. More work, in particular further detailed optical observations, will be needed at the next appearance of this comet.

We have seen in 12.2.1.1. that the change in θ fell in the interval $[0°,24°]$ while the lower limit seems less likely. On the other hand, a high value of 24° could in fact yield a drastic change in echo bandwidth over the period of observation if θ is close to 0° at the start or at the end of the observing period. Indeed the value of $\text{Sin}\theta$ could in this case vary from 0. to 0.4.

Concerning the rotation period of the nucleus, we have seen that only two separate estimations of P_s have been made from optical observations (Whipple (private comm.), Larson (1982)). Unfortunately, these values are very model dependent and have large error bars.

Using the radar results however, we may constrain the quantity $P_s/\text{Sin}\theta$. From equation (12.1), using $B < 0.5$ Hz and $R > 0.4$ km, we find: $P_s/\text{Sin}\theta > 2$ days. Further optical observations would obviously be useful at the next appearance of this comet to permit separation of P_s and θ.

A table of the values of R (km) is given below for B = 0.5 Hz and for a few values of P_s and θ (Table 12.1).

The radius obtained from the radar cross-section is less model-dependent and seems the more significant, in view of the large uncertainties in P_s and θ.

In summary, a value for R of about one kilometer seems a reasonable choice, compatible with both analyses.

TABLE 12.1

RADIUS AS A FUNCTION OF P_s AND θ

		θ (Degrees)		
	R	10	50	90
P_s (Days)	2	2.4	0.6	0.4
	4	4.8	1.2	0.8

12.4. Limits on the number density of dust particles in the coma.

Following the analysis carried out in section 11.3, and considering the radar system parameters valid for the Grigg-Skjellerup observations, we can estimate an upper limit on the number density of millimeter-sized dust grains in the coma. Using the same analysis as detailed in section 11.3, we find for comet Grigg-Skjellerup upper limits on the number of grains in the coma:

TABLE 12.2

Size	ice	olivine	magnetite iron sulfide
mm	$3 \cdot 10^{17}$	$1.2 \cdot 10^{17}$	$6 \cdot 10^{16}$
cm	10^{11}	$4.5 \cdot 10^{10}$	$2 \cdot 10^{10}$

These values are of the same order as those found for Encke because the observing conditions were very similar.

Figure Captions for Chapter 12.

Figure 12.1.a through 12.1.d. Individual summations of the power received for each of the four transmitted frequencies. The presence of a signal corresponding to the echo in these four plots is strong evidence for the real (non-spurious) nature of the echo observed. The abscissa represents the spectral element numbers, from 1 to 370.

Figure 12.2. Variations of the radar cross-section presented by the nucleus of the comet Grigg-Skjellerup as a function of time. The errors bars correspond to ±1 standard deviation.

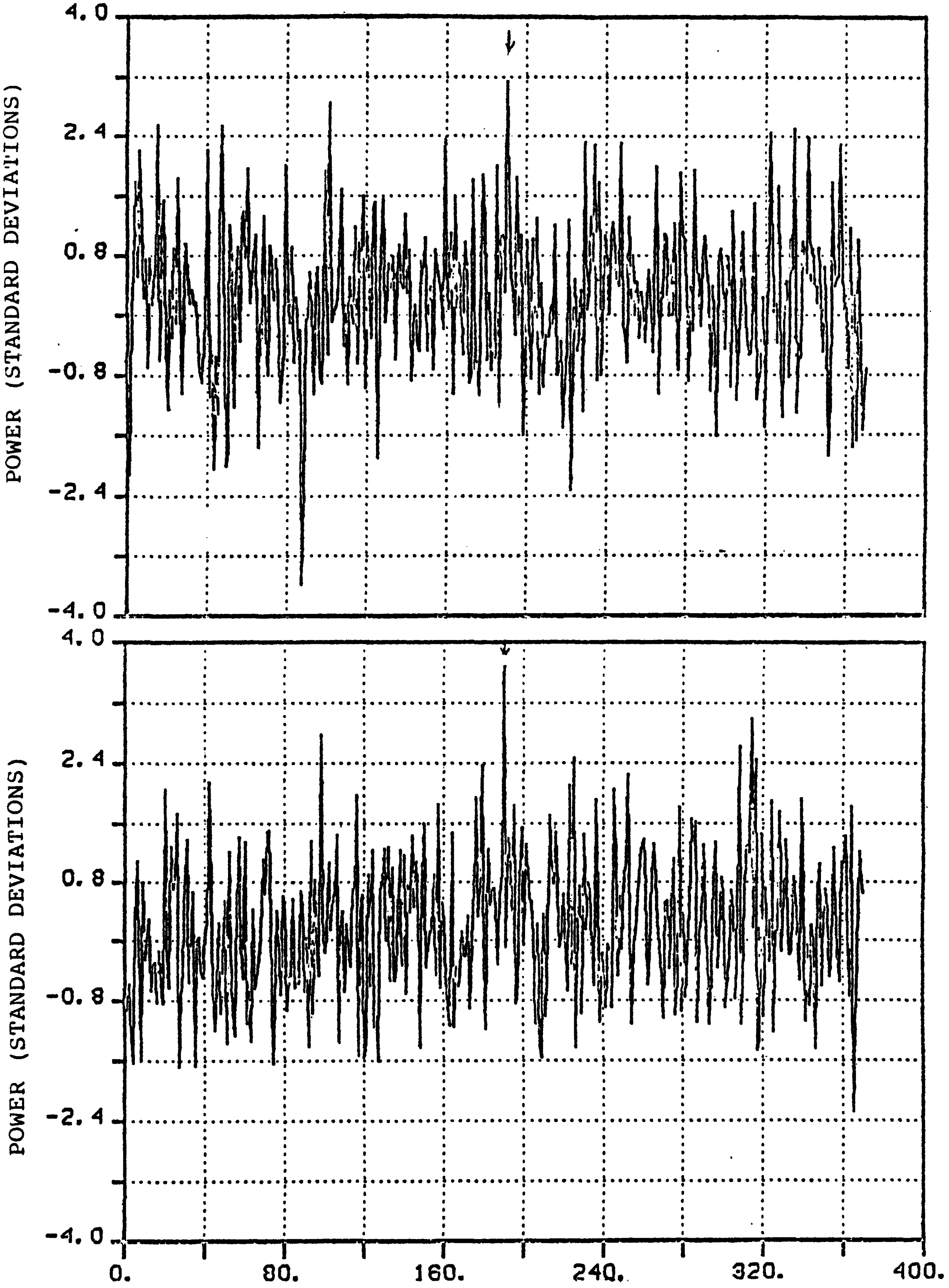

FREQUENCY (SPECTRAL ELEMENT #)

Fig. 12.1a (top) and 12.1b (bottom)

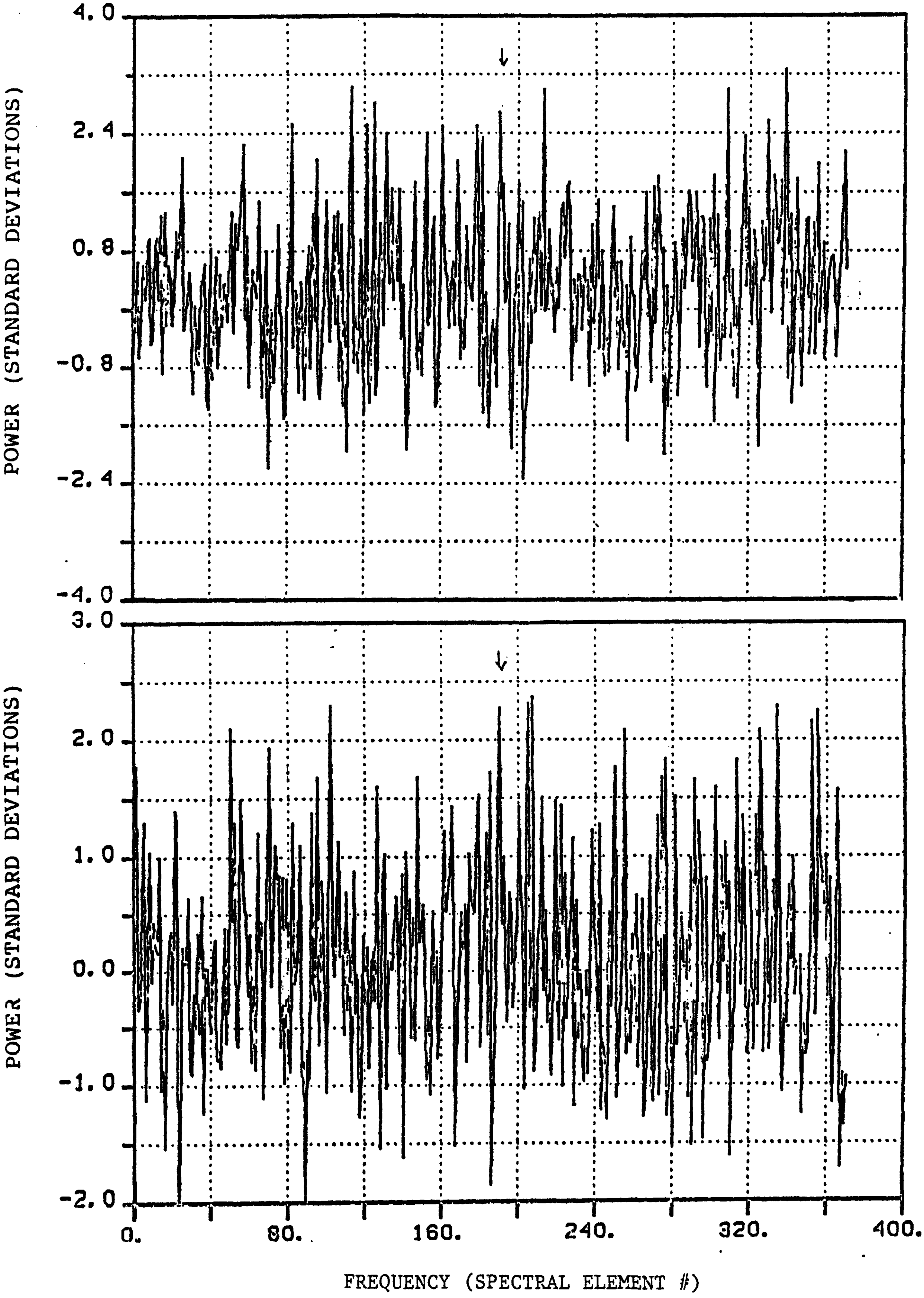

Fig. 12.1c (top) and 12.1d (bottom)

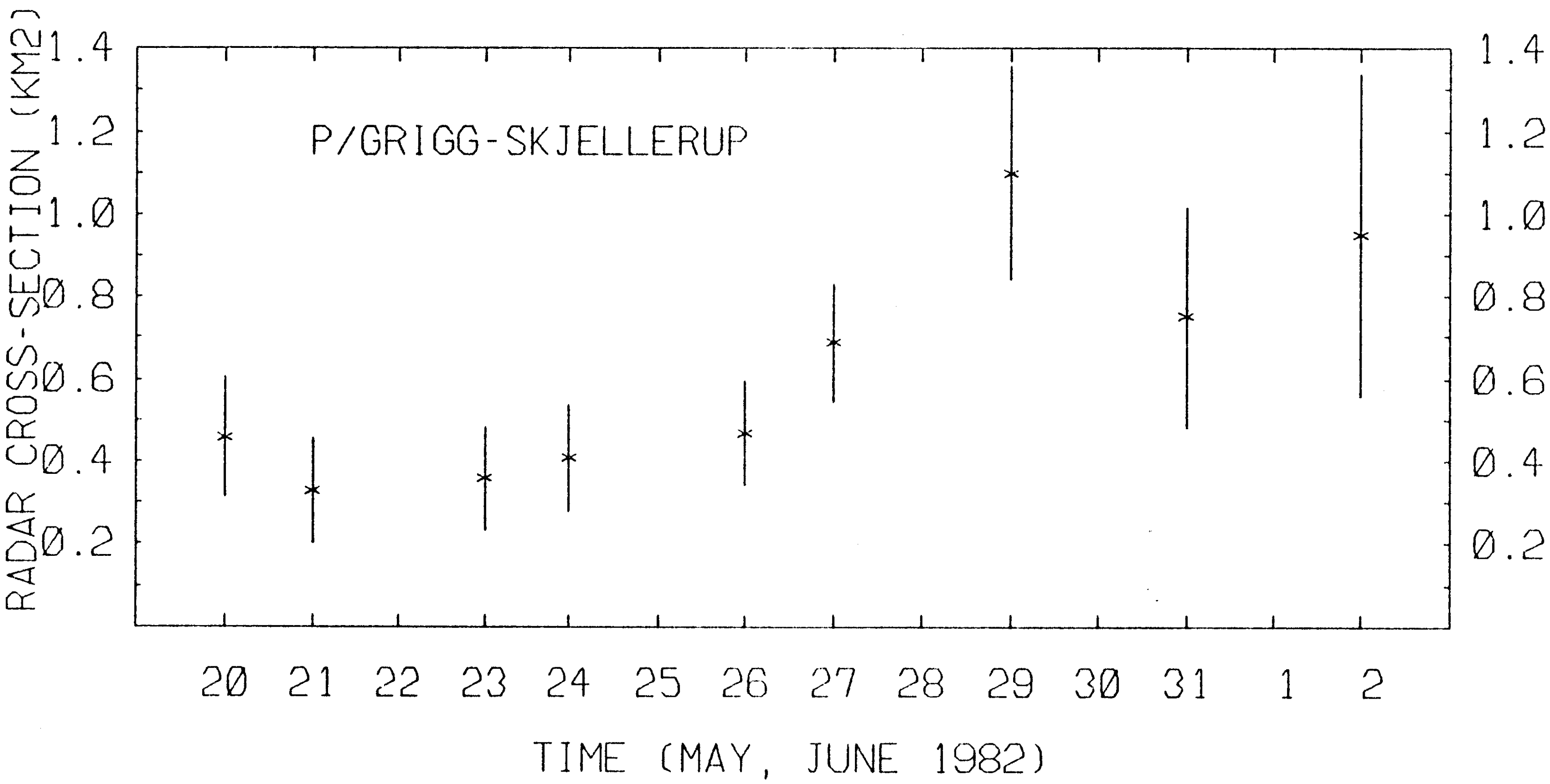
P/GRIGG-SKJELLERUP
RADAR CROSS-SECTION (KM2)
1.4
1.2
1.0
0.8
0.6
0.4
0.2
20
21
22
23
24
25
26
27
28
29
30
31
1
2
TIME (MAY, JUNE 1982)

Fig. 12.2

PART H. COMET AUSTIN AND COMET CHURYUMOV-GERASIMENKO

DATA ANALYSIS AND INTERPRETATION

CHAPTER 13

COMET AUSTIN: DATA ANALYSIS AND INTERPRETATION

13.1 Cross-correlation

The plots of the weighted sum of the data for comet Austin obtained on separate days have been given in chapter 7. Those spectra have been smoothed with various filters, using various values for the scattering exponent n and the effective filter bandwidth EFB. Figures 13.1 through 13.6 show the corresponding plots for n = 1 and EFB = 3.5 Hz, respectively, for the single days August 8, 9, 10, 11, 12 and the combination 8, 9, 10, and 11. It is clear from these plots that although there are values of the signal-to-noise ratio close to 3 standard deviations, there is no certain evidence for an echo from the nucleus of comet Austin. A value close to 4 standard deviations at -25 Hz is apparent in the final smoothed spectrum. The echo power is tabulated in Table 13.1 for the corresponding region of the total unsmoothed spectrum (August 8, 9, 10 and 11).

TABLE 13.1

TABULATED ECHO POWER

(Spectral region of highest signal-to-noise ratio)

Echo Power (Standard Deviations)							
-0.23	0.81	1.06	2.14	2.88	1.22	-0.06	0.37

The fact that, from examination of the data of individual days, this "peak" seems due in large part to the contribution of the August 11 data, considered along with its 13 Hz offset from the expected location of the echo according to the latest ephemeris, do not argue in favor of a detection.

13.2 Upper limits on the radar cross-section and size of the target

In the absence of a detectable echo, we can place an upper limit of about 3 standard deviations on the maximum signal-to-noise ratio per spectral element. Assuming the target has a limb-to-limb bandwidth B and a scattering law with a scattering exponent $n = 1$, we can obtain an upper limit for the target radar cross-section:

$$\sigma_{max}^{2} = \sum_{i=-m}^{m} [\, 3 \, (1 - (2f_i/B)^2)^{n/2}]^2 \, \sigma_{rms}^{2} \qquad (13.1)$$

$$\text{or} \quad \sigma_{max} = 3 \, \sigma_{rms} \, S \quad \text{where} \quad S = [\sum_{i=-m}^{m} (1 - (2f_i/B)^2)]^{1/2}$$

where $m = [B/2]$ (m is the largest integer inferior or equal to $B/2$), $f_i = i$ and σ_{rms} is the standard deviation of the noise fluctuations per spectral element, expressed in km^2. We have $\sigma_{rms} = 0.06$ km^2 for comet Austin, both for the O.C. and S.C. components. Assuming a lower limit of 0.04 on the scattering efficiency A of the target (which corresponds to a radar geometric albedo of 0.01), we get:

$$R_{max} = [\, \sigma_{max} \, / \, 0.04\pi]^{1/2} \qquad (13.2)$$

A plot of R_{max} as a function of B is given in figure 13.7.

On the other hand, the parameter B is itself a function of the target's size. In order to get an absolute upper limit on B, and thus on σ_{max}, we will use the following considerations: for any given value B of the limb-to-limb bandwidth of the echo, there exists a minimum compatible value of the target radius:

$$R_{min} = \lambda B P_{min} \, / \, 8\pi \mathrm{Sin}\theta_{max} \qquad (13.3)$$

where P_{min} is the shortest spin period compatible with the gravitational stability of the nucleus ($P_{min} \approx 4$ hrs, Whipple (1982), Wyckoff (1982)), and θ_{max} is equal to 90°. A plot of R_{min} as a function of B is given in figure 13.7. Any physically possible value of B should then satisfy the inequality:

$$R_{min} < R_{max}$$

thus let us find B such that $R_{min} = R_{max}$, i.e. such that

$$\lambda B P_{min} / 8\pi \; - \; [\, \sigma_{max} / 0.04\pi]^{1/2} = 0 \qquad (13.4)$$

Since $f_i = i$, S can be written:

$$S = [\sum_{-m}^{m} (1 - (2i/B)^2)]^{1/2} = [(2m+1) - (4\sum_{-m}^{m} i^2 / B^2)]^{1/2}$$

$$= [(2m+1) - (8m(m+1)(2m+1)/6B^2)]^{1/2}$$

so that equation (13.4) becomes:

$$3639 \; 10^{-6} \; B_{max}{}^2 - [(2m+1) - (8m(m+1)(2m+1)/6B_{max}{}^2)]^{1/2} = 0$$

Solving for B_{max}, we get:

$$B_{max} \approx 37 \text{ Hz}, \qquad \text{which yields} \qquad R_{max} \approx 2.7 \text{ km}$$

Note that if we increase the assumed spin period from its absolute lower limit of 4 hours to a value of 8 hours, which is relatively low for comets, we get $B_{max} \approx 23$ Hz and $R_{max} \approx 2.4$ km. A value of 0.1 instead of 0.04 for the scattering efficiency would further lower the upper limit on the radius to $R_{max} \approx 2.0$ km. Thus since larger values for P, A, and a value for θ lower than 90° are much more likely than the absolute limits set earlier, we consider a value of 2 km a very reasonable upper limit on the radius of the nucleus.

13.3 Upper limit on the number of grains in the coma.

Here we use the method described in section 11.3 to study the number of millimeter- and centimeter-sized grains in the coma of comet

Austin.

We have here:

$D \simeq 0.326$ AU $G \simeq 71.5$ dB $P_t \simeq 310$ kW

$T_s \simeq 42$ K $t \simeq 11000$ sec $k \simeq 1.38\ 10^{-23}$ J/K

and we obtain values close to the values given for Grigg-Skjellerup (see section 12.4).

It should be noted that in the case of comet Austin, more and larger icy grains should be expected than in the other comets studied here. Indeed, in new comets the grains which form the icy grain halo are relatively large (centimeter-sized), would not be vaporized significantly in the acceleration region (Gibson and Hobbs, 1981), and could fill relatively large volumes (diameters of the order of 1000 km).

Figure captions for chapter 13.

Figure 13.1. Plot of the weighted sum of the data for August 8 smoothed with a filter of parameters n = 1 and EFB = 3.5 Hz.

Figure 13.2. through 13.5. Plot of the smoothed data as above, for the individual days August 9, 10, 11, and 12.

Figure 13.6. August 8, 9, 10, and 11. Smoothed data. The 4 peak at -25 Hz is mostly due to the contribution of August 11, and this reduces its credibility; furthermore, the corresponding frequency is not the one expected for an echo from the target. We thus feel that there is no evidence for a detectable echo from the target.

Figure 13.7. Extremal limits on the value of the radius of the nucleus of comet Austin, and resulting absolute upper limit on the target total bandwidth and size.

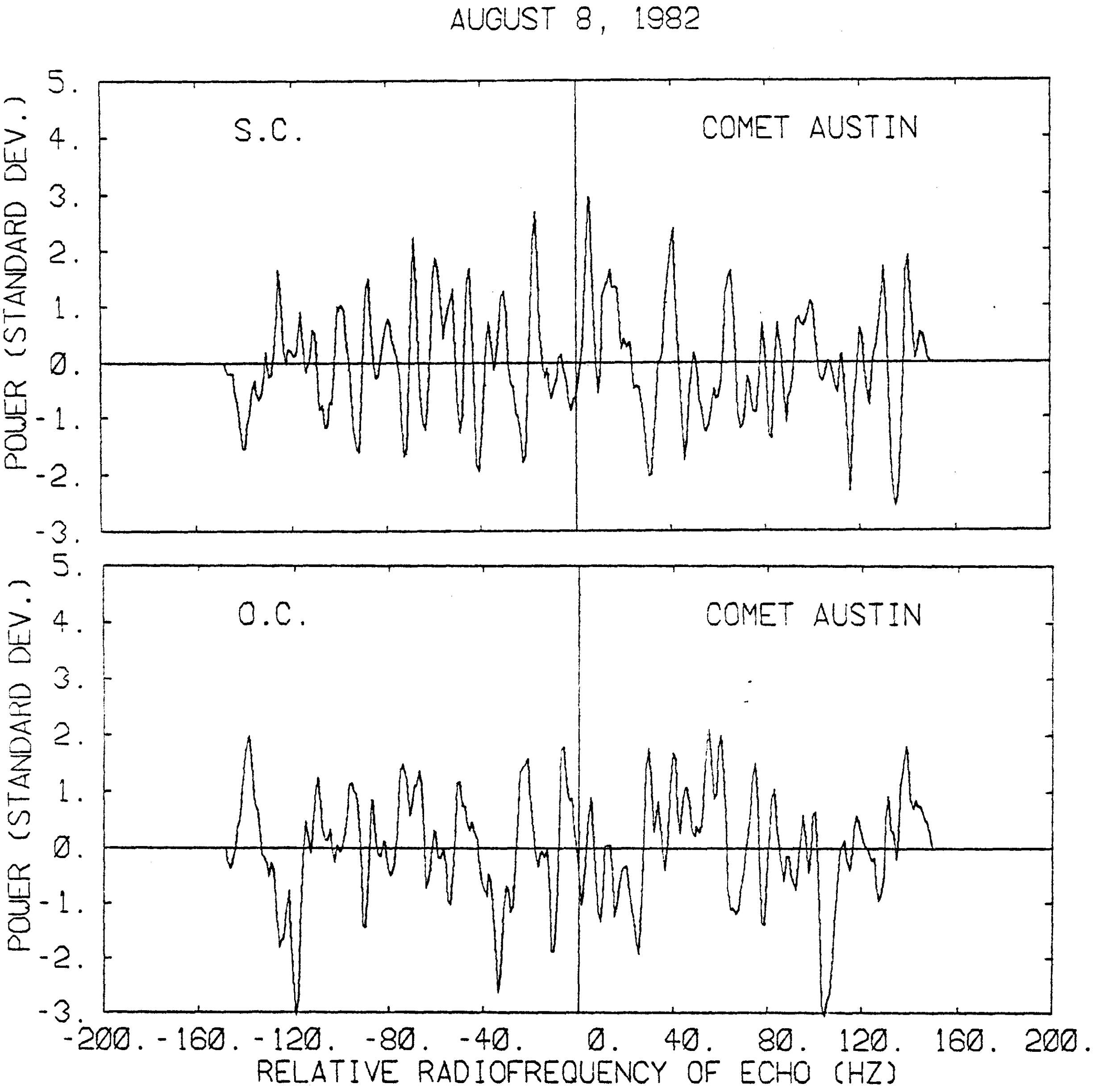
AUGUST 8, 1982
S.C.
COMET AUSTIN
O.C.
COMET AUSTIN
POWER (STANDARD DEV.)
5.
4.
3.
2.
1.
0.
-1.
-2.
-3.
-200.
-160.
-120.
-80.
-40.
0.
40.
80.
120.
160.
200.
RELATIVE RADIOFREQUENCY OF ECHO (HZ)

Fig. 13.1

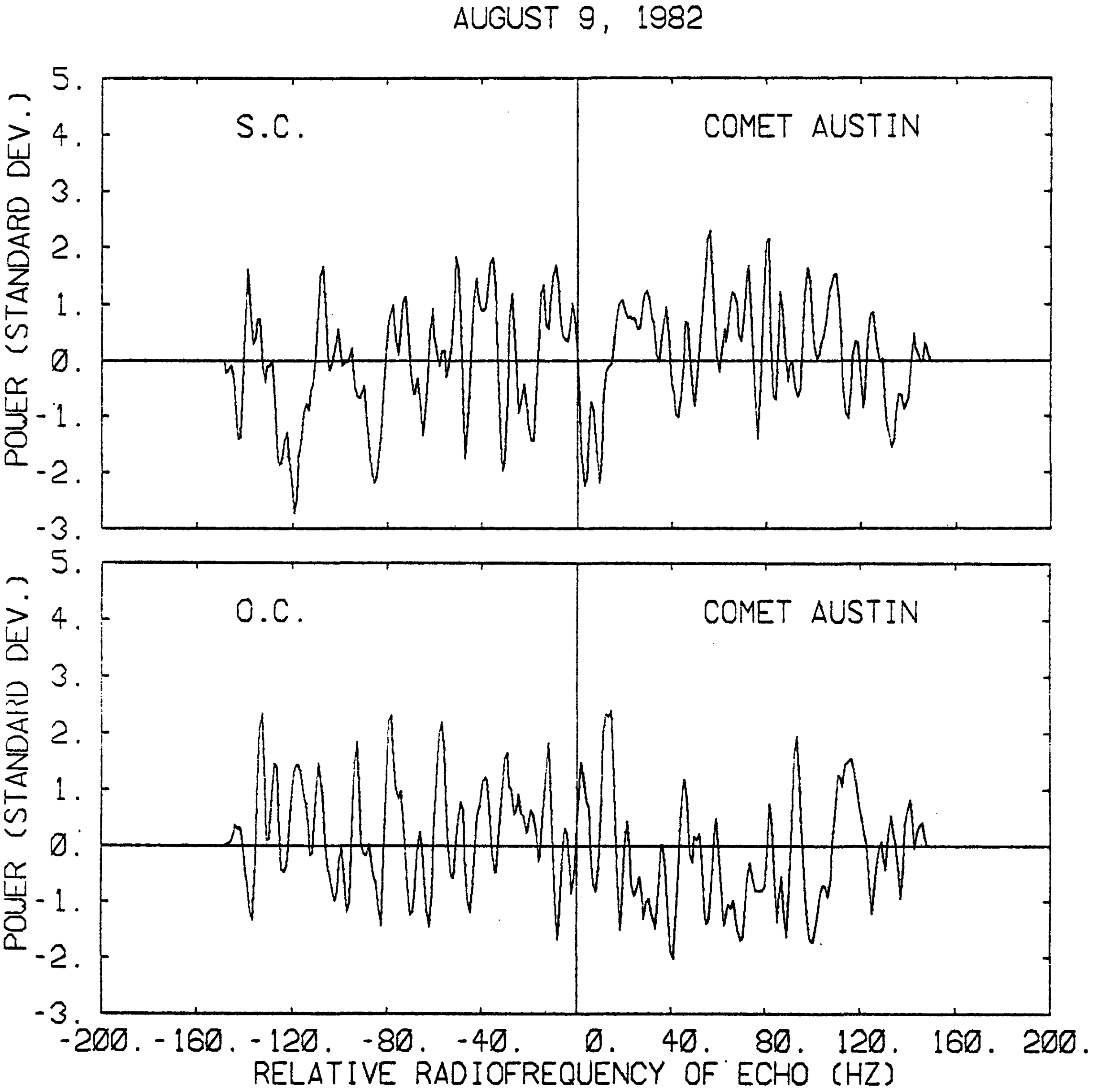
AUGUST 9, 1982
S.C.
COMET AUSTIN
O.C.
COMET AUSTIN
POWER (STANDARD DEV.)
POWER (STANDARD DEV.)
5.
4.
3.
2.
1.
0.
-1.
-2.
-3.
-200.
-160.
-120.
-80.
-40.
0.
40.
80.
120.
160.
200.
RELATIVE RADIOFREQUENCY OF ECHO (HZ)

Fig. 13.2

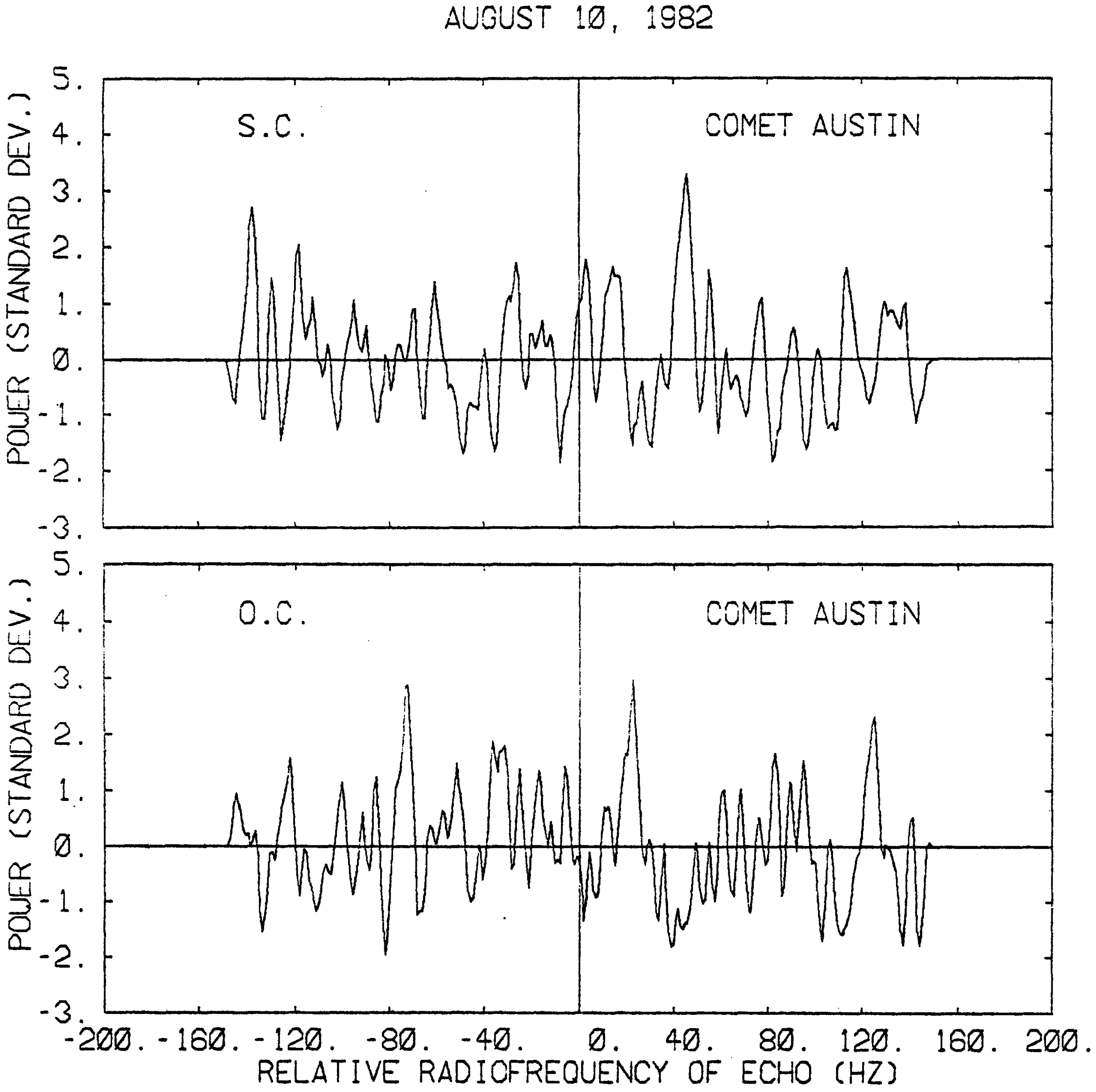
AUGUST 10, 1982
S.C.
COMET AUSTIN
O.C.
COMET AUSTIN
POWER (STANDARD DEV.)
POWER (STANDARD DEV.)
5.
4.
3.
2.
1.
0.
-1.
-2.
-3.
-200.
-160.
-120.
-80.
-40.
0.
40.
80.
120.
160.
200.
RELATIVE RADIOFREQUENCY OF ECHO (HZ)

Fig. 13.3

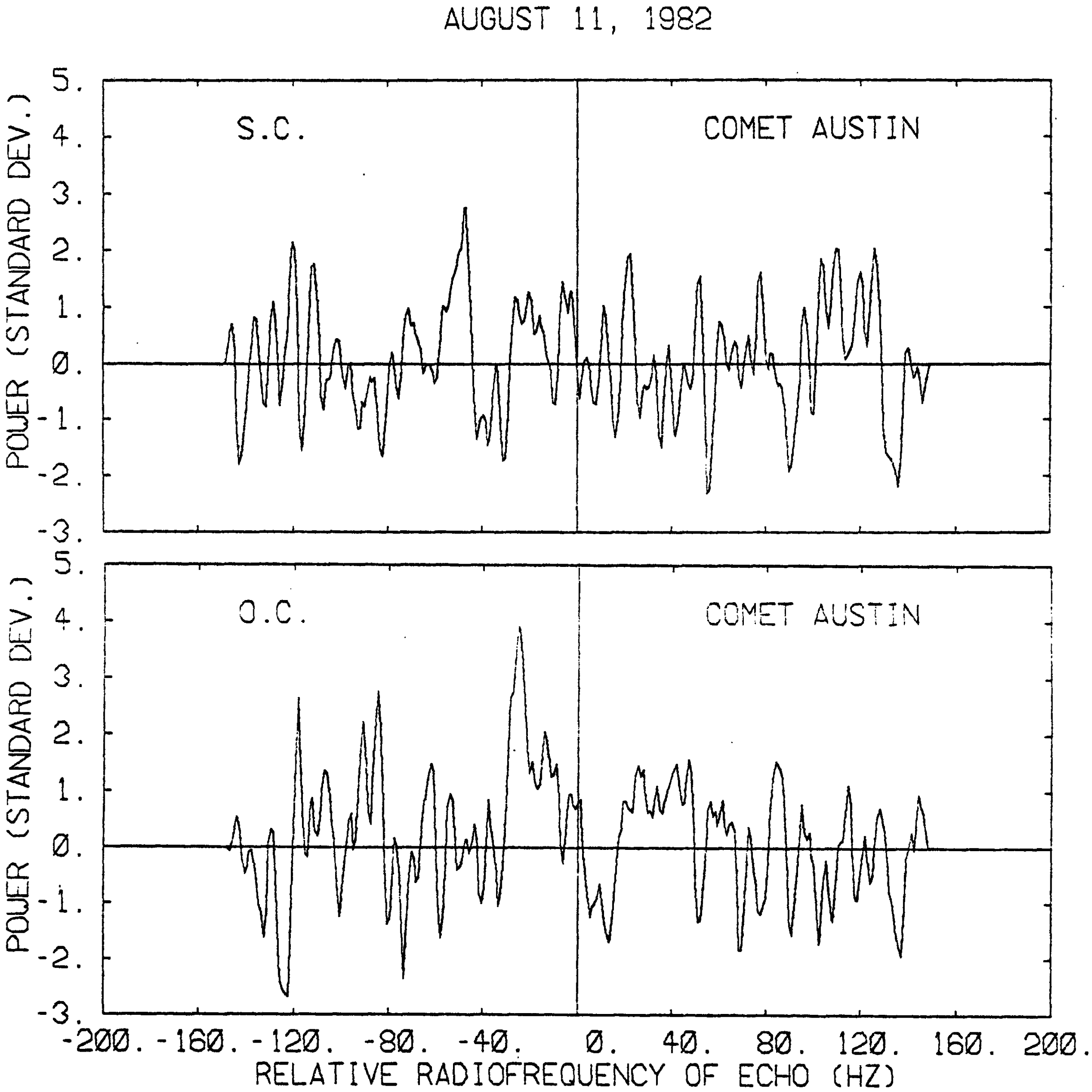
AUGUST 11, 1982
S.C.
COMET AUSTIN
O.C.
COMET AUSTIN
POWER (STANDARD DEV.)
POWER (STANDARD DEV.)
5.
4.
3.
2.
1.
0.
-1.
-2.
-3.
-200.
-160.
-120.
-80.
-40.
0.
40.
80.
120.
160.
200.
RELATIVE RADIOFREQUENCY OF ECHO (HZ)

Fig. 13.4

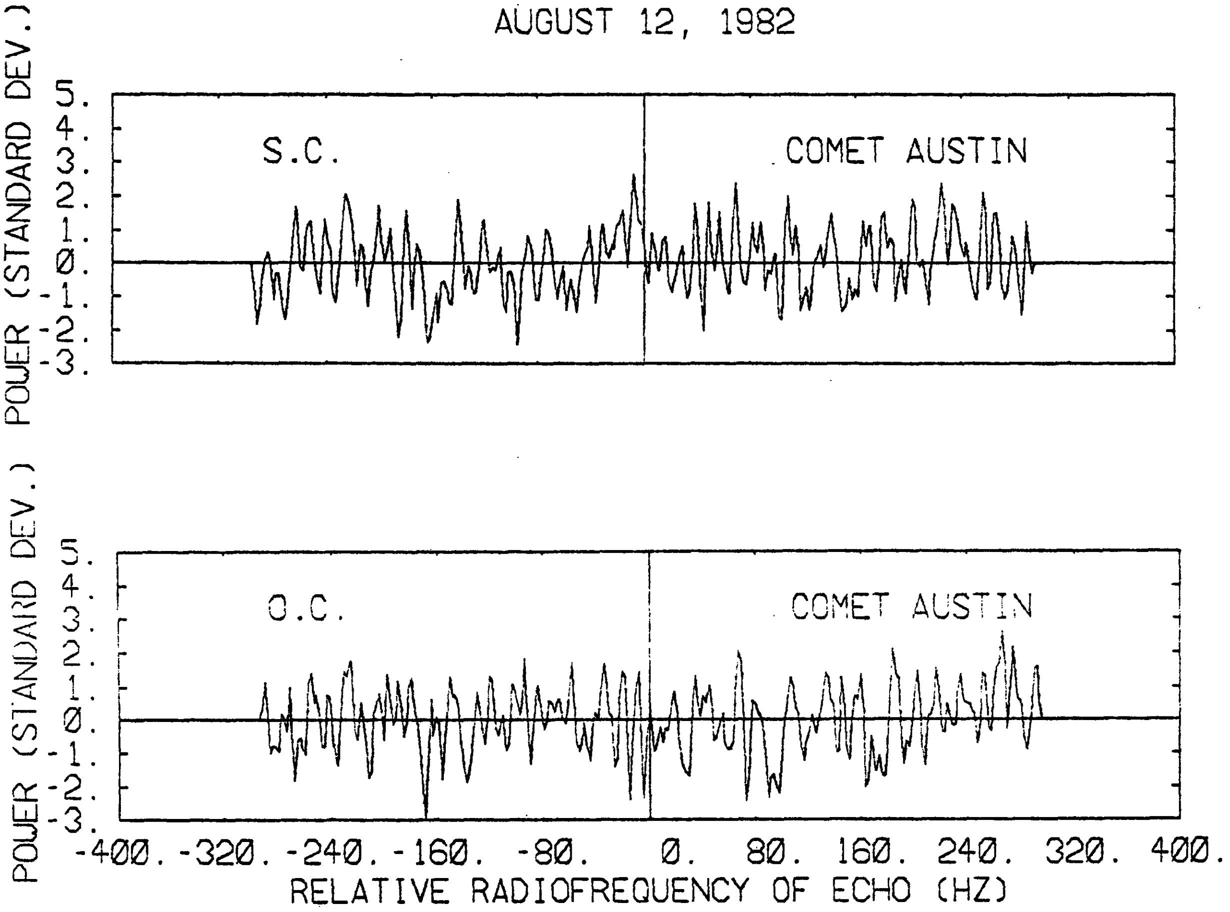
AUGUST 12, 1982
POWER (STANDARD DEV.)
5.
4.
3.
2.
1.
0.
-1.
-2.
-3.
S.C.
COMET AUSTIN
POWER (STANDARD DEV.)
5.
4.
3.
2.
1.
0.
-1.
-2.
-3.
O.C.
COMET AUSTIN
-400.
-320.
-240.
-160.
-80.
0.
80.
160.
240.
320.
400.
RELATIVE RADIOFREQUENCY OF ECHO (HZ)

Fig. 13.5

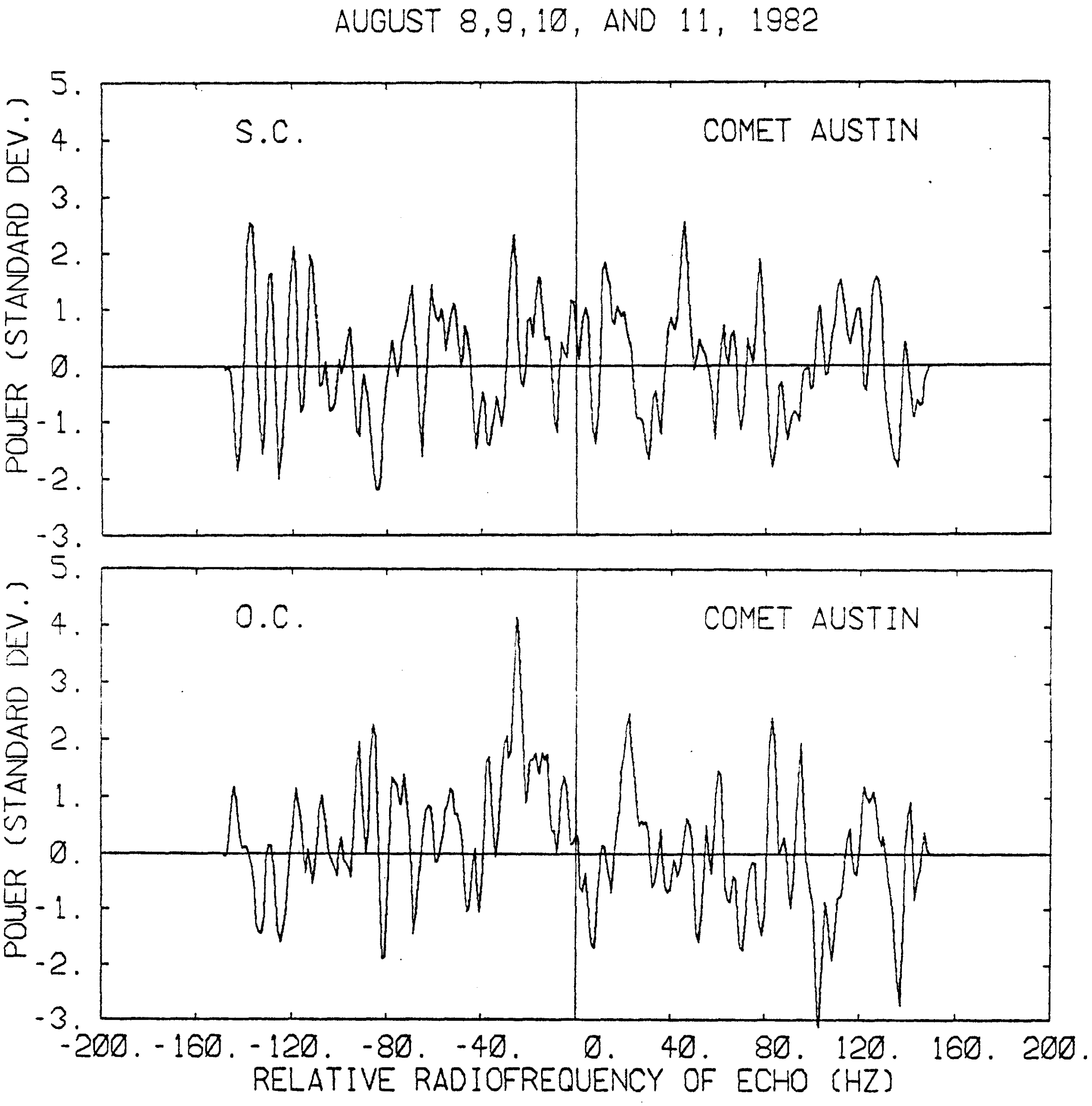
AUGUST 8,9,10, AND 11, 1982
S.C.
COMET AUSTIN
O.C.
COMET AUSTIN
POWER (STANDARD DEV.)
POWER (STANDARD DEV.)
5.
4.
3.
2.
1.
0.
-1.
-2.
-3.
-200.
-160.
-120.
-80.
-40.
0.
40.
80.
120.
160.
200.
RELATIVE RADIOFREQUENCY OF ECHO (HZ)

Fig. 13.6

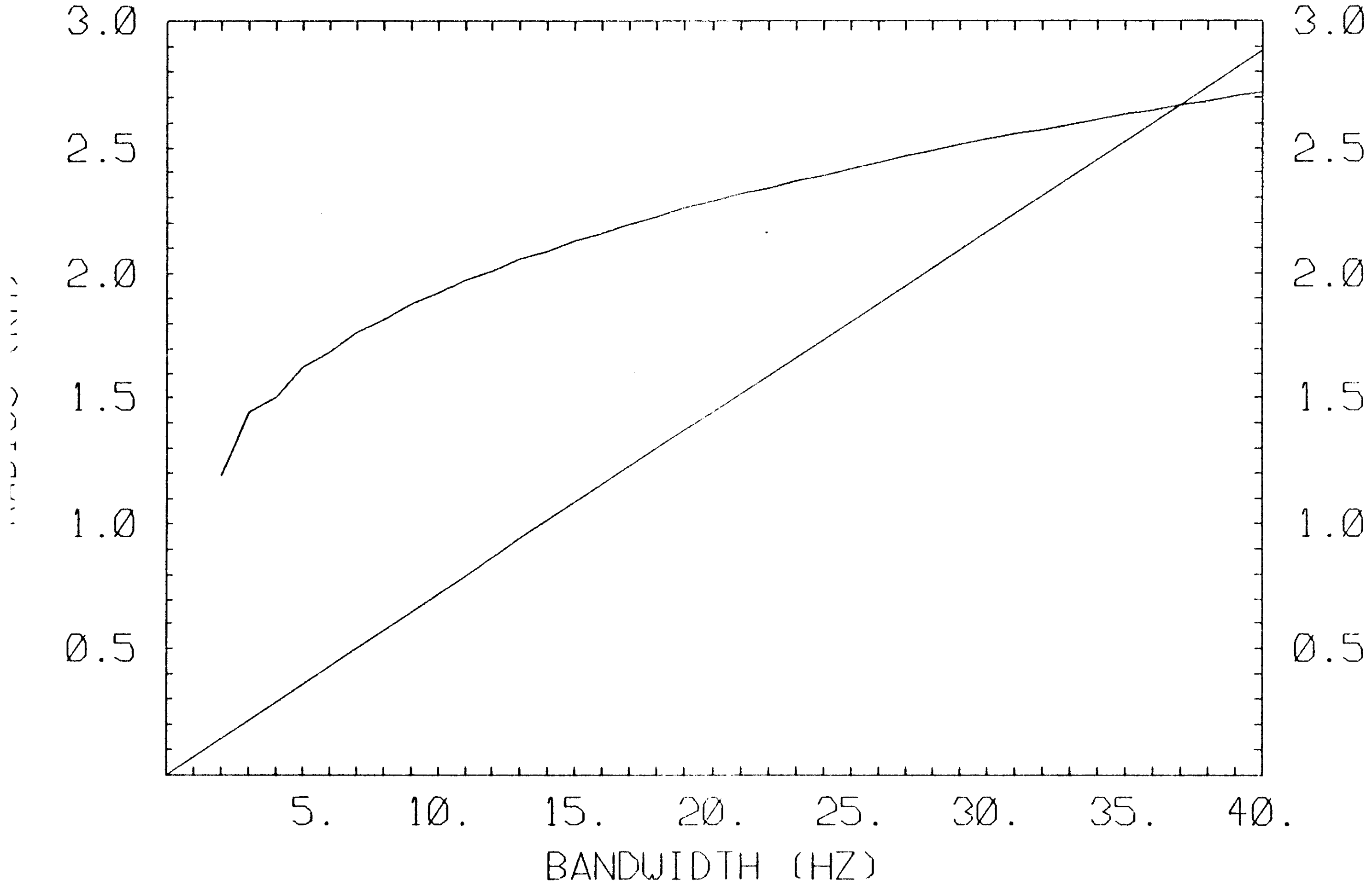
3.0
2.5
2.0
1.5
1.0
0.5
3.0
2.5
2.0
1.5
1.0
0.5
5.
10.
15.
20.
25.
30.
35.
40.
BANDWIDTH (HZ)

Fig. 13.7

CHAPTER 14

COMET CHURYUMOV-GERASIMENKO: DATA ANALYSIS AND INTERPRETATION

14.1. Cross-correlation

The spectra corresponding to the weighted sum of the data for each single day of observation as well as for the combination of the eight days have been smoothed using various filter shapes. Figure 14.1 shows the result of this analysis only for the combination of all days and using a smoothing filter defined by $n = 1$ and an effective filter bandwidth EFB = 3 Hz. When using different values of EFB, we notice that this value (i.e. 3Hz) yields a maximum signal-to-noise ratio of about 3σ, the maximum being located in the spectral element 188. One is referred to Table 8.4 to see the corresponding values in the unsmoothed spectrum. Although the frequency of the peak is within the ephemeris uncertainties, the evidence is too weak to claim a detection. We can however put an upper limit on the size of the nucleus.

14.2. Upper limits on the radar cross-section and size of the target

We have carried out an analysis similar to the analysis described for comet Austin in chapter 13. Here however, the standard deviation of the final (unsmoothed) spectrum for the weighted sum of the whole set of data is (expressed in km^2):

$$\sigma_{rms} \simeq 0.1\ \mathrm{km}^2 \text{ both in the O.C. and in the S.C. sense.}$$

The absolute upper limit on the total bandwidth of the echo satisfies:

$$2183\ 10^{-6}\ B_{max}{}^2 - [(2m+1) - (8m(m+1)(2m+1)/6B_{max}{}^2] = 0$$

Solving for B_{max}, we get $B_{max} \simeq 52$ Hz, $\sigma_{max} \simeq 1.8\ \mathrm{km}^2$ and $R_{max} \simeq 3.7$ km. This is however a very conservative upper limit because of the values considered for P, A, and θ. We will settle on a value of 3 km, as a more likely upper limit.

14.3. Upper limit on the number of grains in the coma.

From optical observations, comet Churyumov-Gerasimenko is found to be a very dusty comet (much more so than Grigg-Skjellerup, for instance). Hanner (1982, private communication) has obtained dust production for small particles, between 0.1 μm and 10 μm in size, for these two comets. However, there is no data available on number of particles with sizes in the millimeter to centimeter range. Our procedure to study this range has been described in earlier chapters. For comet Churyumov-Gerasimenko, we have:

$$D \approx 0.404 \text{ AU} \quad G \approx 71.2 \text{ dB} \quad P_t \approx 400 \text{ kW}$$

$$T_s \approx 50 \text{ K} \quad t = 20415 \text{ sec} \quad k \approx 1.38\ 10^{-23} \text{ J/K}$$

so that the upper limit we get on the number of grains is a factor of 2 higher than the one obtained for comet Grigg-Skjellerup.

Figure captions for chapter 14.

Figure 14.1. Spectrum of the weighted sum of all the data, smoothed with a filter of parameters n = 1 and EFB = 3 Hz.

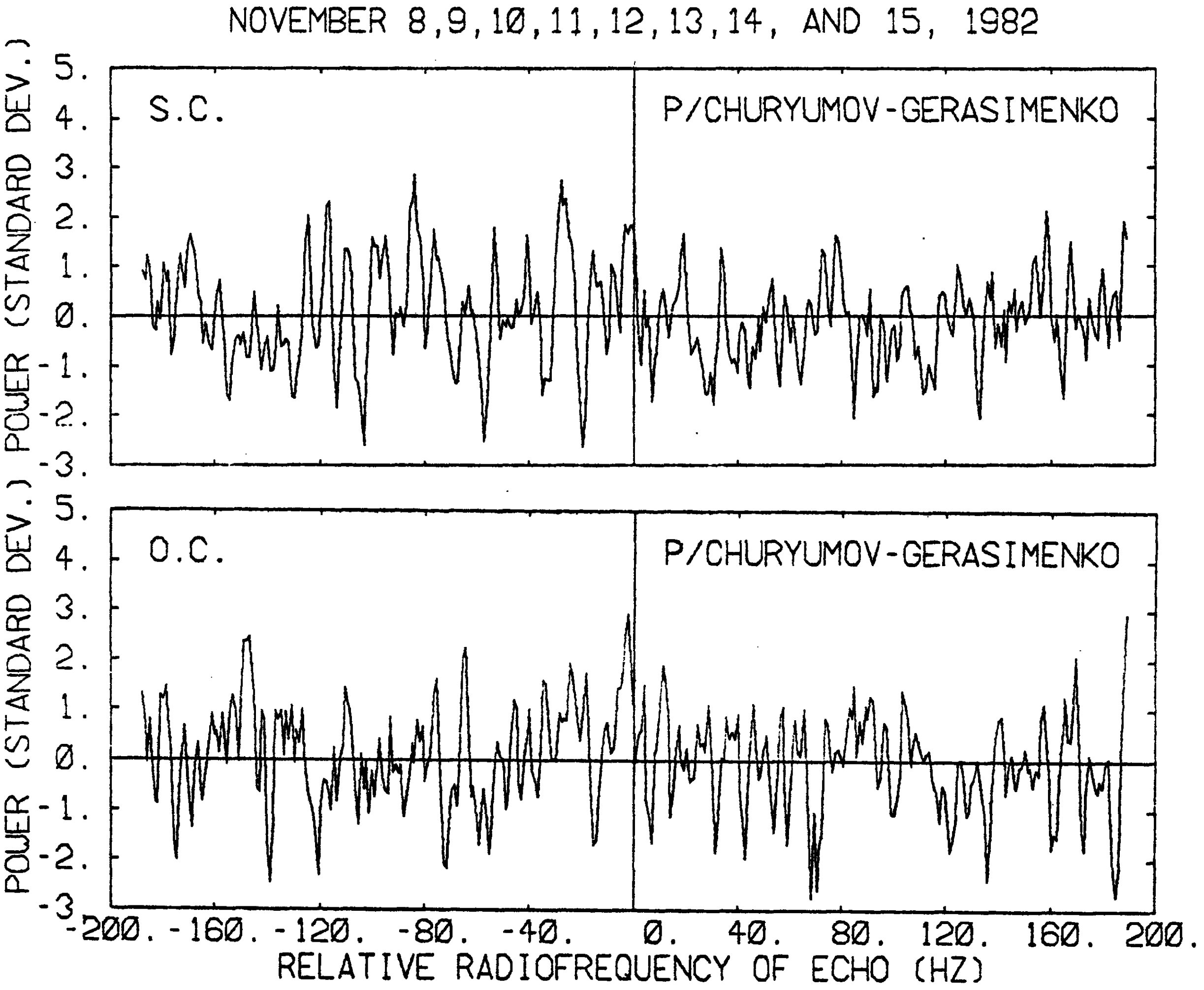
NOVEMBER 8,9,10,11,12,13,14, AND 15, 1982
S.C.
P/CHURYUMOV-GERASIMENKO
O.C.
P/CHURYUMOV-GERASIMENKO
POWER (STANDARD DEV.)
5.
4.
3.
2.
1.
0.
-1.
-2.
-3
-200. -160. -120. -80. -40. 0. 40. 80. 120. 160. 200.
RELATIVE RADIOFREQUENCY OF ECHO (HZ)

Fig. 14.1

PART I. SUMMARY: THE NATURE OF COMETARY NUCLEI FROM RADAR OBSERVATIONS

CHAPTER 15

IMPLICATIONS OF THE RADAR RESULTS FOR THE NATURE OF COMET NUCLEI

15.1. Summary of the results.

- Radar cross-sections and size of nuclei.

We have found the following ranges or upper limits on the radar cross-sections and radii of the four comets studied:

TABLE 15.1

LIMITS ON RADAR CROSS-SECTION AND RADIUS FOR FOUR COMETS

Comet	$\sigma_{o.c.}$ (km^2)	$\sigma_{s.c.}$ (km^2)	μ_c	R (km)
P/Encke	1.11 ± 0.55	-	-	0.4 - 3.6
P/Grigg-Skjellerup	0.50 ± 0.13	< 0.15	< 0.3	0.4 - 2.2
P/Churyumov-Gerasimenko	< 0.5	< 0.5	-	< 2
Austin	< 0.3	< 0.3	-	< 1.5

- The upper limits obtained for the number of grains in the coma are given in Table 15.2.

TABLE 15.2

UPPER LIMITS ON THE NUMBER OF GRAINS IN THE COMA OF FOUR COMETS

Comet	Grain Size	Assumed grain composition Ice	 Olivine	 Magnetite Iron Sulfide
Encke	mm	$4.5\ 10^{17}$	$1.5\ 10^{17}$	$7.5\ 10^{16}$
	cm	$1.5\ 10^{11}$	$6\ 10^{10}$	$3\ 10^{10}$
Grigg-Skjellerup	mm	$3\ 10^{17}$	10^{16}	$6\ 10^{16}$
& Austin	cm	10^{11}	$4.5\ 10^{10}$	$2\ 10^{10}$
Churyumov-Gerasimenko	mm	$6\ 10^{17}$	$2\ 10^{17}$	10^{17}
	cm	$2\ 10^{11}$	$9\ 10^{10}$	$4\ 10^{10}$

Thus our radar results allow us to place an upper limit of the order of 10^{17} millimeter-sized particles and about $5 . 10^{10}$ centimeter-sized particles in the coma of these comets.

15.2. Discussion

The most important result of this study is the actual detection of two comet nuclei as evidence for the presence of a discrete solid body as the source of all the material ejected in the coma and tail, and the fact that these observations discredit the dust-swarm models. Also, for the two comets detected, we do not find evidence for the presence of double or multiple nuclei.

Looking at the quantitative aspect of these results, we notice that all four nuclei studied, and we include the earlier negative result for comet d'Arrest as well, are kilometer-sized or smaller objects. Although comet Encke and Grigg-Skjellerup are the two comets having the shortest orbital period, they are otherwise typical comets and thus can be considered as representative of the class of comets with very short orbital period. Comet Churyumov-Gerasimenko (6.6 yrs orbital period) and d'Arrest (6.2 yrs period) are also essentially typical short-period comets. The new comet Austin on the other hand seems to be a typical long-period comet, looking very much like the comets Ikeya 1963I, Kobayashi-Berger-Milon, and others, not only in morphology, but also in physical characteristics such as production rates of gas and dust.

Although our sample contains only four comets, it seems representative of both short-period and long-period comets and suggests that comet nuclei may be, on the average, even smaller than believed before, i.e. smaller than about two kilometers in radius.

In particular, such a small size, considered along with the observation that comets have low tensile strength and overall homogeneity showing the same structure on the inside as on the outside (derived from the behavior of split comets), indicates that most comets probably do not have a rocky core and thus should not evolve into very compact asteroidal objects. Furthermore, comets more likely formed in the Uranus-Neptune region than closer to the sun (Donn and Rahe, 1982, Fernandez and Ip, 1982). The behavior of new comets relative to old comets could be explained just by a difference in activity (i.e. surface structure). For instance, starting with a new comet containing large clumps of dust and ice, and assuming that the exposed surface is made of 50% dust and 50% ice, if these two components do not present significant asymmetries in their distribution then the nucleus should not present any special active area and the coma should not exhibit any periodic structure. These two components can however be present on the surface in small separate areas without affecting the previous conclusion. Then after a number of revolutions, the former more icy areas should not only be depleted in some of their ices, thus leaving mostly dust behind them, but also the large particles of dust trapped in the escaping volatiles could fall back to cover both the icy and dusty areas. With time, this should yield a surface with increasingly dusty coverage and with the more and more noticeable presence of active areas, just because of their higher and higher singularity in the mostly dusty surface. In particular this would temporarily or permanently shield other volatiles present on the inside, those volatiles being able to escape only in bursts after the surface reaches a high enough temperature to provoke an explosive ejection of the trapped volatiles. This theory seems confirmed by the values of the production rates for H_2O obtained for Grigg-Skjellerup and Austin (Feldman, private communication, and Weaver et al. (1982)) which show a much higher production rate for the latter. Since from our results the sizes of the two nuclei seem similar, it indicates that the difference is due to the actual areas of the surfaces of exposed volatiles and not to the sizes of the nuclei.

The radar observations of comet Grigg-Skjellerup have yielded the highest signal-to-noise ratio. The detection of an echo only in the same sense of circular polarization as transmitted has indicated that the power returned from the target arises mostly from quasi-specular reflection at the surface of the nucleus, so that the surface of the nucleus must exhibit some smoothness on scales larger than the radar wavelength.

Finally, considering the wealth of data obtained in the last decade, it seems that one cannot rule out the possibility that various families of comets of different structures and compositions could exist; however our understanding of the mechanism of their formation and ejection into the outer solar system is still too poor to undertake a classification.

Figure captions for chapter 15.

Figure 15.1. Representation of a comet nucleus according to the model suggested. Both for a new and an old comet. It is hypothesized that the comet nucleus formed by accretion of small individual cometesimals, yielding an overall uniform structure. After several perihelion passages, the surface is blanketed with a crust of dusty material.

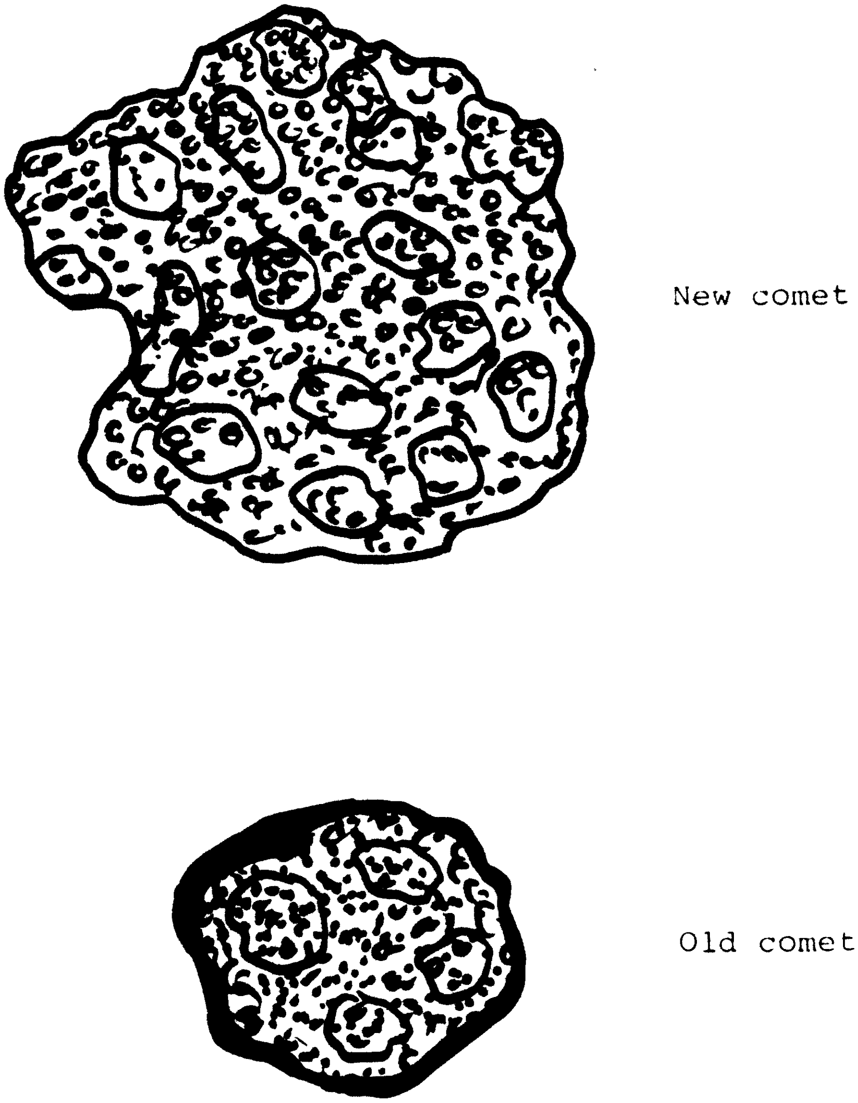

Fig. 15.1

CHAPTER 16

CONCLUSION

16.1. Further related work needed.

The observations described in this thesis will unfortunately not be repeatable for the same comets within the next ten years, although three of them are short-period comets. This is because a close geocentric approach is necessary to allow detection by radar. The only way to add further to our knowledge concerning the three periodic comets studied here will be through detailed optical observations yielding better information on the spin vectors of their nuclei. This, in turn, would allow a more accurate inference on the radius of the nucleus. Such observations could best be done using CCD cameras, and should be performed not only at close approach to the Earth, when near-nucleus dust structures are apparent, but also at large heliocentric distance where the coma is not dominant and a rotational light curve can be obtained. The next appearances of the comets studied are: 1984 and 1987 for Encke, 1987 for Grigg-Skjellerup, and 1989 for Churyumov-Gerasimenko.

On the other hand, if no improvement in the sensitivity of existing radar systems occurs, there will be no good opportunity for radar observations of other comets, at least for those having well-known orbits until at least the 1990's. However, if major radar improvements are made, then we might give special attention to the appearances of the comets Haneda-Campos (1984), Giacobini-Zinner (1985), Borelly and especially Denning-Fujikawa (1987), and Brorsen-Metcalf and Dubiago (1989). The (special) case of comet P/Halley is presented in the next section.

Beside these known comets, it is still possible that a new comet might be discovered that approaches closely to the Earth. Indeed, on the average, one to two new comets crossing the Earth's orbit are discovered every year. Attempting to observe these, however, would require preparing accurate ephemerides and scheduling observations with a short lead time. This, in turn, is contingent upon getting sufficient accurate astrometric determinations of the comet's position before any radar observation take place. We have earlier seen the severity of this problem for comet Austin. Having been discovered in the Southern hemisphere, it had the advantage of about two months of lead time, but also had the disadvantage of a restricted set of available observatories. On the other hand, although a comet might be discovered earlier at greater distances in the northern hemisphere, and would draw more attention from a greater number of observers, the comet would be rapidly heading south out of reach of the major radar systems in the northern hemisphere. At the time of completion of this thesis, early May 1983, radar observations of the new comet IRAS-Araki-Alcock are in planning, both at Arecibo and Goldstone. This comet, discovered in the Northern hemisphere on April 25, 1983, will make a close approach to the Earth about two weeks later at a geocentric distance of about 0.03 AU, i.e. about ten times closer than any other comet observed for this thesis. Such a close approach for a comet has not occurred in more than two hundred years. As discussed above, a successful detection would in large part be the fruit of the outstanding efforts devoted to the preparation of accurate ephemerides in a very short time, and promises to yield a wealth of information on the nucleus.

16.2. The case of comet P/Halley

This comet, known since ancient times, has a 76-year orbital period, with perihelion and aphelion distances respectively of 0.58 and 35.3 AU. Whipple (1981) has estimated some of the physical parameters of its nucleus using data obtained during previous apparitions through 1910. He finds a radius in the range 2.5 to 4 km and expects an average geometric albedo in the range 0.1 to 0.2. The comet was recovered on October 16, 1982 by Jewitt et al. (1982) who find a radius of 1.4 ± 0.2 km for a geometric albedo of 0.5. They found no coma at the comet's heliocentric and geocentric recovery distances of about 11 AU. The bare nucleus was thus probably seen. The values abtained by Jewitt et al. are compatible with the range obtained by Whipple if one assumes a smaller geometric albedo for the bare nucleus

$$p = 0.15 \qquad R = 2.6\ \text{km}$$

$$p = 0.1 \qquad R = 3.1\ \text{km}$$

These values are consistent with values obtained by Belton and Butcher (1982) using 1981-1982 unsuccessful attempts at recovery and earlier 1910 observations.

Whipple has estimated the nucleus spin vector. He found $P_s \approx 10.3$ hrs for the spin period (Whipple, 1981), and a tentative spin axis direction defined by the following coordinates (Whipple, 1983):

$$\text{R.A.} = 225° \pm 25° \text{ and DEC.} = -70° \pm 10°, \quad \text{(equinox 1950.0)}$$

Comet Halley will make two close approaches to the Earth at its 1985/1986 appearance. At its first close approach in November 1985, it will be at a geocentric distance $\Delta \approx 0.61$ AU and at a positive declination. At its second approach it will reach a geocentric distance

$\Delta \approx 0.41$ AU, but at low negative declination. Yeomans has produced extensive ephemerides for this comet (Yeomans, 1981) from which we abstract Table 16.1.

From these data we can see that the comet will be visible only from the Goldstone radar facility in California at its closest approach in April 1986 and at a very low declination, where the radar performance is poor. At the earlier approach in 1985, however, the comet will be observable both from Arecibo and Goldstone, although far below likely detectability at the latter site.

We are evaluating here the detectability of the comet at Arecibo. We use the radar equation with the following presently optimum system parameters:

$$P_t = 420 \text{ kW} \quad T_s = 40 \text{ K} \quad G = 72 \text{ dB}$$

in order to get an optimistic estimate of the signal-to-noise ratio. The geocentric distance will be 0.62 AU between November 26 and November 29, 1985, only. We thus assume an optimum integration time of 4 hours during these four days. The nucleus pole position given above yields an angle of about 54° between the nucleus spin axis and the radar line-of-sight at midtime of observation, on November 27, 1985 (using Yeomans' values (1981) for the comet right ascension and declination:

R.A. = 1 hr 50.905' DEC. = 16° 50.46')

Assuming a radius of 3.5 km, a radar scattering efficiency of about 0.1 for the nucleus, and the rotation period estimated by Fred Whipple, we get:

$$\text{SNR} \approx 2.5\sigma$$

To get a higher signal-to-noise ratio one would need to increase the integration time or to improve the system capabilities.

TABLE 16.1

	1985 approach			1986 approach	
Date	Dec.	Δ (AU)	Date	Dec.	Δ (AU)
1985 11 21	20 18.91	0.65	1986 4 5	-44 04.77	0.46
22	19 52.15	0.64	6	-45 15.84	0.45
23	19 22.04	0.64	7	-46 15.72	0.44
24	18 48.64	0.63	8	-47 0.34	0.43
25	18 12.08	0.63	9	-47 25.83	0.42
26	17 32.59	0.62	10	-47 29.12	0.42
27	16 50.46	0.62	11	-47 8.60	0.42
28	16 6.05	0.62	12	-46 24.45	0.42
29	15 19.78	0.62	13	-45 18.69	0.42
30	14 32.09	0.63	14	-43 54.76	0.43
12 1	13 43.44	0.63	15	-42 16.93	0.44
2	12 54.27	0.64	16	-40 29.64	0.45
3	12 05.02	0.65	17	-38 37.00	0.46

To double the integration to eight hours with eight days of perfect observing conditions would yield only a 3.5σ signal-to-noise ratio with the same value (0.62) for Δ. In fact during the eight days, if one wants to keep good zenith angle and thus observe between November 22 and November 29, then the geocentric distance increases to 0.65 AU which represents an additional loss of almost 1 dB, and if one wants to have the smallest geocentric distance possible, thus observing between November 24 and December 1, then there is a loss of more than 1 dB due to degradation of the gain and system temperature in the last sessions. The only alternative is a drastic improvement in system capabilities. Since multiplying the power by a factor of 2 or reducing the system temperature by a factor of 2 present technical difficulties as well as a high cost, the system gain seems the only parameter likely to be significantly improved. A 3 dB improvement on the two-way gain would permit to obtain slightly more than a 5σ detection in an eight days period. It has to be kept in mind that this assumes smooth observations devoid of technical problems, continuously for eight days with optimum system capabilities, while for the comets observed for this thesis the rate of success did not exceed 70%.

A spin vector very different from the one assumed could allow a higher signal-to-noise ratio, although even a four times longer rotation period (40 hrs) would only double its value, which may not be enough for investigating the scattering properties of the target.

Thus, not only is such a detection unlikely, but even if it were realized, the signal-to-noise ratio would be so low that the scientific return would be of negligible importance compared to the expected return from the encounter of the comet with the different spacecraft to be sent by the E.S.A., the USSR, and Japan. Possibly the only useful information would be the radial velocity of the target, but even this is unlikely to be of much help in the refinement of the comet ephemerides, for predicting the comet's nucleus position at the time of spacecraft encounter many months later (Yeomans et al., 1983).

16.3. Conclusion

This set of observations has been unique, not only because most of the comets studied will not be detectable by radar again before many years, but also because any opportunity for a radar observation of a comet is rare. Finally, the radar observations have allowed the rejection of some theories of the nature of comets while leading to the confirmation of another, i.e. the dusty snowball theory.

APPENDIX 1

THE RADAR EQUATION AND ITS APPLICATION TO THE CASE OF A COMET NUCLEUS.

Radar Equation

In the following discussion we will assume the transmission of a continuous-wave radar signal (CW) with an angular beamwidth much wider than the angle subtended by the target diameter. The radar equation (1) expresses the echo power received back at the radar as a function of the parameters of the radar system and the target radar cross-section (i.e., the intercepting area of a perfectly conducting sphere that would return an amount of energy equal to that seen from the actual target):

$$P_R = \underbrace{\left(\frac{P_T G_T}{4\pi D^2}\right)}_{F_i} \times \sigma \times \left(\frac{A_e}{4\pi D^2}\right) \tag{1}$$

where P_R = received power (W)

P_T = transmitted power (W)

G_T = one-way antenna gain for transmission relative to an isotopic radiator

D = target geocentric distance (m)

σ = target radar cross-section (m^2)

A_e = effective aperture of the receiving antenna (m^2)

The first term F_i represents the flux density per unit area incident on the target. Thus, $F_i \times \sigma$ represents the flux leaving the target in the observer's direction per 4π steradians, resulting in a flux density per unit area $F_i \times \sigma / 4\pi D^2$ at the receiver and in a received power $F_i \sigma A_e / 4\pi D^2$. The effective aperture A_e of the receiving antenna is related to the one-way antenna gain of the receiving antenna by the relation:

$A_e = \lambda^2 G_R/4\pi$ where λ is the wavelength (m).

The radar equation can thus be written:

$$P_R = \frac{P_T G_T G_R \lambda^2 \sigma}{(4\pi)^3 D^4}$$

If the same antenna is used for transmission and reception (monostatic case), then $G_T = G_R = G$.

Radar Cross-section

We assume a monostatic geometry (i.e. the transmitting and receiving antennas are colocated) and we define an angular scattering law $\sigma_o(\phi)$ to represent the radar back-scattering cross-section associated with a unit area on the target at a given angle of incidence, ϕ. $\sigma_o(\phi)$ is a dimensionless function of ϕ.

For a spherical target there are $(1/\cos\phi)$ square meters of target surface for every square meter of incident-wavefront and consequently there are $\sigma_o(\phi)/\cos\phi$ square meters of radar cross-section for every square meter of wavefront.

Echoes from different resolved regions on the surface are statistically independent and can thus be combined as power. For a spherical target of radius R we obtain the total radar cross-section:

$$\sigma = \int_0^R [\sigma_o(\phi)/\cos\phi] \times 2\pi r dr$$

with $r = R\sin\phi$ and $dr = R\cos\phi d\phi$.

thus, $$\sigma = 2\pi R^2 \int_0^{\pi/2} \sigma_o(\phi) \sin\phi d\phi, \qquad (2)$$

and the power backscattered in the observer's direction is $P_o = \sigma F_i$. In the general case of a bistatic experiment (transmitter and receiver not colocated), the angular scattering law $\sigma(\phi,\phi',\theta)$ is a function not only of the angle of incidence ϕ but also of the angles of scattering ϕ' and θ. The radar cross-section can be written in terms of the surface reflectivity ρ and a directivity g defined as follows:

The reflectivity is the ratio of the total scattered power P_s to the total incident power, P_i, with

$$P_s = 2\pi R^2 \int_0^{\pi/2} \sin \phi d\phi \iint_{2\pi \text{ steradian}} \frac{F_i\sigma_o(\phi,\phi',\theta)}{4\pi} d\Omega$$

where $F_i\sigma_o/4\pi$ is the reflected power in watts per steradian.

Now, $P_i = \pi R^2 F_i$ and, thus,

$$\rho = \frac{1}{2\pi} \int_0^{\pi/2} \sin\phi \, d\phi \int_0^{\pi/2} \sin\phi' \, d\phi' \int_0^{2\pi} \sigma_o(\phi,\phi',\theta) \, d\theta$$

and the directivity g is defined as the ratio of the backscattered power actually received to the power that would have been received from a sphere having reflectivity at normal incidence, ρ; thus $g = \sigma/\rho\pi R^2$ and $\sigma = \pi R^2 \rho g$.

The reflectivity ρ is characteristic of the dielectric properties of the target surface while g represents the effects of surface shape.

Scattering Laws appropriate to a cometary nucleus

Comet nuclei are expected to be small bodies with partly icy surfaces. Scattering laws of the form $\cos^n\phi$ have proved useful to describe the backscattering behavior of asteroids and the icy galilean satellites. Since this form is convenient mathematically, we will use it here. In particular, a uniformly bright sphere will correspond to a scattering exponent $n = 1$, while lambert scattering from a sphere will be associated with $n = 2$. We may, therefore, write the scattering function as: $\sigma_o(\phi) = \delta \cos^n \phi$ where δ is a normalization coefficient and σ_o is the specific radar cross-section as defined above. δ may be derived by carrying out the backscattering integration over a sphere and equilibrating the result to the total cross-section: $\rho g \pi R^2$.

$$\sigma = 2\pi R^2 \int_o^{\pi/2} \delta \cos^n \phi \sin\phi \, d\phi$$

$$\sigma = 2\pi R^2 \delta \left| \frac{u^{n+1}}{n+1} \right|_0^1$$

$$\sigma = \frac{2\pi R^2 \delta}{n+1} = \pi R^2 \rho g \quad \text{so that } \delta = \rho g \; \frac{n+1}{2}$$

In practice, for the detection of a target, one wants to maximize the signal to noise ratio. Let us assume, as a first step, that the spectral density of the echo is constant from limb to limb. Then the signal to noise ratio can be expressed as:

$$(SNR)_o = \frac{P_R}{kT_s B} \times (B\tau)^{1/2} ,$$

where P_R is the received power as defined in (1), k is Boltzmann's constant, T_s is the receiver system temperature, B is the receiver bandwidth (assumed rectangular to match the echo width), and τ is the integration time. We note that kT_sB represents the mean noise power in the bandwidth B while $(B\tau)$ is the number of independent noise samples in B observed for a time τ. Thus, the quantity $kT_sB/(B\tau)^{1/2}$ is the fluctuation power with which the echo must compete.

We have:

$$P_R = \frac{P_t G_t G_R \lambda^2}{(4\pi)^3 D^4} \times \pi R^2 \sigma \quad \text{(assuming a spherical target of radius R)}$$

while $B = \frac{4R\Omega\sin\alpha}{\lambda}$

is the bandwidth of the echo (Doppler broadening of the signal due to the rotation of the target). Ω is the rotation rate of the target in radians/sec and α is the angle between the radar line of sight and the target's spin axis. The signal-to-noise ratio can then be written:

$$(SNR)_o = \frac{P_t G_t G_R \lambda^2}{(4\pi)^3\, D^4} \times \pi R^2 \rho g \times \frac{1}{kT_s} \times \frac{\lambda}{4R\Omega\sin\alpha}^{1/2} \times \tau^{1/2}$$

or, with $G_t = G_R = G$

$$(SNR)_o = \left(\frac{P_t G^2 \lambda^{5/2} \tau^{1/2}}{128\pi^2 kT_s}\right) \times \left[\frac{(\rho g)^2 R^3}{D^8 \Omega\sin\alpha}\right]^{1/2}$$

or in terms of the antenna effective aperture:

$$(SNR)_o = \left(\frac{P_t G A_e \lambda^{1/2} \tau^{1/2}}{32\pi kT_s}\right) \times \left[\frac{(\rho g)^2 R^3}{D^8 \Omega\sin\alpha}\right]^{1/2} \qquad (3)$$

where the first term between brackets is a function of the radar system parameters and the second term depends on the target distance, spin orientation, size and surface nature.

A more detailed study, taking into account the actual (non-rectangular) shape of the echo spectrum, shows that the signal-to-noise ratio is maximized by choosing a detection filter matched to the power spectral density distribution $P_r(f)$ of the received signal. The signal-to-noise ratio for optimum detection has been given by Muhleman et al. (1965) as:

$$SNR = \frac{1}{kT_s} \left[\tau \int P_r^2(f)\, df\right]^{1/2} \qquad (4)$$

Jurgens and Bender (1977) define the spectral density $\sigma(f)$ such that:

$$P_r(f) = \frac{P_t G_t A_e}{(4\pi D^2)^2}\,\sigma(f)$$

and, by calculating $\sigma(f)$ using a $\cos^n\phi$ scattering law, they obtain:

$$\sigma(f) = \frac{\sigma_\odot \pi^{1/2} R^2}{2\,f_1}\,(n+1)\,\frac{\Gamma[(n+1)/2]}{\Gamma[(n/2)+1]} \times \left[1 - \left(\frac{f}{f_1}\right)^2\right]^{n/2}$$

f_1 being the center-to-limb bandwidth (i.e. one-half of the limb-to-limb bandwidth B). They then evaluate (4) and obtain:

$\mathrm{SNR} = (\mathrm{SNR})_\odot \times \eta(n)$, that is

equation (3) multiplied by a detection efficiency factor which is equal to 1 if the spectral density is constant from $-f_1$ to $+f_1$ and greater than 1 otherwise. The expression for $\eta(n)$ is:

$$\eta(n) = \frac{n+1}{2^{1/2}\pi^{1/4}}\,\frac{\Gamma[(n+1)/2]}{\Gamma[(n/2)+1]} \times \left[\frac{\Gamma(n+1)}{\Gamma(n+\frac{3}{2})}\right]^{1/2}$$

We give some discrete values and a plot of η below:

n	1	2	3	4	5	10
$\eta(n)$	1.04	1.10	1.15	1.20	1.24	1.41

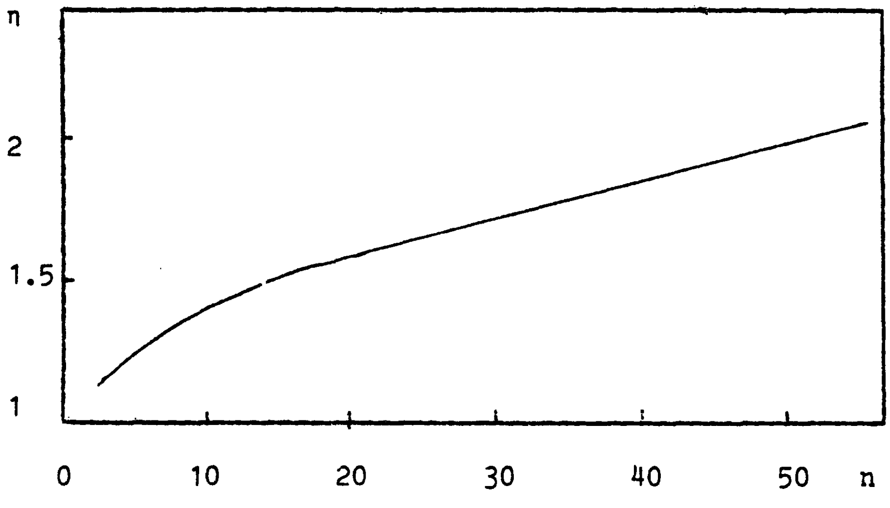

Example: Assuming a spherical nucleus of radius $R = 1.5$ km with a scattering efficiency $\sigma_o = 0.1$ for Encke, along with a rotation period of 6 1/2 hrs and a constant spectral density from limb-to-limb ($\eta=1$), we can estimate an a priori signal-to-noise ratio using the following system parameters:

$P_t = 400$ kw, $G = 71$ dB, $\lambda = 12.6$ cm, $T_s = 40$ K, $\tau = 1$ hr.

Along with a geocentric distance of about 0.3 AU this yields $\mathrm{SNR} \sim 3\sigma_{rms}$, where σ_{rms} is the standard deviation of the fluctuations in noise power.

APPENDIX 2

FREQUENCY SWITCHING TECHNIQUE

As described in section 3.3.1.b the transmitted frequency was switched among 4 different frequencies and dwelt for 10 seconds on each of them. The data recorded on tape as described in section 3.3.3. are organized ,for each file or RTT cycle, as a series of records representing 10-second-average spectra R_i, each of them corresponding to the transmission of a frequency F_i. These spectra, collected for a time long compared with T = 10 sec were then summed , the start of each interval having been delayed from the corresponding start of the transmission by the round-trip time of the echo in order to maintain synchronism with the cycle of frequency switching. As a consequence, for each file, the data set obtained consists of blocks of four records (each one corresponding to the reception of one of the four transmitted frequencies). Each of these blocks, or raw spectra, can be segmented into four parts in order to remove the instrumental effects from the spectra of the received signal. The following algorithm is based on the fact that we have some knowledge of the mean noise power.

Let's call the four transmitted frequencies F_1, F_2, F_3, F_4. We define the quantity R_{ij} $(i,j = 1 \rightarrow 4)$ to represent each of the four equal quarters <u>j</u> of each of the four spectra <u>i</u>. If R_{ii} contains an echo then the R_{ij} $(j \neq i)$ do not. We obtain a "background" spectrum for R_{11} for instance by forming the average $[R_{21} + R_{31} + R_{41}]/3 = B_1$. We then remove this background from the "signal" R_{11} and divide by this background, point by point (there are 365 points for instance for P/Encke). Then we do the same thing for R_{22}, R_{33}, R_{44} and we sum all these contributions then divide by 4; so for each point k (k = 1,365) of the spectrum, we have the value of the "raw spectrum" s(k) as we define it:

$$s(k) = \frac{1}{4} \sum_{j=1}^{4} \frac{R_{jj}(k) - \frac{1}{3} \sum\limits_{\substack{i=1 \\ i \neq j}}^{4} R_{ij}(k)}{\frac{1}{3} \sum\limits_{\substack{i=1 \\ i \neq j}}^{4} R_{ij}(k)}$$

Now we want to normalize this reduced spectrum to the root-mean-square of the noise fluctuations.

Let's calculate σ_{R11} and σ_{B1}. For simplicity let's first go back and normalize the raw power spectra R_{ij} to the mean noise power: For a given frequency cell of width B_r (frequency resolution), the mean noise power in the cell is $P_N = kT_sB_r$, where k is the Boltzmann constant and T_s the receiver system temperature. For an integration time τ and a bandwidth B_r, the rms fluctuation in noise power is:

$$\sigma_\tau = kT_s(B_r/\tau)^{1/2}$$

In fact, we only integrate for τ/N (where N = 4) on each of the four subrecords, so the rms noise associated to a subrecord cell will be:

$$\sigma_{\tau/N} = kT_s(B_rN/\tau)^{1/2}$$

Normalizing the power contained in each frequency cell to the mean noise power present in this cell yields a spectrum R_{ij}/P_N for which the rms noise fluctuation is:

$$\sigma_{R_{ij}/P_N} = \frac{\sigma_{\tau/N}}{kT_sB_r} = (N/B_r\tau)^{1/2}$$

so for instance:

$$\sigma_{R11/P_N} = (N/B_r\tau)^{1/2}$$

Let's deduce

$$\sigma_{\frac{R_{11}-B_1}{B_1}} = \sigma_{\frac{R_{11}/P_N-B_1/P_N}{B_1/P_N}} = \sigma_z$$

For simplicity let's write $r_{11} = R_{11}/P_N$ and $b_1 = B_1/P_N$

then

$$\sigma_z^2 = \sigma_{r_{11}}^2 \left(\frac{\partial z}{\partial r_{11}}\right)^2 \Big|_{\bar{r}_{11},\bar{b}_1} + \sigma_{b_1}^2 \left(\frac{\partial z}{\partial b_1}\right)^2 \Big|_{\bar{r}_{11},\bar{b}_1} + 2\sigma_{r_{11}b_1}^2 \left(\frac{\partial z}{\partial r_{11}}\right)\left(\frac{\partial z}{\partial b_1}\right) \Big|_{\bar{r}_{11},\bar{b}_1}$$

If we assume that r_{11} and b_1 are not correlated, then $\sigma_{r_{11}b_1} = 0$ and the third term is zero.

then

$$\sigma_z^2 = \sigma_{r_{11}}^2 \cdot \frac{1}{\bar{b}_1}^2 + \sigma_{b_1}^2 \cdot \frac{\bar{r}_{11}^{\,2}}{\bar{b}_1^{\,4}}$$

and since $\bar{r}_{11} = \bar{b}_1 = 1$

we get: $\sigma_z^2 = \sigma_{r_{11}}^2 + \sigma_{b_1}^2$

we saw before that

$$\sigma_{R_{11}/P_N} = \sigma_{r_{11}} = (N/B_r\tau)^{1/2}$$

so since $B_1 = [R_{21} + R_{31} + R_{41}]/3$ and in general

$$B_1 = [R_{21} + R_{31} + \dots + R_{N1}]/(N-1)$$

we can thus deduce,

$$\sigma_{B_1/P_N} = \sigma_b = [N/(N-1)B_r\tau]^{1/2}$$

so that $\sigma_z^2 = (N/B_r\tau) + [N/(N-1)B_r\tau]$

$$\sigma_z^2 = N^2/(N-1)B_r\tau$$

If we sum the contributions of the four (and in general N) subrecords as we did, to get s(k), then we get:

$$\sigma_s^2 = \sigma_z^2/N = N/(N-1)B_r\tau$$

So that $\sigma_s = [N/(N-1)B_r\tau]^{1/2}$ (1)

The final background-free spectrum normalized to the rms noise will then be given by:

$$S(k) = s(k)/\sigma_s$$

From equation (1) we can see that, if we fix B_r and τ, then the rms noise is proportional to $C = [N/(N-1)]^{1/2}$. Then by increasing the number of frequencies used we can reduce the rms noise. $C = 1.414$, 1.155 and 1.069 respectively for $N = 2$, 4 and 8, and, although one can gain about 20% in signal-to-noise ratio by using four frequencies instead of 2, the further gain eventually obtained by using 8 frequencies is less important.

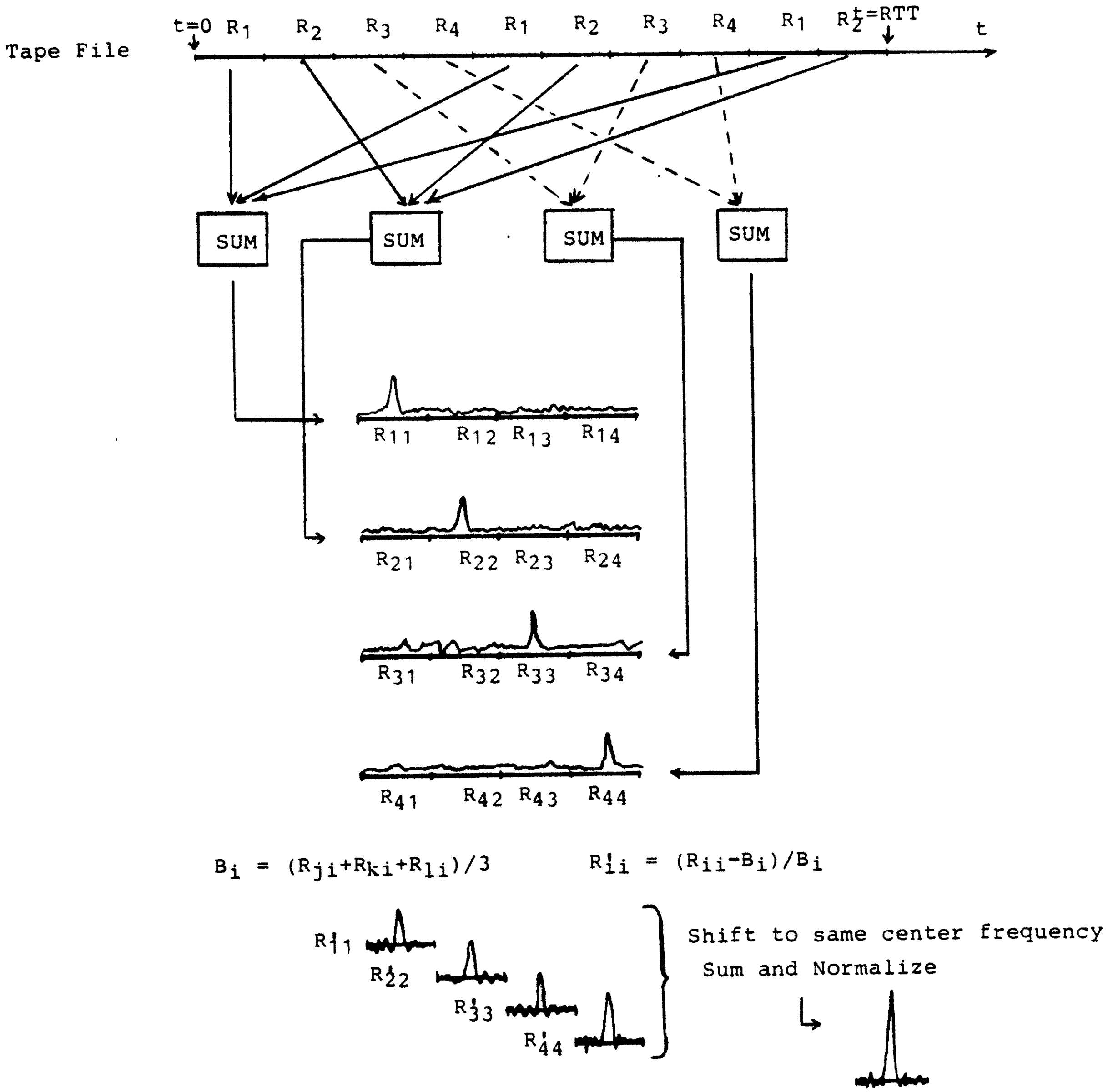
Tape File
t=0
R_1 R_2 R_3 R_4 R_1 R_2 R_3 R_4 R_1 R_2
t=RTT
t
SUM
SUM
SUM
SUM
R_{11} R_{12} R_{13} R_{14}
R_{21} R_{22} R_{23} R_{24}
R_{31} R_{32} R_{33} R_{34}
R_{41} R_{42} R_{43} R_{44}
$B_i = (R_{ji}+R_{ki}+R_{li})/3$
$R'_{ii} = (R_{ii}-B_i)/B_i$
R'_{11}
R'_{22}
R'_{33}
R'_{44}
Shift to same center frequency
Sum and Normalize

Fig. II.1

APPENDIX 3

PROCESSING OF THE ECHO SIGNAL

a) IF to video

A block diagram of the receiving system is given in figure 3.4. We will be most concerned here with the transformations undergone by the received signal after the original high frequency mixing with the (2410 MHz + Doppler) signal. By this single mixing, the received signal is heterodyned to the value $F_H = 30$ MHz $- \Delta f_k$, where Δf_k is related to the increment in transmitted frequency in the frequency-switching process:

Transmitted frequency: $F_k = F_1 + (k-1).\Delta f_s \quad k=1,4$

$$\text{and} \quad \Delta f_k = F_k - 2380 \text{ MHz}$$

For the observations of comet P/Encke we had:

$F_1 = 2379.999328$ MHz and $\Delta f_s = 448$ Hz

while for the other obvservations (G-S, Austin, C-G) we had:

$F_1 = 2379.999430$ and $\Delta f_s = 380$ Hz.

These last parameters are those which we will use as example in the following discussion.

After passing through a band pass filter and before being sampled, the F_H signal is split into two parts which are fed into a set of two phase detectors in a way described below, in order to keep all the information necessary to recover the amplitude and phase of the original signal after sampling.

Each one of the two signals obtained at the output of the power splitter is directed into a phase detector where, in one of the phase detectors, the sine wave is shifted in phase by 90° with respect to the other so that at the output of the two phase detectors, the signals have the same amplitude but are on phase quadrature. The outputs of these two detectors, respectively referred to as cosine and sine channels are sampled separately in an analog/digital (A/D) converter, to yield two series of samples: $x(t_k)$ for the cosine channel and $y(t_k)$ for the sine channel. The main aspects of this technique have been described by Pettengill (1964) and Evans (1968). Basically, one can look at the two series of samples $x(t_k)$ and $y(t_k)$ as the cosine and sine components of the signal, so that by considering them as two orthogonal vector components, their resultant represents the original vector.

b) Sampling

One of the main characteristics which have to be chosen and which determines the sampling parameters is the frequency resolution required in the final spectrum. At the time of observations the timing system of the Arecibo S-band radar could not accommodate frequency resolutions narrower than 1 Hz. So, since the goal was to obtain the finest possible resolution in the comet observations (because of the predicted small size of the nucleus), we settled on a value $\delta f \approx 1$ Hz, with a system capability of $N = 2048$ samples for each channel (choice $N=2^m$ for more efficient computation of the discrete Fourier transform - see Cooley-Tukey algorithm (1965). Here $m=11$).

We were thus led to use a total video bandwidth of about $B \approx 2.1$ KHz ($\approx N \times \delta f$), which corresponds to about 1 KHz on each side of the original center frequency (2380 MHz + Doppler). Consequently, video frequency components in the approximate range -1 KHz to +1 KHz with respect to the center frequency could be accepted. Since we opted for a frequency switching technique using four different frequencies during transmission, the corresponding received frequency has to fall within this bandwidth B. This sets an upper limit of about 500 Hz on the frequency step Δf_s between transmitted frequencies: $4\Delta f_s < B$. On the other hand, a lower limit on Δf_s is set by the need for accommodating comfortably inside the restricted bandwidth Δf_s the uncertainties in the predicted position of the echo (this "restricted bandwidth" is defined as the bandwidth of the final spectrum, after superposition of the records corresponding to the transmission and reception of the four frequencies $F_1 \longrightarrow F_4$. See Appendix 2).

The sampling frequency chosen follows from the sampling theorem which states that "a function whose Fourier transform is zero for $|f| > f_c$ is fully specified by values spaced at equal intervals not exceeding $\zeta = 1/2\ f_c$, save for any harmonic terms with zeros at the sampling points" (Bracewell 1978). The minimum sampling frequency necessary to retain the information relative to the frequencies components $|f| < B/2$ is thus B. This value was adopted (exactly B = 2.092 KHz), resulting in sampling every $\zeta = 478\ \mu s$ (ζ is called the sampling interval, or also the gate width). The signal was thus coherently integrated for a period:

$$T = N \times \zeta \quad (\equiv 978944\ \mu s)$$

The cosine and sine transform are calculated in an array processor and combined so that the squared magnitude of the Fourier transform corresponding to this coherent integration can be stored. Allowing about 100 μs for gate delays and about 2 ms for transfers and real time computations, a sampling cycle takes

$$T_c = 981044\ \mu s \quad (\approx 1\ \text{sec}).$$

c) Final Spectra

The same process is repeated continuously during the time corresponding to the reception of each of the four frequencies. This time is equal to the time during which the transmitter was dwelling on each particular frequency, i.e. T_d = 10 seconds in our case. Thus, during this time period T_d, about ten 1-second sampling cycles can be executed resulting in ten single spectra. The stored squared magnitudes of the Fourier transform for these cycles are summed to yield a single specrum corresponding to the non-coherent integration of the received signal for about 10 seconds. This is repeated for each of the four receiving steps in synchronism with the transmitted sequence. Each 10-second digitized spectrum is then written on tape and represents a single tape record. Each tape file is a set of consecutive blocks of 4 consecutive records. This set corresponds to the reception of the signal during the round-trip time of the signal.

It must be noted that because of the replicating properties of the sampling function, contribution from frequencies located mB (m integer) away from a desired frequency component (desired $\equiv |f| < B/2$) will be added on top of the contribution of this frequency component. In particular, noise power at frequencies $f + mB$ will be added to the power at frequency f. Thus, low-pass filtering has to be done before sampling, to remove, as much as possible, any contribution from noise components localized outside of the desired frequency band. Low-pass filters (see fig. 3.4) have been inserted between the phase detectors and the A/D converter, with a 1 KHz width, approximately matching the width of the band containing the desired frequency components.

Ideal or optimum receiving, which permits to maximize the signal-to-noise ratio for the echo by using a matched filter, i.e. a filter whose impulse response is a time-reversed version of the expected signal, cannot be done using a hardware filter in this case. Indeed, not only the shape and location of the echo from the target is unknown, but also the frequency-switching algorithm implies the need for an extended video bandwidth. The maximization of the signal-to-noise ratio is thus done in the data analysis using smoothing techniques equivalent to "software filtering", such as those described in section 10.1.

References:

A'Hearn, M.F., Dwek, E., and Tokunaga, A.T. (1981). Where is the ice in comets?, *Ap. J.*, *248*: L.147-151.

A'Hearn, M.F., Millis, R.L. and Birch, P.V. (1979). Gas and dust in some recent periodic comets, *A.J.*, *84*, 570-579.

Axford, W.I. and Keller, H.U. (1978). Are comets dirty snowballs or dust swarms?, *Nature*, *273*, 427-428.

Bay, Z. (1946) Reflection of microwaves from the Moon, *Hungaria Acta Physica*, *1*, 1-22.

Bevington, P.R. (1969). *Data reduction and error analysis for the physical sciences*, Mac Graw-Hill, New York.

Bortle, J. (1980). *Sky and Tel.*, *60*, 290.

Bracewell, R. (1978). *The Fourier transform and its applications*, McGraw-Hill, New York.

Breit, G., and Tuve, M. (1926). A test of the existence of the conducting layer, *Phys. Rev.*, *28*, 554-573.

Brin, G.D. (1980). Three models of dust layers on cometary nuclei, *Ap. J.*, *237*, 265-279.

Campbell, D.B., Chandler, J.F., Pettengill, G.H., and Shapiro, I.I. (1977). Galilean satellites of Jupiter: 12.6-centimeter radar observations, Science, 196, 650-653.

Campins, H. and Hanner, M. (1982). Interpreting the thermal properties of cometary dust, in "Comets", L.L. Wilkening Ed., Univ. of Arizona Press, 341-356.

Chaisson, E.J., Ingalls, R.P., Rogers, A.E.E., and Shapiro, I.I. (1975). Upper limit on the radar cross-section of the comet Kohoutek, Icarus, 24, 188-189.

Churyumov, K.I., and Gerasimenko, S.I. (1972). Physical observations of the short-period comet 1969IV, in "The motion, evolution of orbits and origin of comets", I.A.U. symposium 45, D. Reidel and Springer-Verlag, 27-34.

Cuzzi, J.N., and Pollack, J.B. (1978). Saturn's rings: Particle composition and size distribution as constrained by microwave observations, Icarus, 33, 233-262.

De Witt, J.M., Jr., and Stodola, E.K. (1949). Detection of radio signals reflected from the Moon, Proc. IRE, 37, 229-242.

Delsemme, A.H. (1979). Empirical data on the origin of "new" comets, in "Dynamics of the solar system", Proceedings of the 81st symposium of the International Astronomical Union held in Tokyo, Japan, 23-26 May

1978, 265-269.

Delsemme, A.H., and Miller, D.C. (1971). Physico-chemical phenomena in comets,III, The continuum of comet Burnham (1960 II), Planet.Space Sci., 19, 1229-1257.

Delsemme, A.H., and Rudd, D.A. (1973). Albedos and cross-sections of the nuclei of comets 1969IX, 1970II, and 1971I, Astron. Astrophys., 28, 1-6.

Donn, B. and Rahe, J. (1982). Structure and origin of cometary nuclei, in "Comets", L.L. Wilkening Ed., Univ. of Arizona Press, 203-226.

Encke, J.F. (1844). Ueber den Cometen von Pons, Abhandl. Berlin, 73-99.

Evans, J.V. (1968). Modulation, demodulation, and data processing applied to radar astronomy, in "Radar Astronomy", Evans and Hagfors Ed., MacGraw-Hill, NY, 499-546.

Evans, J.V., and T. Hagfors, Eds. (1968). Radar Astronomy. McGraw-Hill, New York.

Fay, T.D., and Wisniewski, W. (1978). The light curve of the nucleus of comet d'Arrest, Icarus, 34, 1-9.

Fernandez, J.A., and Ip, W.-H. (1981). Dynamical evolution of a cometary swarm in the outer planetary region, Icarus, 47, 470-479.

Fink, U., and Sill, G.T. (1982). The infrared spectral properties of frozen volatiles, in "Comets", L.L. Wilkening Ed., Univ. of Arizona Press, 164-202.

Finson, M.L. and Probstein, R.F. (1968). A theory of dust in comets I. Model and equations. Ap. J., 154, 327-352.

Gibson, D.M., and Hobbs, R.W. (1981). On the microwave emission from comets, Ap. J., 248, 863-866.

Green, D.W.E., and Morris, C.S. (1981). The 1980 apparition of periodic comet Encke. International Comet Quarterly, 3, 10-12.

Green, P.E. (1968). Radar measurements of target scattering properties, in "Radar Astronomy", Evans and Hagfors Ed., McGraw-Hill, NY, p.32.

Greenberg, J.M., Wang, R.T.,and Bangs, L. (1971). Extinction by rough particles and the use of Mie theory, Nature Phys. Sci., 230, 110.

Hanner, M. (1980). Physical characteristics of cometary dust from optical studies, In Solid Particles in the Solar System, (IAU symposium 90), eds. I. Halliday and B.A. McIntosh (Dordrecht: Reidel), 223-236.

Hellmich, R., and Keller, H.U. (1981). On the visibility of nuclei of dusty comets, Icarus, 47, 325-332.

Hey, J.S., and Stewart, G.S. (1947). Radar observations of meteors, *Proc. Phys. Soc. London*, *59*, 858.

Houziaux (1959). *Bull. Acad. Belg.*, *45*, 218.

Huebner, W.F., and Wiegert, A. (1966) Ice grains in comet comas, *Zs. f. Astrophys.*, *64*, 185-201.

Ip, W.-H., and Axford, W.I. (1982). Theories of physical processes in the cometary comae and ion tails, in "*Comets*", L.L. Wilkening, Ed., Univ. of Arizona Press, 588-634.

Jewitt, D.C., Danielson, G.E., Gunn, J.E., Westphal, J.A., Schneider, D.P., Dressler, A., Schmidt, M., and Zimmerman, B.A. (1982). Periodic comet Halley (1982i), recovery, IAU circular 3737, Central Bureau for Astronomical Telegrams.

Joss, P.C. (1973). On the origin of short-period comets, *Astron. & Astrophys.*, *25*, 271-273.

Jurgens, R.F., and Bender, D.F. (1977). Radar detectability of asteroids, a survey of opportunities for 1977 through 1987, *Icarus*, *31*, 483-397.

Jurgens, R.F., and Goldstein, R.M. (1976). Radar observations at 3.5 and 12.6 cm wavelengths of asteroid 433 Eros, *Icarus*, 31, 483-497.

Kamoun, P.G., Campbell, D.B., Ostro, S.J., Pettengill, G.H., and Shapiro, I.I. (1982). Comet Encke: Radar detection of the nucleus, Science, 216, 293-295.

Kamoun, P.G., Pettengill, G.H., and Shapiro, I.I (1982). Radar detectability of comets, in "Comets", L.L. Wilkening Ed., Univ. of Arizona Press, 288-296.

Kerr, D.E. (1951). in "Propagation of short radio waves", Mac Graw-Hill Book Company, First Edition.

Kresak, L. (1973). Short comets at large heliocentric distances, Bull. Astr. Inst. Czeck, 24, 264.

Lagrange , Additions a la connaissance du Temps pour 1814.

Laplace (1904). Oeuvres Completes, 13, 88.

Larson, S.M., and Minton, R.B. (1972). Photographic observations of comet Bennett (1970II), in Proceedings of the Tucson Comet Conference, Comets: Scientific Data and Missions, G.P. Kuiper and E. Roemer Ed., 183-208.

Levin, J. (1965). Power spectrum parameter estimation, Trans. IEEE PGIT It-11, 100-107.

Lyttleton, R.A. (1953). The comets and their origin, Cambridge

University Press.

Lyttleton, R.A. (1977). What is a cometary nucleus?, Q.J.Roy. Astr.Soc., 18, 213-233.

Marsden, B.G. (1967). One hundred periodic comets, Science, 155, 1207-1213.

Marsden, B.G. (1979). Catalog of cometary orbits, Central Bureau for Astronomical Telegrams, I.A.U., Third Edition.

Marsden, B.G., and Roemer, E. (1978). Comets in 1975, Q. Jl. R. astr. soc., 19, 59-89.

Marsden, B.G., and Sekanina, Z. (1974). Comets and non-gravitational forces VI. Periodic Comet Encke 1786-1971. A.J., 79, 413-419.

Morris, C.S. (1983). The 1982 apparition of periodic comet Grigg-Skjellerup, International Comet Quarterly, 5, 1, 3-5.

Muhleman, D.O., Goldstein, R.M., and Carpenter, R. (1965). A review of radar astronomy,I . IEEE Spectrum, 2, 44-55.

Ney, E.P. (1974). Multiband photometry of comets Kohoutek, Bennett, Bradfield and Encke, Icarus, 23, 551-560.

Ney, E.P. (1982). Optical and infrared observations of bright comets in the range 0.5 to 20 microns, in "Comets", L.L. Wilkening Ed., Univ. of Arizona Press, 323-340.

Ney, E.P., and Merrill, K. (1976). Comet West and the scattering function of cometary dust, Science, 194, 1051-1053.

Ney, E.P. (1982). Visibility of comet nuclei, Science, 215, 397-398.

O'Dell, C.R. (1973). A new model for cometary nuclei, Icarus, 19, 137-146.

Oort, J.H. (1950). The structure of the cloud of comets surrounding the solar system and a hypothesis concerning its origin, Bull. Astr. Inst. Netherlands, XI, 408, 91-110.

Oort, J.H., and Schmidt, M. (1951). Differences between new and old comets, Bull. Astr. Inst. Netherlands, XI, 419, 259-270.

Opik, E. (1932). Note on stellar perturbations of nearly parabolic orbits, Proc. Am. Acad. Arts Sci., 67, 169-183.

Ostro, S.J., Campbell, D.B., Pettengill, G.H., and Shapiro, I.I. (1980). Radar observations of the icy Galilean satellites, Icarus, 44, 431-440.

Pettengill, G.H. (1964). Spectral measurement techniques in planetary radar. Radio Science Journal of Research, Nat. Bur. of Stan., vol.

68D, 9, 1025-1029.

Pettengill, G.H., Ostro, S.J., Shapiro, I.I., and Campbell, D.B. (1979). Radar observations of asteroid 1580 Betulia, Icarus, 40, 350-354.

Pettengill, G.H., and Jurgens, R.F. (1979). Radar observations of asteroids, in "Asteroids", Tom Gehrels Ed., Univ. of Arizona Press, 206-211.

Price, R. (1968). Detectors for radar astronomy, in "Radar astronomy", Evans and Hagfors Ed., McGraw-Hill, NY, 547-614.

Roemer, E. (1962). Activity in comets at large heliocentric distance, Pub. Astr. Soc. Pacific, 74, 351-365.

Roemer, E. (1963). Comets: Discovery, orbits, astrometric observations, In The Moon, Meteorites and Comets, eds. B.M. Middlehurst and G.P. Kuiper (Chicago: University of Chicago Press), 527-549.

Roemer, E. (1966). The dimensions of cometary nuclei. Memoires Soc. Roy. Sci. Liege, sec. 5, 12, 23-28.

Schatzman, E. (1953). La structure et l'evolution des noyaux cometaires, Memoires Soc. Roy. Sci. Liege, Ser. 4, 13, 353-356.

Sekanina, Z. (1974). On the nature of the anti-tail of comet Kohoutek (1973f).I, A working model, Icarus, 23, 502-518.

Sekanina, Z. (1976a). Has the cometary nucleus been resolved?, in The Study of Comets, part II, eds. B. Donn et al,(NASA SP-393) 537.

Sekanina, Z. (1976b). A probability of encounter with interstellar comets and the likelihood of their existence, Icarus, 27, 123-133.

Sekanina, Z. (1979). Fan-Shaped coma, orientation of rotation axis and surface structure of a cometary nucleus. I. Test of a model on four comets, Icarus, 37, 420-442.

Sekanina, Z. (1981). Rotation and precession of cometary nuclei, Ann. Rev. Earth Planet. Sci., 9, 113-145.

Sekanina, Z., and Miller, F.D. (1973). Comet Bennett 1970II, Science, 179, 565-567.

Sekanina, Z., and Schuster, H.E. (1978). Dust from periodic comet Encke: Large grains in short supply, Astron. Astrophys., 68, 429-435.

Sekanina, Z., and Schuster, H.E. (1978). Meteoroids from periodic comet D'Arrest, Astron. Astrophys., 65, 29-35.

Spinrad, H. (1981). Spectroscopy of comet P/Encke in 1980-81. (JPL report).

Van Woerkom, A.J.J. (1948). On the origin of comets, Bull. Astr. Inst. Netherlands, X, 399, 445-472.

Vsekhsvyatskii, S.K. (1964). "Physical characteristics of comets", Translation from Russian, Israel Program for Scientific Translations (NASA TT F-80, OTS 62-11031).

Wallis, M.K. (1982). Dust-gas dynamics in real comets, in "Comets", L.L. Wilkening Ed., Univ. of Arizona Press, 357-369.

Weaver, H.A., Feldman, P.D., Festou, M.C., A'Hearn, M.F., and Keller, H.U. (1981). IUE observations of faint comets, Icarus, 47, 449-463.

Westphal, W.B., and Sils, A. (1972). Dielectric constant and loss data, Technical report AFML-TR-72-39, Mass. Inst. of Tech., 145-147.

Whipple, F.L. (1950). A comet model. I. The acceleration of comet Encke. Ap. J., 111, 375-394.

Whipple, F.L. (1951). A comet model. II. Physical relations for comets and meteors. Ap. J., 113, 464-474.

Whipple, F.L. (1963). On the structure of the cometary nucleus. In The Moon, Meteorites and Comets, eds. B.M. Middlehurst and G.P. Kuiper (Chicago: University of Chicago Press), 639-664.

Whipple, F.L. (1978a). Comets, in Cosmic Dust, ed. J.A.M. McDonnell (New York: J. Wiley and Sons), 1-73.

Whipple, F.L. (1978b). Cometary brightness variation and nucleus structure. Moon and Planets, 18, 343-359.

Whipple, F.L. (1981). On observing comets for nuclear rotation, Processing of a workshop on "Modern Observational Techniques for Comets", held at Goddard Space Flight Center in Oct. 1980.

Whipple, F.L. (1981). Notes on the P/Halley nucleus, in Proc. International Meeting on the Giotto mission, Noordwijkerhout, Netherlands, 27-28 April 1981 (ESA SP-169).

Whipple, F.L. (1982). The rotation of cometary nuclei, in "Comets", L.L. Wilkening Ed., Univ. of Arizona Press, 227-250.

Whipple, F.L. (1983). Cometary nucleus and active regions, in "Proc. of the Intern. Confer. on Cometary Exploration", Budapest, in press.

Whipple, F.L., and Huebner, W.F. (1976). Physical processes in comets, Ann. Rev. Astr. Astrophys., 14, 143-172.

Whipple, F.L., and Sekanina, Z. (1979). Comet Encke: precession of the spin axis, non-gravitational motion, and sublimation, Astron. J., 84, 1894-1909.

Wright et al. (1979). Comet plasma densities deduced from refraction of occulted radio sources, Icarus, 38, 123-135.

Wyckoff, S. (1982). Overview of comet observations, in "Comets", L.L.

Wilkening Ed., Univ. of Arizona Press, 3-55.

Wyckoff, S., and Wehinger, P.A. (1976). On the ionization and excitation of H_2O^+ in comet Kohoutek (1973f), Ap. J., 204, 616-625.

Yeomans, D.K. (1981). The comet Halley handbook, an observer's guide, JPL - 400/91, NASA.

Yeomans, D.K., Jacobson, R.A, Williams B.G., and Chodas, P.W. (1983). Comet Halley ephemeris uncertainties in 1985-1986, in "Proc. of the Intern. Confer. on Cometary Exploration, Budapest, in press.